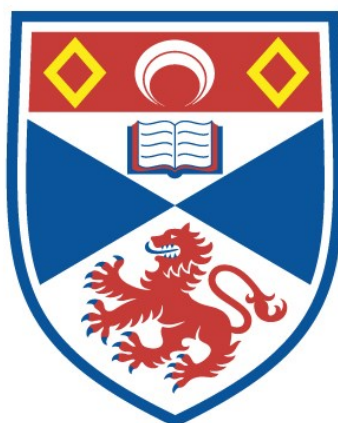X-RAY CRYSTALLOGRAPHIC ANALYSIS OF ADORABLE ZEOLITES AND METAL-ORGANIC FRAMEWORKS

Susan Elizabeth Henkelis

A Thesis Submitted for the Degree of PhD
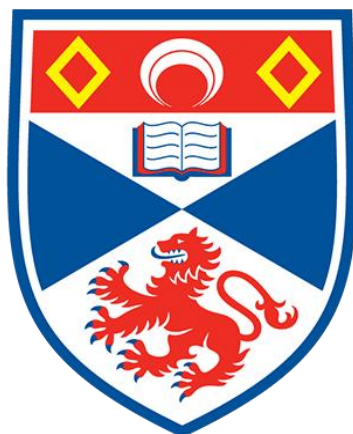at the
University of St Andrews

2019

Full metadata for this item is available in
St Andrews Research Repository
at:
http://research-repository.st-andrews.ac.uk/

Please use this identifier to cite or link to this item:
http://hdl.handle.net/10023/17923

X-ray Crystallographic Analysis of ADORable Zeolites and Metal-Organic Frameworks

Susan Elizabeth Henkelis

This thesis is submitted in partial fulfilment for the degree of

Doctor of Philosophy (PhD)

at the University of St Andrews

February 2019

DECLARATIONS

I, Susan Elizabeth Henkelis, do hereby certify that this thesis, submitted for the degree of PhD, which is approximately 45,000 words in length, has been written by me, and that it is the record of work carried out by me, or principally by myself in collaboration with others as acknowledged, and that it has not been submitted in any previous application for any degree.

I was admitted as a research student at the University of St Andrews in September 2015.

I received funding from an organisation or institution and have acknowledged the funder(s) in the full text of my thesis.

Date   Signature of candidate

Supervisor's declaration

I hereby certify that the candidate has fulfilled the conditions of the Resolution and Regulations appropriate for the degree of PhD in the University of St Andrews and that the candidate is qualified to submit this thesis in application for that degree.

Date   Signature of supervisor

Permission for publication

In submitting this thesis to the University of St Andrews we understand that we are giving permission for it to be made available for use in accordance with the regulations of the University Library for the time being in force, subject to any copyright vested in the work

not being affected thereby. We also understand, unless exempt by an award of an embargo as requested below, that the title and the abstract will be published, and that a copy of the work may be made and supplied to any bona fide library or research worker, that this thesis will be electronically accessible for personal or research use and that the library has the right to migrate this thesis into new electronic forms as required to ensure continued access to the thesis.

I, Susan Elizabeth Henkelis, confirm that my thesis does not contain any third-party material that requires copyright clearance.

The following is an agreed request by candidate and supervisor regarding the publication of this thesis:

Printed copy

No embargo on print copy.

Electronic copy

No embargo on electronic copy.

Date   Signature of candidate

Date   Signature of supervisor

Underpinning Research Data or Digital Outputs

Candidate's declaration

I, Susan Elizabeth Henkelis, understand that by declaring that I have original research data or digital outputs, I should make every effort in meeting the University's and research funders' requirements on the deposit and sharing of research data or research digital outputs.

Date   Signature of candidate

Permission for publication of underpinning research data or digital outputs

We understand that for any original research data or digital outputs which are deposited, we are giving permission for them to be made available for use in accordance with the requirements of the University and research funders, for the time being in force.

We also understand that the title and the description will be published, and that the underpinning research data or digital outputs will be electronically accessible for use in accordance with the license specified at the point of deposit, unless exempt by award of an embargo as requested below.

The following is an agreed request by candidate and supervisor regarding the publication of underpinning research data or digital outputs:

No embargo on underpinning research data or digital outputs.

Date   Signature of candidate

Date   Signature of supervisor

ACKNOWLEDGMENTS

First and foremost, I would like to say a big thank you to Russell for giving me the opportunity to join the REM group. The countless opportunities to present at conferences, the ongoing support and guidance and allowing me to follow my dreams outside of academia, and perhaps more importantly his appreciation for decent baked goods.

I would especially like to thank Paul for his ever-present support, solitaire expertise and words of advice - which occasionally were kind. I couldn't have completed this PhD without his unparalleled knowledge of porous materials and on-going tutelage.

Thank you to all members of the Morris group, especially Sam, Simon and Cameron. Without you guys I wouldn't have achieved as much as I have and I'm sure I would have sacked it in a long time ago. The cake, the coffee and the wine – all the necessary components to daily PhD life were always in plentiful supply. I hope Coffee and Wine Club continue when I'm gone.

Without Suzi, my life at St Andrews would have been very different. I'm not sure which one of us was the bad influence, but every event whether small or large always involved copious amounts of wine. I thank her for not judging my love of crime dramas, eclectic taste in music, love of pyjamas, or the ever-present smell of horse that always seemed to permeate our flat.

Mum and Dad – thank you for indulging my attempt at a career with animals, even if it did all fall through just from one visit to a Chemistry Open Day. Mum – I couldn't have done this without you, you have been my constant throughout the last 4 years. Of course this was always helped by copious amounts of gin.

When people talk about looking up to their siblings, no one could have done that more than me. James and Nic you showed me that hard work really does pay-off. Thank you.

Finally, and probably the most important, thank you to my unruly, arrogant and obnoxious horse, Morris.

"Just Keep Swimming"

Dory

ABSTRACT

This thesis largely focuses on the mechanistic analysis of the Assembly-Disassembly-Organisation-Reassembly (ADOR) process through a range of crystallographic techniques including powder X-ray diffraction and Pair Distribution Function (PDF) analysis and subsequent analysis using solid-state kinetics.

Chapter 4 describes the development of a new standard protocol to using the ADOR process. The protocol describes the development of a procedure used for identifying the optimum conditions (time of reaction, temperature, acidity, etc.) for the ADOR process. In developing the protocol, Ge-containing **UTL** zeolites were subjected to hydrolysis conditions using both water and hydrochloric acid as media, which provides an understanding of the effects of temperature and pH on the Disassembly (D) and Organisation (O) steps of the process that define the potential products. Samples were analysed by powder X-ray diffraction to yield a time course for the reaction at each set of conditions.

Chapter 5 continues work on the ADOR process and presents the first kinetic study on the two most prominent steps in the process; Disassembly and Organisation. By using solid-state kinetic models, Avrami-Erofeev and its linear equivalent Sharp-Hancock, the dependence on temperature and presence of liquid water was investigated and the activation energy of the rearrangement process quantified. Work on the rearrangement step aimed to understand where the silica species intercalates from and which material formed as the kinetic and thermodynamic product from the reaction.

Chapter 6 describes a study into the Disassembly and Organisation steps of the ADOR process through *in situ* Pair Distribution Function (PDF) analysis. This hopes to shed light on the selectivity of the ADOR process in different media and the mechanism by which the double-four-ring (d4r) breakdown.

On a different note, Chapter 7 describes the refinement of synthesis conditions used to prepare poly-crystalline CPO-27-M (MOF-74) with lower concentrations of base and at low temperature. Refinement of the synthesis of single crystal CPO-27-Mg, -Zn and UTSA-74 was undertaken and the necessary components to forming large single crystals understood.

PUBLICATIONS

Publications Arising from this Thesis:

Chapter 4:

S. E. Henkelis, M. Mazur, C. M. Rice, G. P. M. Bignami, P. S. Wheatley, S. E. Ashbrook, J. Čejka, and R. E. Morris, *Nature Protocols*, 2019, **14**, 781-794

Chapter 5:

S. E. Henkelis, M. Mazur, C. M. Rice, P. S. Wheatley, S. E. Ashbrook, and R. E. Morris, *J. Am. Chem. Soc.*, 2019, **141**, 4453-4459

Chapter 6:

S. E. Henkelis, S. A. Morris, M. Mazur, P. S. Wheatley, L. N. McHugh, and R. E. Morris, *J. Mater. Chem. A*, 2018, **6**, 17011-17018

Chapter 7:

S. E. Henkelis,* L. McCormick, D. B. Cordes, A. M. Z. Slawin, and R. E. Morris, *Inorg. Chem. Commun.*, 2016, **65**, 21-23

S. M. Vornholt,‡ S. E. Henkelis, ‡* and R. E. Morris, *Dalton Transactions*, 2017, **46**, 8298-8303

S. E. Henkelis, S. M. Vornholt, D. B. Cordes, A. M. Z. Slawin, P. S. Wheatley, and R. E. Morris, *CrystEngComm.*, 2019, Accepted

TABLE OF CONTENTS

CHAPTER 1: INTRODUCTION

In the following introduction, zeolites and the issues surrounding the preparation of new zeolites is discussed (the zeolite conundrum), followed by an in-depth discussion on each fundamental step of the ADOR process and how new "unfeasible" daughter zeolites can be prepared from parent germanosilicates.

1.1.   Porous Solids

Crystalline porous solids can be described as materials that have regular voids throughout the material, these could take the form of cavities, channels or interstices.[1] The characteristics of porous materials vary greatly depending on the size, shape and composition of the internal voids and this can be exploited to create a porous material with desirable characteristics for a specific application,[2] for example zeolites are excellent candidates for heterogeneous catalysis.[3–8] Uses of important porous materials include catalysts,[9–12] ceramics,[13–15] pigments,[16,17] membranes,[18–21] sensors,[22] electrodes and batteries.[23–25] Many of the porous materials prepared and used in industry today include Metal-Organic frameworks (MOFs)[26–32] and zeolites (Figure 1.1).[9–12,33–38]
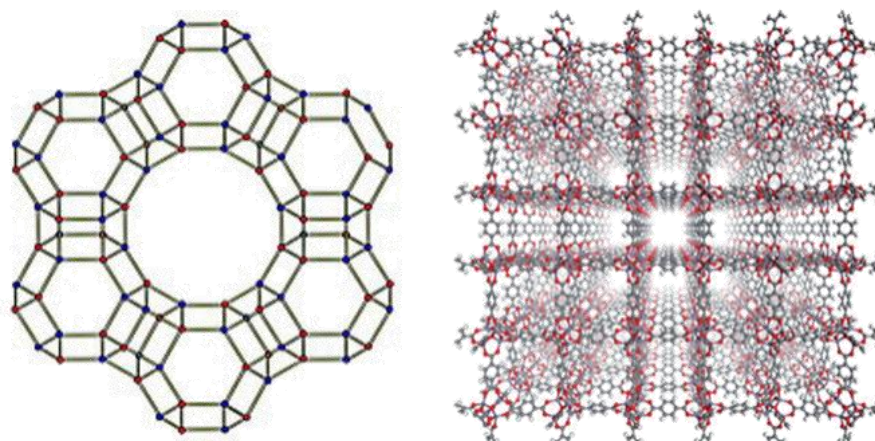
Figure 1.1. The channel systems shown in Zeolite-Y (left) with the T-O-T bonds shown by grey lines, and MOF-5 (right) where the channels are made of zinc metal clusters and 1,4-benzodicarboxylate.

1.2.   Zeolites and their Conundrum

The history of zeolites dates back to 1756 when Axel F. Cronstedt, a Swedish mineralogist, first discovered and identified peculiar properties of minerals found in a copper mine in Lapland, Sweden. He found that when the mineral stilbite was heated in a blow-pipe, it appeared to boil, as such he coined the term zeolite from the Greek words ζέω = to boil and λίθος = stone.[39] Zeolites have since been characterised as porous materials made up of corner-sharing TO_4 tetrahedral units, where the T atom is traditionally silicon or aluminium, but can also be germanium, iron, phosphorus etc. Each TO_4 unit represents the zeolites primary building unit (PBU), these PBUs can then be built up to form 2- or 3-dimensional networks with different size channel systems dependent on synthesis conditions (Figure 1.2).
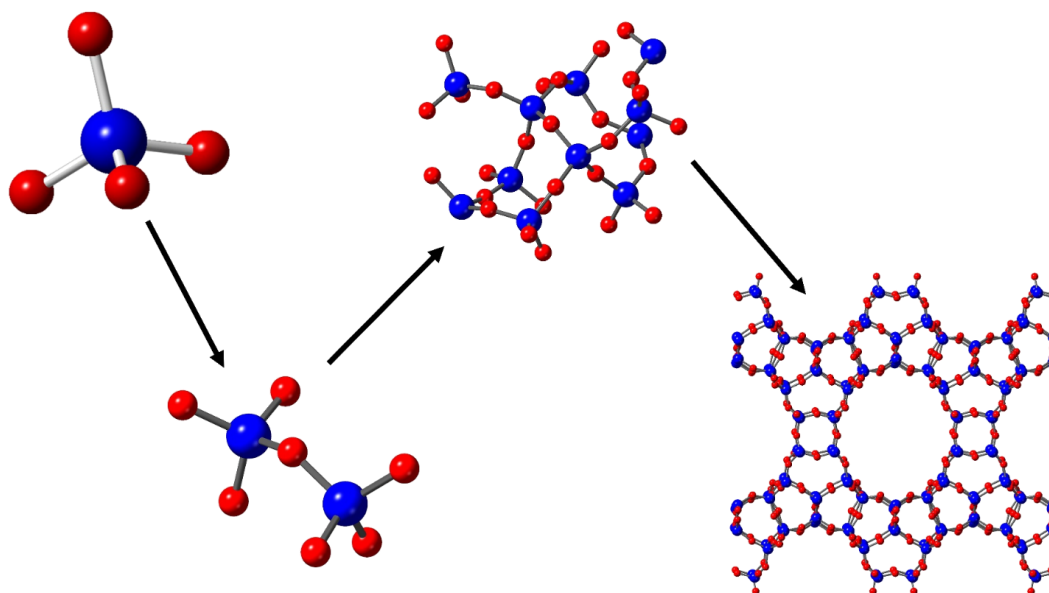
Figure 1.2. A schematic to show the connectivity of TO_4 tetrahedra to form parent zeolite **UTL**.

Today, there are 239 synthetic zeolites in the International Zeolite Association (IZA)[40] database and each of these zeolites tends to form as the lowest density structure possible when made using traditional hydrothermal synthesis. The "zeolite conundrum" can be visualised in Figure 1.3, where each black dot represents a potential (theoretical) zeolite that could be made. However, all zeolites in the IZA database lie on the correlation line shown in red.[41] Clearly a new approach is needed to break through the synthesis barrier and access

the countless other structures possible. To do this, a top-down synthetic approached termed the Assembly-Disassembly-Organisation-Reassembly (ADOR) process [42–45] has been developed to produce new "unfeasible" zeolites that lie off the traditional correlation line by exploiting the inherent weakness in germanosilicates. This will be discussed in detail below.
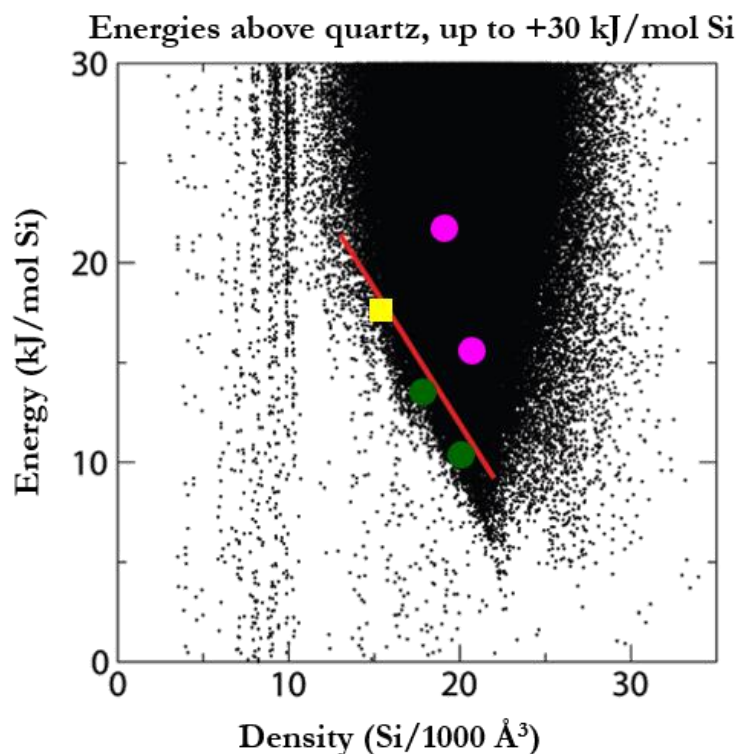
Figure 1.3. The zeolite conundrum. Each black dot represents a theoretical zeolite. The traditional correlation line is shown in red. **UTL** – yellow square, IPC-2 and IPC-4 – green circles, "unfeasible" IPC-9 and IPC-10 – pink circles. Figure adapted from reference 46.

1.3.   Applications of Zeolites

High silica zeolites are an important class of microporous solids that are widely used in industry. The many different structural topologies available to zeolites open up many different potential uses and so there remains a strong drive to prepare new zeolites. They are one of the most important families of heterogeneous catalysts in use today,[47,48] but are also used in a wide variety of other applications from ion exchange and water softening, through to medical applications.

The 3-dimensional channels can be tuned to accommodate organic molecules of a similar size and can selectively sort out these organic molecules by size/shape exclusion. In the 1950s Union Carbide used zeolites to separate unsaturated aliphatic hydrocarbons in an industrial setting. This, and the synthesis of zeolites A, X, and Y, paved the way for zeolites to be used as molecular sieves and ultimately increased the amount of zeolite research being undertaken.

Zeolites can also be used in water softening applications by using their channel system to exchange loosely bound water molecules and cations from within the framework with ions from the aqueous solution. In water softening, Ca^{2+} ions are removed from the water.[49]

1.4.   Synthetic Approaches to Zeolites

There are two general umbrellas that describe the synthetic approaches to forming new zeolites. Traditional, where the zeolite is formed through successive crystallisation processes, and therefore the porosity is incorporated during the initial synthesis. The pore system can also be achieved through post-synthetic manipulation of pre-formed zeolites.[12]

1.4.1.   Traditional Synthetic Methods

Forming new zeolites by traditional synthetic methods can be achieved in 3 ways, hydrothermal, solvothermal, and ionothermal synthetic approaches.

1.4.1.1. Hydrothermal

Zeolites, in general, follow Ostwald's law of successive reactions. The law states that the first amorphous phase is consumed and replaced by a thermodynamically meta-stable second phase, this then continues until the most stable phase is formed. This is apparent in the hydrothermal synthesis of zeolites, whereby the successive crystallisation of solids in aqueous media occurs at temperatures above the boiling point of water and autogenous pressure in a Teflon-lined steel autoclave. Templates and structure-directing agents (SDAs) may be added

at this stage to direct the synthesis to afford a desired product. In general terms, a typical zeolite synthesis is as follows:

i. Silica, germania and/or alumina reactants are mixed with a cationic source in a basic solution. If directing agents are to be used, they would be added in this step.

ii. The aqueous reaction mixture (solution or gel) is heated to high temperatures (100-150 °C) and high pressure in a Teflon-lined steel autoclave for 2-14 days.

iii. The reaction mixture remains amorphous during an induction period.

iv. The zeolite nuclei begin to crystallise to successively form primary building units, secondary building units and then polyhedra until all amorphous material has been consumed and only the zeolite remains.

v. The zeolite product is collected by filtration, washed with water and dried.

1.4.1.1.1. Templates and Structure-Directing Agents

Many zeolite syntheses involve the use of a template. There are three different types of templates: "true" templates that direct the framework to adopt the configuration unique to the template; structure-directing agents, which direct a specific product to form; space-filling species.

When designing a new template, there are criteria that must be fulfilled for it to be effective:

(i) The surface properties should match the properties of the reaction mixture.

(ii) They need to be stable at the synthesis temperature.

(iii) Once the template is removed, the zeolite must remain stable.[12]

The size and shape of the templates can be used to effectively control the pore size of the zeolite produced, however many templates are expensive, and the lengthy synthesis time limits the synthesis of zeolites to conventional laboratory settings.

Cationic organic structure-directing agents work in two ways, (1) they balance the charge of the framework or (2) they fill the void place in zeolites. As the surface of the zeolite is hydrophobic, the organic will fill these areas, separating from the aqueous mixture. As such, by packing into the channel systems of the zeolite, the thermodynamic stability can be greatly increased. Such organics direct the nucleation process and therefore only one product can

be afforded. An example of this is the synthesis of **UTL**. The synthesis of **UTL** is directed by a SDA - (6*R*,10*S*)-6,10-dimethyl-5-azoniaspiro[4,5]decane hydroxide.

Mineralizers such as sodium hydroxide (OH⁻) have a direct impact on the synthesis dynamics and essentially dissolve silica/alumina etc. providing a reversible T-O-T hydrolysis, which is essential for the formation of a crystalline product. More recently, fluoride (F⁻) has been used as a mineralizer and structure-directing agent. It allows the synthesis to be conducted at neutral/acidic conditions with reduced amount of water, and as such this has led to the formation of all-silica zeolites.[50]

1.4.1.2. Solvothermal

Solvothermal synthesis of zeolites is essentially the same as the hydrothermal method discussed above, with one major difference: the solvents used are of low polarity. For example, triethylene glycol and 1,4-dibutanediol. By using solvothermal synthesis, it is possible to obtain the zeolite product as large single crystals, thus allowing their structure to be determined by single crystal X-ray diffraction. An example of this, is the synthesis of Si-MFI. Microwave-assisted solvothermal synthesis in isopropanol afforded Si-MFI as round, flat crystals.[51]

1.4.1.3. Ionothermal

Ionic liquids are a class of organic solvents that have high polarity and a pre-organised solvent structure. They have a high thermal stability making them ideal candidates for synthesising materials by hydro/solvothermal conditions.

Ionothermal synthesis uses ionic liquids as both the solvent and structure directing agent (template) to prepare both zeolites and metal-organic frameworks. It was thought that by using solely ionic liquids instead of SDAs, the competition between the solvent and the template could be removed, which would ultimately increase the templating effect of the organic. Ionothermal synthesis has successfully been used to make new zeotype materials including novel AlPOs, CoAlPOs and GaPOs.[52]

1.4.2. Post-synthetic Manipulation

A pre-assembled 3-dimensional zeolite can be post-synthetically modified to introduce additional porosity by way of demetallation techniques. Layered zeolite precursors can undergo delamination, swelling or pillaring to afford new zeolites.

1.4.2.1. Demetallation

Demetallation is the term used to remove framework atoms (Al, B, Ge, Si, Ti etc.) which introduces extra porosity into the structure. Breaking these bonds can be done by treating chemically (acid or alkali), hydrothermally (steaming) or physically (radiation). The zeolites prepared in this manner have an additional intra-crystalline pore system and typically exhibit a wider pore size distribution.[12]

Removing only the aluminium (dealumination) creates zeolites with an intra-crystalline pore system, however the Si/Al ratio can be drastically changed, as such changing the acidic properties of the material. The connectivity of the pores after dealumination is often low.

Desilication however, can occasionally create extra porosity without a substantial impact on the acidic properties, and with a highly interconnected pore system. Tuning the treatment conditions (time, temperature, concentration of base) allows the size and volume of the pores to be easily controlled.[12]

1.4.2.2. Layered Zeolite Precursors

Layered zeolite precursors can undergo separation of the layers to create a "house of cards", an array of zeolite-type layers that contain inter-lamellar mesoporosity. In many cases, 3-dimensional zeolites can be formed from a layered zeolite precursor upon calcination, for example the zeolite **FER** is afforded from the calcination of its layered precursor PREFER.[53,54] More interestingly, some zeolites can only be obtained via their layered precursor, examples include, **NSI**, **CDO**, **RRO**, **RWR**, and **PCR**.[55] Modifying the layered precursor before calcination can lead to more than one 3-dimensional zeolite afforded, and this is dependent on the post-synthetic approach chosen. These layered materials can be treated similarly to clay or clay-based materials, which introduces mesoporosity between

separated layers, by way of intercalation and pillaring. Figure 1.4 highlights how one layered zeolite precursor (MCM-22P) can form a family of zeolites through delamination, pillaring and swelling.[56] Layered materials can be manipulated by new techniques such as silylation[57] and the Assembly-Disassembly-Organisation-Reassembly (ADOR) process.[44] This thesis will primarily focus on the ADOR approach to synthesise new zeolites.
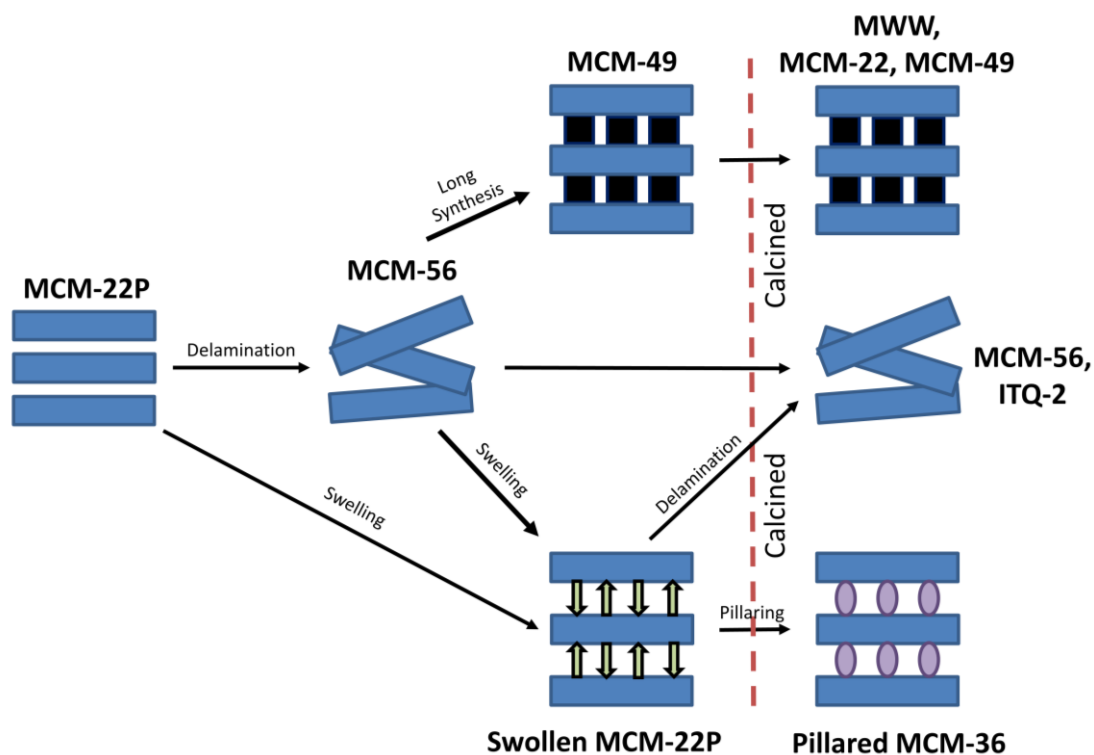
Figure 1.4. The MCM-22 family. A schematic showing the top-down approach to forming new zeolites from one layered material. The dashed red line shows uncalcined (left) and the materials produced after subsequent calcination (right).

1.5.   Germanosilicates

Tetravalent germanium can be isomorphically incorporated into the structure of many traditional silicates by substituting some (or all) silicon for germanium. Germanium is a larger cation than silicon so will preferentially occupy space in the double-four-ring (d4r) rather than in the layers of the zeolite. The bond lengths (Ge-O; 1.74 Å) and angles (Ge-O-Ge; 130-140 °) differ to those of Si-O-Si (1.62 Å and >140 °) and as such, due to the longer bond length and smaller angle around the cation, the strain in the d4r can be released.[55]

Current germanosilicates include but are not limited to **UTL**,[43,59,60] **ITH**,[42] **ITR**,[42] **IWR**,[42] **IWW**,[45] **UOV**[61,62] and the recently discovered SAZ-1[60]. These germanosilicates all contain d4r's, with the germanium preferentially occupying the d4r and have successfully been used in the ADOR process (Figure 1.5).
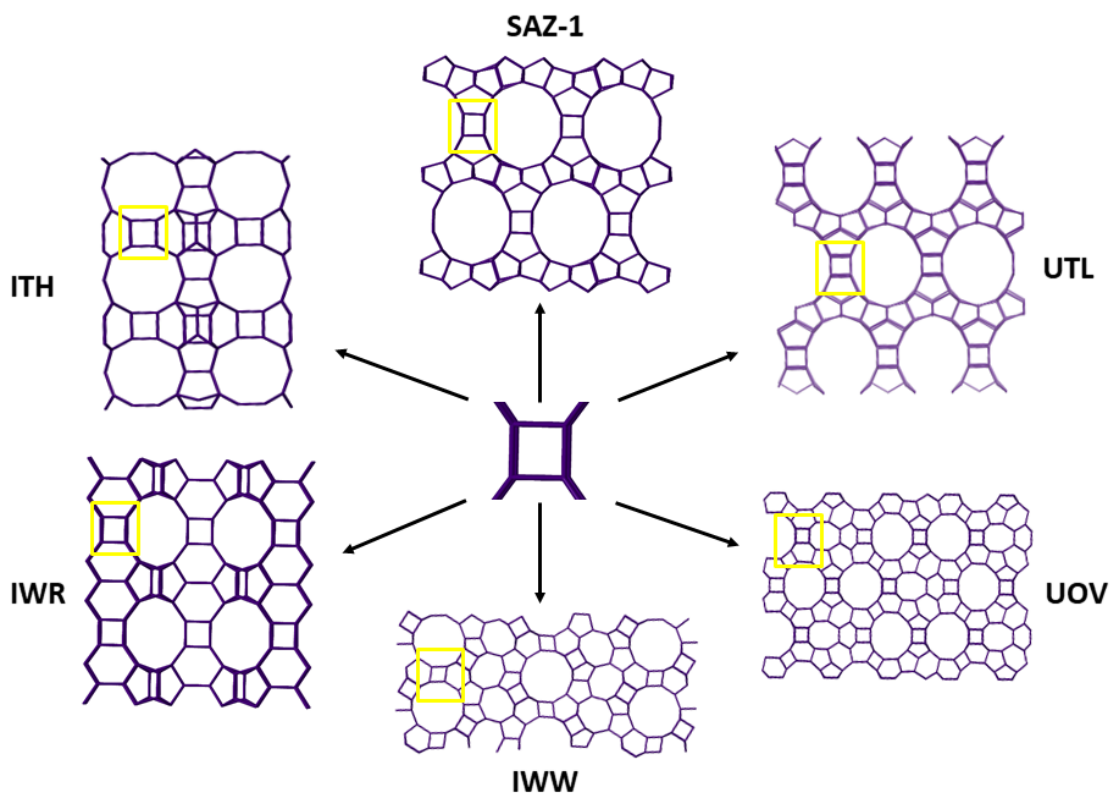
Figure 1.5. Double-four-ring containing germanosilicates currently used in the ADOR process. d4r are highlighted by a yellow box.

A well-known paper published in *J. Phys. Chem. C.* by Corma *et al.*, studied the effect of different amounts of GeO_2 added to the reaction mixture of silica zeolites. The feasibility was calculated computationally and a range of germania and silica zeolites produced. They showed that due to the presence of d4r, zeolite Beta-C (**BEC**) could potentially be formed as either a pure germania, pure silica, or a mixture of the two.[64] The Ge-containing polymorph C from **BEC** was synthesised by using the hydroxide form of benzyl-DABCO (DABCO = 1,4-diazabicyclo[2.2.2]octane; BD^+) as a SDA. However, when the reaction was synthesised without germanium, a different structure ZSM-12 (**MTW**) was afforded (Figure 1.6).[65] This strongly suggests that Ge does indeed promote the formation of the d4r units.
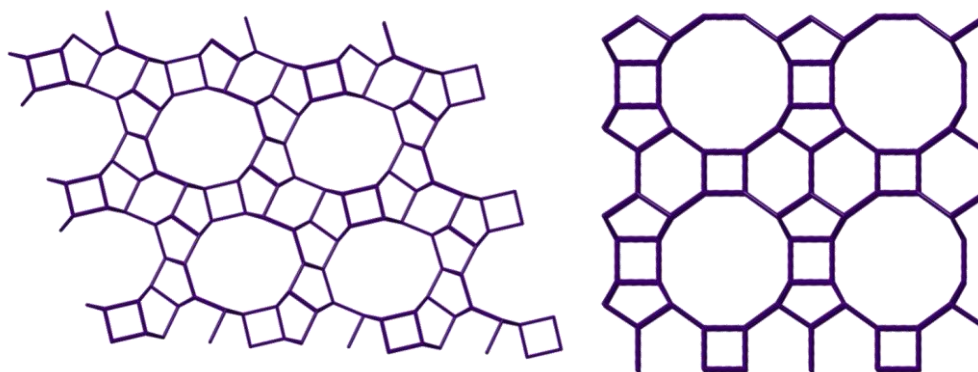
Figure 1.6. The crystallographic structures of **MTW** (left) and Polymorph C (right).

1.6.   The ADOR Process

The recently developed Assembly-Disassembly-Organisation-Reassembly (ADOR) process takes a predetermined parent zeolite and selectively breaks it apart by exploiting the chemical weakness inherent in germanium-rich d4r. The layers that are left behind can be suitably reorganised into a new position by a structure-directing agent (SDA) or aqueous hydrochloric acid and after subsequent calcination form new daughter zeolites. **UTL** was the first layered zeolite to be successfully used in the ADOR process and has produced 6 daughter zeolites, IPC-2 (**OKO**), IPC-4 (**PCR**), IPC-6 (***PCS**), IPC-7[46] and "unfeasible" zeolites IPC-9 and IPC-10 (Table 1.1).[43] Zeolites that are termed "unfeasible" do not form as the lowest energy structure and therefore they do not lie on the traditional correlation line.

Table 1.1. The correlation between layered zeolite precursor and the daughter zeolite produced through ADOR under typical conditions. All zeolites afforded from parent Ge-**UTL**.

Precursor Material	Acid	Post-synthetic modification	Calcined Zeolite	SBU
IPC-1P	0.1 M HCl	N/A	IPC-4	Direct oxygen linkages
IPC-1P	0.1 M HCl	1. Intercalate with choline-OH, RT, 6 hr 2. Calcine	IPC-9	Direct oxygen linkages (layer shifted)
IPC-6P	1.5 M HCl	N/A	IPC-6	Alternate direct oxygen linkages and s4r
IPC-1P	0.1 M HCl	1. Intercalate with choline-OH, RT, 6 hr 2. Direct with diethoxydimethyl silane in 1 M HNO$_3$, 175 °C, 24 hr 3. Calcine	IPC-10	s4r (layer shifted)
IPC-2P	12 M HCl	N/A	IPC-2	s4r
IPC-7P	5 M HCl	N/A	IPC-7	Alternate s4r and d4r

1.6.1. Discovery

In 2011 Roth *et al.* discovered that upon exposing **UTL** to aqueous conditions, a lamellar material was produced as the structure began to degrade. This removed the d4r whilst preserving the **UTL**-like layers. This was the first 3-dimensional to 2-dimensional transformation to produce a lamellar material, IPC-1P (Institute of Physical Chemistry – 1 Precursor). The new layered zeolite precursor was characterised primarily with X-ray diffraction and then further analysed by Fourier Transform Infrared Spectroscopy (FTIR), transmission electron microscopy (TEM) and nitrogen sorption.[59]

The archetype parent zeolite, **UTL**, was first produced by 2 groups in 2004. It was given the name IM-12 (Institut Français du Pétrole/Mulhouse-12)[66] by Paillaud *et al.* and ITQ-15

(Instituto de Tecnología Química-15)[67] by Corma *et al.* and assigned the IZA code **UTL**. It was synthesised with 1,1,3-trimethyl-6-azonia-tricyclo-[3.2.1.4]decane hydroxide and (6S, 10S)-6,10-dimethyl-5-azoniaspiro[4.5]decane hydroxide as structural-directing agents (SDA), respectively. It contains a 12 x 14-ring channel system that run perpendicular to each other in the *b-c* plane with 0.95 x 0.71 nm² (14-ring) and 0.85 x 0.55 nm² (12-ring) dimensions. **UTL**'s structure can be described as dense 2-dimensional layers, similar to **FER**, that are separated by d4r bringing units as pillars (Figure 1.7).

UTL crystallises in space group *C 2/m* with the unit cell:

a = 28.996(4) Å   β = 104.91(0) °

b = 13.967(9) Å   V = 4872.48 Å³

c = 12.449(3) Å
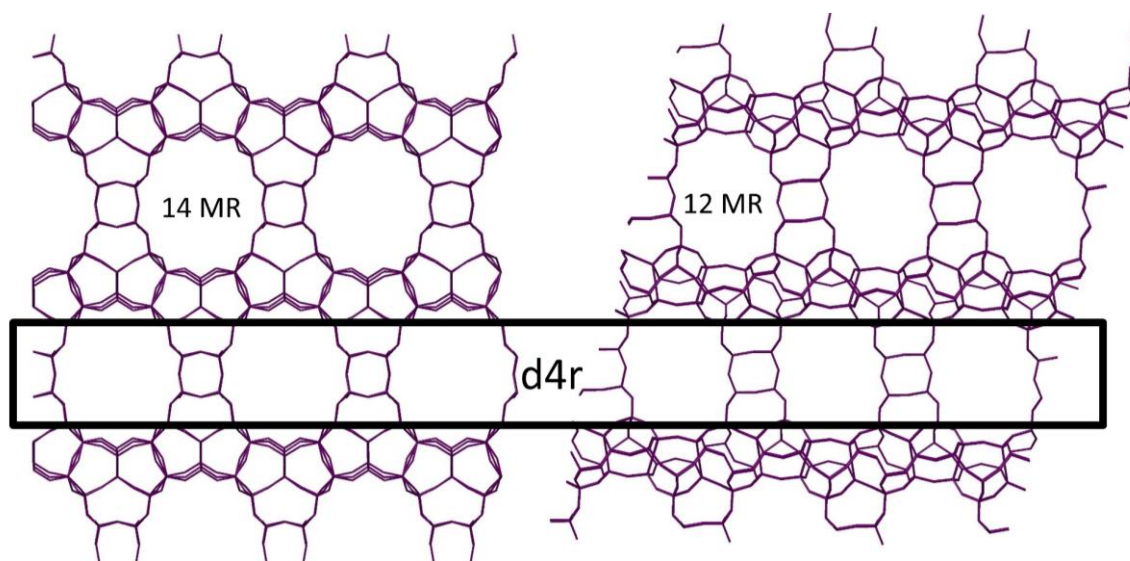
Figure 1.7. The channel systems in **UTL**; down the *c*-axis with a 14-MR channel system (left) and down the *b*-axis with a 12 MR channel system (right). The germanium-rich double four rings are highlighted with a black box and each membered ring annotated.

The structure of IPC-1P was first thought to be similar to MCM-22P, therefore further experiments were carried out on the lamellar material which aimed to modify the inter-layer separation by means of swelling and stabilisation. As such treating IPC-1P under different

conditions resulted in the formation of different products (Figure 1.8). Upon directly calcining IPC-1P, a poorly defined structure with a reduced S_{BET} (270 m^2/g), IPC-1 was afforded.[59]
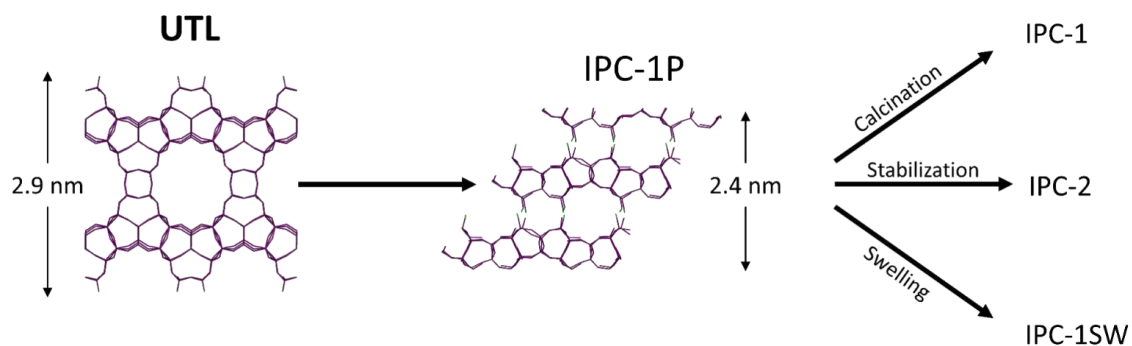
Figure 1.8. A schematic showing the formation of IPC-1P from hydrolysing parent **UTL** and the subsequent products afforded from calcination, stabilisation ad swelling. Silanol groups on IPC-1P are coloured green. See Table 1.1 for typical synthesis conditions. Figure adapted from ref 59.

Following on from this discovery, in 2013 a flagship paper was produced by Roth *et al.*[60] that describes the ADOR process in detail for the first time. It showed that not only was it possible to fully disassemble **UTL** through hydrolysis, but the layered material, IPC-1P produced could be suitably reorganised by using a structure-directing agent, and then the Si-O-Si bonds reformed through calcination to produce two new high-silica zeolites (Figure 1.9), IPC-2 (**OKO**) and IPC-4 (**PCR**).
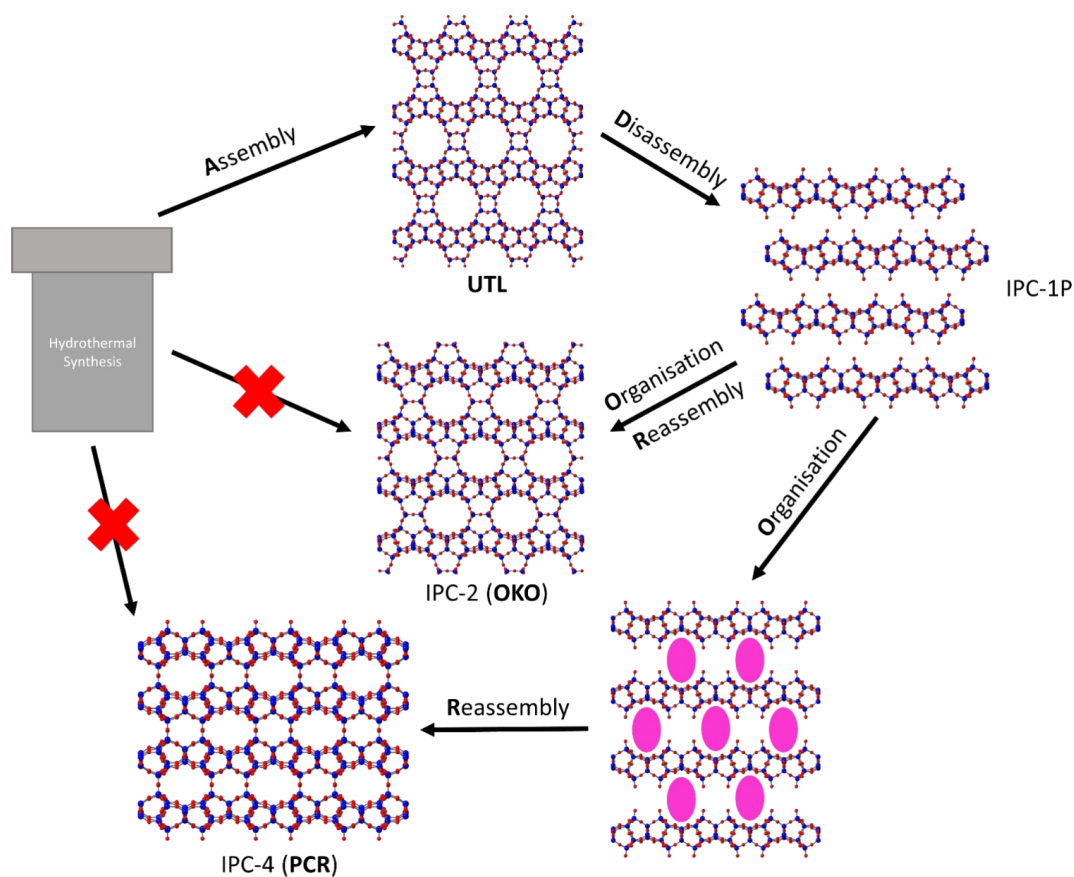
Figure 1.9. A schematic of the first confirmed case of utilising the ADOR process to afford new zeolites. Parent **UTL** is disassembled through hydrolysis into IPC-1P and then suitably rearranged into IPC-4 (**PCR**) or IPC-2 (**OKO**). IPC-4 is made up of IPC-1P layers connected by oxygen bridges; IPC-2 consists of IPC-1P layers connected by s4r. Both structures were unable to be prepared from traditional hydrothermal synthesis at the time of publication. Figure adapted from ref 60.

The following sections will describe each step in the ADOR process individually and in detail.

1.6.2.   Assembly

The first step in the ADOR process is Assembly. A key feature required for the success of the ADOR method is the structure and chemistry of the parent zeolite that is assembled in the first step of the process. Research so far has concentrated on parents that have silica-

rich layers linked by germanium-rich cubic units, termed d4rs.[39,66,68–70] Generally, to be successful in the ADOR process, these d4r units must contain enough Ge to break the connections between the layers (for example in **UTL** – Si/Ge >4.3) and as the Ge is hydrolysed, allowing the parent zeolite to be disassembled.[71,72] The specific location of the Ge within the structure is often difficult to determine without highly specialised diffraction experiments.[73] There are several known zeolite topologies that are currently successful in the ADOR process. These include **UTL**,[43,59,60] **ITH**,[42] **ITR**,[42] **IWR**,[42] **IWW**,[45] **UOV**[61,62] and the recently discovered SAZ-1.[63] Many other d4r-containing zeolites may be successful in the future, but these have yet to be applied.

1.6.3. Disassembly

The second step in the ADOR process is Disassembly. This involves selectively removing the Ge from the Ge-rich d4r by aqueous or acid hydrolysis. The selective weakness in Ge-O-Ge and Ge-O-Si bonds allows for the facile hydrolysis of the Ge and a collapse or "unzip" of the 3-dimensional layered parent zeolite framework to form the dense silicate layers. This hydrolysis, and subsequent collapse of the inter-layer region can be mapped by powder XRD by ultimately following the d_{200} inter-layer spacing peak. This is highlighted by a shift from 14.48 Å for **UTL** to 10.5 Å for IPC-1P (Figure 1.10). The hydrolysis is rapid and is not dependant on the hydrolysis media (pH) or the temperature of the reaction system, but solely on the presence of liquid water (see Chapter 4).
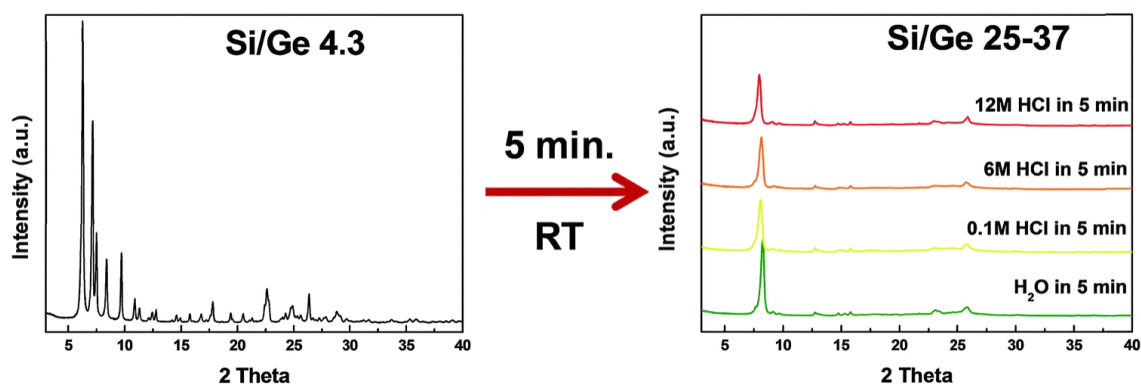
Figure 1.10. Powder X-ray diffraction patterns of **UTL** (left) and after subsequent hydrolysis treatment in increasing levels of acidic media (right); water (green), 0.1 M HCl (yellow), 6 M HCl (orange), and 12 M HCl (red). Figure adapted from ref 46.

Energy dispersive X-ray (EDX) spectroscopy can be used to quantify the amount of Ge removed from the structure and a Si/Ge ratio produced. Once fully hydrolysed the d4r are removed and silanol (Si-OH) groups reside on the surface of the layers. Si^{29} MAS-NMR can be used to compare the Q^3 to Q^4 ratio of the daughter material in comparison to the parent. The silanol groups can be referred to as the Q^3 sites and the Q^4 sites are the fully tetrahedrally coordinated SiO_4 (Figure 1.11).
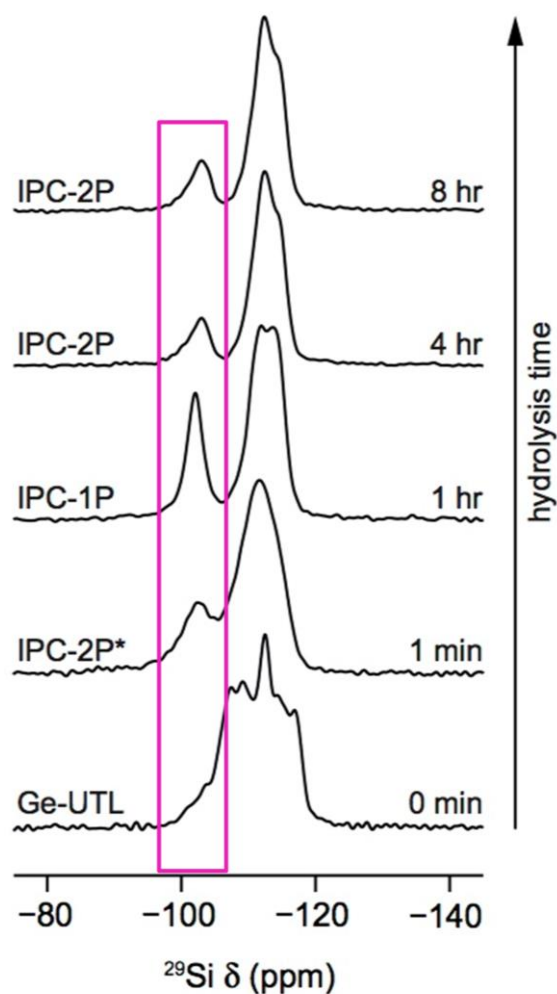
Figure 1.11. ^{29}Si (9.4 T, 10 kHz MAS) NMR spectra of calcined Ge-**UTL** parent zeolite, and subsequent hydrolysis after 1 min, 1 hr, 4 hr and 8 hr. The change in intensity of Q^4 (Si(OSi)$_4$) and Q^3 (Si(OSi)$_3$(OH)) species is monitored over this time period. An increase in silanol (Q^3) sites can be seen up to 1 hr and then a decrease up to 8 hr as the silanol groups are consumed during rearrangement. Q^3 sites highlighted by a pink box. This figure will be reproduced in Chapter 4.

1.6.4.   Organisation

The next step is Organisation. This involves orientating the layers produced from hydrolysis (Disassembly) in a way that upon calcination new bonds form, either as direct oxygen linkages, s4r, d4r or a mixture of two and ultimately forms a new zeolite. This step can be done in 2 ways, intercalation using a structure-directing agent or hydrochloric acid.

1.6.4.1.   Organisation by Intercalation

To produce new zeolites from the disordered layered material IPC-1P, the layers must be re-orientated in to a new position. This can be done by using a species that either shifts the layers through hydrogen bonding (SDA) or covalently bonds with the silanol groups on the surface of the layers (Figure 1.12).
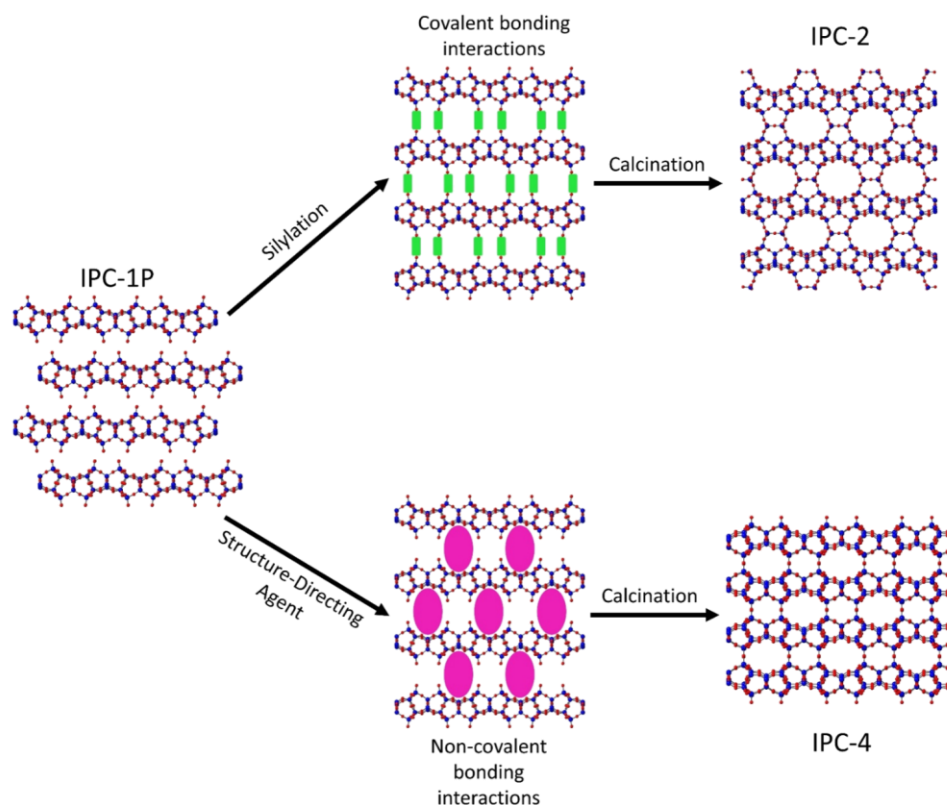
Figure 1.12. The two methods of organising the layers of IPC-1P to form crystalline 3D frameworks. Top - IPC-2 (silylation; green rectangles) through covalent bonding interactions. Bottom - IPC-4 (SDA – octylamine; pink ovals) by non-covalent bonding interactions. Silicon – blue, Oxygen – red. Hydrogen atoms have been omitted for clarity in IPC-1P.

The key to using intercalation to produce new zeolites is the correct alignment of surface silanol groups that upon calcination at high temperature, connect to form a regular 3-dimensional structure. When the d4r are removed through hydrolysis and the germanium has been effectively deintercalated, silanol quadruplets are revealed on the surfaces. The large concentration of surface silanols in IPC-1P, when compared to other 2-dimensional zeolites (e.g. MCM-22) increases the number of potential structures after the layers are rearranged and fully connected.

1.6.4.2. Intercalation of Silica-Containing Species

By using an organic (SDA) that forms non-covalent bonds (e.g. hydrogen bonds) with the silanol groups on the surface of the layers, the layers can be suitably shifted with respect to one another. Structure-directing agents (SDA) such as dipropylammonium hydroxide, hexylamine, and octylamine have been used successfully to form swollen, highly crystalline and high energy structures.

For example, daughter zeolite IPC-4 can be made from IPC-1P by using octylamine as an intercalating agent. IPC-4 crystallises in the $C\ 2/m$ space group, comprising dense silicate layers connected by direct oxygen linkages (see section 1.5.6. for unit cell). Intercalating IPC-1P with choline chloride affords the "unfeasible" daughter zeolite IPC-9 after subsequent calcination.[43] Choline chloride acts to stabilise a lateral shift in the c-axis, and upon calcination the choline chloride is burnt out and the layers condense to form a fully connected 3-dimensional structure (Figure 1.13).
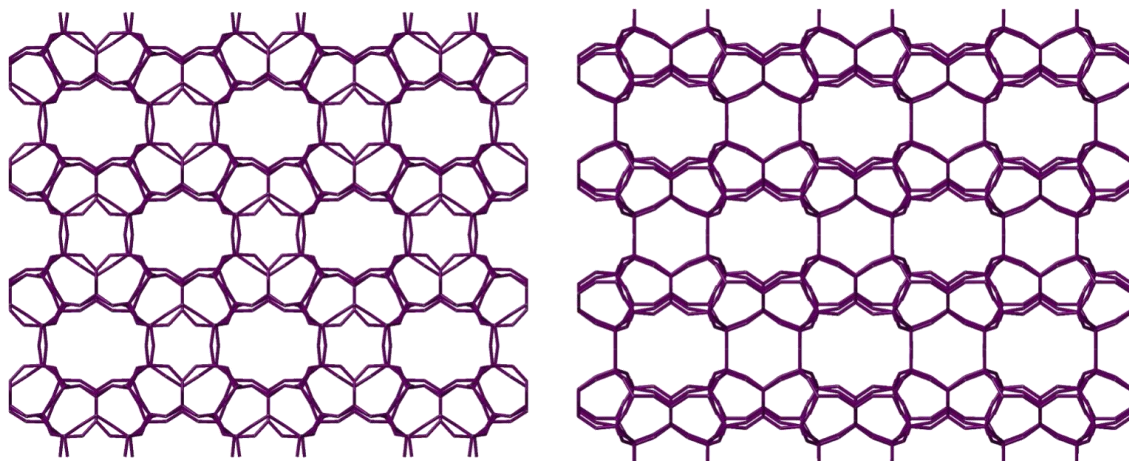
Figure 1.13. Frameworks of IPC-9 (left) and IPC-4 (right) as viewed down the *c*-axis.

IPC-9 crystallises in the *C 2/m* space group and consists of a 7 x 10 membered ring channel system to create medium sized pores. The structure of IPC-9 also has inter-layer direct oxygen linkages, similar to IPC-4, however the layers are shifted by half a unit cell along the *c*-axis. IPC-9 has the following unit cell:

a = 18.6695(26) Å β = 102.409(34) °

b = 13.8984(15) Å

c = 12.1020(30) Å

Another way to orientate the layers is by using a species such as silane that covalently bond with the silanol groups and condense to form inter-layer structural building units (SBU). An example of this includes the formation of "unfeasible" IPC-10.[43] After organising the IPC-1P layers first with choline, one can use a silylating agent to form s4r units connecting the silicate layers. This creates a zeolite that has 9 x 12 membered-ring channel system that intersects along the *b-c* plane. The structure, similarly to IPC-4 and IPC-9, is analogous to IPC-2 (see section 1.5.6. for unit cell) but with the layers once again shifted by half a unit cell in either the *b-* or *c*-axis. Allowing a shift in either direction causes disorder within the structure (Figure 1.14). IPC-10 forms in space group *P-1* with the unit cell:

$a = 26.755(6)$ Å	$\alpha = 90.0$ °
$b = 13.942(8)$ Å	$\beta = 82.112(7)$ °
$c = 12.069(8)$ Å	$\gamma = 57.853(0)$ °
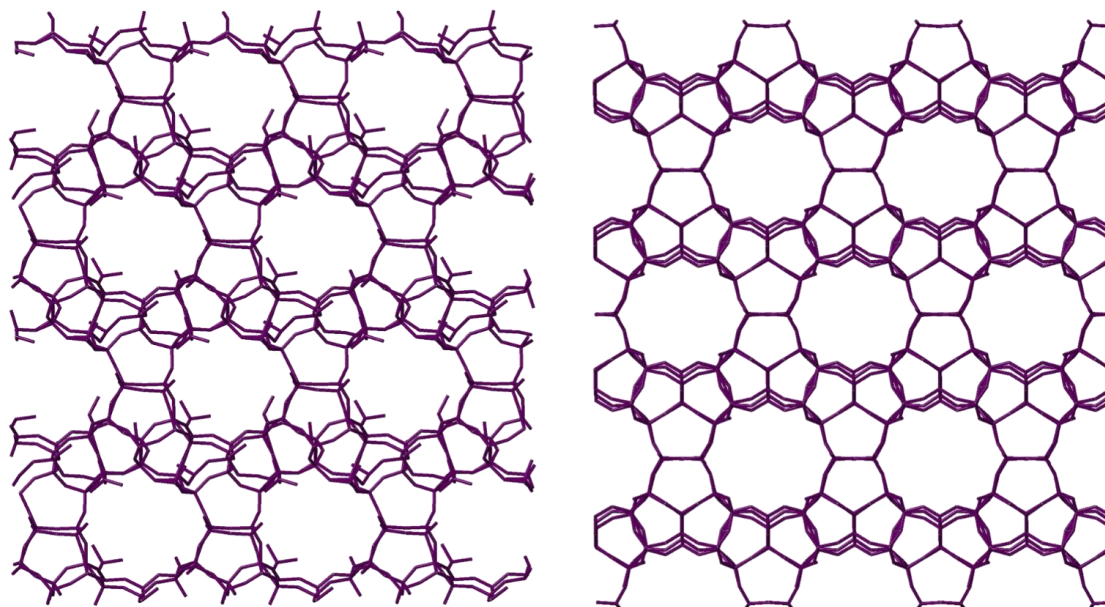
Figure 1.14. The frameworks of IPC-10 (left) and IPC-2 as viewed down the *c*-axis (right).

1.6.4.3. Organisation with Aqueous Hydrochloric Acid

An easier and more direct method of organising the layers is to continue reacting the hydrolysis mixture in hydrochloric acid at constant temperature, thus allowing the layers to self-organise. Using different concentrations of hydrochloric acid can change the product that is formed, under high molarity conditions IPC-2 (**OKO**) is formed and under low molarity conditions IPC-4 (**PCR**) is afforded (Figure 1.15).

IPC-4 crystallises in the monoclinic space group *C 2/m* consisting of a 10 x 8 membered-ring channel system with unit cell:

$a = 20.143(7)$ Å	$\beta = 115.65(10)$ °
$b = 14.072(3)$ Å	
$c = 12.522(3)$ Å	

IPC-2 crystallises in the same monoclinic space group as IPC-4 (*C 2/m*) with a 12 x 10 membered-ring channel system with unit cell:

a = 24.163(8) Å   β = 109.12(8) °

b = 13.833(2) Å

c = 12.351(6) Å
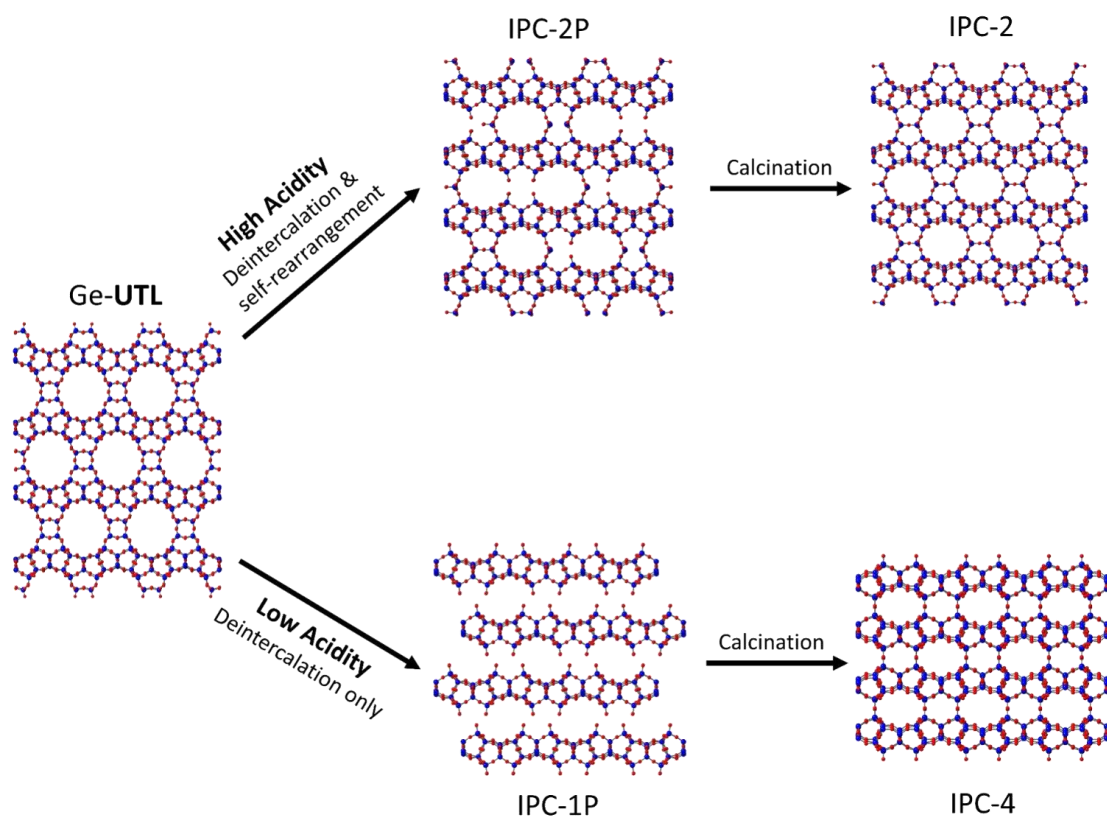
Figure 1.15. Schematic to show the pathways undertaken when the system is in high acidity (M > 8) to form IPC-2 through a deintercalation followed by a self-rearrangement (TOP) and low acidity (M < 0.1) to form IPC-4 by deintercalation only (BOTTOM).

In 2014, a study reported by Wheatley *et al.*,[46] showed the pH dependence of hydrolysis and subsequent rearrangement. It was found that the rate of the initial hydrolysis (Disassembly) does not depend greatly on the pH of the hydrolysis medium. Unlike the hydrolysis however, the rearrangement process is influenced by the acidity of the reaction media. When HCl of < 0.1 M is used, IPC-4 (**PCR**) is formed preferentially after reassembly; increasing the molarity shows a steady increase in inter-layer spacing, and materials such as IPC-6 (***PCS**)

can be formed. When the acidity is high enough, all reactions formed IPC-2 (**OKO**), and due to the increased rate of reaction, IPC-6P is not formed (as seen in Pathway 1, Figure 1.15).[46] Time is also an important variable in the reaction outcome (Figure 1.16).
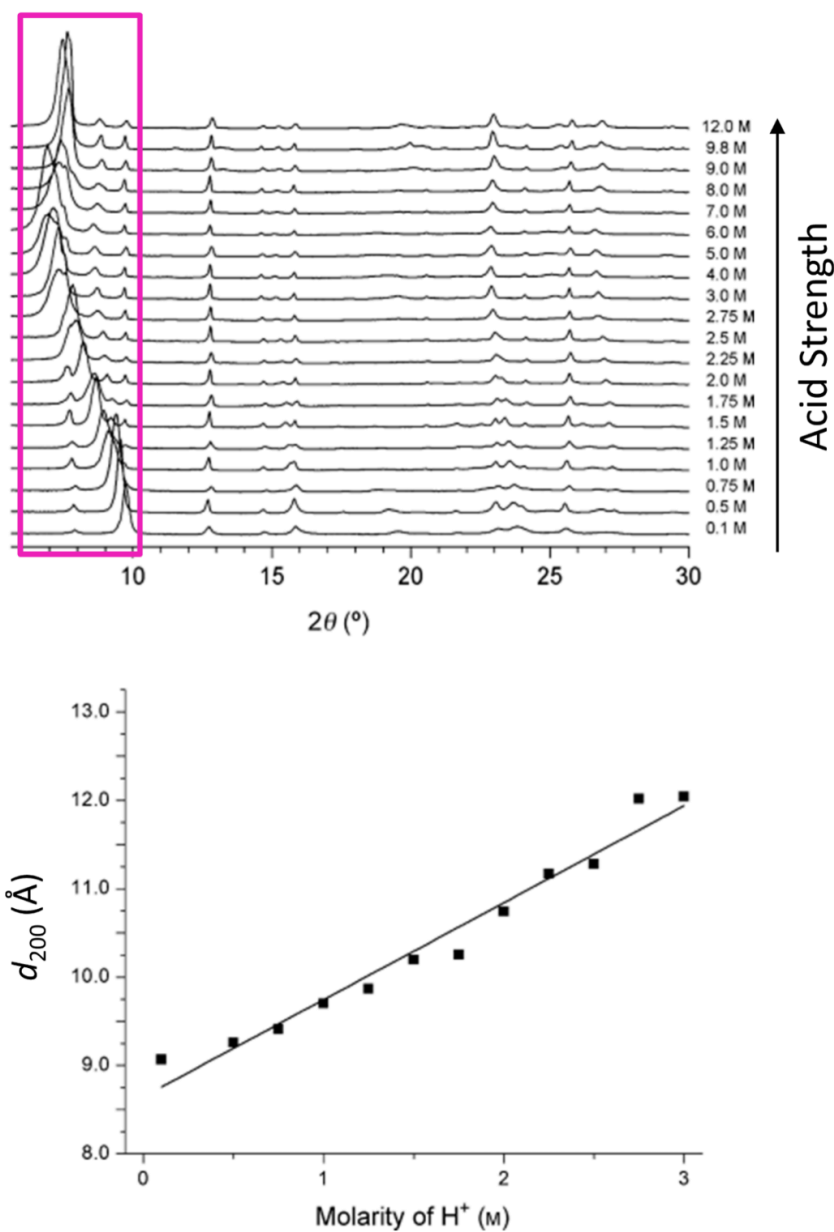
Figure 1.16. The dependence of acid strength on the inter-layer spacing as seen by: Top - the PXRD patterns highlighting a 2θ peak shift with increasing acidity; Bottom - the linear trend between acid strength and d spacing up to 3 M HCl. The d_{200} inter-layer peak is the peak of interest to see the inter-layer spacing change with acid strength, this is highlighted by a pink box. Figure adapted from ref 46.

IPC-6 is an interesting structure with local disorder throughout the material. It consists of alternating layers of direct oxygen linkages and s4r. To quantify the structure and fully analyse the powder patterns produced, the pattern was indexed and then a computationally derived structure was modelled against it. Indexing the PXRD gave the structure to be in the *C 2/m* space group with unit cell (Figure 1.17):

a = 20.765(4) Å   β = 101.32(0) °

b = 13.904(8) Å

c = 12.400(2) Å
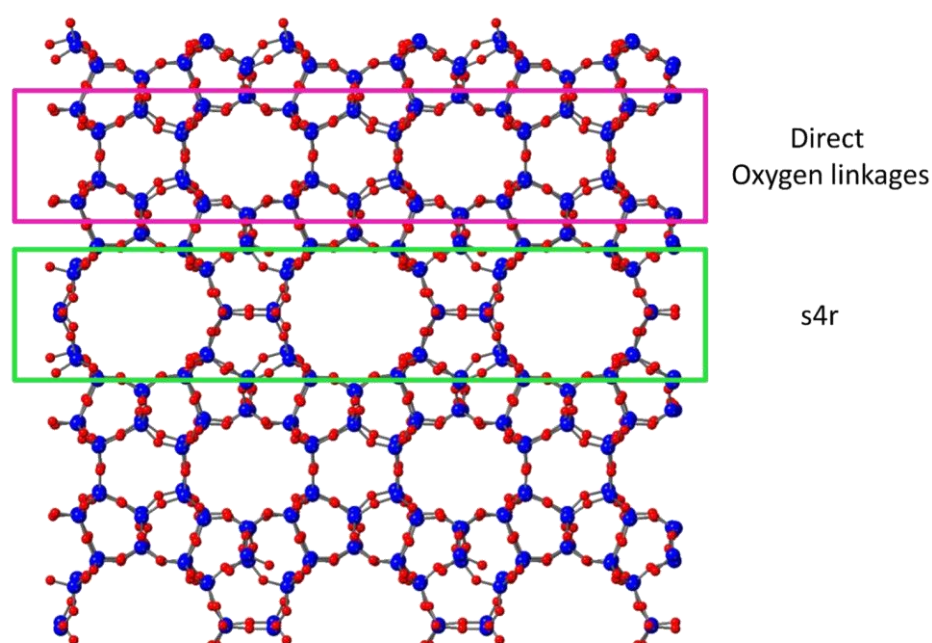
Figure 1.17. The IPC-6 framework with alternating layers of s4r and direct oxygen linkages. s4r - green box; direct oxygen linkages - pink box.

Such diversity of outcomes points to a complex mechanism that must be understood in detail if the full potential of the process is to be realised. The different outcomes depend on the conditions used, and it is therefore very easy to miss prospective products by not surveying the potential conditions over a sufficient range. This will be discussed in detail in Chapter 4.

1.6.5.   Reassembly

The final step in the ADOR process is Reassembly. This step involves reconnecting the layers after they have been organised into their new position. Reforming the new silicate bonds is irreversible and can be achieved through calcination. This involves heating the zeolite precursor at temperatures exceeding 500 °C.

Layered materials can be treated with silanes (silylation), this results in inter-lamellar expanded zeolites (IEZs).[73] These materials are often not fully connected as the silanes that are introduced only connect to two tetrahedral silica. Using the ADOR process however, allows for fully connected daughter zeolites to be afforded, this is due to the presence of silanol quadruplets. These silanol quadruplets can then covalently bond with the alkoxysilane silylating agent to form fully connected s4r units, and as such a "true zeolite".

1.7.   Metal-Organic Frameworks

Metal-Organic Frameworks (MOFs) were discovered in 1989 by Robson[74] and can be classed as inorganic-organic hybrid compounds consisting of metals or metal clusters connected by organic ligands (Figure 1.18) through reticular synthesis. The ligands act as spacers, allowing an open porous 3-dimensional structure to be created, with a very high surface area and pore volume.[75-77] In 2012, the International Union of Pure and Applied Chemistry (IUPAC) defined a MOF as "MOF, is a Coordination Polymer (or alternatively a Coordination Network) with an open framework containing potential voids".
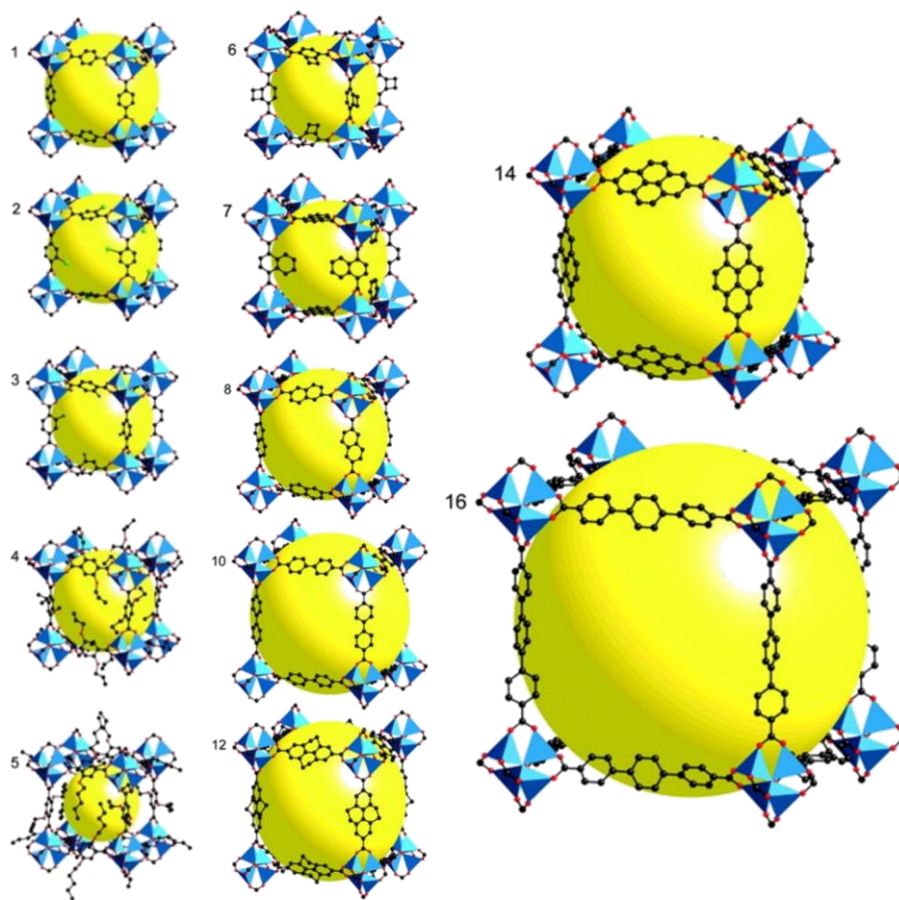
Figure 1.18. The isoreticular series of IRMOF-n MOFs produced by Yaghi *et al.* Each corner is comprised of a cluster [OZn$_4$(CO$_2$)$_6$] around an oxygen-centred Zn$_4$ tetrahedron that is bridged by six carboxylates of an organic linker. Colour scheme is as follows: Zn (blue polyhedra), O (red spheres), C (black spheres). The large internal yellow spheres represent the largest van der Waals spheres that would fit in the cavities without touching the frameworks. All hydrogen atoms have been omitted for clarity. Figure adapted from reference 77.

Within the past decade there have been more than 20,000 different MOFs reported and studied.[78] This is due to the flexibility with which the constituents' geometry, size and functionality can be varied.[78] This section will hope to shed light on the astounding functionalities of metal-organic frameworks, in particular the CPO-27-M (M = Co, Cu, Fe, Mg, Ni, Zn) family (also termed MOF-74) and how its large surface area and stable structure upon coordinated solvent loss makes it an ideal candidate for gas storage and release, specifically with nitric oxide (NO).[79]

Customising the linker (organic ligand) allows the stability and void space in each MOF to be tuned. There are many linkers that are "traditionally" used in MOF synthesis, usually containing a carboxylate group, but could include groups such as amino,[80,81] azo[82] or quinones.[83]

The metal ions are an integral part of the MOF structure. When solvent is removed from the material a vacant site can be generated in their coordination sphere, such empty sites are termed coordinatively unsaturated sites (CUS). These CUS have a high affinity for guest molecules such as NO, and as they are involved in the chemisorption process, have the ability to enhance the gas storage properties of materials.

1.7.1. Synthesis of MOFs

There are many different ways to synthesise new or existing Metal-Organic frameworks, including but not limited to: electrochemistry, thin films, microwave-assisted heating, solvothermal, mechanochemistry and sonochemistry. A few of these will be discussed in more detail below.

1.7.4.1. Solvothermal

Similarly to that of zeolites, solvothermal synthesis is the crystallisation of solid products out of non-aqueous solution performed in a stainless steel autoclave at very high temperature and autogenous pressure.

With MOFs, the control of the size, shape and morphology of the final product is difficult, however using advances in computational chemistry and by constructing a CoRE MOF database, MOF structures can be predicted, allowing synthesis to be designed around the predicted MOF.[84] Along with control there are many other problems and questions to overcome when designing a synthesis:

- **The pH of the system.** If the pH is too low, the linkers used may not deprotonate. If the pH is too high, the linkers may deprotonate too fast and result in low quality samples due to reduced opportunities for "self-healing"

- **The solvent used.** In some cases, slightly changing the solvent used changes the MOF formed. For example, changing the solvent from dimethylformamide (DMF) to diethylformamide (DEF) changes the MOF afforded from *F*-MOF-4 to Cu-*F*MOF-4B. Such MOFs were structurally different fluorinated MOFs (*F*-MOF)[85]

- **Temperature of the system.** Quite often cooling the reaction mixture slows down the kinetics of reaction and therefore yields larger crystals with less defects

- **Environmentally friendly synthesis vs. increased crystallinity**

1.7.4.2. Modulated

The question of whether sacrificing crystallinity to create an environmentally friendly (aqueous solutions) synthesis is often important. Often, MOFs are prepared in harsh organic solvents such as DMF, and contain high levels of a toxic base. A way to overcome this and improve the environmental impact of the reaction is to use a modulator to direct the synthesis of a desired MOF. Common modulators include benzoic acid, salicylic acid and acetic acid. These modulators are dissolved in an aqueous solvent (alcohol or water) and therefore replace base and reduce the amount of harsh organic solvent needed. Moreover, the yield is significantly improved with the particle size greatly increased and the morphology more consistent throughout the entire batch.

HKUST-1 is one such MOF that has been investigated in this manner. It was found that without a modulator present in the synthesis mixture, the MOF formed rapidly producing low quality crystallinity. Adding a monocarboxylic acid as a modulator, the morphology and kinetics of reaction were more controlled whilst still retaining high surface area and pore volume. [86]

1.7.4.3. Electrochemical Synthesis

Electrochemical synthesis is the synthesis of chemical compounds using electrons as the main reactant source. Electrochemical synthesis in batch is advantageous over many chemical routes as it reduces the difficulty in obtaining compounds that may be inaccessible through traditional syntheses. This may be due to the decreased reaction temperatures, or the use of a milder base or solvent. The electrochemical method is atom economical with a

high conversion of reactants to products. As a metal electrode is used, electrons are the main reactant source, therefore there is no need for external reagents and can thus be viewed as a clean reaction. These methods can be cheap to carry out and can often be selective towards the product formed, as seen in the case of Fe^{II}/Fe^{III} when changing from anhydrous to ambient conditions.[87]

Coordination compounds can be formed through electrochemistry when a field potential is specified between a sacrificial anode and metal cathode (Figure 1.19). These act as a source of metal ions and free electrons to facilitate the formation of complexes, or more recently MOFs.
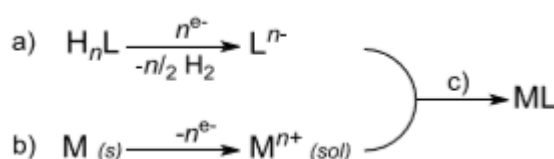
Figure 1.19. General principle of electrochemical synthesis; L = ligand, n = number of electrons, M = metal electrode. a) reduction of ligand, b) oxidation of sacrificial anode, c) combination of metal and ligand to form the coordination complex.

As can be seen from Figure 1.19, the oxidation state of the metal generated is dependent on the number of reduction sites the ligand has. Ligands with one reduction site such as N-heterocyclic carbenes (NHCs) are able to generate a 1+ metal ion in the electrochemical system, whereas ligands such as salen that have two reduction sites are able to generate a 2+ metal ion. When a copper anode is applied, Cu^{II} is produced and salen can coordinate in an equatorial fashion around the metal.[87]

Recently $Cu_3(BTC)_2$ (HKUST-1) was synthesised electrochemically, by placing two copper electrodes (acting as both sacrificial anode and cathode) in an electrochemical cell containing ethanol, 1,3,5-benzenetricarboxylate (H_3BTC) and tetrabutylammonium tetrafluoroborate (TBA TFB; electrolyte) under anhydrous conditions. After 2.5 hr at a constant voltage of 30 V blue precipitates of the MOF could be seen and were subsequently collected by centrifugation.[88]

1.7.2. General Applications

MOFs can achieve very high porosity giving them the potential for countless applications such as catalysis,[89] biomedicine,[90–94] gas adsorption and delivery,[76,95–99] and sensing.[100] Such MOFs are generally characterised by their extremely large Brunauer-Emmett-Teller surface areas (S_{BET}), astounding internal surface areas, (approaching 6000 m^2 g^{-1})[90] and high structural/compositional flexibility.[100]

Reversible adsorption of the framework can occur in some MOFs when exposed to external stimuli, such as adsorption of guest molecules, pressure, temperature, and ultraviolet (UV) light.[101] These responses, in the form of framework modification, are often reversible. For example, MOFs that possess coordinated solvent molecules can undergo solvent exchange and de-/re-solvation without loss of structure. Such properties permit the potential application of MOFs in high-performance molecular recognition and highly selective and controlled guest insertion and release.[102]

1.7.3. Gas Storage and Release using MOFs

The release of anthropogenic toxic pollutants into the atmosphere is a threat that has become a growing concern worldwide.[103] Many of the world's toxic gases are as a result of fuel burning and through this burning causes many problems such as smog and acid rain, thus gas storage is of much interest for environmental purposes.[103]

As stated previously, the reversibility of MOF frameworks upon dehydration allows for guest insertion of many molecules such as C_2H_2,[102,104] CO,[76,102] CO_2,[105,106] H_2,[97,107] H_2S,[90,96] and NO[91,108] making them excellent receptacles for toxic gas storage and release.

1.7.4. Biomedical Applications of MOFs

MOFs are currently being studied as delivery agents for drug and therapeutic molecules. For the potential to carry drug molecules into the body the framework of a MOF must contain pores large enough to contain the drug within it, some examples include MIL-53[109] and MIL-100.[109,110] Ibuprofen can be loaded into the pores of MOFs by using a $scCO_2$-hexane

(supercritical carbon dioxide) solution. This scCO₂ drying method increases the internal surface area of each MOF and as such large payloads of ibuprofen can be loaded.[109]

NO, although a known pollutant, contributes to a wide range of biological functions in the human body. Examples include the regulation of vascular homeostasis, triggering an immune response, enabling neurotransmission and facilitating penile erection.[111–117] Work in the Morris group is underway to develop CPO-27 (Coordination Polymer of Oslo) as a receptacle to carry NO to produce vascular relaxation.[108]

1.7.5. CPO-27-M

CPO-27-M (Co, Cu, Fe, Mg, Ni, and Zn) is one of the most studied and well-known MOFs. It consists of 2,5-dihydroxyterephthalic acid (dhtp) as the linker source forming stable hexagonal channels lined with metal-coordinating solvent molecules that can be removed to form open metal sites (Fig. 1.20). These MOFs are highly porous with S_{BET} of 1039 – 1542 $m^2 \, g^{-1}$ [100] making them excellent for gas adsorption.
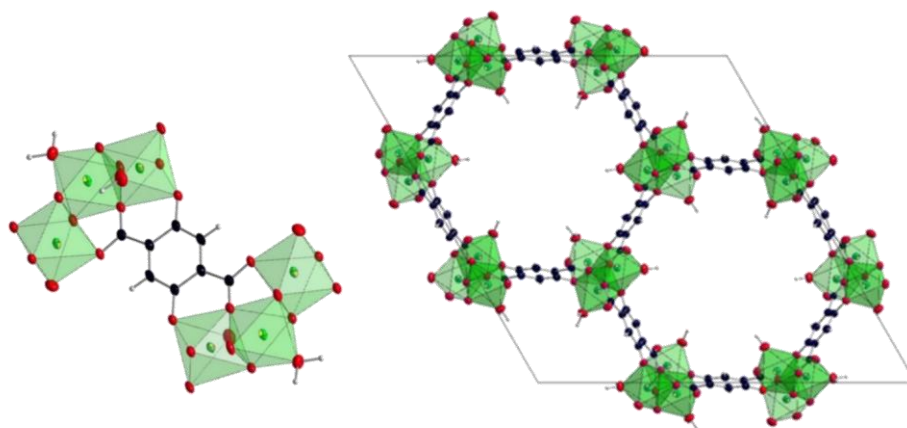
Figure 1.20. The monomeric building blocks of CPO-27-Mg, highlighting the 2,5-dihydroxyterephthalic acid linker and coordinated water molecules (left). Unit cell of CPO-27-Mg as viewed down the *a*-axis. Mg SBU = green.

The traditional synthetic route to these MOFs is primarily solvothermal, using high temperature and pressure, base and a strong organic solvent. Research has and still is being

undertaken to overcome these harsh conditions and prepare the MOFs at room temperature[118,119] and reflux using aqueous conditions.[95,118,119] These conditions typically only make poly-crystalline powders. Work is undergoing to afford single crystals without the need for the necessary base or liquid water.

A recently discovered analogue of the CPO-27 family, UTSA-74[120,121] is of much interest due to its channel system. The material exhibits the zinc structural building unit (SBU) in both tetrahedral and octahedral coordination, thus giving rise to a large and small pore channel system (Fig 1.21). When prepared each octahedral Zn^{2+} has 1 axial bound water molecule pointing into the pore and 1 pointing out. This configuration and channel system makes UTSA-74 an ideal candidate for gas separation in industrial applications such as flue streams.
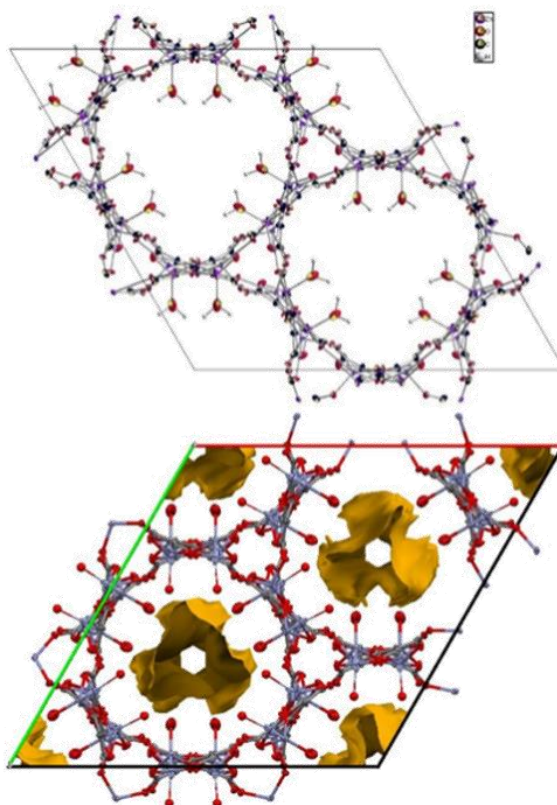
Figure 1.21. Structures of UTSA-74 showing Zn^{2+} in both tetrahedral and octahedral coordination, giving rise to a small and large pore channel system. Each octahedral Zn^{2+} has 1 axial bound water molecule pointing into the pore and 1 pointing out (TOP). Void space with solvent molecules bound, showing the pores are blocked (BOTTOM). Viewed along the c-axis. Figure will be reproduced in Chapter 7.

1.8.   References

1   K. Meyer, P. Lorenz, B. Böhl-Kuhn and P. Klobes, *Cryst. Res. Technol.*, 1994, **29**, 903–930.

2   T. Yang, H. Lin, X. Zheng, K. P. Loh and B. Jia, *J. Mater. Chem. A*, 2017, **5**, 16537–16558.

3   K. P. de Jong, J. Zečević, H. Friedrich, P. E. de Jongh, M. Bulut, S. van Donk, R. Kenmogne, A. Finiels, V. Hulea and F. Fajula, *Angew. Chemie.* 2010, **49**, 10074-10078.

4   D. Procházková, M. Bejblová, J. Vlk, A. Vinu, P. Štěpnička and J. Čejka, *Chem. - A Eur. J.*, 2010, **16**, 7773–7780.

5   J. Čejka, A. Corma and S. Zones, Eds., *Zeolites and Catalysis*, Wiley-VCH Verlag GmbH & Co. KGaA, Weinheim, Germany, 2010.

6   G. Centi and S. Perathoner, in *Zeolites and Catalysis*, Wiley-VCH Verlag GmbH & Co. KGaA, Weinheim, Germany, 2010, pp. 745–774.

7   M. Moliner, C. Martínez and A. Corma , *Angew. Chemie.*, 2015, **54**, 3560–3579.

8   J. Peréz-Ramírez, D. Verboekend, A. Bonilla and S. Abelló, *Adv. Funct. Mater.*, 2009, **19**, 3972–3979.

9   M. Dams, L. Drijkoningen, B. Pauwels, G. Van Tendeloo, D. E. De Vos and P. A. Jacobs, *J. Catal.*, 2002, **209**, 225–236.

10   M. . Alcón, A. Corma, M. Iglesias and F. Sánchez, *J. Organomet. Chem.*, 2002, **655**, 134–145.

11   B. Yilmaz and U. Müller, *Top. Catal.*, 2009, **52**, 888–895.

12   J. Cejka, R. E. Morris and P. Nachtigall, Eds., *Zeolites in Catalysis*, Royal Society of Chemistry, Cambridge, 2017.

13   M. Ghasemifard, S. M. Hosseini and G. H. Khorrami, *Ceram. Int.*, 2009, **35**, 2899–2905.

14   T. Fukasawa, M. Ando, T. Ohji and S. Kanzaki, *J. Am. Ceram. Soc.*, 2001, **84**, 230–232.

15   S. Sciences, *Nanocrystalline Ceramics Synthesis and Structure*, Springer Berlin Heidelberg, 2002.

16   R. E. Day, *Polym. Degrad. Stab.*, 1990, **29**, 73–92.

17   H. Zollinger, *Color chemistry. Synthesis, properties and applications of organic dyes and pigments*, Verlag Helvetica Chimica Acta, 1987.

18   C. Basheer, A. A. Alnedhary, B. S. M. Rao, S. Valliyaveettil and H. K. Lee, *Anal. Chem.*, 2006, **78**, 2853–2858.

19   H. Iwata and T. Matsuda, *J. Memb. Sci.*, 1988, **38**, 185–199.

20   J. Khandurina, S. C. Jacobson, L. C. Waters, R. S. Foote and J. M. Ramsey, *Anal. Chem.*, 1999, **71**, 1815–1819.

21   H. Iwata, M. Oodate, Y. Uyama, H. Amemiya and Y. Ikada, *J. Memb. Sci.*, 1991, **55**, 119–130.

22   M. Tiemann, *Chem. - A Eur. J.*, 2007, **13**, 8376–8388.

23   P. Novák, W. Scheifele, M. Winter and O. Haas, *J. Power Sources*, 1997, **68**, 267–270.

24   C.-J. Bae, C. K. Erdonmez, J. W. Halloran and Y.-M. Chiang, *Adv. Mater.*, 2013, **25**, 1254–1258.

25   T.-C. Weng and H. Teng, *J. Electrochem. Soc.*, 2001, **148**, A368.

26   G. Li, S. Zhao, Y. Zhang and Z. Tang, *Adv. Mater.*, 2018, 1800702.

27   F. Ambroz, T. J. Macdonald, V. Martis and I. P. Parkin, *Small Methods*, 2018, 1800173.

28   W.-Q. Zhang, Q.-Y. Li, J.-Y. Cheng, K. Cheng, X. Yang, Y. Li, X. Zhao and X.-J. Wang, *ACS Appl. Mater. Interfaces*, 2017, **9**, 31352–31356.

29   H. Bin Wu and X. W. Lou, *Sci. Adv.*, 2017, **3**.

30   Z. Liang, C. Qu, W. Guo, R. Zou and Q. Xu, *Adv. Mater.*, 2018, **30**, 1702891.

31   J. Zhu, P.-Z. Li, W. Guo, Y. Zhao and R. Zou, *Coord. Chem. Rev.*, 2018, **359**, 80–101.

32   Y. Cui, M. Rimoldi, A. E. Platero-Prats, K. W. Chapman, J. T. Hupp and O. K. Farha, *ChemCatChem*, 2018, **10**, 1772–1777.

33   P. Shukla, S. Wang, K. Singh, H. M. Ang and M. O. Tadé, *Appl. Catal. B Environ.*, 2010, **99**, 163–169.

34   G. Graziano, *Nat. Rev. Chem.* 2017, **14**.

35   M. Navlani-García, I. Miguel-García, Á. Berenguer-Murcia, D. Lozano-Castelló, D. Cazorla-Amorós and H. Yamashita, *Catal. Sci. Technol.*, 2016, **6**, 2623–2632.

36   M. J. Valero-Romero, S. Sartipi, X. Sun, J. Rodríguez-Mirasol, T. Cordero, F. Kapteijn and J. Gascon, *Catal. Sci. Technol.*, 2016, **6**, 2633–2646.

37   S. Inagaki, S. Shinoda, S. Hayashi, T. Wakihara, H. Yamazaki, J. N. Kondo and Y. Kubota, *Catal. Sci. Technol.*, 2016, **6**, 2598–2604.

38   K. Wijayanti, K. Leistner, S. Chand, A. Kumar, K. Kamasamudram, N. W. Currier, A. Yezerets and L. Olsson, *Catal. Sci. Technol.*, 2016, **6**, 2565–2579.

39   R. Millini, G. Bellussi, S. Smeets, Z. Xiaodong and K. Strohmaier, *Zeolites in Catalysis Properties and Applications*, 2017, vol. 28, 4.

40   C. Baerlocher and L. B. McCusker, Database of Zeolite Structures, http://www.iza-structure.org/databases/, (accessed 10 October 2018).

41   R. Pophale, P. A. Cheeseman and M. W. Deem, *Phys. Chem. Chem. Phys.*, 2011, **13**, 12407.

42   M. Shamzhy, M. Opanasenko, Y. Tian, K. Konysheva, O. Shvets, R. E. Morris and J. Čejka, *Chem. Mater.*, 2014, **26**, 5789–5798.

43   M. Mazur, P. S. Wheatley, M. Navarro, W. J. Roth, M. Položij, A. Mayoral, P. Eliášová, P. Nachtigall, J. Čejka and R. E. Morris, *Nat. Chem.*, 2015, **8**, 58–62.

44   P. Eliášová, M. V. Opanasenko, P. S. Wheatley, M. V. Shamzhy, M. Mazur, P. Nachtigall, W. J. Roth, R. E. Morris and J. Čejka, *Chem. Soc. Rev.*, 2015, **44**, 7177–206.

45   P. Chlubná-Eliášová, Y. Tian, A. B. Pinar, M. Kubů, J. Čejka and R. E. Morris, *Angew. Chemie*, 2014, **126**, 7168–7172.

46   P. S. Wheatley, P. Chlubná-Eliášová, H. Greer, W. Zhou, V. R. Seymour, D. M. Dawson, S. E. Ashbrook, A. B. Pinar, L. B. McCusker, M. Opanasenko, J. Čejka and R. E. Morris, *Angew. Chemie - Int. Ed.*, 2014, **53**, 13210–13214.

47   A. Sartbaeva and S. A. Wells, *Appl. Petrochemical Res.*, 2012, **2**, 69–72.

48   C. Martínez and A. Corma, *Coord. Chem. Rev.*, 2011, **255**, 1558–1580.

49   S. Wang and Y. Peng, *Chem. Eng. J.*, 2010, **156**, 11–24.

50   R. Xu and Wiley InterScience (Online service), *Chemistry of zeolites and related porous materials : synthesis and structure*, John Wiley & Sons (Asia), 2007.

51   X. Chen, J. Yu and X. Cao, *Stud. Surf. Sci. Catal.*, 2007, **170**, 432–437.

52   E. R. Parnham and R. E. Morris, *Acc. Chem. Res.*, 2007, **40**, 1005–1013.

53   W. J. Roth, B. Gil, W. Makowski, B. Marszalek and P. Eliášová, *Chem. Soc. Rev.*, 2016, 45.

54   L. Schreyeck, P. Caullet, J. C. Mougenel, J. L. Guth and B. Marler, *Microporous Mater.*, 1996, **6**, 259–271.

55   W. J. Roth, P. Nachtigall, R. E. Morris and J. Čejka, *Chem. Rev.*, 2014, **114**, 4807–4837.

56   W. J. Roth, in *Studies in Surface Science and Catalysis*, Elsevier, 2005, vol. 158, pp. 19–26.

57   H.-T. Vu, F. M. Harth and N. Wilde, *Front. Chem.*, 2018, **6**, 1–9.

58   P. Kamakoti and T. A. Barckholtz, *J. Phys. Chem. C*, 2007, **111**, 3575–3583.

59   W. J. Roth, O. V. Shvets, M. Shamzhy, P. Chlubná, M. Kubů, P. Nachtigall and J. Čejka, *J. Am. Chem. Soc.*, 2011, **133**, 6130–6133.

60   W. J. Roth, P. Nachtigall, R. E. Morris, P. S. Wheatley, V. R. Seymour, S. E. Ashbrook, P. Chlubná, L. Grajciar, M. Položij, A. Zukal, O. Shvets and J. Čejka, *Nat. Chem.*, 2013, **5**, 628–633.

61   V. Kasneryk, M. Opanasenko, M. Shamzhy, Z. Musilová, Y. S. Avadhut, M. Hartmann and J. Čejka, *J. Mater. Chem. A*, 2017, **5**, 22576–22587.

62   V. Kasneryk, M. Shamzhy, M. Opanasenko, P. S. Wheatley, S. A. Morris, S. E. Russell, A. Mayoral, M. Trachta, J. Čejka and R. E. Morris, *Angew. Chemie.*, 2017, **56**, 4324–4327.

63   D. S. Firth, S. A. Morris, P. S. Wheatley, S. E. Russell, A. M. Z. Slawin, D. M. Dawson, A. Mayoral, M. Opanasenko, M. Položij, J. Čejka, P. Nachtigall and R. E. Morris, *Chem. Mater.*, 2017, **29**, 5605–5611.

64   G. Sastre and A. Corma, *J. Phys. Chem. C*, 2010, **114**, 1667–1673.

65   A. Corma, M. T. Navarro, F. Rey, J. Rius and S. Valencia, *Angew. Chemie*, 2001, **113**, 2337–2340.

66   J.-L. Paillaud, B. Harbuzaru, J. Patarin and N. Bats, *Science*, 2004, **304**, 990–2.

67   A. Corma, M. J. Díaz-Cabañas, F. Rey, S. Nicolopoulus and K. Boulahya, *Chem. Commun.*, 2004, 1356–1357.

68   J. J. Gutiérrez-Sevillano, S. Calero, S. Hamad, R. Grau-Crespo, F. Rey, S. Valencia, M. Palomino, S. R. G. Balestra and A. R. Ruiz-Salvador, *Chem. - A Eur. J.*, 2016, **22**, 10036–10043.

69   X. Liu, U. Ravon, F. Bosselet, G. Bergeret and A. Tuel, *Chem. Mater.*, 2012, **24**, 3016–3022.

70   G. M. Johnson, A. Tripathi and J. B. Parise, *Chem. Mater.*, 1999, **11**, 10–12.

71   E. Verheyen, L. Joos, K. Van Havenbergh, E. Breynaert, N. Kasian, E. Gobechiya, K. Houthoofd, C. Martineau, M. Hinterstein, F. Taulelle, V. Van Speybroeck, M. Waroquier, S. Bals, G. Van Tendeloo, C. E. A. Kirschhock and J. A. Martens, *Nat. Mater.*, 2012, **11**, 1059–1064.

72   T. Blasco, A. Corma, M. J. Díaz-Cabañas, F. Rey, J. A. Vidal-Moya and C. M. Zicovich-Wilson, *J. Phys. Chem. B*, 2002, **106**, 2634–2642.

73   P. Wu, J. Ruan, L. Wang, L. Wu, Y. Wang, Y. Liu, W. Fan, M. He, O. Terasaki and T. Tatsumi, *J. Am. Chem. Soc.*, 2008, **130**, 8178–8187.

74   B. F. Hoskins and R. Robson, *J. Am. Chem. Soc.*, 1989, **111**, 5962–5964.

75   N. Hosono and S. Kitagawa, *Acc. Chem. Res.*, 2018, **51**, 2437-2446

76   S. Chavan, J. G. Vitillo, E. Groppo, F. Bonino, C. Lamberti, P. D. C. Dietzel and S. Bordiga,

J. Phys. Chem. C, 2009, **113**, 3292–3299.

77   M. Eddaoudi, J. Kim, N. Rosi, D. Vodak, J. Wachter, M. O'Keeffe and O. M. Yaghi, *Science*, 2002, **295**, 469–72.

78   H. Furukawa, K. E. Cordova, M. O'Keeffe, O. M. Yaghi, M. O'Keeffe and O. M. Yaghi, *Science (80-.).*, 2013, **341**, 1230444.

79   A. C. McKinlay, B. Xiao, D. S. Wragg, P. S. Wheatley, I. L. Megson and R. E. Morris, *J. Am. Chem. Soc.*, 2008, **130**, 10440–10444.

80   N. Zhao, F. Sun, P. Li, X. Mu and G. Zhu, *Inorg. Chem.*, 2017, **56**, 6938–6942.

81   D. Sarma, K. V. Ramanujachary, S. E. Lofland, T. Magdaleno and S. Natarajan, *Inorg. Chem.*, 2009, **48**, 11660–11676.

82   L.-L. Dang, X.-J. Zhang, L. Zhang, J.-Q. Li, F. Luo and X.-F. Feng, *J. Coord. Chem.*, 2016, **69**, 1179–1187.

83   S. Halis, A. K. Inge, N. Dehning, T. Weyrich, H. Reinsch and N. Stock, *Inorg. Chem.*, 2016, **55**, 7425–7431.

84   Y. G. Chung, J. Camp, M. Haranczyk, B. J. Sikora, W. Bury, V. Krungleviciute, T. Yildirim, O. K. Farha, D. S. Sholl and R. Q. Snurr, *Chem. Mater.*, 2014, **26**, 6185–6192.

85   P. Pachfule, R. Das, P. Poddar and R. Banerjee, *Cryst. Growth Des.*, 2011, **11**, 1215–1222.

86   N. a Li-yan, H. U. a Rui-nian, N. Gui-ling and O. U. Xiao-xia, *Science*, 2012, **28**, 555–558.

87   M. R. M. R. Chapman, S. E. S. E. Henkelis, N. Kapur, B. N. B. N. Nguyen and C. E. C. E. Willans, *ChemistryOpen*, 2016, **5**, 351–356.

88   K. Pirzadeh, A. Asghar Ghoreyshi, M. Rahimnejad and M. Mohammadi, *Korean J. Chem. Eng*, 2018, **35**, 974–983.

89   D. Ruano, M. Díaz-García, A. Alfayate and M. Sánchez-Sánchez, *ChemCatChem*, 2015, **7**, 674–681.

90   P. K. Allan, P. S. Wheatley, D. Aldous, M. I. Mohideen, C. Tang, J. A. Hriljac, I. L. Megson, K. W. Chapman, G. De Weireld, S. Vaesen and R. E. Morris, *Dalton Trans.*, 2012, **41**, 4060–6.

91   N. J. Hinks, A. C. McKinlay, B. Xiao, P. S. Wheatley and R. E. Morris, *Microporous Mesoporous Mater.*, 2010, **129**, 330–334.

92   A. C. McKinlay, P. K. Allan, C. L. Renouf, M. J. Duncan, P. S. Wheatley, S. J. Warrender, D. Dawson, S. E. Ashbrook, B. Gil, B. Marszalek, T. Düren, J. J. Williams, C. Charrier, D. K. Mercer, S. J. Teat and R. E. Morris, *APL Mater.*, 2014, **2**, 124108.

93   S. R. Miller, E. Alvarez, L. Fradcourt, T. Devic, S. Wuttke, P. S. Wheatley, N. Steunou, C. Bonhomme, C. Gervais, D. Laurencin, R. E. Morris, A. Vimont, M. Daturi, P. Horcajada and C. Serre, *Chem. Commun. (Camb).*, 2013, **49**, 7773–5.

94   S. Rojas, P. S. Wheatley, E. Quartapelle-Procopio, B. Gil, B. Marszalek, R. E. Morris and E. Barea, *CrystEngComm*, 2013, **15**, 9364.

95   D. Cattaneo, S. J. Warrender, M. J. Duncan, R. Castledine, N. Parkinson, I. Haley and R. E. Morris, *Dalton Trans.*, 2015, **45**, 618–629.

96   S. Chavan, F. Bonino, L. Valenzano, B. Civalleri, C. Lamberti, N. Acerbi, J. H. Cavka, M. Leistner and S. Bordiga, *J. Phys. Chem. C*, 2013, **117**, 15615–15622.

97   P. D. C. Dietzel, B. Panella, M. Hirscher, R. Blom and H. Fjellvåg, *Chem. Commun.*, 2006, 959.

98   T. Grant Glover, G. W. Peterson, B. J. Schindler, D. Britt and O. Yaghi, *Chem. Eng. Sci.*, 2011,

66, 163–170.

99   A. C. McKinlay, J. F. Eubank, S. Wuttke, B. Xiao, P. S. Wheatley, P. Bazin, J.-C. Lavalley, M. Daturi, A. Vimont, G. De Weireld, P. Horcajada, C. Serre and R. E. Morris, *Chem. Mater.*, 2013, **25**, 1592–1599.

100   L. Garzón-Tovar, A. Carné-Sánchez, C. Carbonell, I. Imaz and D. Maspoch, *J. Mater. Chem. A*, 2015, **3**, 20819–20826.

101   G. Férey and C. Serre, *Chem. Soc. Rev.*, 2009, **38**, 1380–99.

102   S. Chavan, F. Bonino, J. G. Vitillo, E. Groppo, C. Lamberti, P. D. C. Dietzel, A. Zecchina and S. Bordiga, *Phys. Chem. Chem. Phys.*, 2009, **11**, 9811–22.

103   E. Barea, C. Montoro and J. A. R. Navarro, *Chem. Soc. Rev.*, 2014, **43**, 5419–30.

104   U. Böhme, B. Barth, C. Paula, A. Kuhnt, W. Schwieger, A. Mundstock, J. Caro and M. Hartmann, *Langmuir*, 2013, **29**, 8592–600.

105   W. L. Queen, M. R. Hudson, E. D. Bloch, J. a. Mason, M. I. Gonzalez, J. S. Lee, D. Gygi, J. D. Howe, K. Lee, T. a. Darwish, M. James, V. K. Peterson, S. J. Teat, B. Smit, J. B. Neaton, J. R. Long and C. M. Brown, *Chem. Sci.*, 2014, **5**, 4569–4581.

106   S. R. Caskey, A. G. Wong-Foy and A. J. Matzger, *J. Am. Chem. Soc.*, 2008, **130**, 10870–1.

107   M. H. Rosnes, M. Opitz, M. Frontzek, W. Lohstroh, J. P. Embs, P. A. Georgiev and P. D. C. Dietzel, *J. Mater. Chem. A*, 2015, **3**, 4827–4839.

108   A. C. Mckinlay, B. Xiao, D. S. Wragg, P. S. Wheatley, I. L. Megson and R. E. Morris, *J. Am. Chem. Soc.*, 2008, **130**, 10440–10444.

109   K. Matsuyama, N. Hayashi, M. Yokomizo, T. Kato, K. Ohara and T. Okuyama, *J. Mater. Chem. B*, 2014, 7551–7558.

110   P. Horcajada, C. Serre, M. Vallet-Regí, M. Sebban, F. Taulelle and G. Férey, *Angew. Chem. Int. Ed. Engl.*, 2006, **45**, 5974–8.

111   P. C. Ford and I. M. Lorkovic, *Chem. Rev.*, 2002, **102**, 993–1017.

112   K. Peikert, L. J. McCormick, D. Cattaneo, M. J. Duncan, F. Hoffmann, A. H. Khan, M. Bertmer, R. E. Morris and M. Fröba, *Microporous Mesoporous Mater.*, 2015, **216**, 118–126.

113   A. W. Carpenter, J. A. Johnson and M. H. Schoenfisch, *Colloids Surfaces A Physicochem. Eng. Asp.*, 2014, **454**, 144–151.

114   A. W. Carpenter and M. H. Schoenfisch, *Chem. Soc. Rev.*, 2012, **41**, 3742–52.

115   M. T. Gladwin, J. H. Crawford and R. P. Patel, *Free Radic. Biol. Med.*, 2004, **36**, 707–17.

116   M. R. Melis and A. Argiolas, *Eur. J. Pharmacol.*, 1995, **294**, 1–9.

117   P. Pacher, J. S. Beckman and L. Liaudet, *Physiol. Rev.*, 2007, **87**, 315–424.

118   S. M. Vornholt, S. E. Henkelis and R. E. Morris, *Dalton Trans.*, 2017, **46**, 8298–8303.

119   S. E. Henkelis, L. J. McCormick, D. B. Cordes, A. M. Z. Slawin and R. E. Morris, *Inorg. Chem. Commun.*, 2016, **65**, 21–23.

120   B. Bueken, H. Reinsch, N. Heidenreich, A. Vandekerkhove, F. Vermoortele, C. E. A. Kirschhock, N. Stock, D. De Vos and R. Ameloot, *CrystEngComm*, 2017, **19**, 4152–4156.

121   F. Luo, C. Yan, L. Dang, R. Krishna, W. Zhou, H. Wu, X. Dong, Y. Han, T.-L. Hu, M. O'Keeffe, L. Wang, M. Luo, R.-B. Lin and B. Chen, *J. Am. Chem. Soc.*, 2016, **138**, 5678–5684.

CHAPTER 2:
AIMS

This thesis largely focuses on the mechanistic analysis of the Assembly-Disassembly-Organisation-Reassembly (ADOR) process through a range of crystallographic techniques including *in situ* and *ex situ* powder X-ray diffraction, *in situ* and *ex situ* Pair Distribution Function (PDF) analysis, solid-state NMR spectroscopy and solid-state kinetics using the Avrami-Erofeev and Sharp-Hancock equations. This hopes to shed light on the selectivity of the ADOR process in different media and the mechanism by which the d4r breakdown and the silica species intercalate to build up a new daughter zeolite.

On a different note, a study into the refinement of synthesis conditions used to prepare polycrystalline powders of Metal-Organic frameworks, namely CPO-27-M (MOF-74) and single crystal CPO-27-Mg, -Zn and UTSA-74 was undertaken. The aim was to understand the effects of base, temperature and modulator to tune the synthesis into producing either powders or single crystals in a facile manner. The work included understanding the effect of the metal cation and crystal size on uptake and release of nitric oxide.

CHAPTER 3: EXPERIMENTAL TECHNIQUES

3.1.   Solvothermal Synthesis

Solvothermal synthesis is a technique used to afford solid materials that are typically crystalline and are produced by reacting at autogenous pressure.[1] This pressure is produced by reacting at temperatures above the boiling point of the solvent used, which reduces the viscosity of the solvent promoting diffusion. This allows a range of materials to be produced that under normal conditions would not be able to be synthesised. Reaction mixtures are placed in a Teflon-lined steel autoclave and heated (> 1 bar, > 100 °C) for days or even weeks (Figure 3.1).

Figure 3.1. A standard autoclave showing the steel autoclave unit (1), steel autoclave screw-on lid (2), Teflon liner with lid (3), outer disc (4), inner disc (5) and spring (6).

3.1.1.   Synthesis of Zeolites

In nature, zeolites are produced from a silica condensation under high temperatures and intense pressure, to give a material with a high thermal stability (up to 1000 °C). In a

laboratory setting, they are prepared under mild conditions with alumina and/or silica sources and an alkali hydroxide solution to produce a gel. This gel is then charged into an autoclave and heated for up to 2 weeks above 100 °C.[2]

This approach was first used by Barrer and Milton in the 1940s, to synthesise zeolite A, P, and X.[3] The field has since expanded with the use of a fluoride source, the addition of new elements such as copper, iron and germanium, and the use of ammonium cations. The use of ammonium cations in the synthesis allows a high Si/Al ratio to be achieved, thus allowing for the first high-silica zeolite, zeolite beta, to be produced. Hydrothermal synthesis differs from solid-state synthesis as it allows for the formation of products that have high crystallinity and purity with a low energy consumption and reduced air and liquid waste pollution.[4]

Although hydrothermal synthesis seems a relatively simple technique, it remains a challenge to control and predict the chemistry of reaction. This is because controlling the chemistry of zeolite formation is a fine balance between nucleation and crystallisation, precipitation, and polymerisation. Each of these depends on different internal and external factors, such as batch composition, water, alkalinity, ageing, temperature, seeding and stirring.[2]

The zeolite and MOF samples afforded using hydro/solvothermal synthesis were produced in 15 - 50 mL General-Purpose Acid Digestion Vessel Parr steel autoclaves with Teflon inserts. Three Carbolite High-Temperature Laboratory Ovens, model PF60, were used to induce hydrothermal conditions from 2 – 7 days at temperatures of 100 – 200 °C.

3.2.   X-ray Crystallography[5–7]

X-ray crystallography is a technique used to determine the atomic structure of a crystal. Measured experimental intensity is combined with additional phase information to compute an electron density map. Radiation is produced from the bombardment of a metal with high energy electrons. When electrons enter the atmosphere of a metal ion, they decelerate, and *Bremsstrahlung* radiation is emitted. These high energy electrons then collide with a core electron from the 1s orbital, which causes its ejection. This creates a vacancy that must be filled, and this occurs by the relaxation of a 2p or 3p electron. The excess transition energy is emitted as radiation of a specific wavelength. Typical metals used are molybdenum and copper as their emitted radiation corresponds to X-ray photons. The laboratory machines

used in this work exhibit copper $K\alpha_1$ radiation with wavelength 1.5406 Å and molybdenum $K\alpha$ radiation with wavelength 0.71075 Å.

3.2.1.   The Unit Cell

The molecules, atoms or ions in a crystal are arranged in three dimensions with an orderly repeating pattern. The simplest repeating unit, the unit cell, is repeated throughout the crystal by translational symmetry to form a lattice. The crystal lattice is an ordered array of symmetry-equivalent points, and as such any atom placed on a lattice point is identical to any other atom on another lattice point. The unit cell (Figure 3.2), therefore contains all symmetry elements of the structure. The unit cell is a parallelpiped which can be quantised by lengths *a*, *b* and *c* (corresponding to vectors between lattice points), representing coordinates with angles α, β and γ (e.g. α is the angle between the *b*- and *c*-axes).
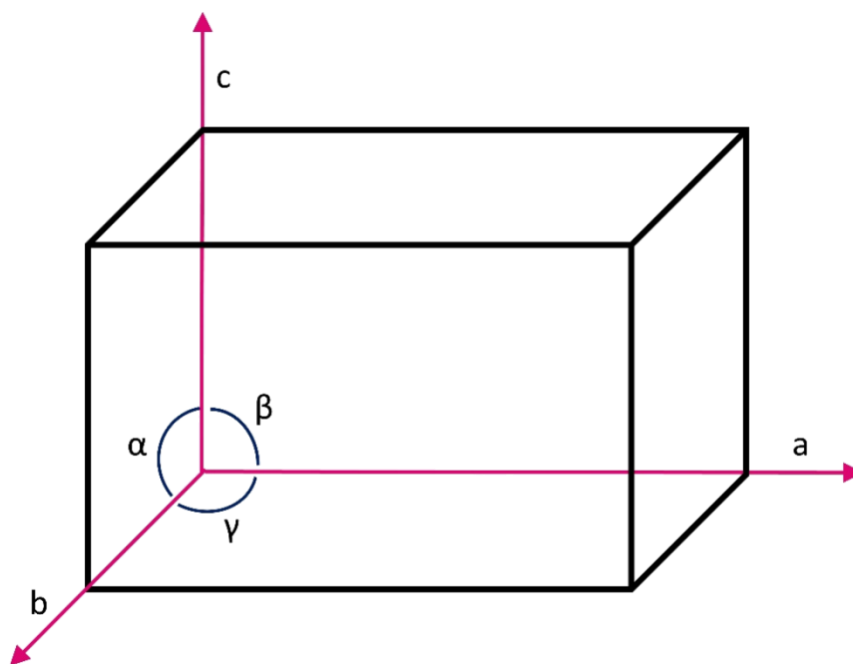
Figure 3.2. A schematic of the unit cell with coordinates shown.

The unit cell is defined based on the positions of the lattice points, for example in a Primitive cell (P), there is one lattice point per unit cell, with an eighth in each corner. Other lattices have more than one lattice point, for example centred lattices (A, B or C side-centred) have

two lattice points per unit cell, body centred (I) have two lattice points and face centred have four lattice points per unit cell.

Point groups, defined by the symmetry of individual molecules, describe the rotation and reflection symmetry elements that leaves one fixed point (the origin). In the solid state, glide planes and screw axes are formed when translational symmetry acts on the point symmetry, thus expanding the point group into a space group. In total there are 230 space groups, these describe all possible combinations of symmetry elements within the seven crystal systems. The combination of the crystal systems, restrictions and unit cell centring afford the fourteen Bravais lattices. These lattice centrings identify the location of the lattice points in the unit cell and are classified as Primitive (P), Body-Centred (I), Face-Centred (F), Base-Centred (A, B, C) and Rhombohedral (R) (Table 3.1).[8]

Table 3.1. The seven crystal systems and their unit cell restrictions, with the fourteen corresponding Bravais lattices for each crystal system.

Crystal System	Restrictions on unit cell	Bravais Lattice type
Triclinic	$a \neq b \neq c$ $\alpha \neq \beta \neq \gamma$	P
Monoclinic	$a \neq b \neq c$ $\alpha = \gamma = 90°$ $\beta \neq 90°$	P, C
Orthorhombic	$a \neq b \neq c$ $\alpha = \beta = \gamma = 90°$	P, C, I, F
Tetragonal	$a = b \neq c$ $\alpha = \beta = \gamma = 90°$	P, I
Cubic	$a = b = c$ $\alpha = \beta = \gamma = 90°$	P, F, I
Trigonal	$a \neq b \neq c$ $\alpha = \beta = \gamma \neq 90°$	P, R
Hexagonal	$a = b \neq c$ $\alpha = \beta = 90°$ $\gamma = 120°$	P

Understanding the symmetry operations within a crystal (space group) allows one to fully describe the crystal structure from the smallest unique part of the crystal – the asymmetric unit.

3.2.2. X-ray Diffraction[5–7,9]

Interference effects are termed diffraction and are caused when a wave encounters an obstacle and is scattered, this then causes a change in the intensity. In 1912, Max von Laue first discovered X-ray diffraction and found that the wavelength of X-ray radiation (ca. 1 Å) is in the same order of magnitude as the inter-atomic spacing in crystals. When the path difference between the incident and diffracted beams is a whole number of wavelengths, constructive interference is produced, and a peak/spot is formed. When no peak/spot is present, destructive interference has been produced. From this diffraction a 3-dimensional model of the structure can be found showing bond distances and angles.

Soon after the introduction of the Laue equation, W. H. Bragg and W. L. Bragg proposed a much simpler equation. Bragg proposed that the atoms in a lattice are arranged in parallel sets of equally-spaced planes in a crystal, and the incident X-rays are then "reflected" off these planes by passing through lattice points (Figure 3.3). This means that the angles of both incidence and reflectance must be equal, and the incoming/outgoing beams must all lie in one plane. As such to observe constructive interference, the path difference must be an integer number of wavelengths. Spots (single crystal) or peaks (powder) in diffraction patterns are then produced.
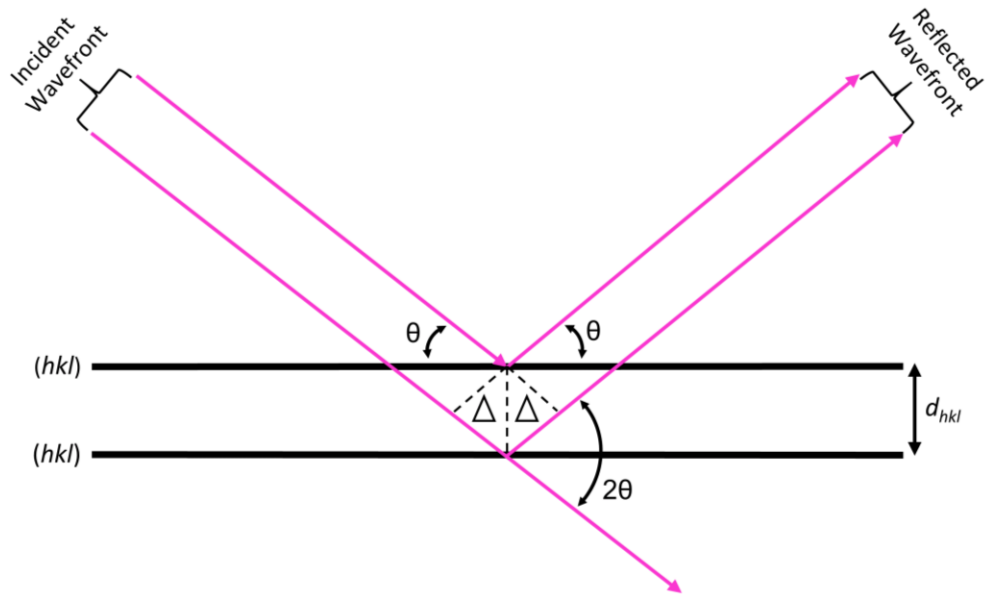
Figure 3.3. A representation of Braggs Law.

From the simple diagram an equation can be derived as:

$$2d_{hkl}sin\theta = n\lambda$$

Where *n* is an integer, θ and 2θ are the Bragg angles, *hkl* are miller indices, and d_{hkl} is the inter-planar spacing. From this we can say that the path difference is:

$$2\Delta = 2d_{hkl}sin\theta$$

And the constructive interference is:

$$2\Delta = n\lambda$$

Miller plane indices (*hkl*) are a set of three integers that correspond to fractional coordinates that lie along the axes set by the unit cell. For example, the *200* plane runs parallel to the *b* and *c*-axes but cuts the *a*-axis at 1/2. (Figure 3.4). If the *200* plane was to be drawn for every unit cell in the crystal structure, then infinite repeats of the planes will be produced, separated by length d_{200}. If atoms reside close to or on these planes in a regular array, then the incoming X-rays are "reflected" and a diffraction spot is observed at the scattering angle, 2θ when constructive interference has occurred. In this work, this spacing represents the inter-layer separation in both parent and hydrolysed zeolites.
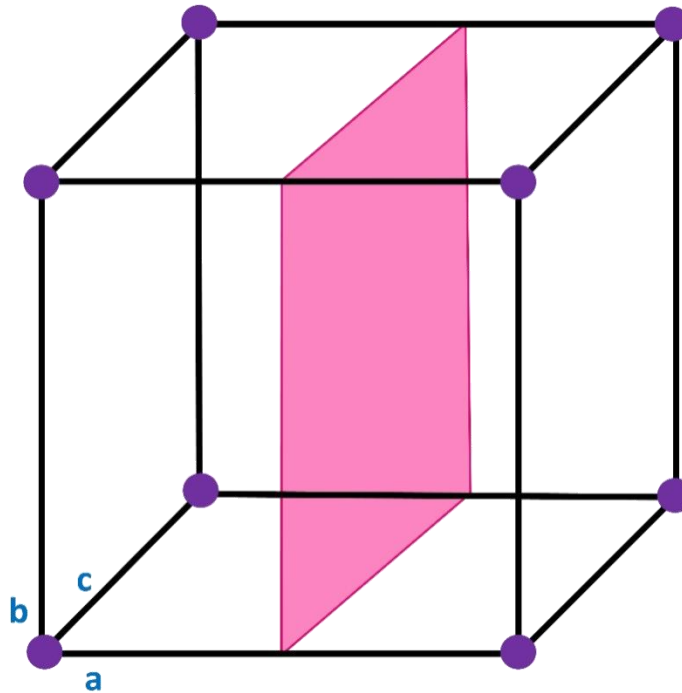
Figure 3.4. The *200* Miller plane that intersects halfway through the *a*-axis and the origin of both the *b* and *c*-axes.

Since many materials such as salts, organics, and inorganics can form crystals through natural or induced methods, X-ray crystallography has become fundamental in probing the structure of such crystals and in the development of their respective scientific fields.

The diffraction pattern is produced from the Fourier Transform of the electron density within the unit cell. Scattering of X-rays by the unit cell can be defined by the peak intensities:

$$I_{hkl} \propto |F_{hkl}|^2$$

Where intensity, I_{hkl} is proportional to $|F_{hkl}|$. Where $|F_{hkl}|$ is the collective scattering power of the atoms in the unit cell. Each reflection is a wave containing both phase and amplitude. This is represented by a complex number *i.* Thus for an atom *j*, the scattering factor is *f_j* and coordinates x_j, y_j, z_j. The structure factor F can be calculated:

$$F_{hkl} = \sum_{j=1}^{N} f_i \, exp2\pi i(hx_j + ky_j + lz_j)$$

This equation can be applied to every reflection to produce a set of structure factors, which each contain phase and amplitude. Phases are lost during a diffraction pattern and therefore must be calculated. The Fourier Transform of all the structure factors affords the total electron density, p within the unit cell.

$$p(xyz) = \frac{1}{V}\sum_{hkl} F_{(hkl)}exp[-2\pi(hx + ky + lz)]$$

3.2.3.   Single Crystal X-ray Diffraction[6]

When crystals are large enough and of sufficient quality to be collected from solution and crystallography, the diffraction pattern produces an array of spots in certain positions varying with intensity dependent on the crystal structure (Figure 3.5).
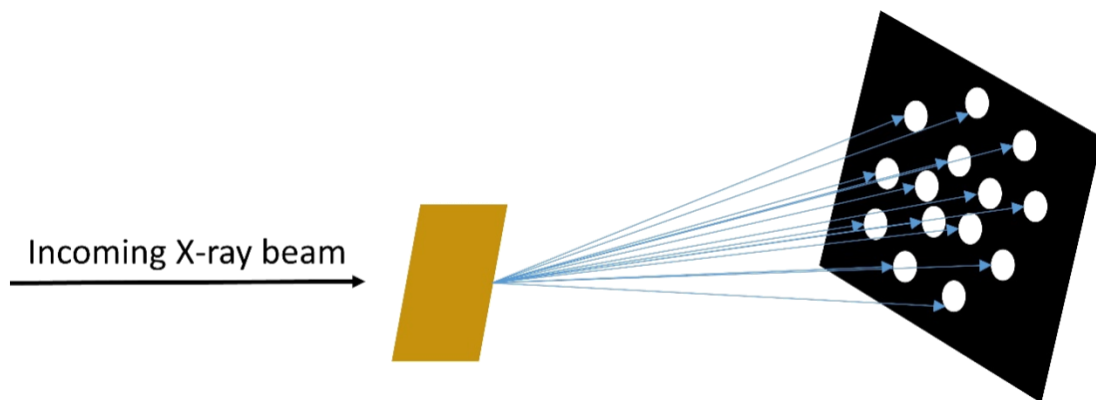
Figure 3.5. A diagram to show the incident beam and reflected X-rays from a crystal, producing its diagnostic pattern of spots.

Crystals are first examined under a microscope to determine crystal size and shape. Typically, the size of a crystal must be bigger than 5 x 5 x 5 μm to diffract sufficiently (diffractometer dependant) so that data can be recorded. The crystals should be of a regular shape without defects such as twinning, cracks, consistent colour, and consistent shape. Problems such as these can be visualised by changing the polarisation of light when under the microscope. All crystals, except those with cubic symmetry or some high-symmetry, should polarize the light in all 90 ° of rotation. This means that if defects (cracks, twinning etc.) are present, the light will be extinguished at different angles.

The geometry, symmetry and intensity of diffraction spots correspond to certain elements of the crystals structure. The spots lie in certain positions and are said to have a certain geometry, these are generated at the detector by an individually scattered X-ray beam. The geometry relates directly to the geometry of the unit cells and can therefore tell us the repeat distances between molecules. The symmetry of spots describe the space group and crystal system to which the crystal belongs to. Finally, the varied intensities of each spot holds all the information available on the positions of the atoms in the unit cell. This occurs as it is the combination of their individual interactions with X-rays that generates different amplitudes for different directions of scattering. Therefore, by measuring the different intensities, a full molecular structure can be determined.

3.2.4. Powder X-ray Diffraction[10,11]

Single crystal X-ray diffraction is a powerful tool to analyse the structure of materials. However, this requires one perfect crystal of sufficient size to be rotated in the X-ray beam to generate the whole pattern. Many materials, such as zeolites, do not produce crystals big enough to analyse efficiently so the material is ground into a powder and analysed by powder X-ray diffraction.

Polycrystalline materials are made up of randomly orientated crystals of size $10^{-7} - 10^{-4}$ m. A sample must be ground using a pestle and mortar so that preferred orientation is not seen in the powder pattern. Upon entry to the X-ray beam, powders diffract in all possible directions controlled by the Bragg equation.

Unlike the spots seen in single crystal X-ray diffraction patterns, powder patterns are made up of a series of rings (diffraction cones) emanating from the origin defined by the direction of the incident beam (Figure 3.6). The diffraction cones are made up of diffraction spots from the Miller planes from each individual crystallite. The powder rings are then collected and then integrated to reduce in two dimensions. This produces a pattern from which one can ascertain whether the material is crystalline and phase pure. A model can be constructed and refined against the experimental pattern through two types of refinement, Pawley and Rietveld.
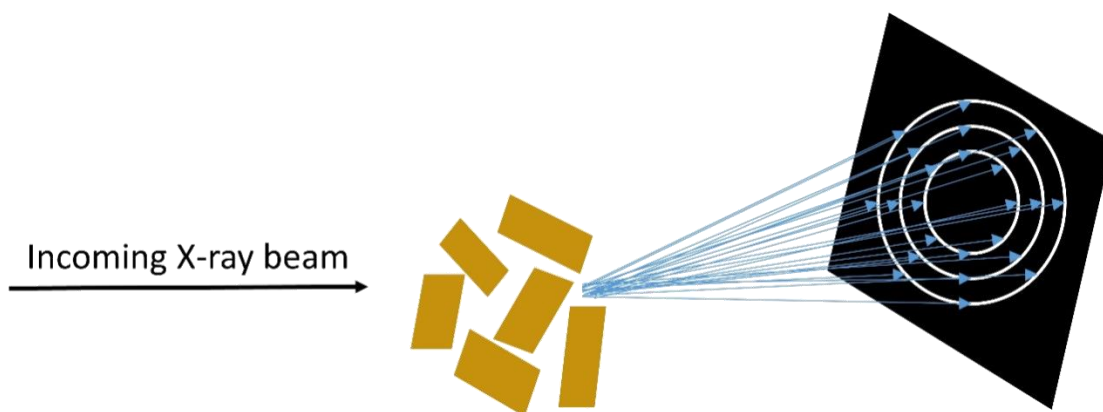
Figure 3.6. A diagram to show the incident beam and reflected wavelengths from a polycrystalline powder, producing its diagnostic pattern of rings.

3.2.4.1. Data Collection and Processing

In this work, powder data were collected using two experimental "in-house" set-ups, flat plate (or discs) and capillaries.

Flat Plate: Samples were ground and then packed into aluminium discs. The sample has to be flush with the surface of the disc and the surface of the sample to be flat in order to record accurate 2θ values. The sample must be packed tightly so that the sample doesn't fall out when tilted in the diffractometer. Data were collected on a Panalytical Empyrean diffractometer monochromated with a curved Ge(111) crystal in reflectance mode operating Cu K$_{\alpha 1}$ radiation.

Capillary: Samples were ground and packed into 0.5 mm borosilicate capillaries by vibrating the sample down the capillary using forceps to pack tightly at the bottom. The capillary is then attached to the goniometer within the machine and centred in the beam. The capillary is rotated at constant speed whilst being bombarded by X-rays. The run time, step size and 2θ range can be controlled using the WINXPOW program. Data were collected on a STOE STADIP operated in capillary Debye-Scherrer mode, using Cu K$_{\alpha 1}$ radiation.

3.2.4.1.1. Rietveld Refinement[9,12–14]

H. M. Rietveld first introduced a full-profile refinement in 1966, whereby a model is fitted to experimental PXRD data without the need to extract individual intensities. During refinement, a non-linear least squares is used to minimise the difference between observed and calculated values:

$$Least\ Squares = \sum_i w(y_c - y_o)^2$$

Where w is the weighting factor applied to an individual point and y_o and y_c are the observed and calculated intensities, respectively. Using the least squares method, the zero-point, background and peak shapes must first be refined before refining other parameters including unit cell and coordinates. Refining only the profile parameters, leads to a structure-less fit, known as a Pawley fit.

To follow the progress of the minimisation, there are many statistics that can be used, two of the most common are R_{WP} and χ^2. The expected profile, R_{exp} and the weighted R-factor, R_{WP} are a measure of how well a model and experimental PXRD fit:

$$R_{WP} = \sqrt{\frac{LS}{\Sigma\, wy_o{}^2}}$$

$$R_{exp} = \sqrt{\frac{N}{\Sigma\, w(y_o)^2}}$$

Where N is the number of profile points. The goodness of fit, χ^2 can then be sought by comparing R_{exp} and R_{WP}. As R_{WP} approaches R_{exp}, the value of χ^2 moves closer to 1. A value of close to 1 indicates a good refinement and suggests the model fits well with the observed data.

$$\chi^2 = \left(\frac{R_{WP}}{R_{exp}}\right)^2$$

3.2.5.   Pair Distribution Function Analysis[15–19]

Pair distribution function (PDF) analysis is a diffraction technique that describes the probability of finding two atoms at given inter-atomic distances, *r* without relying on Bragg diffraction from the material (Figure 3.7).
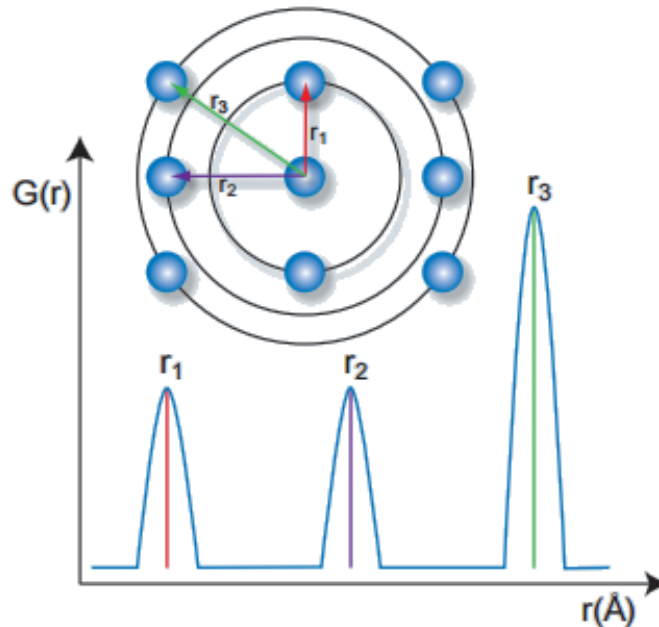
Figure 3.7. Inter-atomic distances corresponding to peaks in PDF.

Diffuse scattering in traditional diffraction techniques is regarded as background noise as only well-ordered materials are studied. As long-range order decreases, defects redistribute the scattering intensity around the Bragg peak. As such the diffuse scattering can be interpreted as probing local order. As the PDF is calculated from both the Bragg diffraction and the diffuse scattering intensities, it is a useful tool for probing such samples that cannot show long-range order, for example glasses (Figure 3.8). As such the resulting diffraction pattern of these materials would be a continuous distribution of scattering intensity over the angle range which cannot be analysed by Bragg methods. Historically, this technique has been used to characterise the structures of liquids and glasses but has since been used for fully or semi-crystalline materials such as Metal-Organic frameworks and zeolites.

Until recently, analysis of solids by PDF resulted in large termination errors due to limited Q-ranges accessible on typical laboratory X-ray sources. However, analysis through PDF has

become increasingly used due to the improved availability of instruments at synchrotron sources and user-friendly software. It allows for structure changes in both solid-solid transformations and crystallisation of solids to be monitored *in situ.*
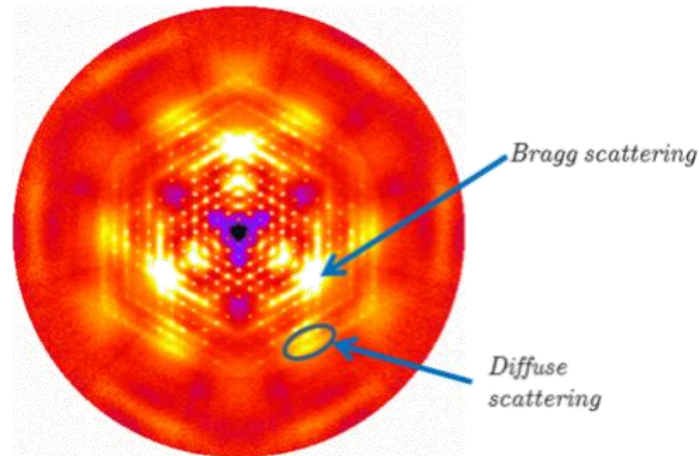
Figure 3.8. Bragg and Diffuse scattering in a crystal.[20]

Constructive interference is formed when long-range order is present in a material. Therefore, in samples like a liquid when there is deviation in long-range order, the conditions for Bragg diffraction are destroyed. Scattering is then redistributed in reciprocal space around the Bragg peaks. The redistribution is dependent on the correlation length of the material. A highly crystalline material will have an almost infinite correlation length, whereas the more the sample tends towards amorphousness the lower the correlation length. The less crystalline the sample is the more diffuse scattering around the Bragg peaks is produced.

PDF treats both the Bragg diffraction and diffuse scattering in equal quantities, thus probing the local order of a structure and therefore, allowing amorphous material to be analysed. A total scattering experiment monitors the scattering intensity variation with scattering vector. The total scattering, Q is the magnitude of the scattering vector **S**, which now is no longer confined by the Laue conditions and can take any value such that:

$$Q = \frac{4\pi sin\theta}{\lambda}$$

Experimental intensity data, $I(Q)$ is made up of several components, coherent scattering, $I_{coh}(Q)$, incoherent scattering, $I_{incoh}(Q)$, multiple scattering, $I_{MS}(Q)$ and scattering from the background, $I_{BG}(Q)$.

$$I_{experimental}(Q) = I_{coh}(Q) + I_{incoh}(Q) + I_{MS}(Q) + I_{BG}(Q)$$

The coherent scattering contains all structural information, therefore the incoherent, multiple and background must be subtracted by applying various corrections to the data before a Fourier transform can be undertaken. These intensity data can then be normalized to give a function with units scattering-per-atom, the structure function, $S(Q)$. The structure function is essentially a powder diffraction pattern that oscillates around 1 at high Q where c_i is the concentration of atom species i and f_i is the X-ray form factor of atom species i.

$$S(Q) = \frac{I^{coh}(Q) - \sum c_i |f_i(Q)|^2}{|\sum c_i f_i(Q)|^2} + 1$$

Sharp peaks at low Q-values can be seen due to the Bragg intensity, with wider peaks at higher Q-values due to diffuse scattering. The intensity of the peaks at high Q decrease due to the Debye-Waller factor. The Debye-Waller factor smooths the features of the structure function as it represents the thermal motion and quantum zero-point energy of the sample atoms. Therefore at ca. 30 Å^{-1} little meaningful information can be gathered.

$S(Q)$ can be transformed to the more commonly reported reduced structure factor $F(Q)$ by a simple relationship:

$$F(Q) = (S(Q) - 1)Q$$

$F(Q)$ is directly related to the reduced pair distribution function, $G(r)$, via a Fourier transform:

$$G(r) = \frac{2}{\pi} \int_{Q_{min}}^{Q_{max}} Q\,[S(Q) - 1]\sin(Qr)\,dQ$$

$$= \frac{2}{\pi} \int_{Q_{min}}^{Q_{max}} F(Q)\sin(Qr)\,dQ$$

The $G(r)$ is most commonly used as it is directly calculated from the normalised scattering data and as it is equally weighted throughout the whole r-range, therefore it allows one to

easily interpret and model the peaks. All PDFs shown in this work refer to *G(r)* exclusively (Figure 3.9).
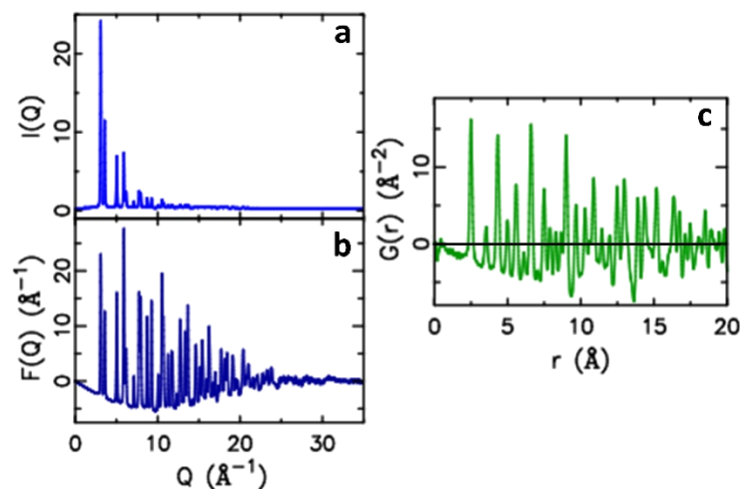
Figure 3.9. a - Raw intensity data, *I(Q)*; b - normalised reduced scattering function, *F(Q)*; c - pair distribution function, *G(r)*. Figure adapted from the PDFGetX2 user manual.[21]

3.2.5.1. Data Collection and Processing

Data collection is essentially the same as standard powder X-ray diffraction typically using a 1-dimensional detector in Debye-Scherrer mode where the *Q*-range is determined by the wavelength of the diffractometer.

$$Q_{max} = \frac{4\pi sin\theta}{\lambda}$$

A more common method of acquiring PDF data is by using rapid acquisition PDF measurements (RAPDF), whereby PDF data is collected in one-shot. RAPDF was used for all *ex situ* PDFs collected in this work, with a collection time of 300 sec. A well-ground sample of zeolite was packed in Kapton (polyimide) capillaries and sealed with Epoxy resin. High energy X-rays are fired through the capillary and scattering is collected by a 2-dimension large-area detector lying perpendicular to the incoming beam. Like PXRD, scattering appears as rings of data. The background is determined by collecting the Kapton capillary without sample, and the distance between the sample and detector determined using a ceria (CeO_2) standard. *In situ* PDF collection will be discussed in sections 3.2.7.1 and 3.2.7.2.

Once the 2-dimensional data has been collected it must be integrated to produce a 1-dimensional graph of $I(Q)$. The sample-detector distance can be used to convert to the 2θ angle from which the ring was scattered, this is done in FIT2D.[22] The beamstop must be masked before the data can be processed further, this can also be achieved in FIT2D. A *.chi* file is produced from this processing and contains intensity data as a function of Q. $I_{experimental}(Q)$ as described before is made up of four components. The incoherent, multiple scattering and scattering related to the background must all be removed before the Fourier transform can take place. This can be done in PDFGetX2,[21] by inputting sample background information, chemical composition and experiment geometry to produce $S(Q)$. After scaling the background to the sample so that termination ripples below 1.3 Å are as small as possible, the $G(r)$ was produced by a Fourier transform.

From the experimental PDF, four types of information can be extracted directly before modelling and refinement takes place. These are crystallinity, bond lengths, thermal or static disorder and coordination number.[11]

Crystallinity: R_{max} is a value that states which peaks are discernible above background noise. This allows one to gain an insight into the crystallinity of the sample. For example, the more ordered the sample, the more atom-to-atom distances will be visible out to a large distance (ca. > 100 Å).

Bond lengths: In the experimental PDF the peak positions at distance r, relate to the atom-atom bond lengths within the material. For example, a peak positioned at 1.6 Å correlates to a T-O (T = Si, Ge) bond length in germanosilicates. These peak positions are particularly useful to observe *in situ*, to monitor structural changes in a material when exposed to heat, acid or alkali conditions.

Disorder: Static or thermal disorder can be envisaged by the width of the peaks in the PDF. The more disordered a material is, the wider the peaks will be. If high temperatures are employed, the peaks will be wider due to the increased amount of excited vibrational states, and therefore a wider range of inter-atomic distances are possible.

Coordination number: If the composition of the material and the atoms of the peak under question are known, one can integrate under the peak to understand the coordination number. This is only useful at lower r-regions however, as above this, peak overlap is prominent.

By using a feasible computational model, one can gain further insight into the structure of the material analysed by PDF. The model is refined against the experimental data in a least-squares-type refinement in the PDFGui software package.[23] The refinement is analogous to a traditional Rietveld approach and can be achieved by defining structural and experimental parameters and then refining to get the best fit possible (Figure 3.10). In this work, the computational models refined against the PDFs, with the refinement parameter R_{cut} set at 3.38 Å, the maximum distance where correlated motion still has an effect on the material. All fits had a lower limit of 1.38 Å, peaks below here do not have any physical meaning as heavy atom contacts shorter than this are not possible for germanosilicates. Such peaks can be attributed to experimental and Fourier termination errors.
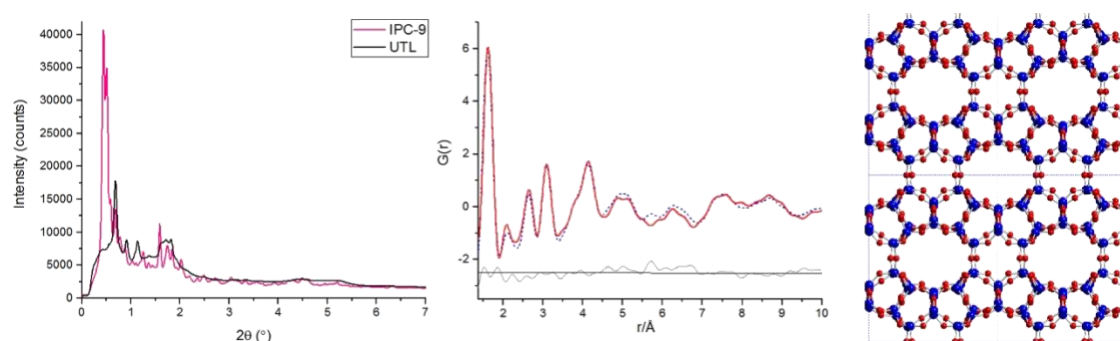
Figure 3.10. LEFT - Initial powder X-ray diffraction patterns of parent **UTL** (pink) and "unfeasible" daughter zeolite IPC-9 (black); MIDDLE - Refinement of an IPC-9 model against experimental PDF data. Red solid line is experimental line, blue dashed line is the calculated PDF from the model and the grey line is the difference between the two offset by -2.5; RIGHT – The PDF refined model of IPC-9 viewed along the c-axis, Si – blue, O – red.

Another method of PDF refinement is to use a "big box" or Monte-Carlo process. The Monte-Carlo method is a general method of modelling which uses statistical principles, i.e. gambling. If we assume that the density $p(r)$ is described by a set of atomic positions (r_v), and move one atom by a certain amount. This move is either rejected or accepted and then repeated many times for each atom. The process is stopped when one can no longer improve the value of r.

3.2.6. Synchrotron Radiation

Laboratory X-ray sources prove useful in analysing materials, allowing one to identify whether the material is crystalline, phase pure and through a search-and-match identify whether the material is the desired product from reaction. It is a relatively cheap and efficient way to obtain good data. However, for analysis such as PDF or Rietveld refinements, a synchrotron source is necessary to obtain data of a high enough standard.

A synchrotron is a particle accelerator. Electrons (or positrons) are produced in an electron gun and then accelerated to the speed of light using a high potential in a linear accelerator. Magnetic fields in the outer storage ring are used to cause the electron to turn in a circular path and accelerate. When travelling around the ring, they are deflected by the magnets and as such emit electromagnetic radiation at a tangent to the electrons orbit. This radiation is then channelled to a beamline where it is monochromated for the required experimental set-up.

Insertion devices are periodic magnets that stimulate brilliant, forward-directed radiation; these are added into accelerator tracks in the storage ring. There are two types of insertion devices wigglers and undulators, both of which can provide several orders of magnitude higher flux than simple bending magnets.

Wigglers periodically laterally deflect or wiggle the electron beam inside the ring. This causes a change in acceleration and as the wavelength has been decreased, the frequency increases. As frequency is directly proportional to energy, wigglers have higher energy. Beamline I15 at the Diamond Light Source (DLS), UK uses wigglers (Figure 3.11).

Undulators consist of periodic dipole magnets, where the electrons are forced to oscillate and therefore radiate energy. This energy produced is very intense and concentrated into a narrow energy band. Beamline 11-ID-B at the Advanced Photon Source (APS), USA direct energy using undulators.
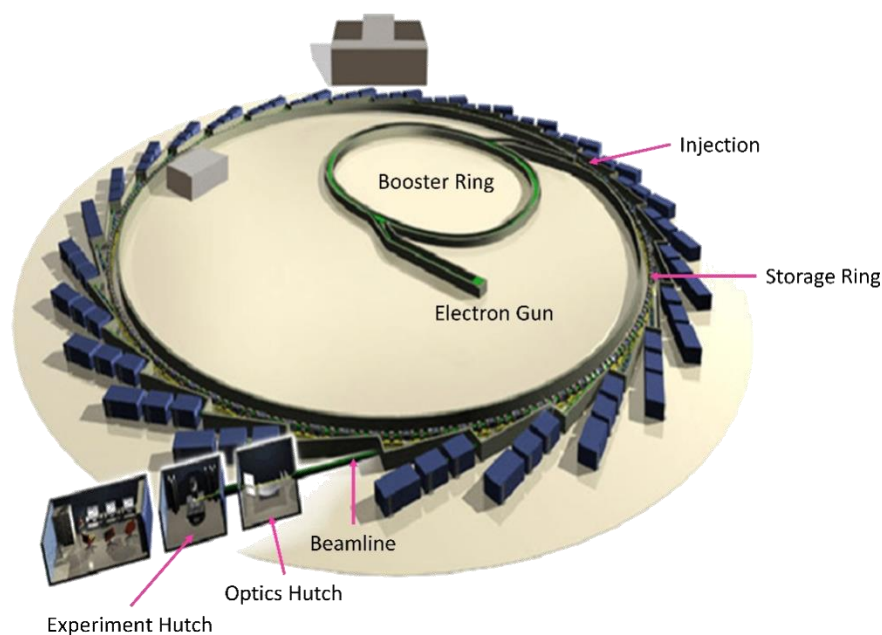
Figure 3.11. A schematic of Diamond Light Source synchrotron. Figure adapted from www.diamond.ac.uk.

3.2.6.1. Brass Environmental Cell – Beamline I15, Diamond Light Source

PDF analysis (Chapter 6) was used to monitor the hydrolysis (Disassembly) and rearrangement (Organisation) steps in the ADOR process. *In situ* PDF measurements were performed at beamline I15 at Diamond Light Source using a custom-made liquid cell adapted for X-ray transmission (Figure 3.12).[24] Measurements were taken using an X-ray beam of energy 72 keV (λ = 0.1722 Å) and an amorphous silicon area detector (PerkinElmer).
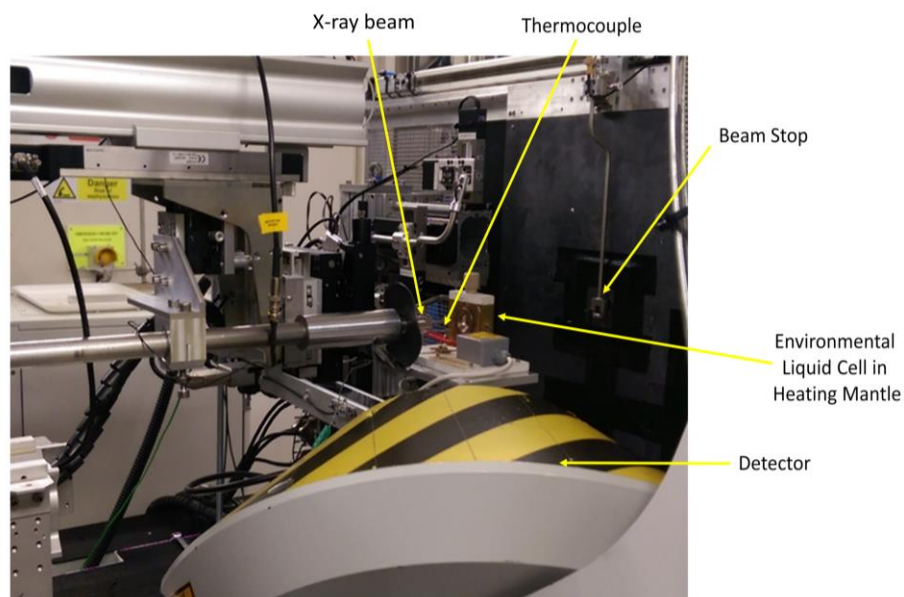
Figure 3.12. Beamline set-up. The brass environmental cell is placed in a heating mantle and three thermocouples attached. Both the heating mantle and cell are placed in the X-ray beam.

Data were collected at 300 s intervals, using a total exposure time of 10 s per scan. For all PDF experiments, background measurements were taken using the cell, but without the sample present. A ceria (CeO_2) standard was used to determine the sample-to-detector distance.

The cell walls were made up of Kapton windows, Viton and PTFE washers, a piston and a screw, which form an internal void with a diameter of 13 mm with a depth of 3 mm (Figure 3.13). Initially the cell wall was made up with plastic washers, however due to the high concentration of hydrochloric acid present at high temperature, the plastic was swapped for Viton, a polymer known for its high acid and thermal stability.
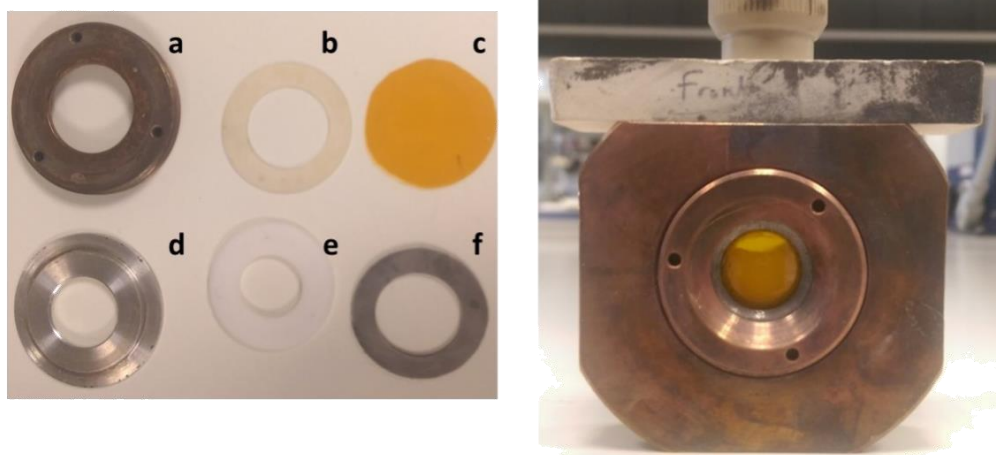
Figure 3.13. (LEFT) The components of the cell. a - screw; b – plastic washer (removed as not acid stable); c – Kapton window; d – piston; e – PTFE washer; f – Viton washer. (RIGHT) The brass environmental cell developed by the Sankar group.[24]

The cell was put together in seven steps (Figure 3.14):

1. One side of the cell wall was built up (steps 4 – 7) and half the desired amount of sample charged into the cell void.
2. The hydrolysis media was added to the sample in one steady portion.
3. The remaining sample was added in small portions and mixed to make a slurry.
4. Once a slurry had formed the Kapton window and Viton washer were added to start the cell window.
5. The PTFE washer was added.
6. The piston was added.
7. The screw was added and tightened with a three-pronged tool.

The cell used here did not allow for stirring or agitation, due to this the deintercalation process that is imperative to forming a fully formed zeolite after organisation does not occur fully. Because of this, the reactions were repeated at the Advanced Photon Source using a custom-made flow cell.
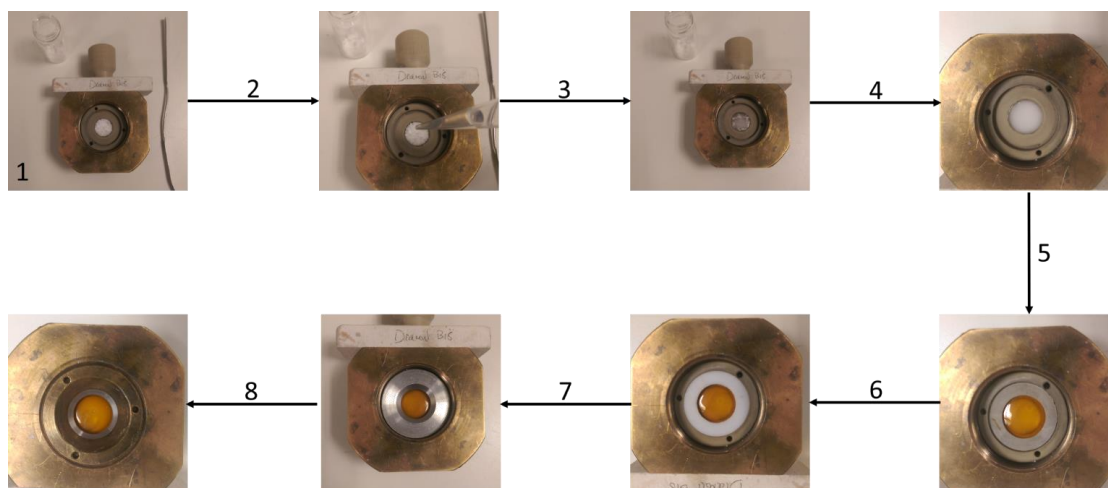
Figure 3.14. A schematic to show how the cell was put together. Step 1 – Half the amount of sample added to the cell window; Step 2 – Hydrolysis media added in one smooth portion; Step 3 – More sample added; Step 4 – Remaining sample added to make a slurry; Step 5 – Kapton window and Viton washer added; Step 6 – PTFE washer added; Step 7 – Piston added; Step 8 – Screw added and tightened with a 3-pronged tool.

3.2.6.2. Custom-built Gas Flow Cell Adapted for Liquids – Beamline 11-ID-B, Advanced Photon Source

As the data collected at the Diamond Light Source was not quantitative due to the lack of agitation the cell could achieve, the reaction conditions were repeated at the Advanced Photon Source on beamline 11-ID-B. A custom-made flow cell was built and customised to allow for liquid media (Figure 3.15 and 3.16).[25]
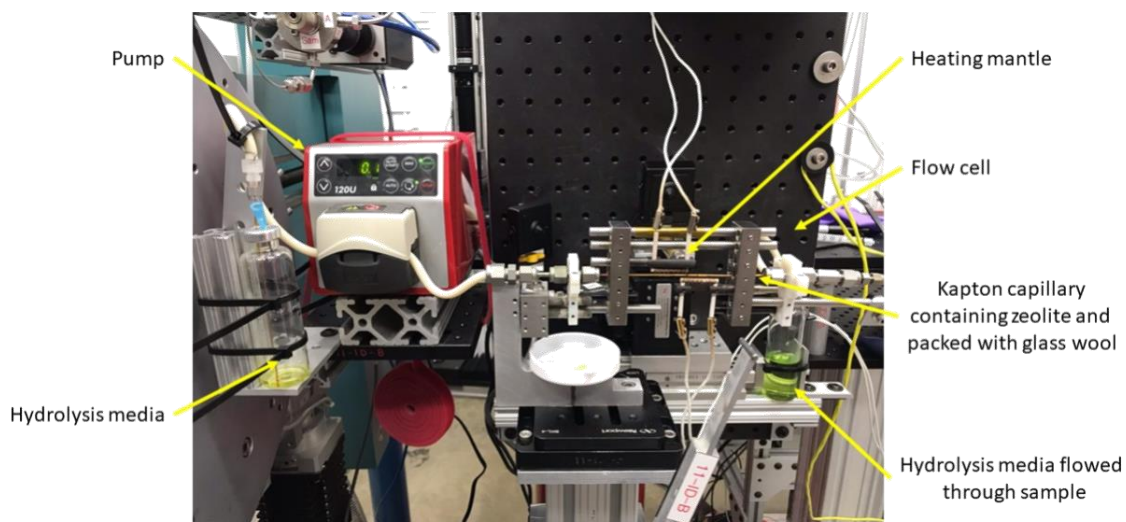
Figure 3.15. A schematic of the custom-made flow cell with pump attached.
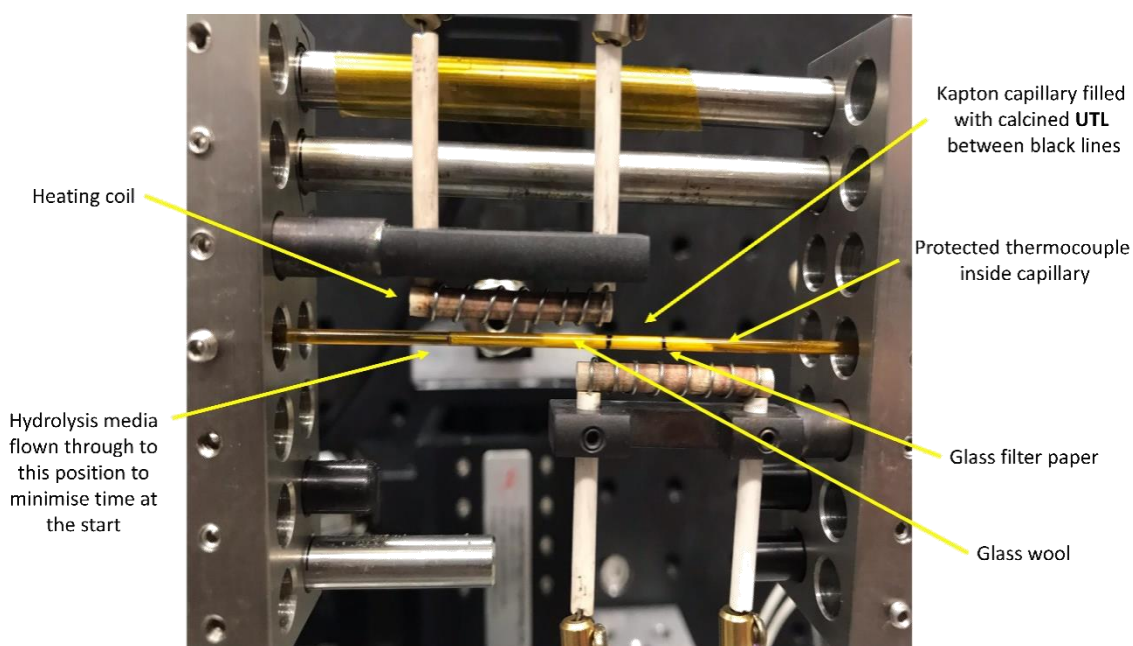
Figure 3.16. Close-up of the heating coils, and capillary within the flow cell.

To prepare the capillary, the Kapton was marked with a black permanent marker to ascertain the required depth of zeolite. One side of the black mark was then plugged with a piece of glass filter paper and glass wool, the ground **UTL** was then packed to the required depth by

vibrating the **UTL** down the capillary using forceps. The other side of the capillary was then plugged in the same manner.

The capillary was threaded through the cell and the protected thermocouple inserted into the open end of the capillary. The thermocouple was protected by a smaller capillary sealed with epoxy resin.

Once set up, the liquid media (water, 6 M hydrochloric acid, 12 M hydrochloric acid) was flown through the pump by a needle inlet for the following times and speeds.

1. Forward flow for 30 sec at 5.0 rpm.
2. Forward flow for 4 min 24 sec at 1.0 rpm whereby the media is now near the sample.
3. Reversed flow for 1 min 30 at 0.2 rpm.
4. The flow is then switched back to forward at a speed of 0.1 rpm.

After step 2 the beam is aligned and the background of acid taken. After step 4 the hutch is searched and the experimented started.

A macro was used to define when the sample was exposed to the X-ray beam. An exposure time of 10 sec (10 sec on 10 sec off) for the first 5 min and 50 sec (50 sec on 10 sec off) for the remaining time was used at a wavelength of 0.2113 °. Every hour a background of acid and darks of both the **UTL** and the background were taken.

The experiment encountered problems when high concentrations of hydrochloric acid was used. As the cell was made out of stainless steel the fittings began to corrode and the reacted hydrolysis media turned a bright green colour due to the nickel composite in the stainless steel. The metal needle inlets also began to corrode so these were switched to polypropylene needles that were glued to Kapton tubing and glued with epoxy resin.

3.3.   Electron Microscopy[26]

3.3.1.   Scanning Electron Microscopy

Electron microscopy uses a high energy electron beam that can probe morphology, surface topography and sample composition of solids. They differ from traditional optical microscopes as they use a beam of electrons to image the sample specimens rather than visible light (Figure 3.17).
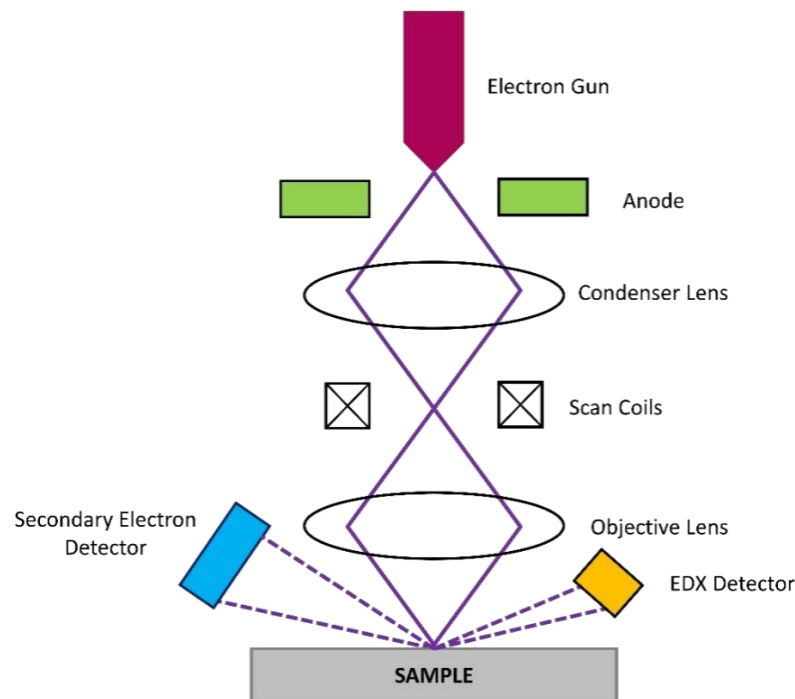
Figure 3.17. Schematic of the set-up of a scanning electron microscope. Electron beam shown in purple.

A general procedure for producing images using an electron microscope can be seen below:

1. An electron gun produces a flow of electrons when under high vacuum.
2. The flow of electrons is accelerated using a positive electric potential.
3. The electrons are focussed using electromagnetic lenses and metal slits to produce a thin, focussed, monochromatic beam.
4. Upon impact of the electron beam with the sample, a range of interactions (secondary scattered electrons, back scattered electrons and characteristic X-rays) occurs which are detected and used to create an image.

SEM images were recorded using a Jeol JSM-5600 scanning electron microscope equipped with a tungsten filament electron gun, operating at a voltage of 5 – 25 kV. Each sample was spin coated in gold, using a Quorom Q150R ES, which reduced the charging effect on the sample.

3.3.2. Energy Dispersive X-ray Analysis

When the primary electron beam collides with the core electrons of an atom in the sample specimen, the core electrons can be ejected. This creates a vacancy in the inner orbital and shifts the atom into an excited state. Similarly, to X-ray diffraction, this causes the relaxation of an electron of higher energy from an outer orbital. The energy difference results in the emission of an X-ray photon with a wavelength related to the energy gap of the orbitals.

This emission differs from atom to atom and therefore allows one to quantify the X-rays produced to a specific element. So, by collecting the X-rays emitted and the relative quantity, it is possible to determine the chemical composition of the sample.

The EDX analysis was recorded on the same SEM instrument at 25 kV, using an Oxford Inca Energy system.

3.3.3. Transmission Electron Microscopy

Transmission electron microscopy (TEM) differs from SEM as SEM creates an image by detecting reflected electrons while TEM uses transmitted electrons (electrons which pass through a sample) to create an image. As a result, TEM offers valuable information on the internal structure of a sample, such as the channel systems and inter-layer spacing in zeolites.

Preparation of the sample for TEM is as follows:

1. The sample is ground in a mortar and pestle.
2. Acetone is added to the ground powder and ground again to create a well dispersed suspension of the sample.
3. A drop of the suspension is dropped on a copper/holey carbon TEM grid.
4. The camera length, sample position and magnification are calibrated using standard gold film methods.

Germanosilicates are extremely sensitive to the electron beam, and therefore care must be taken during the sample preparation and imaging. To avoid sorption of water, samples must be dried in an oven and stored in a vacuum desiccator. The high-resolution transmission electron microscopy (HRTEM) was performed using a Jeol JEM-2011 electron microscope

operating at an accelerating voltage of 200 kV. The HRTEM images were recorded using a 9 Gatan 794 CCD camera.

3.4. Solid-state NMR[27]

Zeolites and other inorganic materials cannot be dissolved in deuterated solvents and therefore cannot be analysed by traditional solution-state NMR. Due to this, solid-state NMR is used, however there are challenges that must be overcome. As zeolites are analysed in the solid-state there is no rapid tumbling of molecules, and as such the broad signal that is normally removed by rapid tumbling in solution, cannot be achieved in the solid-state. To decrease this broad signal that is produced, solid-state NMR uses Magic Angle Spinning (MAS). This is achieved by placing the sample in a ZrO_2 rotor and spinning at an angle of 54.74 ° θ with respect to the direction of the external magnetic field (Figure 3.18).
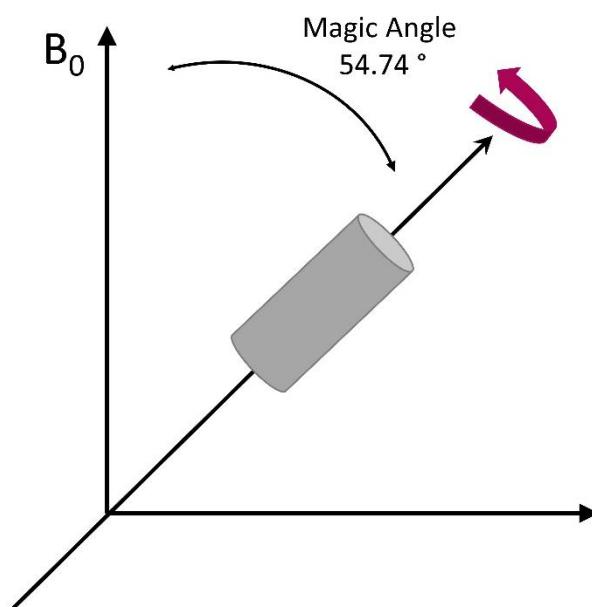
Figure 3.18. A schematic representation of a packed rotor spun at the magic angle - 54.74 °.

Spinning with such precision allows $(3cos^2\theta - 1)$ to become 0, and therefore the anisotropic interaction dependency is removed. Typically for zeolites, the nuclei of interest is ^{29}Si, this has a relatively low abundance of 4%. This means that the acquisition time for collecting solid-state NMR data for zeolites is much longer.

Zeolite samples analysed by solid-state NMR were collected on a Bruker Advance III spectrometer equipped with a 9.4 T wide-bore superconducting magnet, at a Larmor frequency of 79.459 MHz.

3.5.   References

1   G. Demazeau, *J. Mater. Sci.*, 2008, **43**.

2   J. Čejka, *Introduction to zeolite science and practice*, Elsevier, 2007.

3   R. M. Barrer, *J. Am. Chem. Soc.*, 1948, 127–132.

4   R. E. Morris, in *Zeolites and Catalysis*, Wiley-VCH Verlag GmbH & Co. KGaA, Weinheim, Germany, 2010, pp. 87–105.

5   J. P. Glusker and K. N. Trueblood, *Crystal Structure Analysis: A Primer*, Oxford University Press, New York, 2010.

6   W. Clegg, *Crystal structure determination*, Oxford University Press, 1998.

7   A. J. Blake and W. Clegg, *Crystal structure analysis : principles and practice*, Oxford University Press, 2009.

8   E. Prince and T. I. U. of Crystallography, *International tables for crystallography*, Kluwer Academic Publishers, 3rd edn., 2004, vol. C.

9   W. I. F. (William I. F. . David, *Structure determination from powder diffraction data*, Oxford University Press, 2002.

10   V. K. Pecharsky and P. Y. Zavalij, *Fundamentals of powder diffraction and structural characterization of materials*, Springer, 2009.

11   R. E. Dinnebier and S. J. L. Billinge, *Powder diffraction : theory and practice*, Royal Society of Chemistry, 2008.

12   A. Le Bail, *Powder Diffr.*, 2005, **20**, 316–326.

13   R. A. Young, *The Rietveld Method*, Cambridge University Press, 1993.

14   H. M. Rietveld and IUCr, *Acta Crystallogr.*, 1967, **22**, 151–152.

15   S. J. L. Billinge, *Nanostructure studied using the atomic pair distribution function*, 2007, vol. 26.

16   S. J. L. Billinge, *Zeitschrift für Kristallographie - Crystalline Materials*, 2009, *219*, 117-121

17   S. J. L. Billinge and I. Levin, *Science*, 2007, **316**, 561–565..

18   S. J. L. Billinge, in *Local Structure from Diffraction*, Kluwer Academic Publishers, Boston, 2002, pp. 137–156.

19   T. Egami and S. J. L. Billinge, *Underneath The Bragg Peaks: Structural Analysis of Complex Materials - Second Edition.*, 2012, vol. 7.

20   T. R. Welberry and T. Proffen, *J. Appl. Crystallogr.*, 1998, **31**, 309–317.

21   X. Qiu, J. W. Thompson and S. J. L. Billinge, *J. Appl. Crystallogr.*, 2004, **37**, 678.

22   A. P. Hammersley, S. O. Svensson, M. Hanfland, A. N. Fitch and D. Hausermann, *High Press. Res.*, 1996, **14**, 235–248.

23   C. L. Farrow, P. Juhas, J. W. Liu, D. Bryndin, E. S. Božin, J. Bloch, T. Proffen and S. J. L. Billinge, *J. Phys. Condens. Matter*, 2007, **19**, 335219.

24   G. Sankar and W. Bras, *Catal. Today*, 2009, **145**, 195–203.

25   P. J. Chupas, K. W. Chapman, C. Kurtz, J. C. Hanson, P. L. Lee and C. P. Grey, *J. Appl. Crystallogr.*, 2008, **41**, 822–824.

26   J. Goldstein, D. E. Newbury, J. R. Michael, N. W. M. Ritchie, J. H. J. Scott and D. C. Joy,

Scanning electron microscopy and x-ray microanalysis, 2003.

27   J. J. Fitzgerald and S. M. Depaul, *Solid-State NMR Spectroscopy of Inorganic Materials: An Overview*,. American Chemical Society, 1999.

CHAPTER 4:
DEVELOPING A STANDARD
PROTOCOL FOR THE ADOR
PROCESS

4.1.   Aim

The aim of this chapter is to develop a standard protocol, which will allow researchers from other universities and research groups to use the Assembly-Disassembly-Organisation-Reassembly (ADOR) process, and upon following the protocol allow them to identify the different products that are possible from the reaction without recourse to repetitive and time-consuming trial and error. The aim of the protocol is to identify the optimum conditions, such as time of reaction, temperature of the system and pH etc. that one may use to choose a zeolite capable of ADOR and produce new high-silica zeolites, which would be unfeasible through traditional hydrothermal synthesis.

4.2.   Introduction

High-silica zeolites are some of the most important and widely used catalysts in modern industry, and they have potential for application across a wide range of traditional and emerging technologies. The many different structural topologies available to zeolites and zeolitic materials opens up to many different potential uses and so there remains a strong drive to prepare new zeolites.

The ADOR process is a relatively new method of preparing new high-silica zeolites. ADOR differs from traditional zeolite synthetic processes, which generally involves a reversible crystallisation under hydrothermal conditions,[1] in that the final framework-forming step is an irreversible condensation.[2] The consequence of this is that materials produced through ADOR have unexpected energetic properties that would be unlikely to be possible using traditional methods.[3] Due to this, the possibility of preparing materials with different structures than those currently possible increases, and in turn may lead to new and exciting

applications. There are both advantages and limitations to using traditional hydrothermal synthesis and the ADOR process (Table 4.1).

Table 4.1. Differences in preparation of high silica zeolites. Advantages are colour coded blue. Limitations are colour coded red.

Method Factor	Hydrothermal Crystallisation	ADOR
Controllability and predictability of products	Limited control and the product zeolite is not always easy to predict	Use of layers as predefined building unit leads to product being predictable
Diversity of products	Synthesised zeolite may be limited by the reversible nature of crystallisation step	No inherent limitation on the types of products possible
Chemical composition	Zeolites can be prepared using a wide variety composition of reaction mixture	So far limited to germanosilicates as parent materials
Price	Often (but not always) needs expensive organic structure directing agents	Use of expensive germanium in parent materials

The ADOR process is extremely flexible and starting from only one parent zeolite with the **UTL** framework topology a family of six new zeolites, named IPC-2 (**OKO**), IPC-4 (**PCR**), IPC-6 (***PCS**), IPC-7, IPC-9 and IPC-10, can be prepared. The procedure that has been developed in this chapter concentrates on identifying the intermediates that result from the Disassembly/hydrolysis (D) and Organisation/rearrangement (O) stages in the ADOR process, as it is these stages that control the nature of the final product.

There are three main variables that must be controlled: time, temperature and the acidity of the disassembly medium. To ensure that all possible outcomes from the ADOR process are

to be recognised it is incredibly important that sufficient parameter space is sampled. However, the protocol must also be time-efficient so that researchers wanting to use ADOR to synthesise new zeolites are not discouraged from using the method. To achieve this balance, a standard protocol was devised.

4.3. Experimental Procedure

All reagents were obtained from commercial sources and were used without further purification.

4.3.1. Synthesis of SDA - (6*R*,10*S*)-6,10-dimethyl-5-azoniaspiro[4,5]decane hydroxide

1,4-dibromobutane (126 g, 0.5 mol) was added dropwise over 30 minutes to a solution of potassium carbonate (82.9 g, 0.6 mol), 2,6-dimethylpiperidine (56.6 g, 0.5 mol) and acetonitrile (500 mL) at room temperature. The solution was heated to 95 °C and stirred vigorously for 20 hr. After cooling to slightly above room temperature, the reaction was filtered to remove any solids. The solution was then condensed to remove excess acetonitrile and yield the white bromide salt. The solid product was filtered from the acetonitrile solution and washed with diethyl ether (5 x 100 mL). The bromide salt was collected and left to dry in air before ion exchange to form the hydroxide (6*R*, 10*S*)-6,10-dimethyl-5-azoniaspiro[4.5.]decane hydroxide.

4.3.2. Ge-UTL

Germanium dioxide (1.08 g) was dissolved in a solution of (6*R*,10*S*)-6,10-dimethyl-5-azoniaspiro[4,5]decane hydroxide (15 mL, 0.625 M). Fumed silicon dioxide (1.25 g) was added portion-wise to the mixture over 30 min until a homogenous solution was formed. The gel was transferred to a Teflon-lined steel autoclave and heated at 175 °C for 7 days. The zeolite product was collected by filtration, washed with water (200 mL) and dried at 80

°C for 12 hr. To remove the SDA, the as-synthesised zeolite was calcined in a stream of air at 575 °C for 7 hr with a temperature ramp of 1 °C min^{-1}.

4.4. Protocol

The following protocol describes step-wise the procedure to monitoring the Disassembly and Organisation stages. Notes, Cautions, Criticals, Timings and Pause-points are included to aid the reader. Troubleshooting has been attributed to select steps and a Troubleshooting table (Table 4.2) can be found at the end of the protocol. Such Troubleshooting points describe areas where the procedure could go wrong, and what can be done to overcome each problem. The following protocol uses Ge-**UTL** as an archetypal parent zeolite, but this can be exchanged for any known germanosilicate.[4]

The following procedure is presented in an unconventional manner. However, the aim is to breakdown each step so that anyone, no matter the ability or background, can follow the synthesis whilst paying specific attention to areas that are labelled with Troubleshooting or Caution. As such, allow one to use the protocol procedure to take any parent zeolite and see if it is suitable to be used in ADOR.

4.4.1. Protocol Procedure[4]

Preparation of parent zeolite

TIMING 12 days

NOTE Any suitable parent zeolite can be substituted for Ge-**UTL**. Synthetic procedures from previous literature can be used for known zeolites.

1. Prepare parent Ge-**UTL** with molar composition 0.8 SiO$_2$: 0.4 GeO$_2$: 0.4 ROH: 30 H$_2$O according to well-known literature procedure.

TROUBLESHOOTING – Pt 1 (see Table 4.2)

2. Remove the SDA from Ge-**UTL** by calcination of the as-synthesised zeolite in a stream of air at 575 °C for 7 hr with a temperature ramp (uphill) of 1 °C min^{-1},

plateau for 6 hr, and then a temperature ramp (downhill) of 2 °C min^{-1} until room temperature is reached. To prevent accidental disassembly by moisture in the air the sample can be stored in a desiccator to keep it dry.

TROUBLESHOOTING – Pt 2 (see Table 4.2)

Set-up of hydrolysis apparatus

TIMING 1 hr

3. Equip the three-necked round-bottom flask with the condenser and attach to the water.

4. Place the three-necked round-bottom flask in heating mantle with stirrer bar.

5. Add 120 mL water into the three-necked flask. Heat the water to 100 °C and stir at a speed of 600 rpm.

CRITICAL to ensure that the liquid in the experiment remains at the required temperature the heating mantle may need to be set at a higher temperature. Check that the temperature of the liquid is at 100 °C throughout the experiment.

6. Set up the filtration apparatus by way of Buchner flask, funnel and ring. Attach the flask to the water vacuum pump.

7. Prepare pipettes, pipette teats, glass vials, and capillaries for each aliquot taken (ca. 30). Name each vial by the time the sample is taken (Figure 4.1).

CRITICAL Prepare all before moving on to step 8.

Figure 4.1. LEFT – experimental set-up of the reaction flask and filtration apparatus including Buchner flask, funnel and ring; RIGHT – Prepared labelled glass vials and pestle and mortar.

8. Weigh out 600 mg of Ge-**UTL** and grind to a fine powder in the pestle and mortar. The crystallite size at the end of this process is, on average, about 10 μm × 10 μm × 3 μm as measured by scanning electron microscopy.

Hydrolysis procedure

TIMING 8 hr

9. Add the ground Ge-**UTL** to the three-necked round-bottom flask with stirring and start the timer.

10. After 1 min take the first sample (ca. 4 pipettes full, ensuring that solid is present in the sample; c.a. 2.5 to 3 mL of suspension), filter for 50 sec and transfer to a labelled watch glass and place in a drying oven for 5 min at 80 °C.

11. Repeat step 10 every 1 min up to the 5 min mark.

12. After the 5 min mark continue to take samples every 5 min up to 1 hr. Filter each sample taken for 4 min and dry at 80 °C for 5 min.

TROUBLESHOOTING – Pt 12 (see Table 4.2)

13. After 1 hr, continue to take samples every 30 min up to 8 hr (or when the reaction has come to completion). Filter each sample for 5 min and dry in the drying oven at 80 °C for 5 min.

14. Follow steps 10 − 13. After each subsequent drying of a sample, remove from the oven and grind in mortar and pestle until fine.

15. Pack the hydrolysed material in 0.5 mm borosilicate capillaries until half full.

PAUSE POINT Vials containing the capillaries can be sealed with a screw cap and placed in a vacuum desiccator for up to 2 weeks.

TROUBLESHOOTING – Pt 15 (see Table 4.2)

General procedure for zeolite characterisation

Standard procedures for collecting PXRD (option A), solid-state NMR spectroscopy (option B) and TEM (option C). Procedures include the characterisation of PXRD (option D).

(A) Procedure for collecting PXRD data

TIMING 1 hr per sample

(i)   Pack the hydrolysed material in a 0.5 mm capillary. Using forceps to vibrate the material down the capillary.

(ii)   Collect PXRD data using a STOE STADIP powder X-ray diffractometer operated in Debye-Scherrer mode, using a scintillation position-sensitive linear detector, operating CuK α_1 radiation, place the capillary in the holder and centre into the middle of the beam using a microscope. Scan the diffraction pattern for 55 min between 3° and 40° 2θ with a step size of 0.2°.

(B) **Procedure for preparing and collecting samples for solid-state NMR spectroscopy**

TIMING 24 hr per sample

(i) Using a Bruker Advance III spectrometer equipped with a 9.4 T wide-bore superconducting magnet, at a Larmor frequency of 79.459 MHz, collect ^{29}Si solid-state NMR spectra.

(ii) Pack samples into 4 mm ZrO_2 rotors and rotate at a MAS rate of 10 kHz. Weigh rotors before and after packing to determine the mass of zeolite used in the acquisition.

(iii) Using a radiofrequency (rf) field strength of $\sim$83 kHz, with a recycle interval of 120 s, collect magic angle spinning (MAS) spectra. The Q^3:Q^4 ratio can be determined using DMFit (or other suitable program), with errors estimated from multiple fits.

(iv) The commercial probe used does not display a ^{29}Si background signal hence no correction has to be made to the absolute Q^3:Q^4 ratios plotted to reflect this.

(v) Show the chemical shifts relative to TMS (using secondary references of Q^8M^8 (δ(OSi(OMe)$_3$) = 11.5 ppm) for ^{29}Si and l-alanine ($C_3H_7NO_2$ (δ (NH$_2$) = 8.5 ppm) for ^{1}H).

(C) **Procedure for preparing and collecting samples for TEM**

TIMING 1 hr per sample

(i) The high-resolution transmission electron microscopy (HRTEM) was performed using a Jeol JEM-2011 electron microscope operating at an accelerating voltage of 200 kV. The HRTEM images were recorded using a Gatan 794 CCD camera. The camera length, sample position and magnification were calibrated using standard gold film methods.

(ii) Grind the powder sample in mortar with pestle.

CAUTION Germanosilicates are extremely sensitive to the electron beam, care must be taken during the sample preparation and imaging. To avoid sorption of water, samples must be dried in an oven and stored in a vacuum desiccator.

(iii) Add acetone to ground powder, grind again to obtain a well dispersed suspension of zeolite crystals in acetone.

(iv) Using a pipette, place one drop of suspension on the copper/holey carbon TEM grid.

(v) Calibrate the microscope using standard gold film method.

(vi) Image the samples of silicates using HRTEM method. Use minimum electron beam intensity due to instability of samples. Use spot size 3 and gun lens 3.

CAUTION Make sure to spread the beam to reduce the intensity, keeping the beam intensity below 2 pA cm^{-2}.

(vii) Analyse recorded samples by ImageJ program generating the FFT patterns and calculating the *d* spacing's from generated diffraction patterns.

(D) Procedure for analysing PXRD data

(i) Locate the *200* reflection in the PXRD pattern and measure its position as accurately as possible (this is usually best achieved using the fitting program that comes as part of the standard diffractometer software, but could be performed using other software packages equally successfully). The *200* reflection is normally the most intense peak in the pattern, but this can be confirmed by calculating the positions of the reflections using the expected unit cells.

CRITICAL The *200* peak chosen here defines the inter-layer spacing for **UTL**. For other parent zeolites, the orientation of the reported unit cell may mean that the inter-layer distance is defined using a different reflection. The appropriate reflection must be chosen in this stage otherwise results may be incorrect.

CAUTION The *200* peak may be relatively wide during the hydrolysis step due to a mixture of inter-layer connectivity in the material, which means the measurement may be difficult and the error associated with measuring the position of such peaks should be taken into account.

(ii)   Calculate *d* spacing of the *200* peak using the Bragg equation (if your fitting software does not do this automatically for you). This gives the d_{200} peak in Å, and is a direct probe of the layer spacing in the material.

(iii)   Plot d_{200} against time for all data sets. If the *200* reflection moves significantly during the process then this is an important indicator of whether the parent material is susceptible to the ADOR process. The movement of the peak gives an indication of the types of intermediate that are accessible under the conditions of study and to monitor (a) the effect of temperature and (b) the effect of pH.

Table 4.2. Troubleshooting

Step	Problem	Possible Reason	Solution
1	Parent zeolite not crystalline or not of the correct structure	Parent material did not form correctly in the Assembly step	Check the PXRD to make sure the pattern is correct. If the pattern does not match that for the expected parent zeolite then repeat the synthesis of the parent material
2	The parent is amorphous after calcination (by PXRD)	The parent has degraded in the calcination process	Analyse the calcined material PXRD and check material by ^{13}C NMR to detect SDA presence. Repeat calcination with fresh parent zeolite following calcination steps at the correct temperature. This step can vary with different equipment so several attempts may be required
12	Hydrolysis (Disassembly) did not occur	Ge is not regioselectively incorporated; Low amount of Ge in sample – not enough to remove d4r; Too much Ge – XRD shows no peaks suggesting a collapse of the layers	Perform ICP or other elemental analysis to ascertain Si:Ge ratio in material; re-synthesise parent zeolite with better control of Si:Ge ratio
12	Hydrolysis not efficient over a sensible time scale	Disassembly of the inter-layer linkages did not occur, perhaps due to large numbers of stacking faults in the material	Analyse by scanning electron microscopy to look at morphology and HRTEM to detect faulting; Preparation of parent zeolite without intergrowths
15	No evidence of separate rearrangement steps in the reaction profile	The D and O steps may be overlapping dependent on the hydrolysis media used; The induction step has not occurred as the material has not fully hydrolysed before starting to rearrange, this could be a real effect dependent on the parent zeolite used	Take samples over a longer timeframe to determine whether rearrangement will occur or whether the layered material is the only daughter zeolite formed

4.5. Results and Discussion

At the start of this research the ADOR process could be defined as seen in Figure 4.2 below. After assembly of the parent zeolite, Ge-**UTL,** the d4r are hydrolytically removed to form a layered species IPC-1P. These layers are then self-organised into IPC-2P before calcination to form IPC-2.
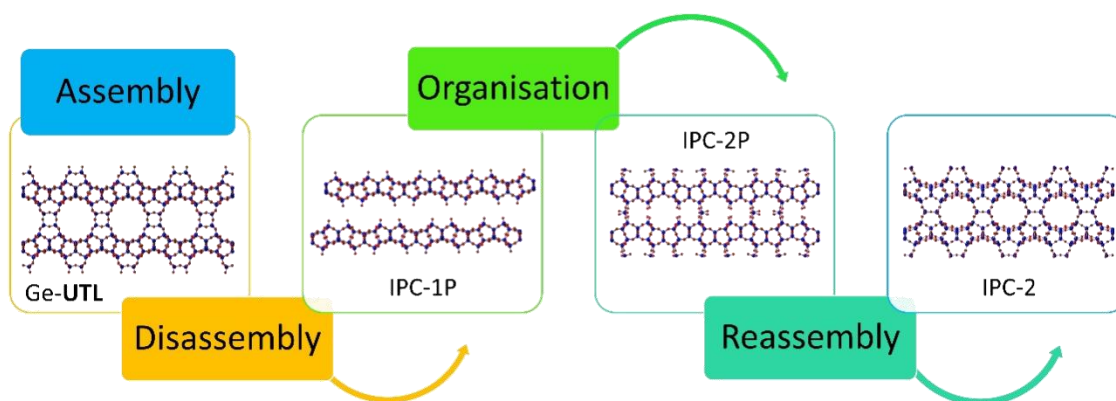

Figure 4.2. A schematic to show the 4 steps in the ADOR process as it stood at the beginning of this research. Initial d4r-containing parent zeolite **UTL** is broken down through hydrolysis, to make the layered intermediate IPC-1P. These layers are organised to IPC-2P through an IPC-6P intermediate before the Si-O-Si bonds are reformed through calcination to form a reassembled material with a different structure from the original assembled parent.

To further the understanding of the ADOR process, a range of experiments were devised and analytical techniques used. These include kinetic analysis of the hydrolysis (D) and rearrangement (O) steps (Chapter 5) and the use of *in situ* Pair Distribution Function (PDF) analysis to monitor the whole process in low volume (Chapter 6). In this chapter, the development of a standard ADOR protocol will be discussed and how this applies to the preparation of new high-silica zeolites.

Germanium-containing **UTL** zeolites were subjected to hydrolysis conditions using five different disassembly media (water, 0.1 M hydrochloric acid (HCl), 1.5 M HCl, 6 M HCl and 12 M HCl) with temperatures ranging from 20 to 100 °C. These conditions provide an understanding of the effects of temperature and pH on the Disassembly and Organisation steps of the process that define the potential products. Samples were taken from the ongoing reaction periodically over a minimum time of 8 hr and each sample was analysed primarily

through powder X-ray diffraction in capillary mode to yield a time course for the reaction at each set of conditions. The 100 °C reaction data set was further analysed by transmission electron microscopy (TEM) and solid-state ^{29}Si NMR spectroscopy and will be discussed in detail below.

4.5.1. The Effect of Temperature

The first reaction set investigated focused on the effect of temperature and as such the acidity was kept constant at pH 7. The hydrolysis (D) and rearrangement (O) mechanisms of Ge-**UTL** through the ADOR process were investigated over a period of 8 – 37 hr using water as the hydrolysis medium at seven different temperatures (100, 92, 85, 81, 77, 70 and 20 °C). Aliquots of sample were taken at specified time intervals and analysed through PXRD. From this PXRD, the d_{200} inter-layer spacing peak was found and the full-width-half-max (FWHM) of this peak measured. The PXRD patterns show the changing crystallinity with change in reaction time.

4.5.1.1. Investigating the 100 °C Reaction

The 100 °C reaction will be discussed first to show specific features in the XRD that will aid the reader in Section 4.5.1.2. The 100 °C reaction was analysed further than all temperatures due to its fast reactivity and clear cut intermediate products at regular time intervals with no overlap. As described previously, samples of the solid suspension were taken at regular intervals from the reaction mixture and PXRD patterns measured for each sample. Figure 4.3 shows selected PXRD patterns for the 100 °C data set, and the inset shows how the position of the *200* reflection varies with time during the reaction. The patterns chosen correspond to the three main intermediates in the ADOR process for Ge-**UTL**: IPC-1P (1hr; 8.5° 2θ, 10.54 Å), IPC-6P (2 hr 30; 7.9° 2θ, 11.1 Å) and IPC-2P (4 hr; 7.5° 2θ, 11.75 Å).
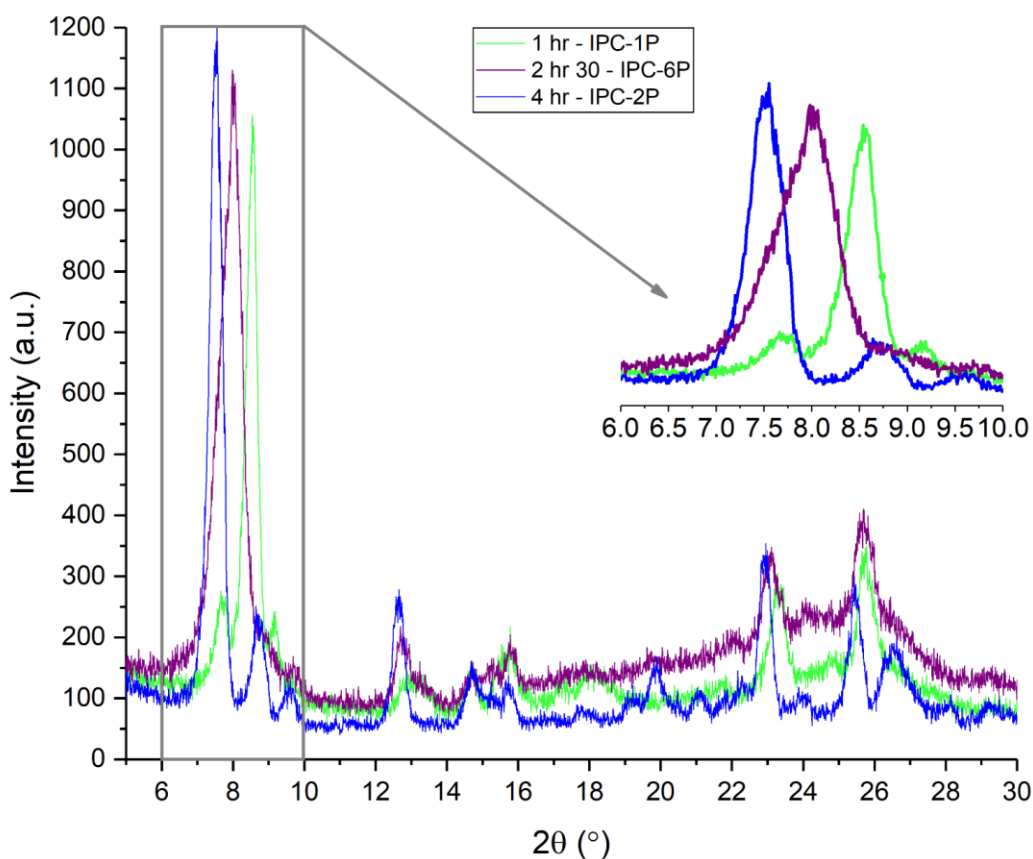
Figure 4.3. Selected PXRD patterns collected at 1 hour, 2 hrs 30 min and 8 hours after the ADOR reaction has started (water as the hydrolysis medium, 100 °C). The inset shows how the position of the *200* reflection shifts with time. The colour coding is the same as that used in Figure 4.15.

Figure 4.4 shows a plot of the time dependency of the *d* spacing of the *200* reflection for all the samples from the 100 °C data set. The plot shows that the parent Ge-**UTL** zeolite (d_{200} = 14.48 Å) is quickly disassembled (hydrolysis and removal of the Ge-rich d4r units) leading to a contraction of the inter-layer distance. After approximately 30 - 60 minutes the value of d_{200} levels off at ~10.5 Å, which corresponds to the IPC-1P intermediate (Figure 4.2) where all the d4r units have been removed from between the layers. At first sight one might imagine that the reaction might have concluded at this time. However, the importance of following the procedure developed for a significant time is obvious, as at longer times further changes occur. There is an induction period, during which IPC-1P is the only product identified in the reaction. After 120 minutes (under these conditions) the d_{200} value increases once again until it plateaus at a value of ~11.75 Å, corresponding to daughter zeolite precursor, IPC-2P (Figure 4.2), where some extra silicon has been incorporated back into the inter-layer space

through a reintercalation/reorganisation reaction. The benefit of following the protocol produced through work in this chapter, is that it allows one to identify the time at the mid-point in the reintercalation process. In this case, this is the intermediate IPC-6P, which is the material where half of the layers have undergone the intercalation and half have not. Once IPC-6P has been calcined, it forms IPC-6 (***PCS**), an alternating (approx.) s4r and direct oxygen linkage containing zeolite (see Chapter 1, Figure 1.17).
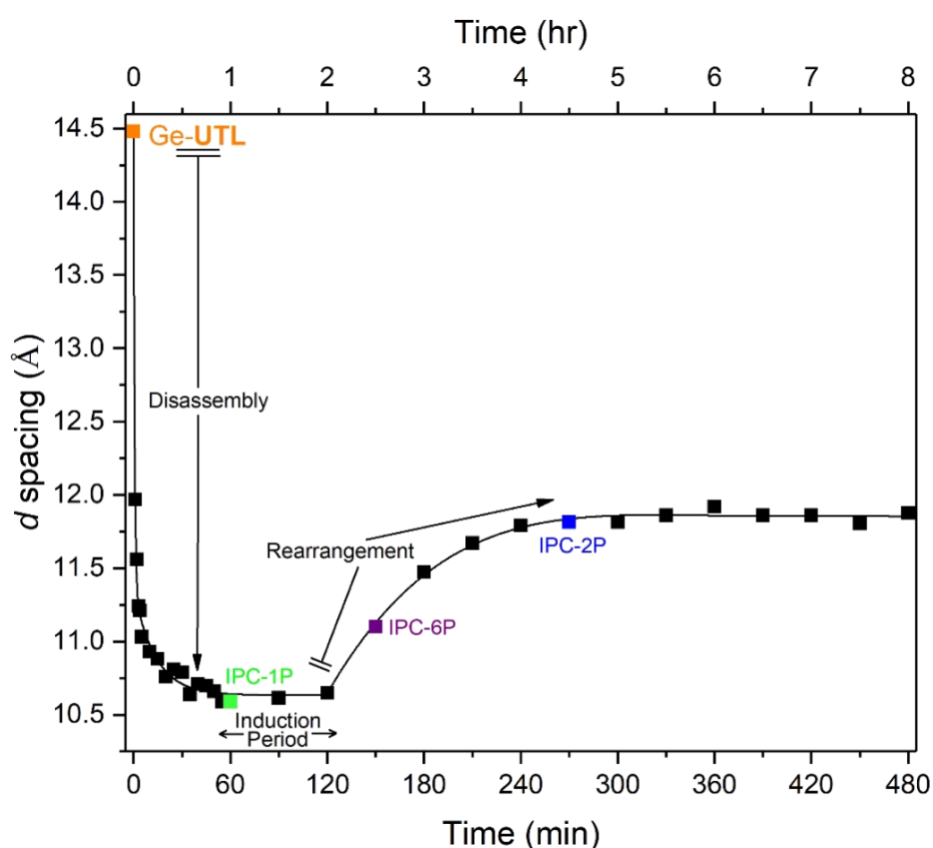

Figure 4.4. A plot of the variation of *d* spacing of the *200* PXRD reflection versus time for the ADOR reaction carried out in water at 100 °C. The plot shows clearly the different regimes of the process. The disassembly of the parent Ge-**UTL** zeolite (orange) happens rapidly and is complete inside 1 hour. There follows an induction period where IPC-1P (green) is the only identifiable product. Following this a new process occurs where the *d* spacing increases, finally forming a different product, IPC-2P (blue) *via* an IPC-6P intermediate (purple). The coloured symbols show the samples whose full PXRD patterns are shown in Figure 4.3. The precision in the measurement of the PXRD *d* spacing is within the symbols on the diagram.

The products of the hydrolysis and rearrangement steps for Ge-**UTL** at 100 °C were further analysed by solid-state ^{29}Si NMR spectroscopy and transmission electron microscopy (TEM). Samples were taken when major structural changes had taken place: 1 min (Ge-IPC-2P*), 1 hr (IPC-1P), 4 & 8 hr (both IPC-2P). The structure and characteristics of the new species Ge-IPC-2P* will be discussed in Chapter 5. A sample was taken and analysed after 8 hr to ensure no further local changes were occurring after forming IPC-2P. Using ^{29}Si MAS NMR spectroscopy, the change in both Q^4 (Si(OSi)$_4$) and Q^3 (Si(OSi)$_3$(OH)) species can be monitored over time (Figure 4.5). The growth of the Q^3 peak after 1 hr, suggests the formation of silanol (Si-OH) groups on the surface of the layers in IPC-1P. After 1 hr the Q^3 peak reduces in intensity as the silanol groups rearrange to Q^4 sites in accordance with Figure 4.2.
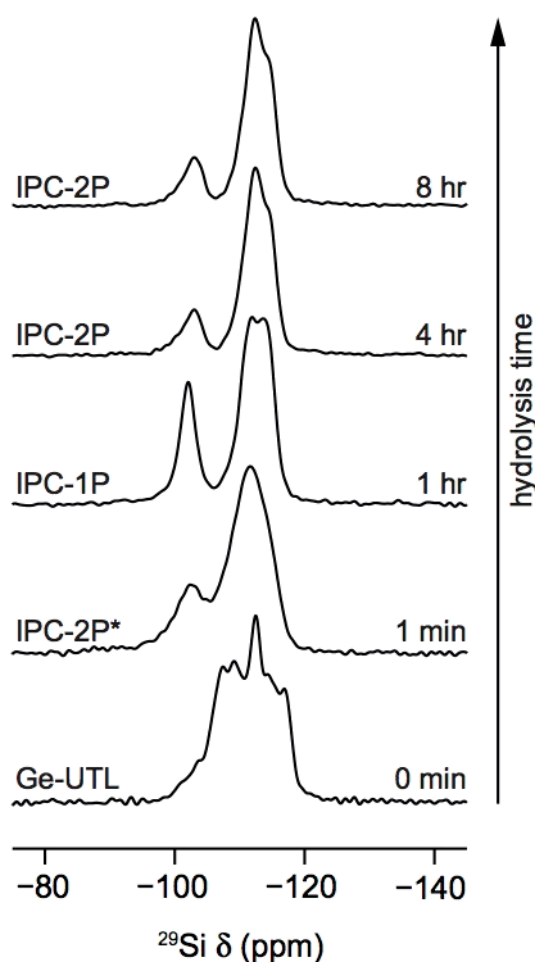

Figure 4.5. ^{29}Si (9.4 T, 10 kHz MAS) NMR spectra of calcined Ge-**UTL** parent zeolite, and subsequent hydrolysis after 1 min, 1 hr, 4 hr and 8 hr. The change in intensity of Q^4 (Si(OSi)$_4$) and Q^3 (Si(OSi)$_3$(OH)) species is monitored over this time period.

After an initial hydrolysis at 1 hr, the ratio of Q^3:Q^4 sites is 1:2.3, thus close to the ideal ratio of 1:2.5 for IPC-1P (Table 4.3). The Q^3:Q^4 ratio continues to decrease as the rearrangement process occurs, leading to a ratio of 1:4.8 upon formation of IPC-2P at 4 hr (ideal IPC-2P Q^3:Q^4 = 1:7). Due to the relative difference between actual and ideal ratios, we can conclude that some silanol groups remain as defects throughout the IPC-2P material.

Table 4.3. Calculated (using DMFit) Q3 : Q4 ratios for the [29]Si environments obtained when Ge-**UTL** is hydrolysed in water at 100 °C.

Time	Q3 %	Q4 %	Q3 : Q4	PXRD structure
Calcined	0	100	∞	Ge-**UTL**
1 hr	30.0	70.0	1 : 2.3	IPC-1P
4 hr	17.4	82.6	1 : 4.8	IPC-2P
8 hr	17.6	82.4	1 : 4.7	IPC-2P

TEM images for three of the most important samples (1 min, 1 hr, and 4 hr) highlighted by XRD were recorded. These materials are highly unstable during radiation. However, the TEM images highlight some loss of crystallinity from parent Ge-**UTL** over the course of 1 min (Figure 4.6) and a clear drop in *d* spacing can be seen over the first hr (IPC-1P), before this increases again to form IPC-2P. The results corroborate those from the XRD data.
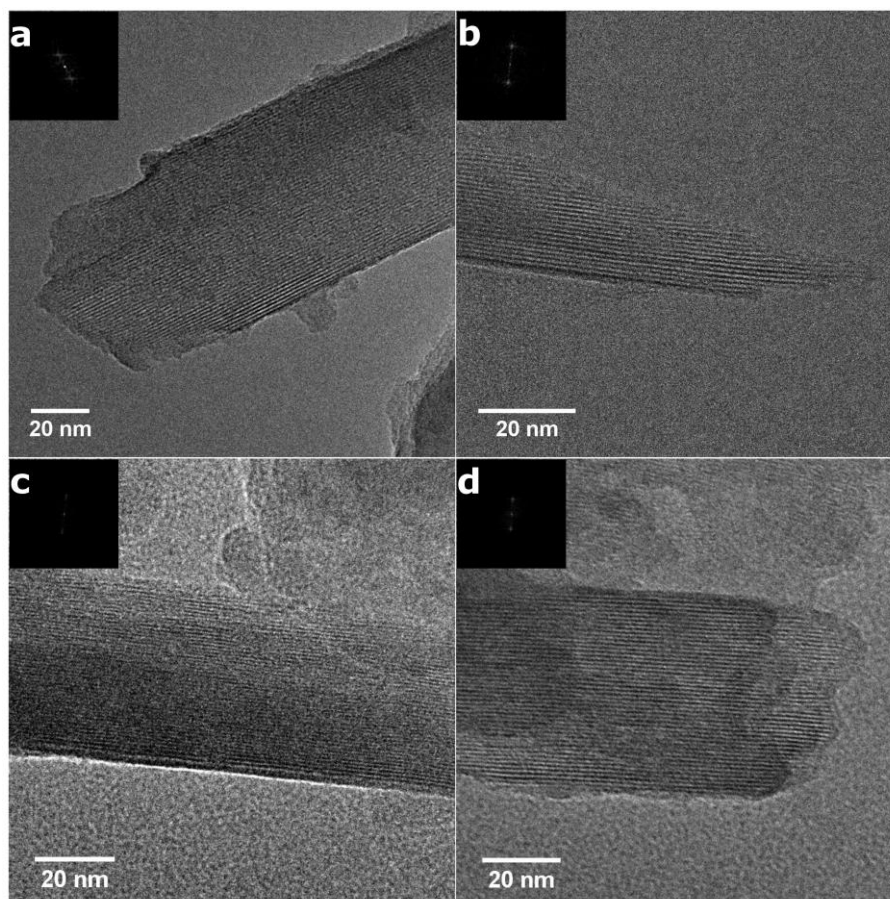
Figure 4.6. TEM images of the samples of Ge-**UTL** hydrolysed in water at 100 ºC. a = parent Ge-**UTL**; b = after 1 min; c = after 1 hr; d = after 4 hr.

4.5.1.2. All Temperatures

The hydrolysis (D) and rearrangement (O) mechanisms of Ge-**UTL** through the ADOR process were investigated over a period of 8 – 37 hr using water as the hydrolysis medium at seven different temperatures (100, 92, 85, 81, 77, 70 and 20 ºC). Each data point in all figures shown in sequence below (Figures 4.7 – 4.13) for data sets 100 – 20 °C, represent the d_{200} inter-layer spacing over time.
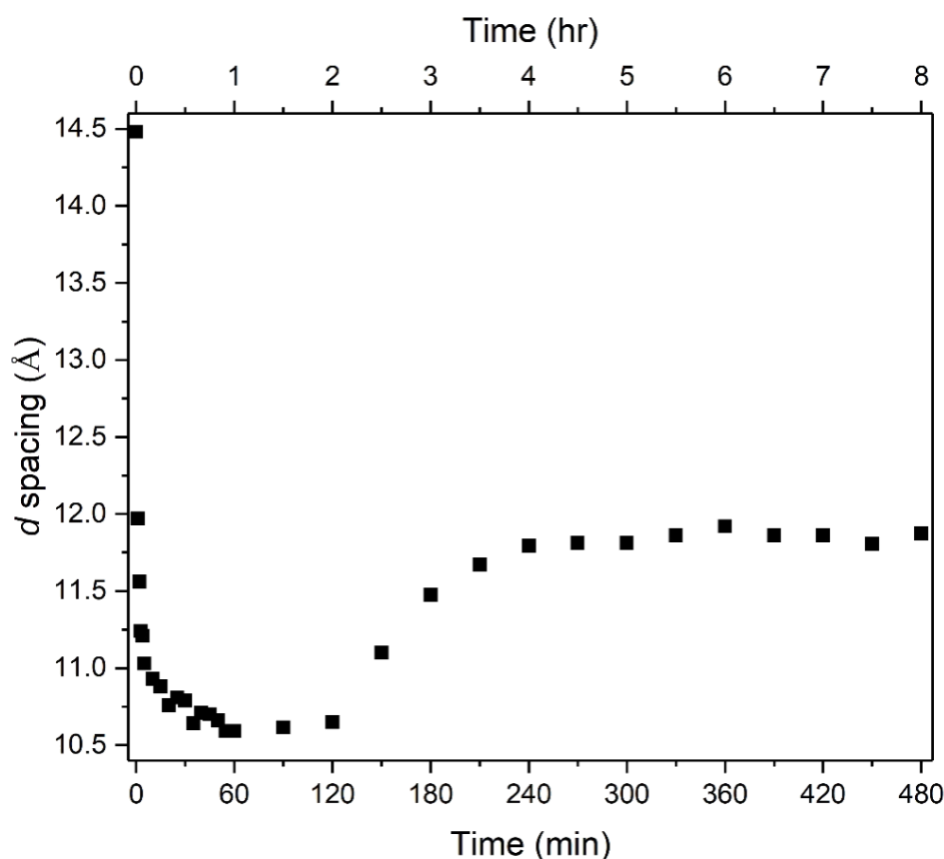
Figure 4.7. A plot of the variation of *d* spacing of the *200* PXRD reflection versus time for the ADOR reaction carried out in water at 100 °C. The disassembly of the parent Ge-**UTL** zeolite (14.48 Å) happens rapidly and is complete inside 1 hr. There follows an induction period for 1 hr where IPC-1P (10.54 Å) is the only identifiable product. Following this a new process (O) occurs where the *d* spacing increases over 2 hr, finally forming a different product, IPC-2P (11.82 Å). The reaction remains stable at IPC-2P from 4 hr. Total reaction time of 4 hr. The precision in the measurement of the PXRD *d* spacing is within the symbols on the diagram.

Decreasing the temperature of the reaction system from 100 °C (Figure 4.7) to 92 °C (Figure 4.8) decreases the rate of rearrangement to IPC-2P (ideal IPC-2P – 11.7 Å) from 2 hr to 4 hr with the induction period also doubled. The rate of hydrolysis is only 30 min for the 92 °C reaction, however as this hydrolysis step is rapid, any small change in timescale of approximately 30 min may be due to human error, such as the time of addition of parent zeolite and size of Ge-**UTL** particles.
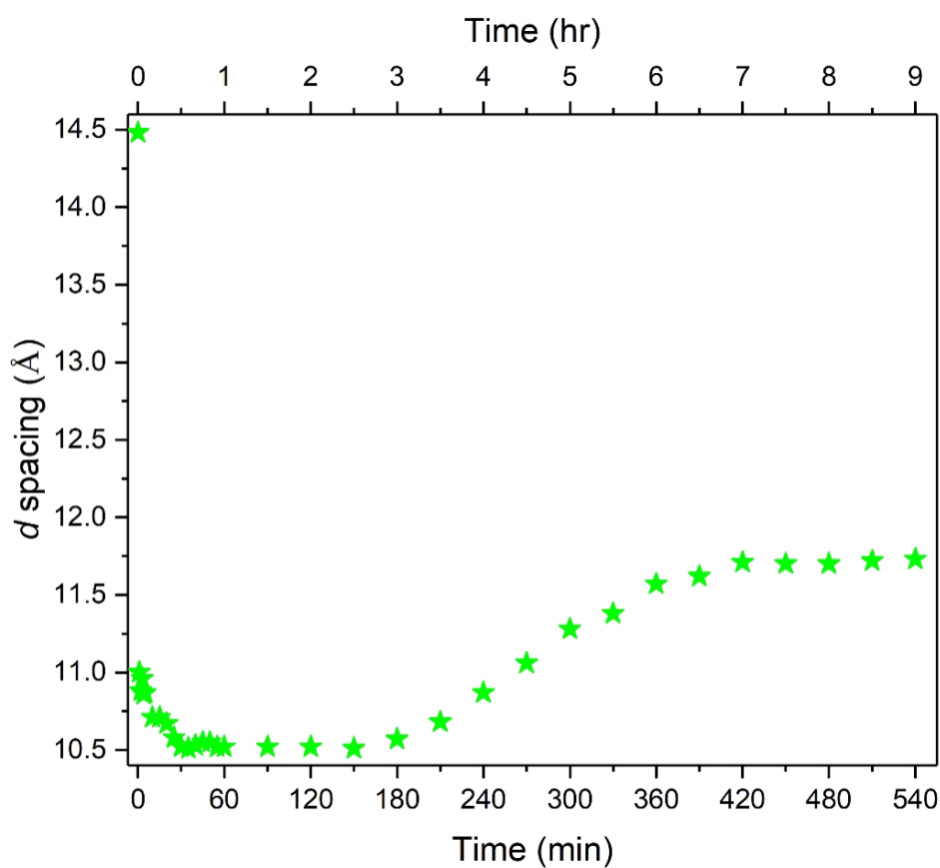
Figure 4.8. A plot of the variation of *d* spacing of the *200* PXRD reflection versus time for the ADOR reaction carried out in water at 92 °C. Hydrolysis (D) of the parent Ge-**UTL** zeolite - 14.48 Å to 10.54 Å; 30 min. Induction period – 2 hr where IPC-1P (10.54 Å) is the only identifiable product. Rearrangement (O) – the *d* spacing increases over 4 hr to form IPC-2P (11.73 Å). The reaction remains stable at IPC-2P from 7 hr. Total reaction time of 7 hr. The precision in the measurement of the PXRD *d* spacing is within the symbols on the diagram.
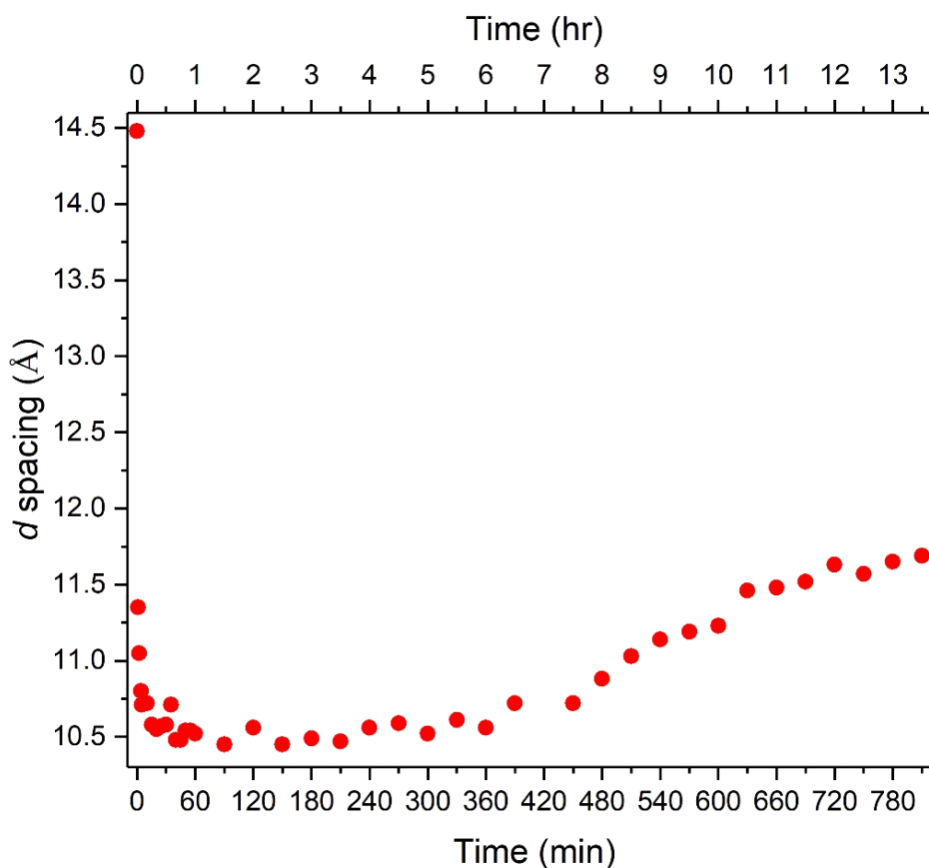
Figure 4.9. A plot of the variation of *d* spacing of the *200* PXRD reflection versus time for the ADOR reaction carried out in water at 85 °C. Hydrolysis (D) of the parent Ge-**UTL** zeolite - 14.48 Å to 10.54 Å; 1 hr. Induction period – 5 hr where IPC-1P (10.54 Å) is the only identifiable product. Rearrangement (O) – the *d* spacing increases over 7 hr 30 to form IPC-2P (11.69 Å). The reaction remains stable at IPC-2P from 14 hr. Total reaction time of 13.5 hr. The precision in the measurement of the PXRD *d* spacing is within the symbols on the diagram.

Once again further reducing the reaction temperature from 92 °C to 85 (Figure 4.9) and 81 °C (Figure 4.10) leads to an increase in reaction time of the rearrangement step from 4 hr to 7 hr 30 and 12 hr for 92, 85 and 81 °C, respectively, with induction times increasing from 2 hr to 5 hr and 7 hr.
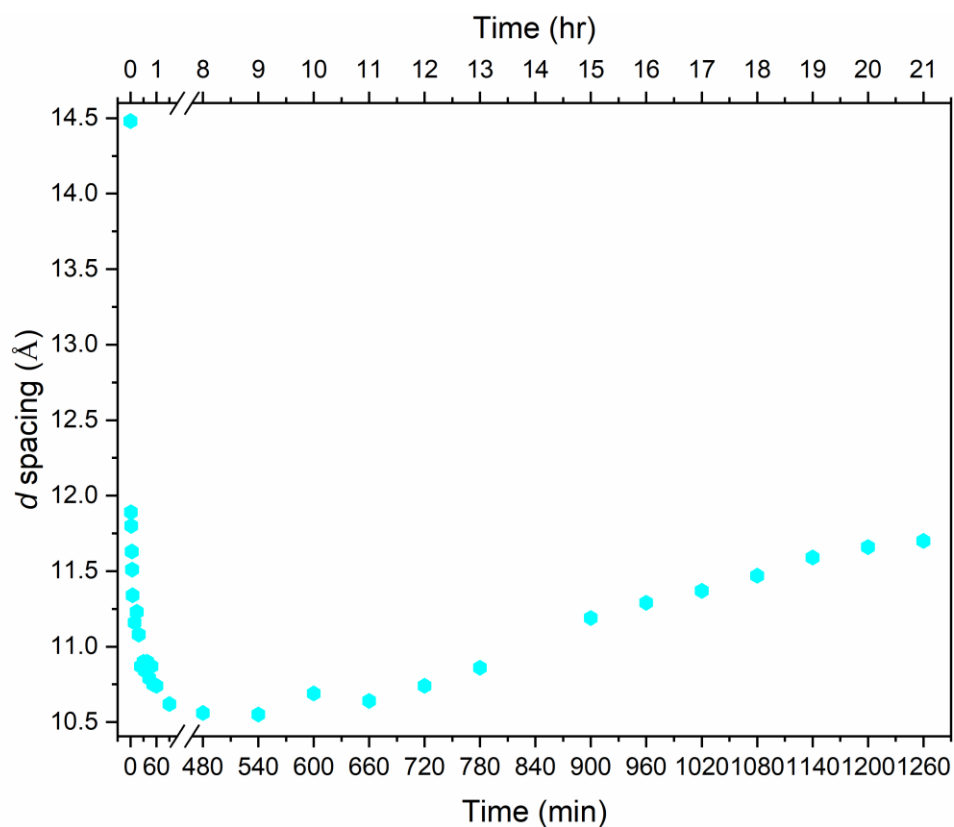
Figure 4.10. A plot of the variation of *d* spacing of the *200* PXRD reflection versus time for the ADOR reaction carried out in water at 81 °C. Hydrolysis (D) of the parent Ge-**UTL** zeolite - 14.48 Å to 10.54 Å; 2 hr. Induction period – 7 hr where IPC-1P (10.54 Å) is the only identifiable product. Rearrangement (O) – the *d* spacing increases over 12 hr to form IPC-2P (11.67 Å). The reaction remains stable at IPC-2P from 21 hr. Total reaction time of 21 hr. The precision in the measurement of the PXRD *d* spacing is within the symbols on the diagram.
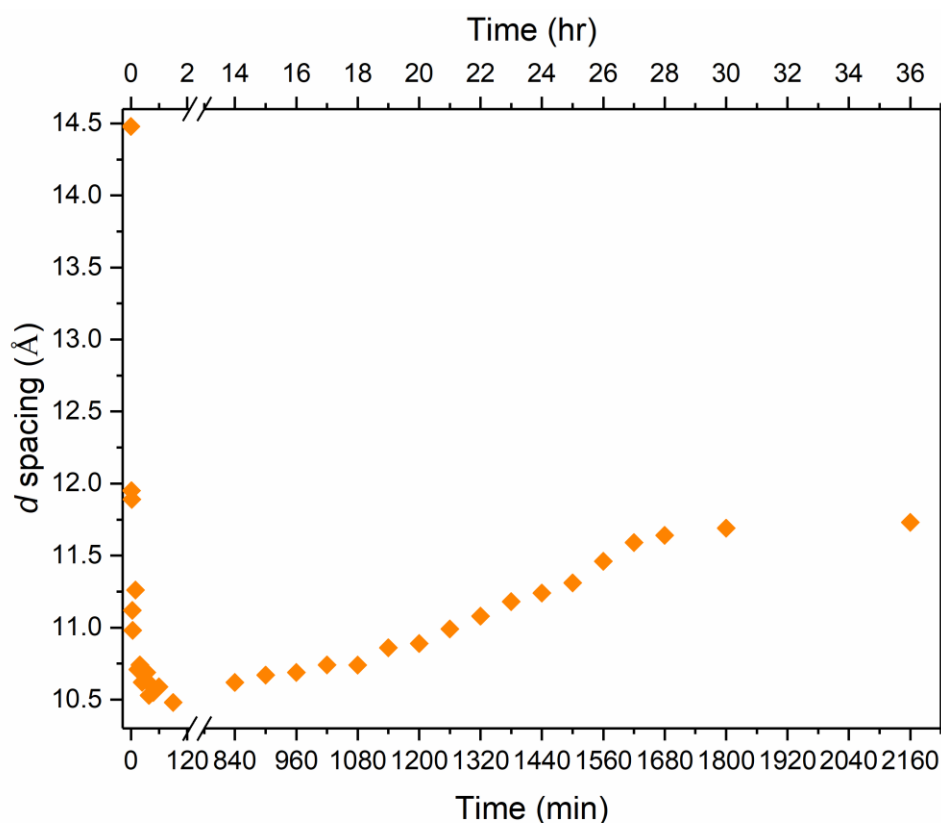
Figure 4.11. A plot of the variation of *d* spacing of the *200* PXRD reflection versus time for the ADOR reaction carried out in water at 77 °C. Hydrolysis (D) of the parent Ge-**UTL** zeolite - 14.48 Å to 10.54 Å; 1 hr. Induction period – 13 hr 30 where IPC-1P (10.54 Å) is the only identifiable product. Rearrangement (O) – the *d* spacing increases over 15 hr to form IPC-2P (11.73 Å). The reaction remains stable at IPC-2P from 31 hr. Total reaction time of 30.5 hr. The precision in the measurement of the PXRD *d* spacing is within the symbols on the diagram.

Comparing the standard reaction at 100 °C to those run at 77 (Figure 4.11) and 70 °C (Figure 4.12), it is clear that there is a strong temperature dependence on the rate of reactivity of the rearrangement (O) step in ADOR, with 77 and 70 °C taking 15 and 16 hr to react, respectively. The induction period is again lengthened considerably from 1 hr (100 °C) to 13 hr 30 (77 °C) and 19 hr (70 °C).
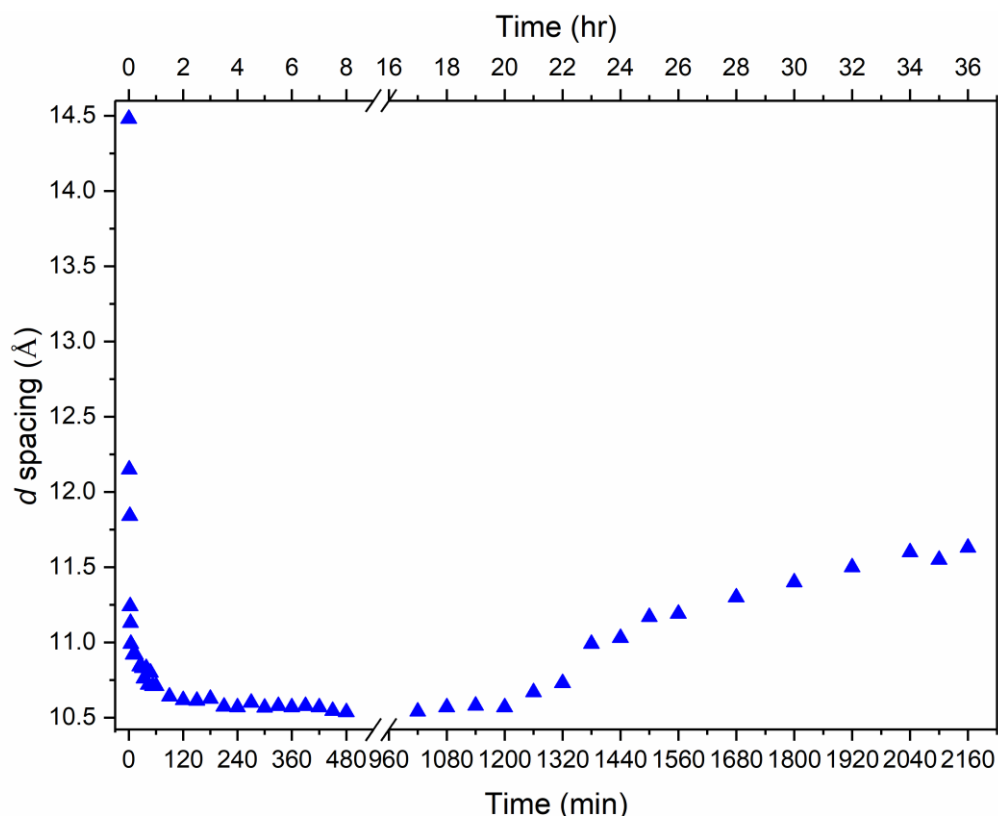
Figure 4.12. A plot of the variation of *d* spacing of the *200* PXRD reflection versus time for the ADOR reaction carried out in water at 70 °C. Hydrolysis (D) of the parent Ge-**UTL** zeolite - 14.48 Å to 10.54 Å; 1 hr. Induction period – 19 hr where IPC-1P (10.54 Å) is the only identifiable product. Rearrangement (O) – the *d* spacing increases over 16 hr to form IPC-2P (11.63 Å). The reaction remains stable at IPC-2P from 36 hr. Total reaction time of 36 hr. The precision in the measurement of the PXRD *d* spacing is within the symbols on the diagram.

Finally, Ge-**UTL** was subjected to conditions of 20 °C in water for a time period of 8 hr (Figure 4.13). Unlike the previous reaction sets with temperatures of 70 °C and above, Ge-**UTL** does not fully hydrolyse to IPC-1P and instead the *d* spacing plateaus at 10.82 Å. It is currently not known why this is the case, as at all other temperatures explored, the temperature of the system seems to have no effect on the rate of hydrolysis (D). Interestingly, with a temperature of only 20 °C this reaction system seems to be acting as if at low volume. Clearly the kinetics of the reaction system need to be increased and as such temperatures above 20 °C are needed to fully hydrolyse the parent Ge-**UTL** and allow for further rearrangement.
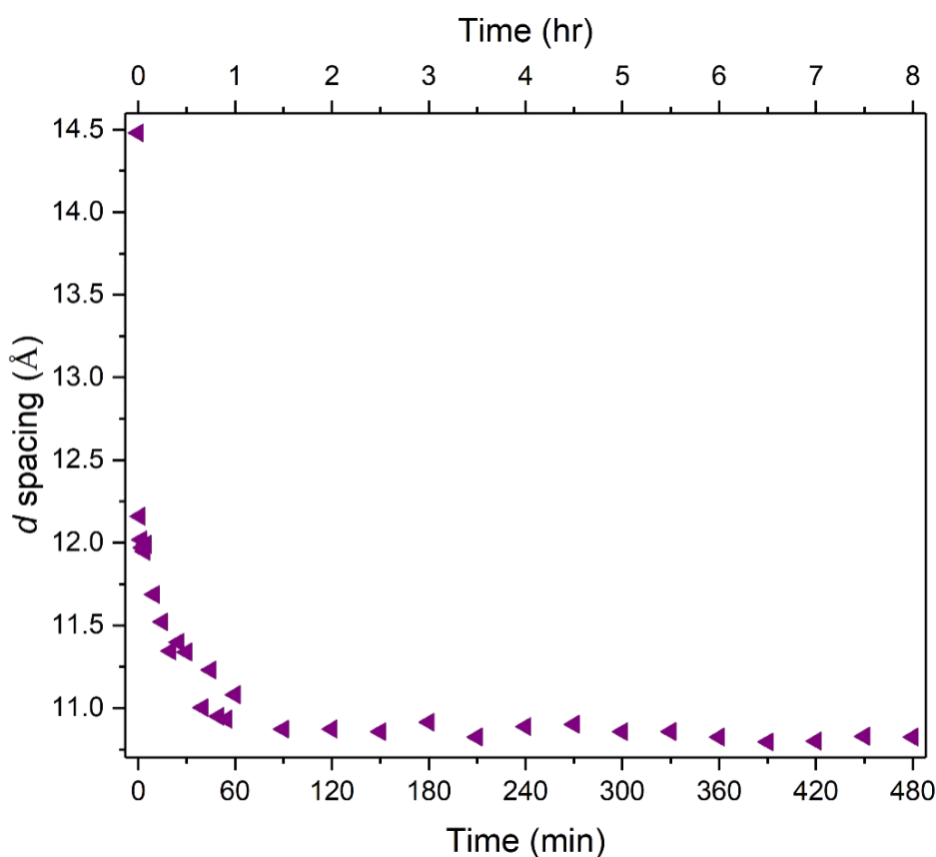
Figure 4.13. A plot of the variation of *d* spacing of the *200* PXRD reflection versus time for the ADOR reaction carried out in water at 20 °C. Hydrolysis (D) of the parent Ge-**UTL** zeolite - 14.48 Å to 10.82 Å; 90 min. After 90 min no further hydrolysis to IPC-1P (10.54 Å) is seen with no rearrangement seen within the timeframe. The precision in the measurement of the PXRD *d* spacing is within the symbols on the diagram.

Due to only a partial collapse of the layers and no rearrangement on a sensible timescale, the reaction run at 20 °C has been removed from further figures and is absent from further data analysis. Figure 4.14 shows the change in *d* spacing with time for all these temperatures. The initial hydrolysis occurs rapidly over the course of 1 hr and several features can immediately be identified. First, it is clear that the initial Disassembly is fast under all conditions. Indeed, it is so fast that the errors associated in accurate measurement of the time are likely to be significant, and limit any quantitative conclusions that can be elucidated from the data for this process, at least under these conditions.

Figure 4.14. Hydrolysis of Ge-**UTL** in water over a time period of 1 hr showing the *d* spacing, d_{200} for 100 °C (black squares), 92 °C (green stars), 85 °C (red circles), 81 °C (cyan hexagons), 77 °C (orange diamonds) and 70 °C (blue triangles). After 1 hour at all temperatures Ge-**UTL** is fully hydrolysed to IPC-1P. The precision in the measurement of the PXRD *d* spacing is within the symbols on the diagram.

Second, the duration of the induction period varies greatly with temperature; as the temperature of the reaction is lowered the induction period increases in length (Figure 4.15).
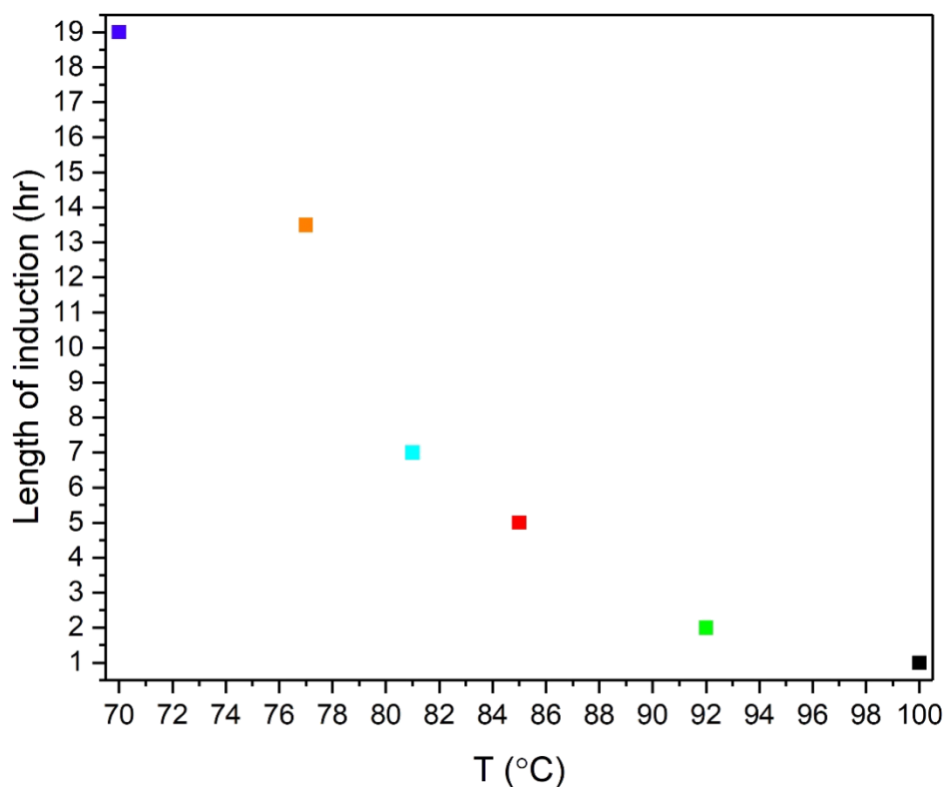
Figure 4.15. Induction length vs. temperature for 100 °C (black), 92 °C (green), 85 °C (red), 81 °C (cyan), 77 °C (orange) and 70 °C (blue).

Third, the rate of the reintercalation/reorganisation step increases with temperature. Clearly, there is the possibility of quantifying reaction rates and apparent activation energies using these data, and this will be discussed in Chapter 5. As it stands, the data yields excellent qualitative information that helps to show which particular set of conditions might be the optimum for the preparation of the desired product, IPC-1P, IPC-6P or IPC-2P. Figure 4.16 below highlights the change in reaction time with decreasing temperature.
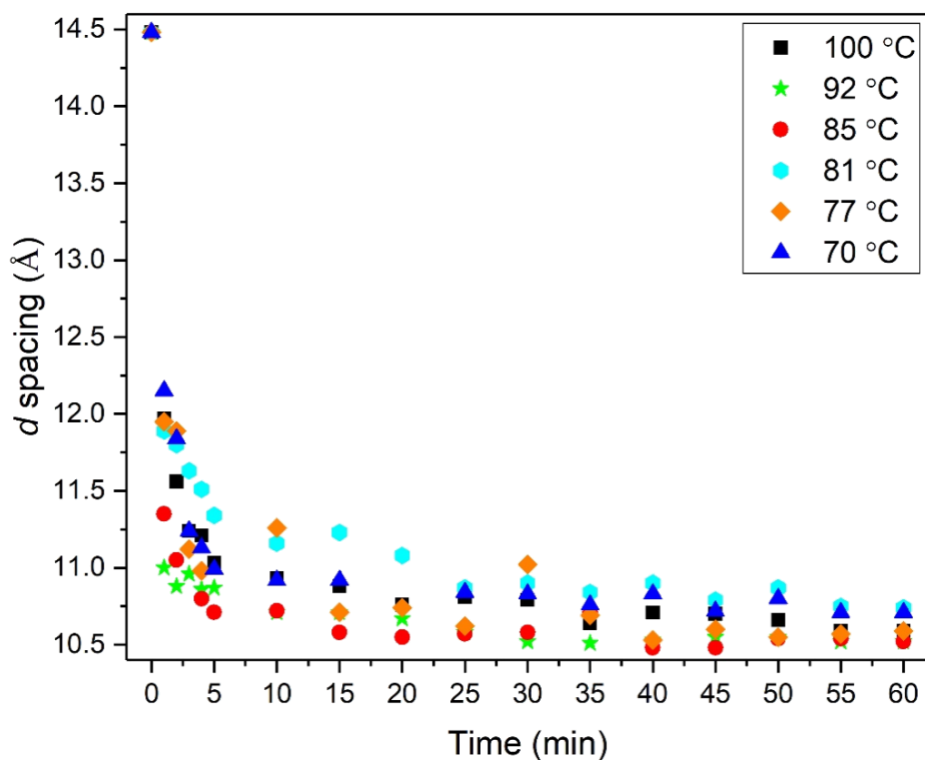
Figure 4.16. The rearrangement of Ge-**UTL** in water over a time period of 1 – 37 hr showing the *d* spacing, d_{200} for 100 °C (black squares), 92 °C (green stars), 85 °C (red circles), 81 °C (cyan hexagons), 77 °C (orange diamonds) and 70 °C (blue triangles). At 1 hour at all temperatures IPC-1P rearranges to IPC-2P after an induction period that varies with temperature (1 – 19 hr). The precision in the measurement of the PXRD *d* spacing is within the symbols on the diagram.

Plotting both the hydrolysis and rearrangement data together allows one to comprehend just how fast the rate of hydrolysis is in comparison to the rate of rearrangement (Figure 4.17). Further analysis using the Avrami-Erofeev model to evaluate the solid-state kinetics of each step will be undertaken and discussed further in Chapter 5.
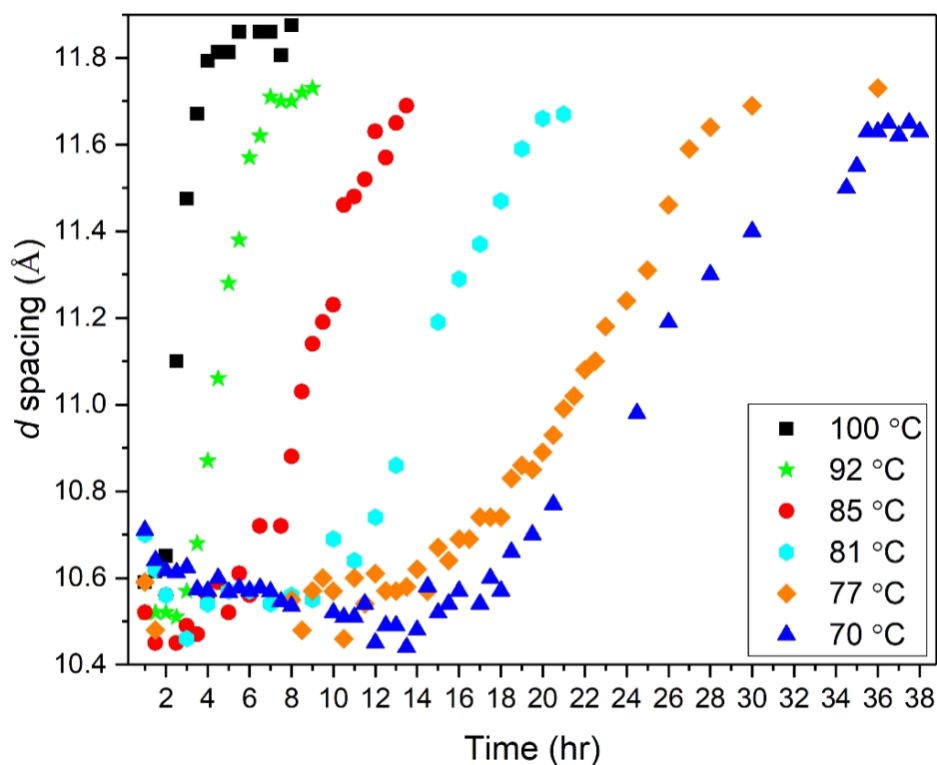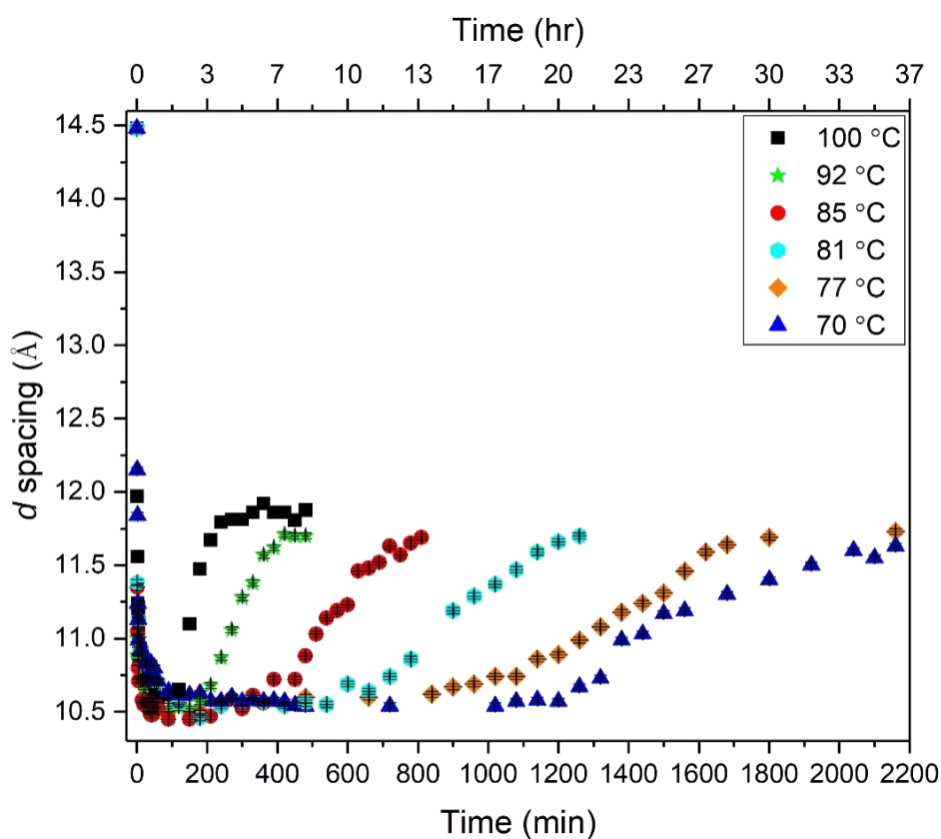
Figure 4.17. The combined results of the hydrolysis and rearrangement of Ge-**UTL** in water over a time period of 37 hr showing the *d* spacing, d_{200} for 100 °C (black squares), 92 °C (green stars), 85 °C (red circles), 81 °C (cyan hexagons), 77 °C (orange diamonds) and 70 °C (blue triangles). After 1 hour at all temperatures Ge-**UTL** is hydrolysed to IPC-1P, which then rearranges to IPC-2P after an induction period that varies with temperature. The precision in the measurement of the PXRD *d* spacing is within the symbols on the diagram and highlighted by black error bars.

4.5.2. The Effect of pH

The hydrolysis and rearrangement mechanisms of Ge-**UTL** were further investigated by varying the concentration of hydrochloric acid (12, 6, 1.5 and 0.1 M). The temperature was kept constant at 20 ºC to ensure only the effect of acid strength was monitored (Figures 4.18 – 4.22).

The reactions undertaken in strong acid (12 and 6 M; Figure 4.18 and 4.19) were rapid, with both the hydrolysis and rearrangement occurring simultaneously and as such neither hydrolyse fully to IPC-1P. In other words, the induction period is reduced to zero and the disassembly never has time to complete before rearrangement occurs.

Figure 4.18. Hydrolysis and rearrangement of Ge-**UTL** over a time period of 8 hr showing the d_{200} spacing for the reaction in 12 M HCl to form IPC-6P. The precision in the measurement of the PXRD d spacing is within the symbols on the diagram.

Interestingly, both the 12 M and 6 M reaction data sets hydrolyse to the same point (11.7 Å; 60 mins), where the 6 M reaction remains stable as IPC-2P. The 12 M reaction however, continues to rearrange past this point to form IPC-6P. It is currently not clear why this is occurring and as such further work is needed to include HCl molarities between 6 and 12 M to understand if this is an anomaly or whether increasing the molarity does indeed lead to a contraction of the inter-layer spacing preferentially.
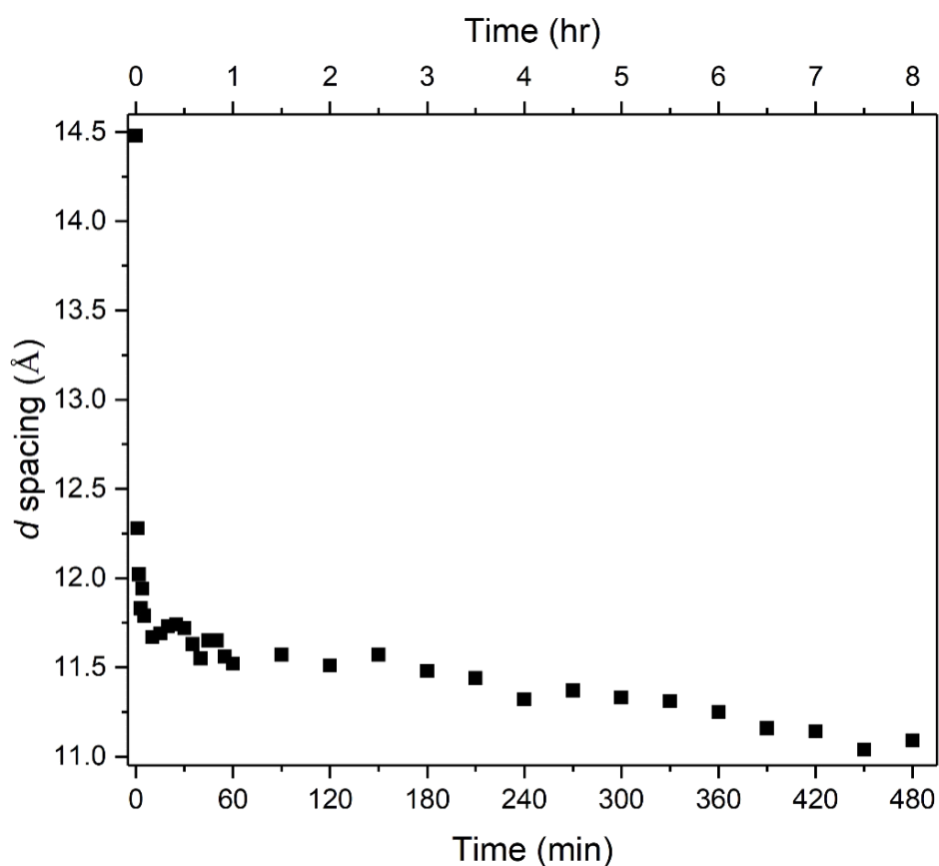
Figure 4.19. Hydrolysis and rearrangement of Ge-**UTL** over a time period of 8 hr showing the d_{200} spacing for the reaction in 6 M HCl to form IPC-2P. The precision in the measurement of the PXRD d spacing is within the symbols on the diagram.

Figure 4.20. Hydrolysis of Ge-**UTL** over a time period of 8 hr showing the d_{200} spacing for the reaction in 1.5 M HCl to form IPC-1P, with no rearrangement of the layers seen over the 8 hr time period. The precision in the measurement of the PXRD d spacing is within the symbols on the diagram.

In 1.5 (Figure 4.20) and 0.1 M HCl (Figure 4.21), the reaction is much slower and a full hydrolysis to IPC-1P can be seen, much more similar to that seen in water. Both the reactions run in 1.5 and 0.1 M complete a full hydrolysis to IPC-1P over the time course of 1 hr, where the material remains stable and does not rearrange within itself over 8 hr. It may be that similarly to the reactions run in water at 85 °C and below, the rearrangement does not occur on a sensible timescale or at least not within 8 hr.
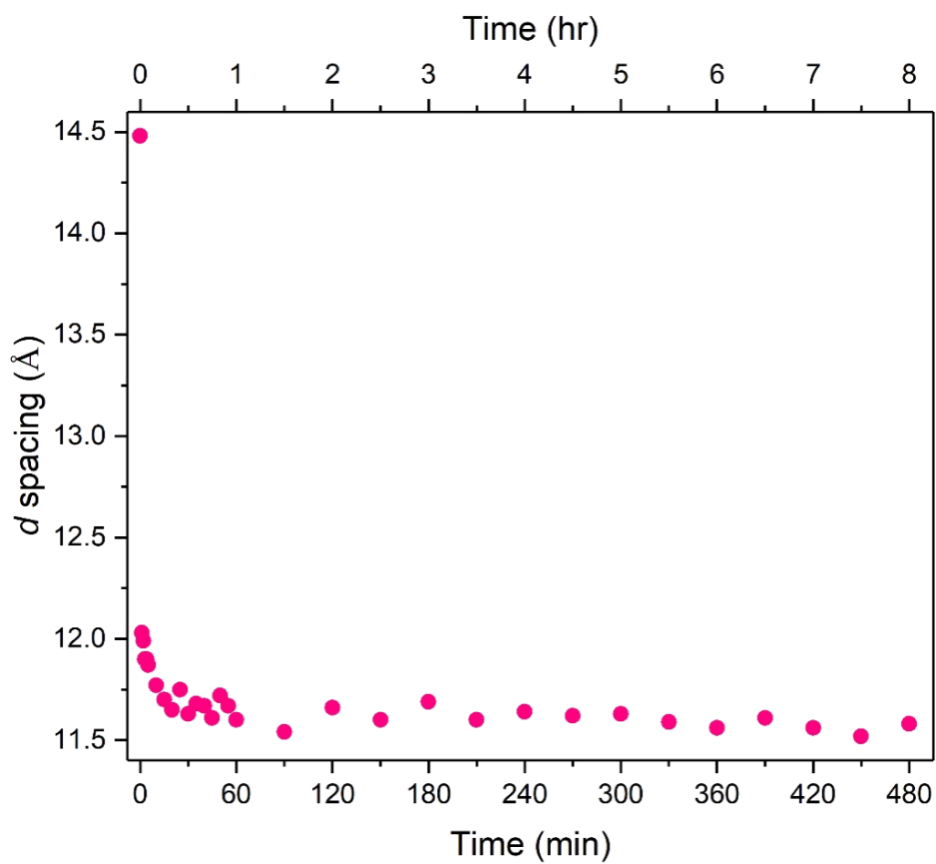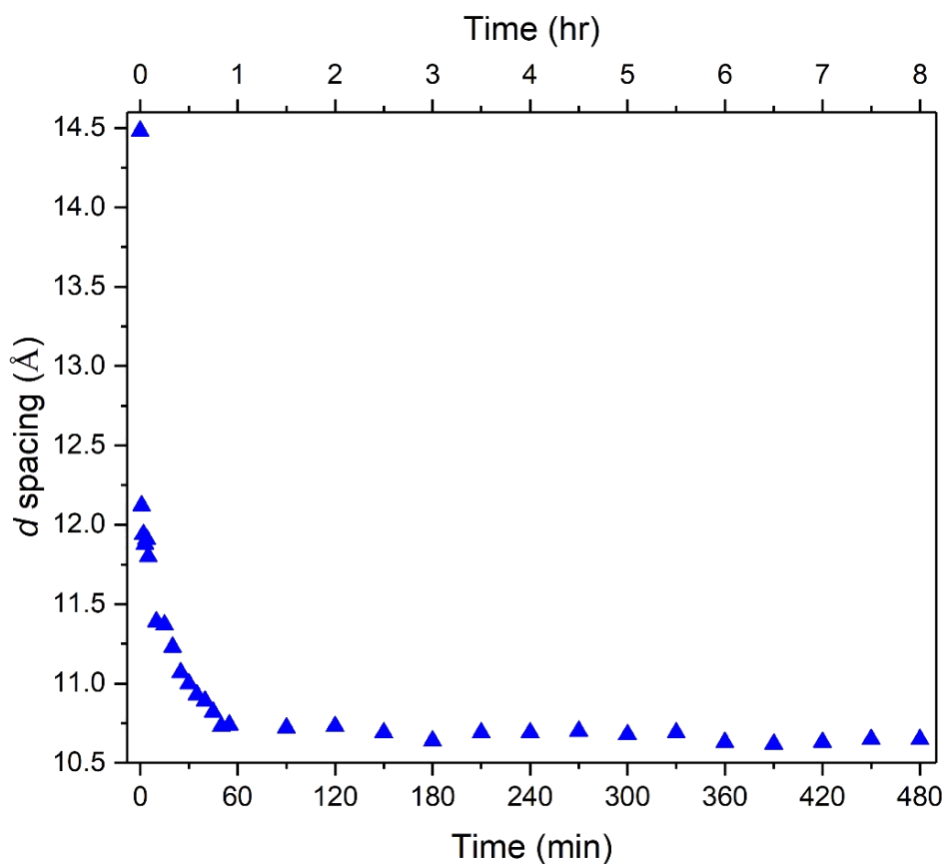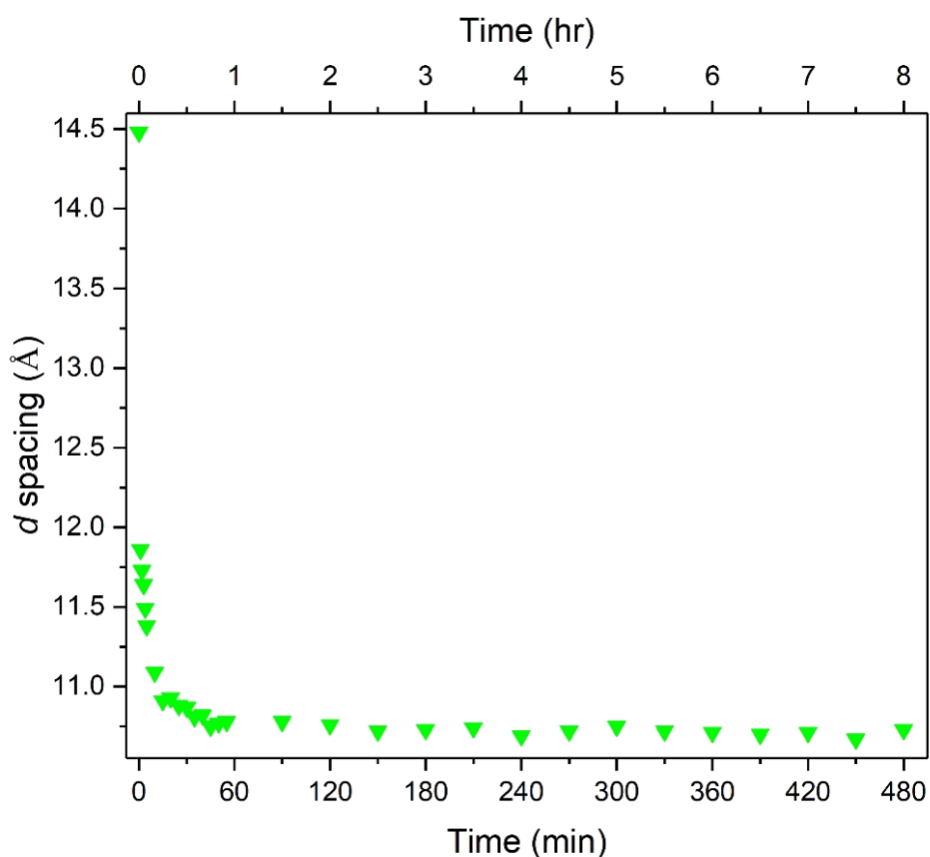
Figure 4.21. Hydrolysis of Ge-**UTL** over a time period of 8 hr showing the d_{200} spacing for the reaction in 0.1 M HCl to form IPC-1P, with no rearrangement of the layers seen over the 8 hr time period. The precision in the measurement of the PXRD d spacing is within the symbols on the diagram.

The combined graph of the inter-connected hydrolysis (D) and rearrangement (O) processes within ADOR for 12, 6, 1.5 and 0.1 M can be seen in Figure 4.22, where it becomes clear the difference in both rate and reactivity between high and low molarities. To understand this clear change further, the experiments should be run starting at 1 M HCl and increase by 1 M each time such that a data set of 1, 2, 3, 4, 5 M HCl etc. can be afforded.
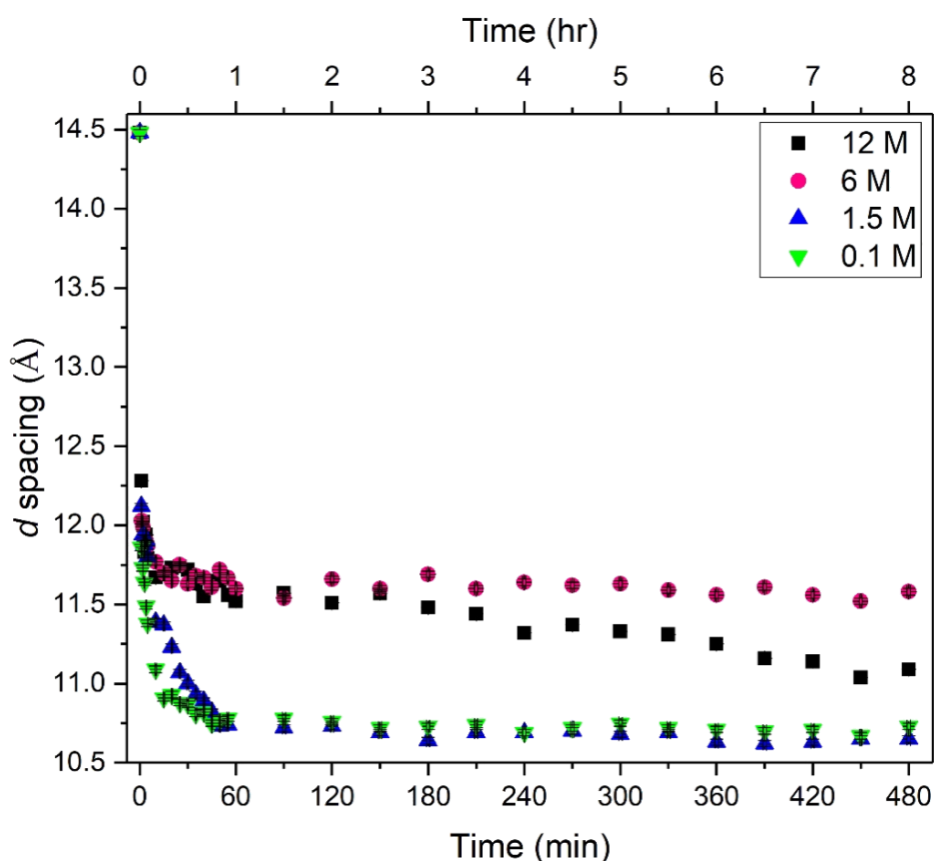
Figure 4.22. The combined results of the hydrolysis and rearrangement of Ge-**UTL** in hydrochloric acid over a time period of 8 hr showing the d spacing, d_{200} for 12 M (black squares), 6 M (pink circles), 1.5 M (blue up triangles) and 0.1 M (green down triangles). The reaction is rapid in both 12 and 6 M HCl, leading to IPC-6P and IPC-2P, respectively. For reactions in 0.1 and 1.5 M HCl, the reaction is slightly slower with the full hydrolysis to the layered material IPC-1P seen over the course of 1 hr. The precision in the measurement of the PXRD d spacing is within the symbols on the diagram and highlighted by black error bars.

4.6.   Applying the ADOR Protocol to other Germanosilicates

The protocol (and the experimental work to complete it) that has been discussed within this chapter has been designed with **UTL** as the parent zeolite topology and will allow researchers to synthesise the previously prepared materials listed: IPC-1P, IPC-2P and IPC-6P and therefore afford IPC-4, IPC-2 and IPC-6 after subsequent calcination at 550 °C. However, perhaps the most important aspect of the protocol is the scaffold it provides for the testing of potential new parent zeolites.

When a researcher has a parent material with the structural features that may make it appropriate as a starting point for the ADOR process, following the procedure within the protocol will provide solid evidence for whether the material is suitable or not. In the ideal circumstance one would know the crystal structure of any parent before embarking on a study using the protocol. However, even if one does not yet know the detailed structure, noting that a major PXRD diffraction peak changes position during the protocol may well indicate that the parent has promise and may provide helpful clues as to the possible structure of the parent.

Substituting a new parent zeolite for the archetypal parent zeolite **UTL** is the simplest approach, but there are clearly potential pitfalls to this and the process is unlikely to work in the same manner for all parent zeolites. Nonetheless, by examining how the protocol differs can provide valuable information on the parent zeolite as well as any ADOR intermediates that may be formed. One such potential problem that may well occur is that the Disassembly step does not work as expected. This could be for two reasons. First, the d_{200} reflection may remain unchanged indicating that there is likely not enough Ge in the structure to enable successful disassembly. The appropriate course of action would therefore be to prepare the parent with an increased Ge content and repeat the protocol. On the other hand, the PXRD patterns collected after the hydrolysis may show significant deterioration to the extent that the reflections may be completely lost. This likely indicates that there is too much Ge in the parent zeolite, a part of it is located in the layers, and the appropriate action in this case is to prepare the parent one with reduced Ge content and repeat the protocol.

If the Disassembly step appears to work successfully, the protocol shows two different possible outcomes. At low acidity, all the inter-layer species are removed from **UTL** but after an induction period atomic species are reintroduced between the layers (Figure 4.11), the length of the induction period depending on the conditions. However, at high acidity the removal of the species from between the layers may never be fully completed (Figure 4.22) before rearrangement leads to the formation of a stable precursor, usually (but not always) analogous to IPC-2P. In other words, under concentrated acid conditions the rearrangement process becomes so fast that the induction period becomes zero and full disassembly to the layered IPC-1P precursor does not have time to occur before the reorganisation to IPC-2P takes place. With different parents this type of behaviour may occur at different conditions and so researchers should really test a good sample of conditions to make sure they do not miss potential ADOR products.

4.7.   Conclusion

In this section, the work contributing to the development of a standard protocol for using the ADOR process to synthesise new high-silica zeolites has been discussed. It was established that when reactions are run solely in water as the reaction medium, the rate of reactivity for the rearrangement (O) process increased with increasing temperature, whilst the rate of hydrolysis remained virtually unchanged over each temperature threshold examined. Moreover, the length of the induction period increased linearly with decreasing temperature from 100 to 70 °C.

Under low acidity (0.1 and 1.5 M HCl), the reaction ran similarly to that of low temperature water, with the full hydrolysis to IPC-1P clearly seen, but with no rearrangement within the 8 hr period. At high acidity (6 and 12 M HCl), the rate of reaction is so fast that the hydrolysis never has time to fully complete before the rearrangement to IPC-2P (6 M) and IPC-6P (12 M) begins. As such the mechanism for the inter-connected hydrolysis and rearrangement is complex and not fully understood at this time.

As a concluding remark – a question often asked is about the universality of the ADOR process. In our experience to date, all germanosilicate zeolites that have the requisite compositional and structural features can be disassembled, organised and reassembled into new zeolites. In that sense the ADOR process is perfectly universal given the limitations on chemistry and topology described. However, the key is to identify the right conditions – and this is where this protocol will find its most enduring impact.

4.8. References

1   C. S. Cundy and P. A. Cox, *Chem. Rev.*, 2003, **103**, 663–701.

2   M. E. Davis and R. F. Lobo, *Chem. Mater*, 1992, **4**, 156–768.

3   M. Mazur, P. S. Wheatley, M. Navarro, W. J. Roth, M. Položij, A. Mayoral, P. Eliášová, P. Nachtigall, J. Čejka and R. E. Morris, *Nat. Chem.*, 2015, **8**, 58–62.

4   S. E. Henkelis, M. Mazur, C. M. Rice, G. P. M. Bignami, P. S. Wheatley, S. E. Ashbrook, J. Čejka and R. E. Morris, *Nat. Protoc.*, 2019, **14**, 781-794.

CHAPTER 5:
KINETIC AND MECHANISTIC ANALYSIS OF THE ADOR PROCESS

5.1.   Aim

The aim of this section follows on from the work conducted previously in Chapter 4. To further the understanding of the hydrolysis (Disassembly) and rearrangement (Organisation) steps in the ADOR process, the aim is to conduct kinetic analysis using two solid-state kinetic models: Avrami-Erofeev and Sharp Hancock, and use these to elucidate information on the kinetics of crystallisation and the activation energy of reaction.
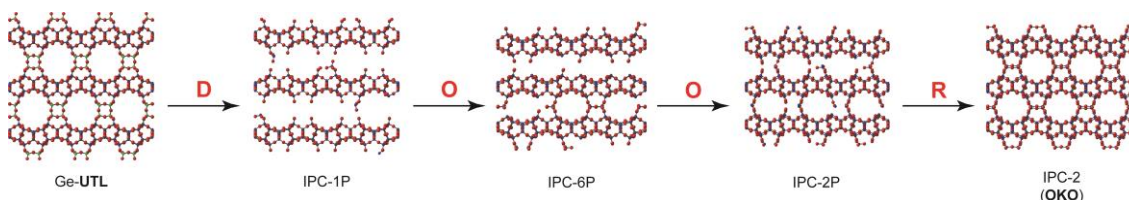
5.2.   Introduction

Figure 5.1. A schematic to show the ADOR mechanism of IPC-2 zeolite synthesis. Assembly - the pre-determined parent zeolite Ge-**UTL** is produced; Disassembly – Germanium is selectively hydrolysed leading to the breakdown of the d4r to form a layered material IPC-1P; Organisation – the IPC-1P layers are suitably re-orientated through a self-organisation process to form IPC-2P via an IPC-6P intermediate; Reassembly – new silicate bonds are formed between the layers to afford IPC-2 upon calcination. Si – blue, Ge – green, O – red.

Figure 5.1 shows the ADOR process as it stood previously to the work in this chapter, elucidated from data collected for the protocol discussed in Chapter 4. The second step in the ADOR process, Disassembly (D), involves the removal of the Ge-rich d4r by aqueous or acid hydrolysis to produce a layered intermediate species (IPC-1P). It is the weakness in

germania bonds (Ge-O-Ge and Ge-O-Si) that allows for the facile hydrolysis of the Ge, which leads to the unzipping of the 3-dimensional layered framework to form dense silicate-rich layers (Figure 5.2).[1,2] The hydrolysis of the parent **UTL** occurs over a time period of 1 hr, where a 60% collapse of the d4r is seen in under 1 min to form Ge-IPC-2P*.
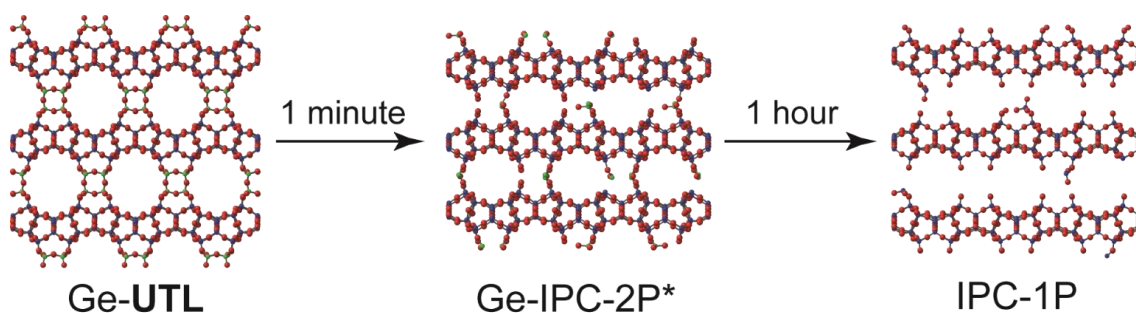

Figure 5.2. Schematic to show the hydrolysis of Ge-**UTL** over the course of 1 hr. After 1 minute the hydrolysis is 60% complete with ca. 60% of the d4r selectively hydrolysed. After 1 hr the hydrolysis has come to completion to form IPC-1P layers. Si – blue, Ge – green, O – red.

The layered species, IPC-1P, can then undergo several different fates depending on the choice of reaction conditions. First, it can be directly reassembled (R) to form a fully connected zeolite called IPC-4 (Figure 5.3). To get a highly crystalline zeolite from the reassembly step, the IPC-1P has to be well organised, either through an intercalation process using a structure-directing-agent (SDA) or by leaving the IPC-1P for the right amount of time so that it self-organises. Alternatively, it is also possible to intercalate the extra silicon that has been afforded from the breakdown of the d4r between the silanol layers, and form a new zeolite precursor called IPC-2P. This zeolite can also form if IPC-1P is left under certain conditions.[3–6] An understanding of this process is the major objective of this work.
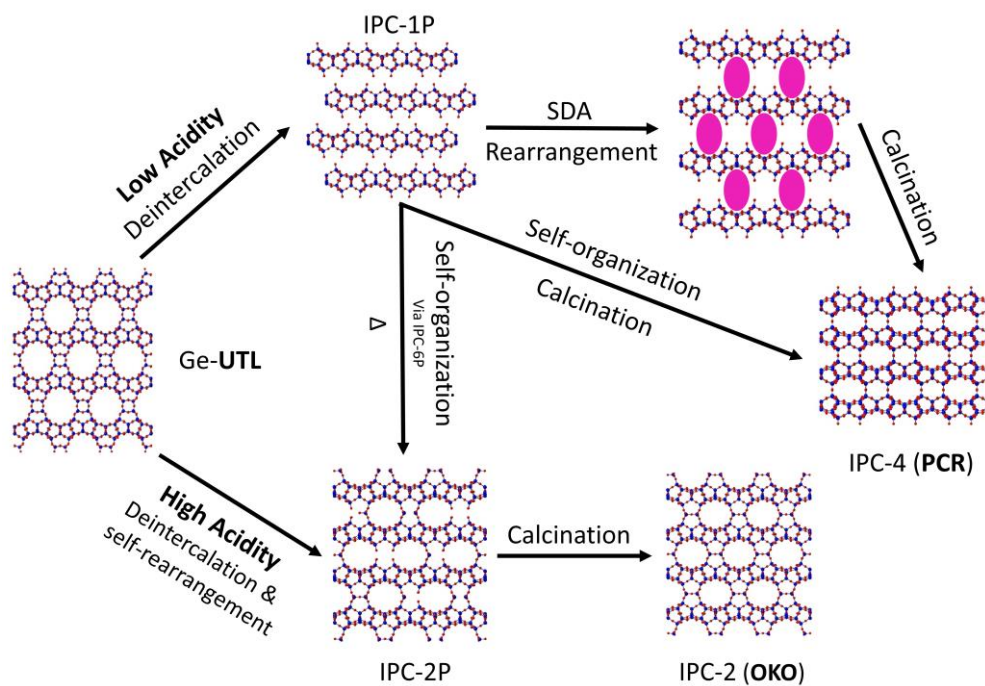
Figure 5.3. Schematic to show the Organisation step as it currently stands. TOP – Low acidity conditions, which forms IPC-4 after calcination and IPC-2 after self-organisation and then calcination; BOTTOM – High acidity conditions.

For the first time, the kinetic analysis of the two most prominent steps (D and O) in the ADOR process have been investigated. This has been found by sampling the reaction and using powder X-ray diffraction to follow the evolution of the lattice spacings (d_{200} peak in XRD) with time. Each data set was fit with the Avrami-Erofeev model and the activation energy of the rearrangement (Organisation) step was found to be 70.1 kJ mol^{-1}.

5.3. Experimental Procedure

Please refer to Experimental in Chapter 4 for the synthesis of Ge-**UTL** and the corresponding SDA - (6*R*,10*S*)-6,10-dimethyl-5-azoniaspiro[4,5]decane hydroxide.

5.3.1. Humidity Study

5.3.1.1. 54.4% Relative Humidity (RH)

A saturated salt solution of 54.4% RH was prepared from an aqueous solution of magnesium nitrate in water (125 g / 100 mL).

5.3.1.2. 75.5% RH

A saturated salt solution of 75.5% RH was prepared from an aqueous solution of sodium chloride in water (359 g / 1000 mL).

5.3.1.3. 97.6% RH

A saturated salt solution of 97.6% RH was prepared from an aqueous solution of potassium sulfate in water (120 g / 1000 mL).

5.3.1.4. Procedure

Saturated salt solutions of 54.4, 75.5, and 97.6% RH were prepared and added to plastic boxes, sealed with a lid and parafilm and allowed to equilibrate for 24 hr. After 24 hr, calcined Ge-**UTL** was added in plastic boats to avoid touching the salt solution. The boxes were sealed and samples taken every week for 6 weeks. Samples were packed in 0.5 mm borosilicate capillaries and analysed by powder X-ray diffraction.

5.3.2. Kinetic Analysis

The temperature dependence of the hydrolysis (D) and rearrangement (O) processes in water were investigated over a temperature range of 70 – 100 °C primarily using the Avrami-Erofeev model:

$$[-ln(1-\alpha)]^{1/n} = k(t - t_{ind})$$

The linear equivalent of Avrami-Erofeev, the Sharp Hancock equation was also employed to corroborate results and increase data quality satisfaction.

$$\ln[-\ln(1-\alpha)] = n\ln(k) + n\ln(t)$$

For each reaction carried out, the Avrami-Erofeev and Sharp Hancock models were fitted to experimental data to calculate the reaction exponent, n and the rate constant, k. The extent of reaction, α was measured using the change in inter-layer d spacing normalised between 0 and 1. t_{ind} was taken to be the time at which the induction period had come to an end before the rearrangement process began.

The effect of temperature on the system was investigated at 100, 92, 85, 81, 77 and 70 °C. Samples were taken periodically over an 8 – 37 hr period, and analysed by powder X-ray diffraction (PXRD) to determine the level of reaction completion and the daughter zeolite being produced. Each sample at the designated time-set was analysed by PXRD and the location of the d_{200} peak recorded. This peak represents the inter-layer distance between the dense silicate-rich layers and as such provides valuable information on the status of reaction, allowing one to elucidate the level of completion at the time taken of sample and the rate of reaction for each data set (Figure 5.4). Figure 5.4 shows the full hydrolysis and rearrangement processes for all temperatures recorded. For individual data sets please refer to Chapter 4.
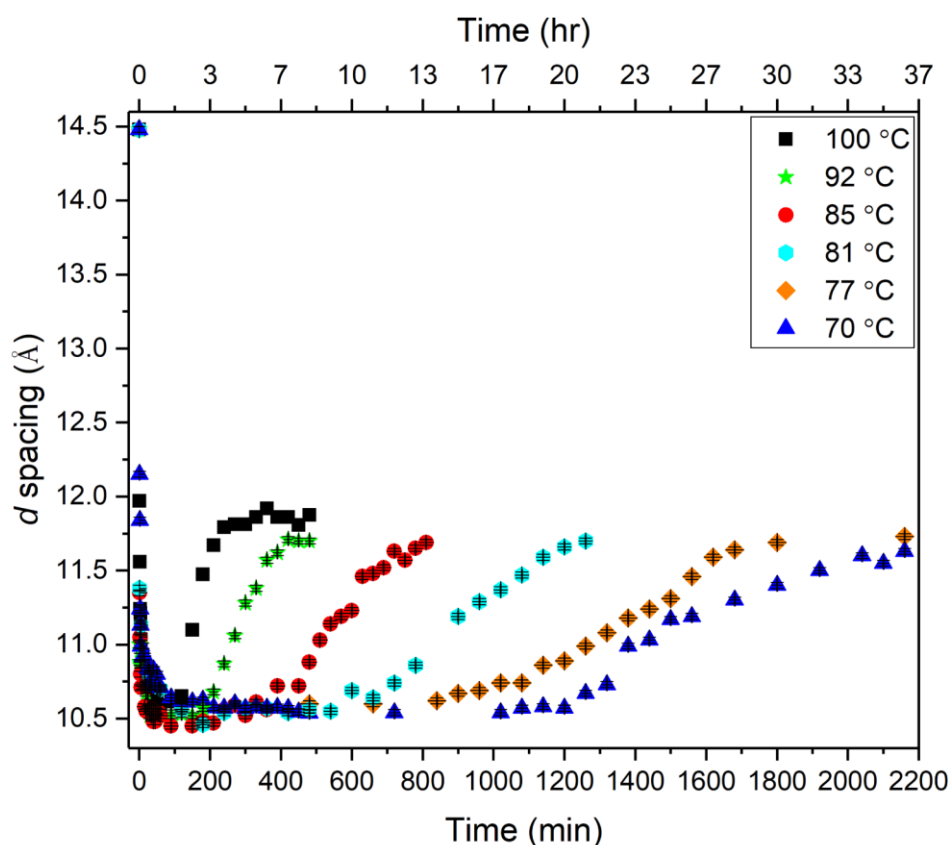
Figure 5.4. The change in d_{200} inter-layer spacing for the hydrolysis and rearrangement steps for the reaction of Ge-**UTL** in water with increasing temperature. 100 °C - black squares, 92 °C - green stars, 85 °C - red circles, 81 °C - teal pentagons, 77 °C - orange diamonds, 70 °C - blue triangles. All data points were fit with an error of ±0.2 Å. Data repeated from Chapter 4.

The Avrami-Erofeev model is well established for modelling solid-state kinetics as it can specifically describe the kinetics for crystallisation and the method and direction of growth of the nucleates in the system. It is well known to be used to monitor phase transitions and understand the mechanisms of intercalation/rearrangement processes.[7–13]

5.4. Results and Discussion

The solid-state kinetics of the hydrolysis (D) and rearrangement (O) steps were investigated to gather information on the mechanism of action at each step. Further analysis on the stability of Ge-**UTL** at 20 °C in a constant humidity of 97.6% (potassium sulfate), 75.5%

(sodium chloride), and 54.4% (magnesium nitrate) were undertaken. The data shown here was collected in Chapter 4.

5.4.1. Kinetics of the Hydrolysis Step

The hydrolysis of Ge-**UTL** in deionised water can be mapped through PXRD and a change in *d* spacing from **UTL** (14.48 Å) to the disordered layered material IPC-1P (10.54 Å) can be clearly seen. The extent of reaction vs. time was plotted for the reactions run at 100, 92, 85, 81, 77, and 70 °C and each plot was fitted with the Avrami-Erofeev model (Figure 5.5) and the Sharp Hancock equation (Figure 5.6). The ratio of zeolite : water is an important factor to be considered, significantly reducing the amount of water effectively reduces the rate of hydrolysis (D) and in low-volume conditions (1 g / 8 mL) the material never fully hydrolyses to IPC-1P. In this work, a ratio of 1 g / 200 mL for zeolite : water was used to ensure full hydrolysis.
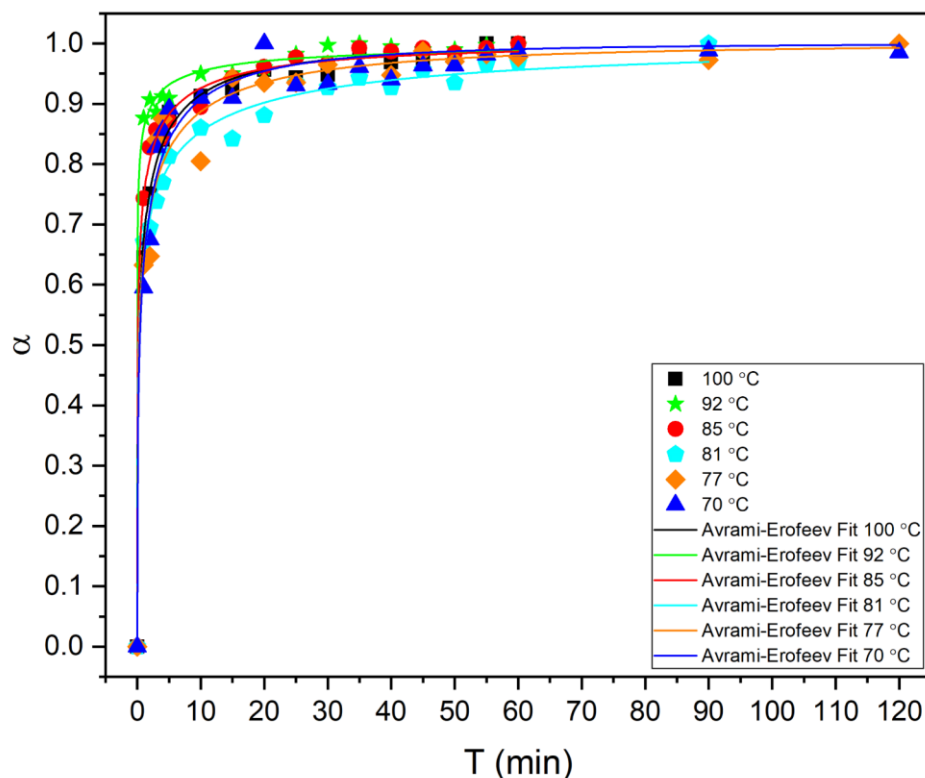
Figure 5.5. Extent of reaction, α, plotted against time for the hydrolysis (D) step. 100 °C - black squares, 92 °C - green stars, 85 °C - red circles, 81 °C - teal pentagons, 77 °C - orange diamonds, 70 °C - blue triangles. Each plot was fitted with the Avrami-Erofeev model.

From both the initial PXRD data and the subsequent Avrami plots it is clear to see that the hydrolysis step is not strongly dependent on the temperature of the reaction system. The Avrami exponent n (n_{AE}) was found to be <1 for each temperature (Table 5.1). An Avrami exponent this low can normally be attributed to diffusion controlled 1-dimensional growth. In this case, because the rate of reaction is so fast and we see a 60% collapse of the d4r within 1 min, the results from the fit are unsuitable for further analysis. The minor changes in reaction time can be attributed to experimental error, such as changes in mixing, and time of addition of parent zeolite.

Although the rate constant k (k_{AE}) is to some degree unreliable, due to the rapid rate of hydrolysis/deintercalation (seen by a change in d spacing), we can assume that the mechanism proceeds without having to overcome a large activation barrier, again suggesting that temperature is not a requirement for the hydrolysis and solely depends on the availability of liquid water.

As the d4r collapse, the material moves through a new species we coin Ge-IPC-2P* (formed after 1 min). This is effectively a single-four-ring (s4r) containing IPC-2P structure, but with germanium still residing between the layers creating local disorder (Si/Ge 10.7). As such, this material has a broad d_{200} peak in XRD patterns. Eventually, once all the inter-layer species are deintercalated IPC-1P is formed.

Occasionally described as a more reliable solid-state model to find n, the Sharp Hancock method[14] (Figure 5.6) was applied by taking natural logarithms of the Avrami-Erofeev equation and the values of n (n_{SH}) and k (k_{SH}) compared for each model (Table 5.1). Again, due to the reaction rate, the results obtained are unsuitable and further analysis using *in situ* techniques is needed to monitor the hydrolysis mechanism on a second timescale.

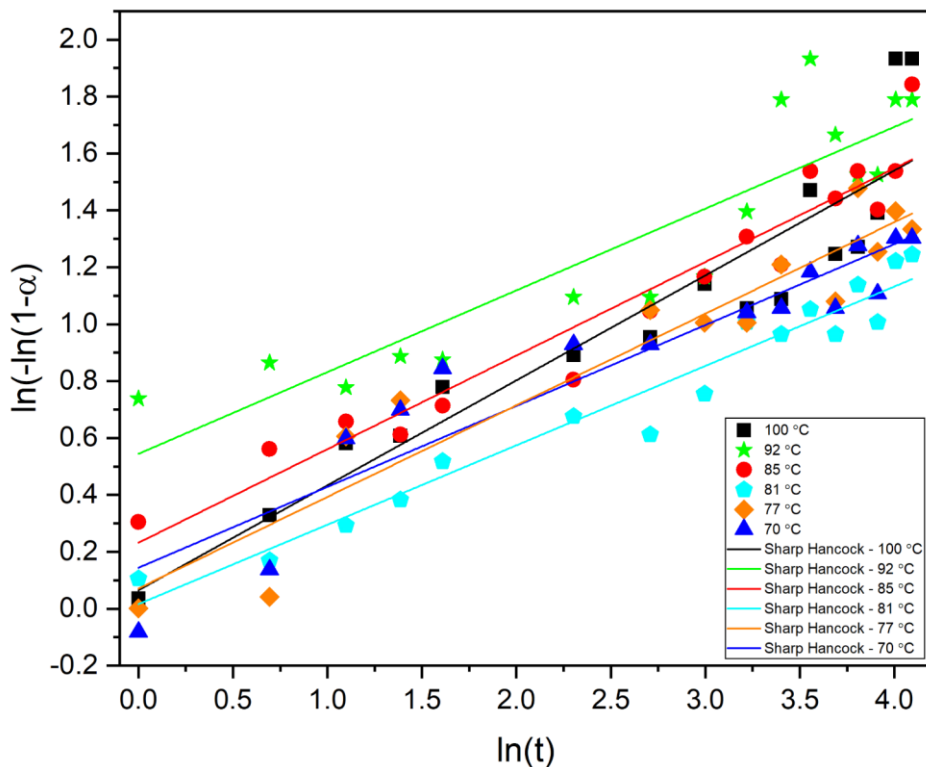
Figure 5.6. The Sharp Hancock plots of the hydrolysis step produced through ln(-ln(1-α)) vs. ln(t). 100 °C - black squares, 92 °C - green stars, 85 °C - red circles, 81 °C - cyan pentagons, 77 °C - orange diamonds, and 70 °C - blue triangles.

Table 5.1. Kinetic parameters obtained by fitting of the crystallisation curves with the Avrami-Erofeev and Sharp Hancock equations for the hydrolysis (D) step. Estimated error to 2dp on *n* and 1dp on *k*.

Temp / °C	n_{SH}	k_{SH} / min^{-1}	n_{AE}	k_{AE} / min^{-1}
100	0.37	1.2	0.35	1.4
92	0.29	6.7	0.20	28.1
85	0.33	2.0	0.28	3.0
81	0.28	1.1	0.27	1.1
77	0.32	1.2	0.33	1.1
70	0.28	1.7	0.37	1.1

5.4.2. Kinetics of the Rearrangement Step

Once the hydrolysis from Ge-**UTL** to IPC-1P had completed, various induction times can be seen before the full rearrangement to IPC-2P, which takes place through the IPC-6P intermediate. IPC-6P is the precursor to a s4r and direct oxygen linkage containing daughter zeolite (IPC-6, see Chapters 1 and 4 for structural details). As such it contains layers of IPC-2P and layers of IPC-1P. Due to this, the d_{200} peak in the powder pattern becomes broader.

A clear temperature dependence on the system can be seen with reaction times increasing from 2 to 22 hr as the temperature decreases from 100 to 70 °C. As temperature increases the time taken to induct decreases dramatically, with 70 °C inducting for 20 hr and 100 °C inducting for only 1 hr.

The Avrami-Erofeev model was fitted to the extent of reaction data, where t-t$_{ind}$ was taken to be the point at which the induction came to an end and the intercalation began (Figure 5.7).
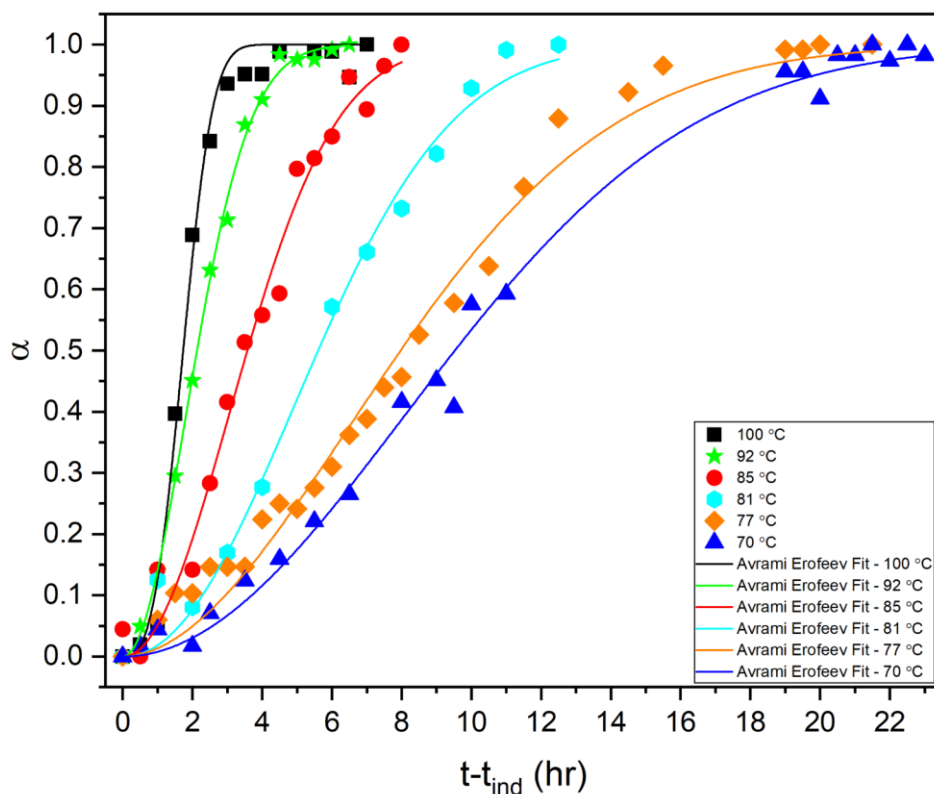
Figure 5.7. Extent of reaction, α plotted against time for the rearrangement (O) step. 100 °C - black squares, 92 °C - green stars, 85 °C - red circles, 81 °C - teal pentagons, 77 °C - orange diamonds, 70 °C - blue triangles. Each plot was fitted with the Avrami-Erofeev model (solid lines).

The Avrami exponent n, was found to be 3 for 100 °C and 2 for all lower temperatures. As the atomic nuclei are pre-formed in all cases the growth is restricted to 3-dimensions ($n = 3$) and 2-dimensions ($n = 2$). As such rearrangement of silicates into the layers is occurring along the x, y and z-axes when $n = 3$, ultimately forming a 3-dimensional connected framework. However, when $n = 2$, rearrangement is only occurring along the x/y, x/z or y/z axes at any one time, this will slow down the rate of forming the fully connected 3D "true zeolite". The rate constant k, decreases from 0.510 min^{-1} at 100 °C to 0.391, 0.233, 0.150, 0.103, and 0.087 min^{-1} for 92, 85. 81, 77, and 70 °C respectively.

The data was once again compared against the Sharp Hancock model and the values for n and k compared (Figure 5.8 and Table 5.2). The values of k are very similar at all temperatures apart from 100 °C, although Sharp Hancock is supposedly a more reliable method of finding k, the experimental data fit with the Avrami-Erofeev model looks to be

superior and therefore the Avrami-Erofeev results will be taken forward for further analysis using the Arrhenius equation to find the activation energy of the rearrangement step.
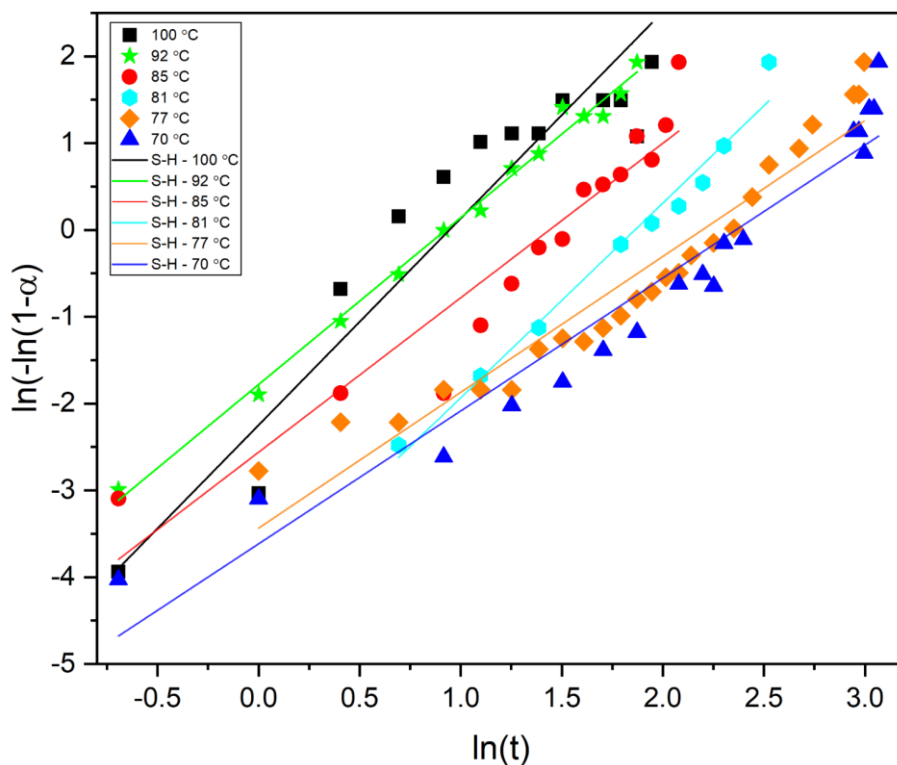

Figure 5.8. The Sharp Hancock plots of the intercalation/rearrangement step produced through ln(-ln(1-α)) vs. ln(t); 100 °C - black squares, 92 °C - green stars, 85 °C - red circles, 81 °C - cyan pentagons, 77 °C - orange diamonds, and 70 °C - blue triangles.

Table 5.2. Kinetic parameters obtained by fitting of the crystallisation curves with the Avrami-Erofeev and Sharp Hancock equations for the rearrangement step. Estimated error to 2dp on n and 2dp on k.

Temp / °C	n_{SH}	k_{SH} / min^{-1}	n_{AE}	k_{AE} / min^{-1}
100	2.38	0.39	2.96	0.51
92	1.92	0.40	2.01	0.39
85	1.77	0.24	2.02	0.23
81	2.24	0.15	2.10	0.15
77	1.56	0.11	1.89	0.10
70	1.53	0.09	1.99	0.09

The activation energy Ea, was calculated to be 70.1 kJ mol^{-1} (Figure 5.9). This was extrapolated from a plot of ln(k) against T^{-1} based on the Arrhenius equation:

$$k = Ae^{-Ea/RT}$$

This activation energy is relatively high when in comparison to the intercalation mechanisms of other layered materials, for example the activation energy required for chlorophenoxyacetates to intercalate (rearrange) into double-layered hydroxides is 43, 53.6 and 61.7 kJ mol^{-1}.[13] The increase in activation energy is linearly dependent on the size of the chlorophenoxyacetate introduced. This suggests the energy needed for silicates to rearrange into the layers is high and may be due to the close proximity of the IPC-1P hydrogen bonded layers. The values of k were taken from the Avrami fittings.
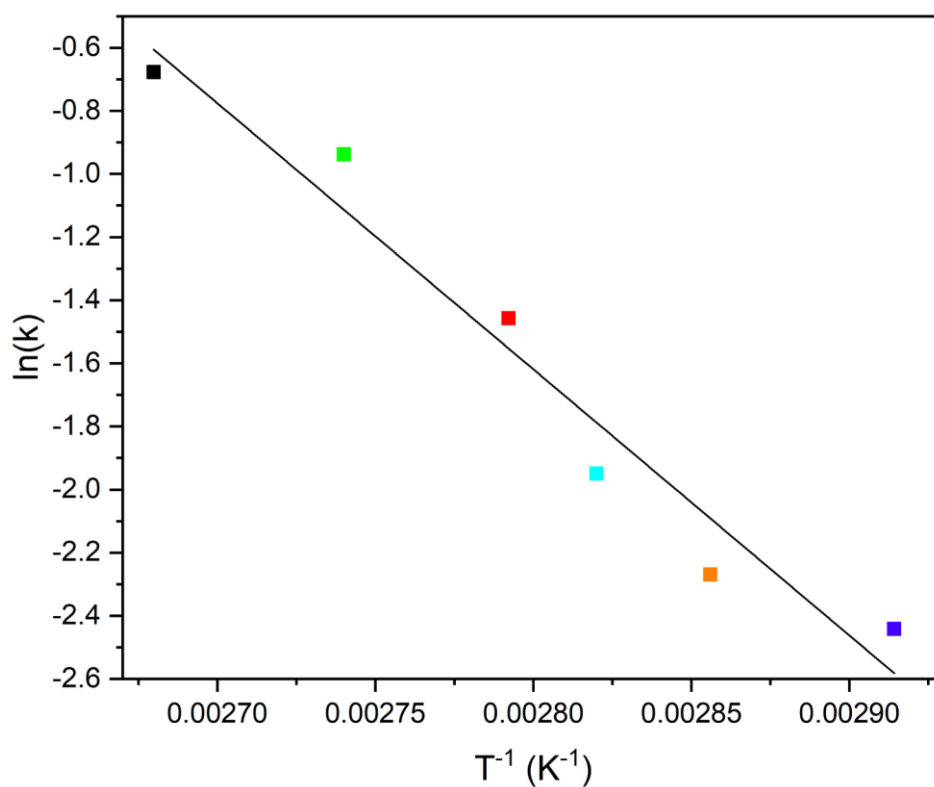

Figure 5.9. Arrhenius plot of ln(k) vs. T^{-1} to attain an activation energy of 70.1 kJ mol^{-1} for the rearrangement from IPC-1P to IPC-2P.

5.4.2.1. Understanding Where the Silicon Intercalates From

Understanding where the silicon rearranges from is imperative to fully understanding the mechanism. An experiment was devised to quantify whether the silicon rearranged from silicates present in the solution after hydrolysis or from the silicon in the silica-rich layers.

Using the 100 °C reaction in water as a standard, once hydrolysis had completed at 1hr30 the suspension was filtered to remove the silicate-rich solution and replaced with fresh water at temperature (known herein as 100 °C_fresh water). The removal of the silicate solution leads to a change in the IPC-1P material, which is likely to be a sub-zeolite[15] in the first instance, with a small inter-layer distance. This material is similar to a solid termed IPC-1, which was the first microporous zeolite to be produced through ADOR. IPC-1 is a very disordered structure that is produced from the disassembly of B-**UTL** after calcination.[16] This material can be visualized by the interlocking of one's fingers, where the palms of the hands are the silica-rich layers and fingers are the silanol groups on the surface of the layers. After reacting for a further 5 hr, the layers have rearranged to IPC-2P (Figure 5.10).
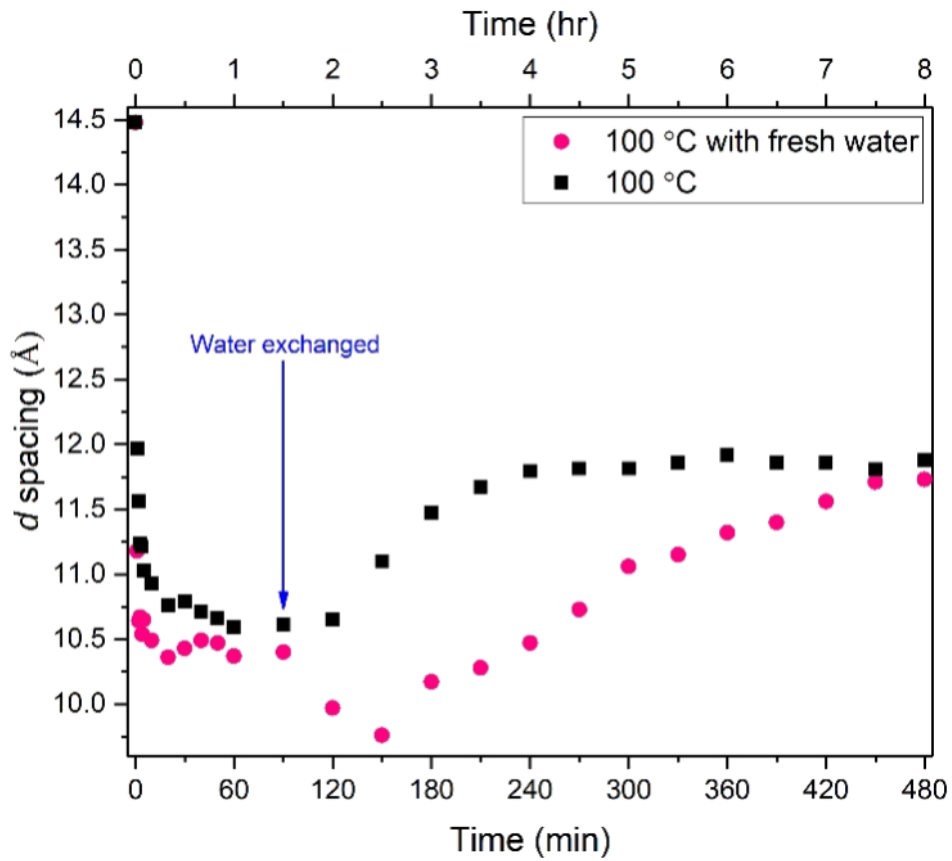
Figure 5.10. The change in d_{200} inter-layer spacing for the hydrolysis and rearrangement steps. 100 °C – black squares, 100 °C_fresh water; water replaced at 90 min – pink circles.

As all sources of silicon in solution have been removed, we can say that the silicon must be rearranging from the silicon-rich layers, thus potentially causing defect sites (Figure 5.11).
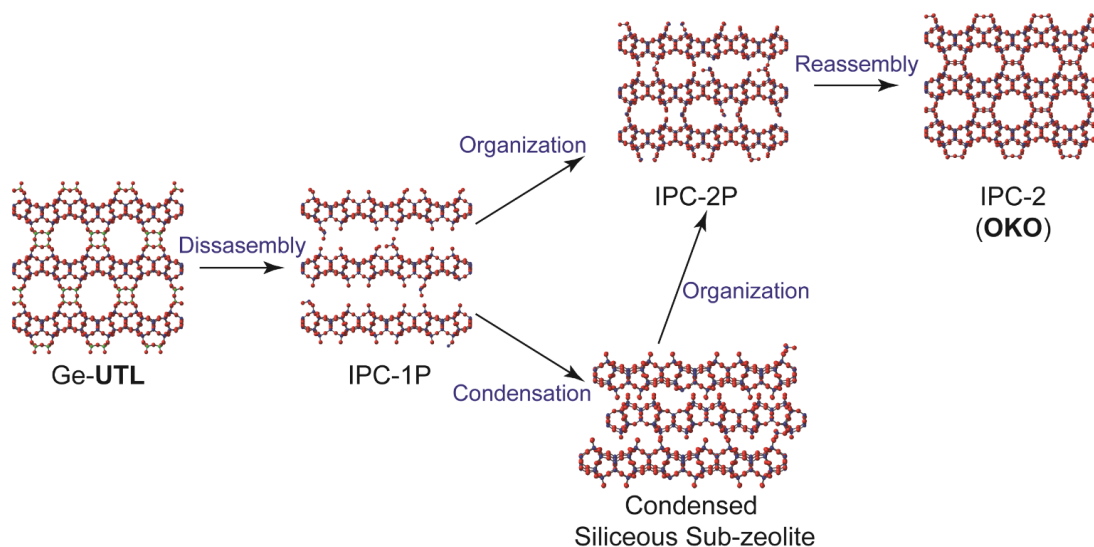
Figure 5.11. A schematic to show the change in structure with change in solution. Disassembly - Ge-**UTL** is first hydrolysed to IPC-1P. Organisation - The layers then self-rearrange to IPC-2P. Condensation – The layers condense further to form a sub-zeolite of IPC-1P, termed IPC-1 and then self-rearrange to IPC-2P. Reassembly – Formation of silicate bonds between IPC-2P to form IPC-2.

The change in reaction time can be quantified. When the silicon rearranges from the layers the time taken to rearrange from IPC-1P increases from 2 hr to 6hr30, thus affirming that rearrangement from silicates present in solution due to the breakdown of the d4r is the preferred method. The kinetics were once again analysed by the Avrami-Erofeev model (Figure 5.12) and the Avrami exponent n, for 100 °C_fresh water was found to be 1, thereby controlling the growth in only 1-dimension. The rate constant k, was found to be similar to that of the 92 °C reaction with a rate constant of 0.405 min^{-1}.
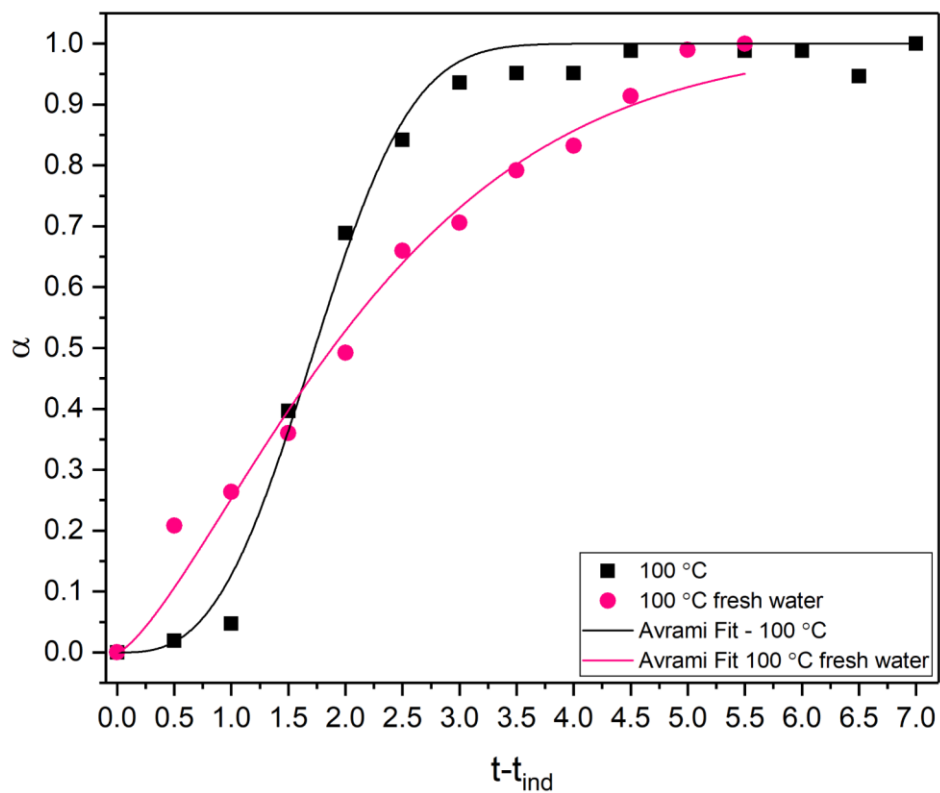
Figure 5.12. Extent of reaction, α plotted against time for the rearrangement (O) step. 100 °C – black squares, 100 °C_fresh water – pink circles. Both plots were fitted with the Avrami-Erofeev model.

As rearrangement to IPC-2P is favoured even when there are no silica species present, we can conclude that IPC-1P is the kinetic product and IPC-2P is the thermodynamic product (Figure 5.13).

Figure 5.13. An overview schematic of each step in the ADOR process for Ge-**UTL** when hydrolysis is carried out at 100 °C in water, with all intermediate materials shown. Pathway 1 shows the rearrangement when silicates are present in solution. Pathway 2 shows the rearrangement following replacement with fresh water at 1hr30.

5.4.3. Humidity Studies of Ge-UTL

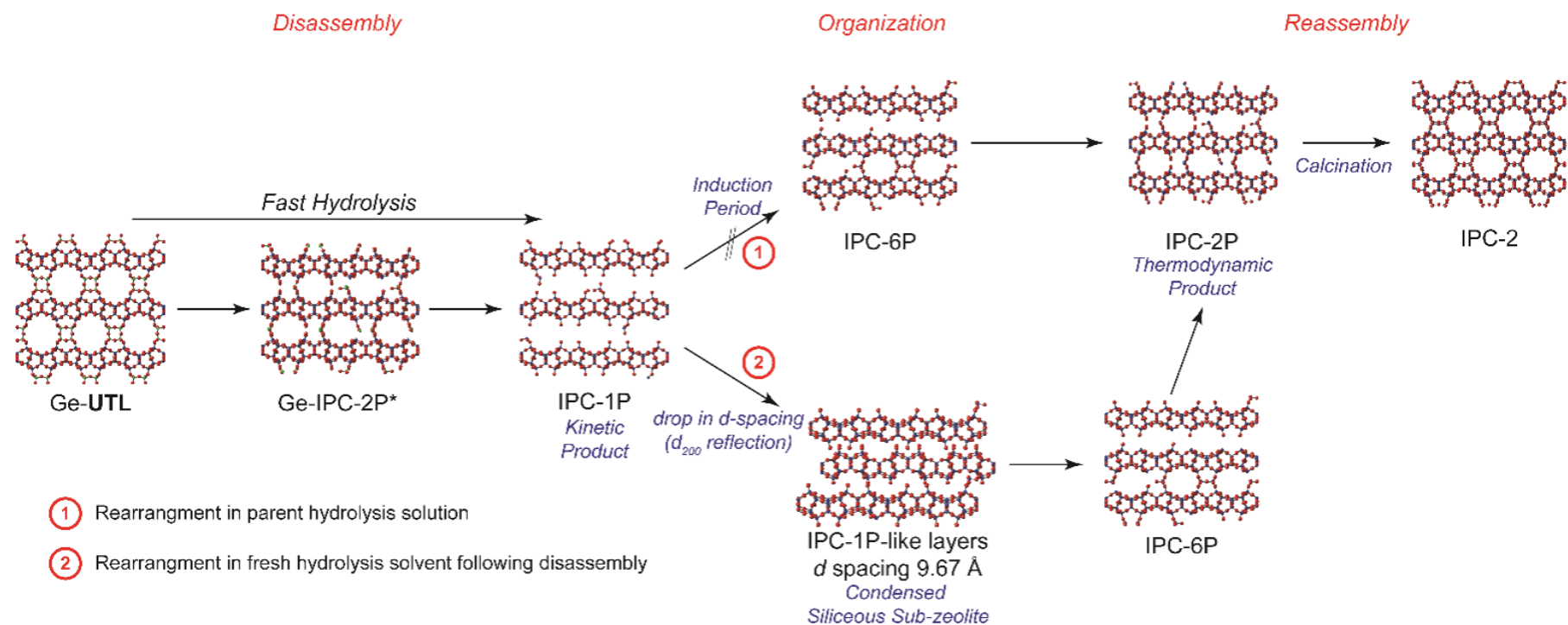To investigate whether calcined Ge-**UTL** is bench-stable over prolonged periods of time, calcined Ge-**UTL** was subjected to three constant relative humidity's (%, RH), 54.4, 75.5 and 97.6 %, with samples taken every week for six weeks.

Figure 5.14. Powder X-ray diffraction patterns for Ge-**UTL** when kept in a sealed environment of 54.4% humidity for 6 weeks; 5 – 10 2θ. Calcined Ge-**UTL** – purple; after 1 week – dark blue; 2 weeks – light blue; 3 weeks – green; 4 weeks – mustard yellow; 5 weeks – orange; 6 weeks – red.

After 1 week at a constant relative humidity (HR) of 54.4% (Figure 5.14), the relative intensity of the d_{200} inter-layer spacing peak has reduced and a change in d spacing from 14.48 to 14.19 Å has occurred. After 6 weeks the d spacing of the d_{200} and the positions of all other peaks in the X-ray diffraction patterns have remained stable.

Figure 5.15. Powder X-ray diffraction patterns for Ge-**UTL** when kept in a sealed environment of 75.5% humidity for 6 weeks; 5 – 10 2θ. Calcined Ge-**UTL** – purple; after 1 week – dark blue; 2 weeks – light blue; 3 weeks – green; 4 weeks – mustard yellow; 5 weeks – orange; 6 weeks – red.

After only 1 week at a constant relative humidity (HR) of 75.5% (Figure 5.15), the relative intensity of the d_{200} inter-layer spacing peak has reduced and a change in d spacing from 14.48 to 14.25 Å has occurred. After 6 weeks the d spacing of the d_{200} and the positions of all other peaks in the X-ray diffraction patterns have remained stable. In all XRD patterns after initial subjection to RH at 54.5, 75.5, and 97.6 % a new peak has arisen at 8.60 2θ (10.27 Å), it is currently not clear what this peak corresponds to, and as such further analysis is needed to understand just how much of an impact the humidity has on the structure.
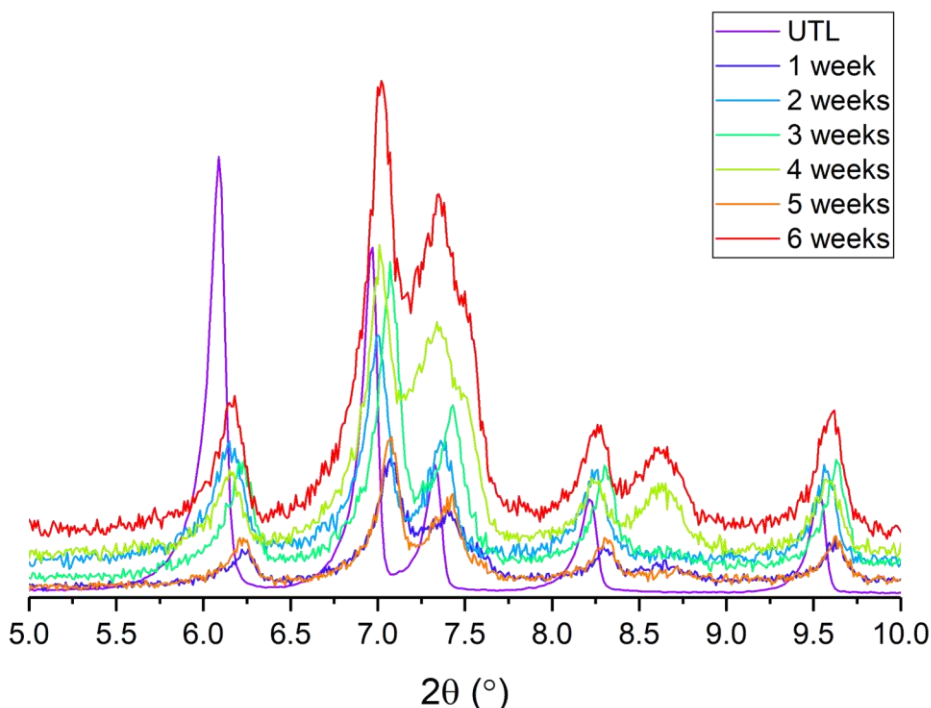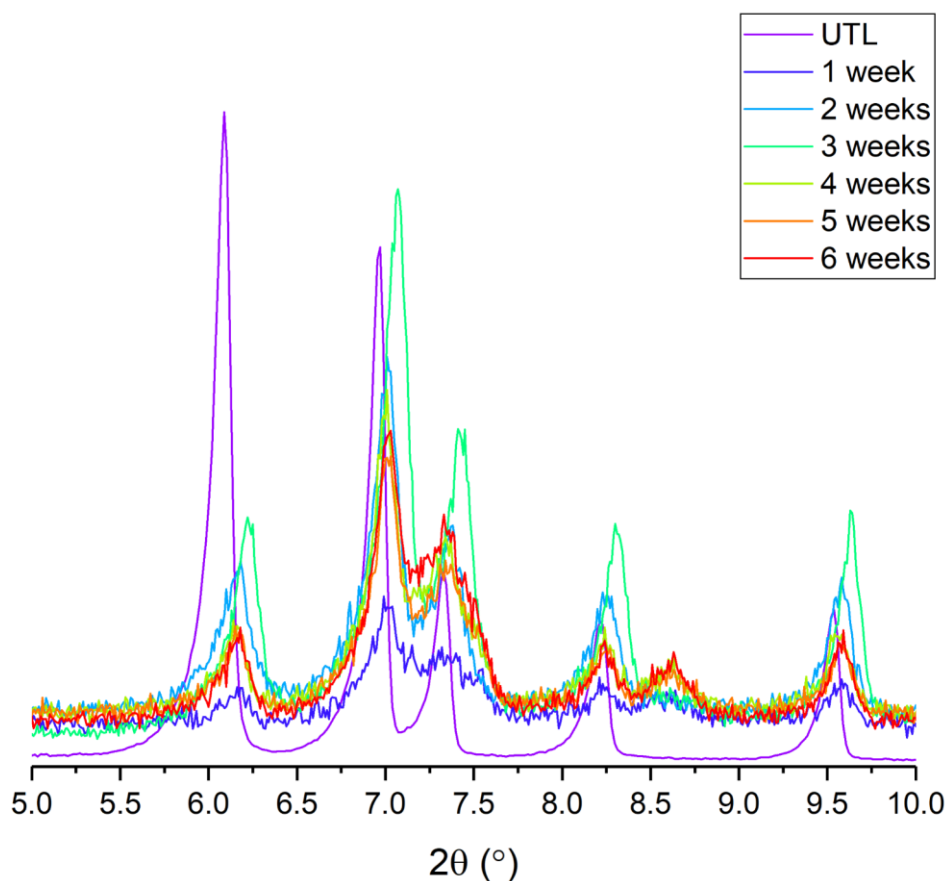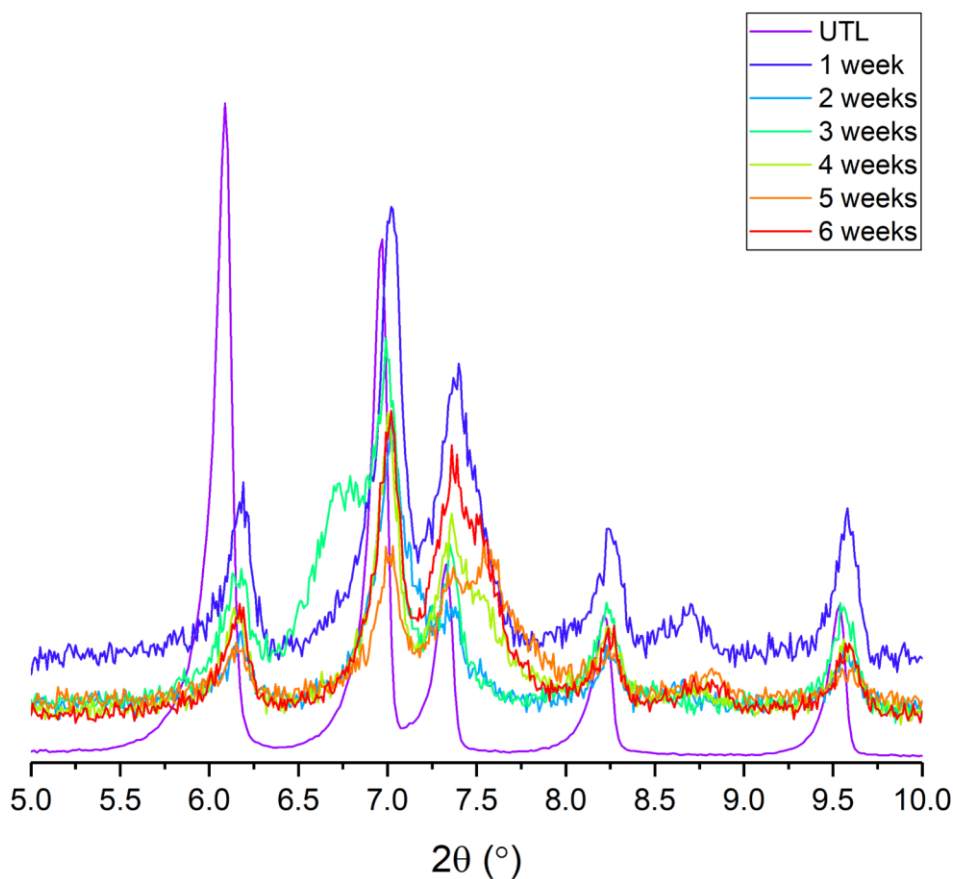
Figure 5.16. Powder X-ray diffraction patterns for Ge-**UTL** when kept in a sealed environment of 97.6% humidity for 6 weeks; 5 – 10 2θ. Calcined Ge-**UTL** – purple; after 1 week – dark blue; 2 weeks – light blue; 3 weeks – green; 4 weeks – mustard yellow; 5 weeks – orange; 6 weeks – red.

Finally, looking at Ge-**UTL** in a constant relative humidity of 97.6% (Figure 5.16), after 1 week the d spacing of the d_{200} inter-layer has moved from 14.48 to 14.22 Å and akin to the other RH investigated, remains stable at this position.

If we compare the relative humidity data of each percentage at the 6 week mark against uncalcined Ge-**UTL**, we can clearly see a very strong similarity between them (Figure 5.17). The relative intensity of the d_{200} peak is the same, however the peak seen at 10.27 Å in the humidity data is not present in the uncalcined sample of Ge-**UTL.** At this stage we can clearly see that although not fully broken down, the amount of water in the saturated salt solution is enough to slightly damage the parent Ge-**UTL**. It may be that as the powder patterns of uncalcined and humidity are so similar, some of the silicate bonds between the layers may have broken, however as we still retain peaks, the majority of the structure

remains intact. Whether this material would be capable of undergoing ADOR after further calcination remains to be seen and future work needs to be done on this. At this stage, as the natural humidity of the air in a laboratory in Scotland is ~60%, we can conclude that Ge-**UTL** remains bench stable for only a few days before needing to be kept in a vacuum desiccator devoid of moisture.
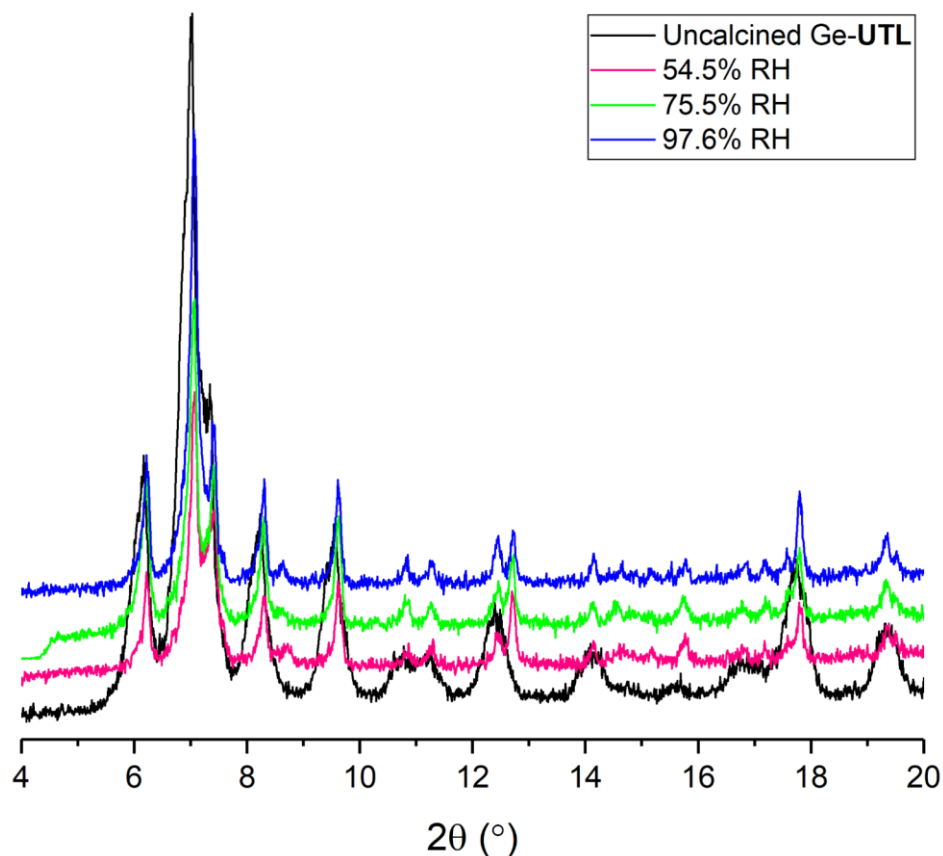
Figure 5.17. Powder X-ray diffraction patterns of uncalcined Ge-**UTL** (black) vs. calcined Ge-**UTL** after being subjected to RH at 54.5% (pink), 75.5% (green) and 97.6% (blue).

5.5.   Conclusion

Germanium-rich **UTL** was subjected to hydrolysis conditions in water as a media to understand the effects of temperature (100, 92, 85, 81, 77, and 70 °C). Solid-state kinetic models, Avrami-Erofeev and Sharp Hancock were employed and it was found that the kinetics of hydrolysis (D) is not dependent on the temperature of the reaction system and solely dependent on the presence of liquid water. The rearrangement process, however, is

directly dependent on temperature and with increasing temperature an increase in rate was observed.

Through use of the Avrami-Erofeev model, n was found to be 3 for 100 °C, 2 for all other temperatures and 1 when the silicate-rich solution is replaced with fresh water, thus confining the growth to 1, 2, and 3-dimensions when n = 1, 2, and 3, respectively. The activation energy of the rearrangement step was 70.1 kJ mol^{-1}. When no silicates are present in solution, the silicon rearranges from the silica-rich layers and may cause defect sites throughout, as such we can now conclusively say that IPC-1P is the kinetic product and IPC-2P is the thermodynamic product.

From humidity studies undertaken on Ge-**UTL** at 54.5, 75.5, and 97.6% (magnesium nitrate, sodium chloride, and potassium sulfate respectively), we can see that the calcined Ge-**UTL** breaks down after 1 week rendering it similar to that of uncalcined Ge-**UTL** and as such only remains bench stable for a few days before needing to be stored in a vacuum desiccator.

As the breakdown of **UTL** in RH (%) never reached IPC-1P (plateaued at 14.22 Å), we can say that there are two processes occurring during disassembly. First, moisture is needed to break down the bonds in the d4r. Second, liquid water is needed to fully flush out the deintercalated species and allow for the layers to come closer together.

5.6.   References

1   P. Kamakoti and T. A. Barckholtz, *J. Phys. Chem. C*, 2007, **111**, 3575–3583.

2   P. S. Wheatley, J. Čejka and R. E. Morris, *J. Vis. Exp.*, 2016,

3   P. Eliášová, M. V. Opanasenko, P. S. Wheatley, M. V. Shamzhy, M. Mazur, P. Nachtigall, W. J. Roth, R. E. Morris and J. Čejka, *Chem. Soc. Rev.*, 2015, **44**, 7177–206.

4   W. J. Roth, P. Nachtigall, R. E. Morris, P. S. Wheatley, V. R. Seymour, S. E. Ashbrook, P. Chlubná, L. Grajciar, M. Položij, A. Zukal, O. Shvets and J. Čejka, *Nat. Chem.*, 2013, **5**, 628–633.

5   M. Mazur, P. Chlubná-Eliášová, W. J. Roth and J. Čejka, *Catal. Today*, 2014, **227**, 37–44.

6   M. Shamzhy, M. Mazur, M. Opanasenko, W. J. Roth and J. Čejka, *Dalton Trans.*, 2014, **43**, 10548.

7   J. S. O. Evans, S. J. Price, H. V. Wong and D. O'Hare, *J. Am. Chem. Soc.*, 1998, **120**, 10837–10846.

8   Y. Du and D. O 'Hare, *Inorg. Chem.*, 2008, **47**, 11839-11846.

9   F. Barroso-Bujans and A. Alegria, *Phys. Chem. Chem. Phys.*, 2017, **19**, 18366–18371.

10   P. Norby, *J. Am. Chem. Soc.*, 1997, **119**, 5215–5221.

11   J. Rahbani, N. M. Khashab, D. Patra and M. Al-Ghoul, *J. Mater. Chem.*, 2012, **22**, 16361.

12   D. Saliba and M. Al-Ghoul, *Philos. Trans. A. Math. Phys. Eng. Sci.*, 2016, **374**.

13   A. Ragavan, A. Khan and D. O'Hare, *J. Mater. Chem.*, 2006, **16**, 4155–4159.

14   X. Duan and D. G. (David G. . Evans, *Layered double hydroxides*, Springer, 2005.

15   J. Čejka, R. E. Morris and P. (Petr) Nachtigall, *Zeolites in catalysis : properties and applications*, .

16   W. J. Roth, O. V. Shvets, M. Shamzhy, P. Chlubná, M. Kubů, P. Nachtigall and J. Čejka, *J. Am. Chem. Soc.*, 2011, **133**, 6130–6133.

17   S. E. Henkelis, M. Mazur, C. M. Rice, P. S. Wheatley, S. E. Ashbrook and R. E. Morris, *J. Am. Chem. Soc.*, 2019, **141**, 4453-4459.

CHAPTER 6:
PAIR DISTRIBUTION FUNCTION ANALYSIS OF ADORable ZEOLITES

6.1.   Aim

The aim of this chapter is to extrapolate information from Pair Distribution Function (PDF) analysis of both *ex situ* and *in situ* data conducted at Diamond Light Source (DLS), UK on Beamline I15, and the Advanced Photon Source (APS), IL USA on beamline 11-ID-B. Using this information, it is the hope that one can create and understand a full mechanism based on both diffuse and Bragg scattering. This analysis is run in conjunction with Chapters 4 and 5. Here we look at the process in low volume to understand the difference in material produced when in both high and low volume of hydrolysis media and perhaps more importantly, whether **UTL** hydrolyses fully to IPC-1P.

6.2.   Introduction

As the ADOR mechanism proceeds, some crystallographic order is lost as the 2-dimensional layers are formed. This makes traditional diffraction methods unsuitable for studying the process *in situ*. However, Pair Distribution Function (PDF) analysis proves to be useful in probing these disordered structures as the technique does not rely on crystallographic order.

As discussed in Chapter 3, the PDF, $G(r)$, is the distribution of density of inter-atomic distances in a given material. The PDF can be obtained directly from high energy X-ray or neutron diffraction by a Fourier transform of the scattering intensity data. The main advantage of this technique is that while traditional diffraction methods only use Bragg scattering, PDF analysis is a total scattering method that treats both the sharp Bragg peaks and the broad diffuse scattering equally, thus allowing one to probe both amorphous and crystalline materials on short- and long-range order.

Understanding the mechanisms of creation and modifications of zeolites is still not complete. This chapter will focus on the detailed insight into the mechanism of hydrolysis of germanosilicates, highlighting the great potential of *in situ* PDF analysis.

6.3.   Experimental Procedure

Parent Ge-**UTL** was prepared in accordance with the procedure shown in Chapter 4. All daughter zeolites prepared below were calcined in a stream of air at 575 °C for 7 hr with a temperature ramp of 1 °C min^{-1}.

6.3.1.   IPC-2

Ge-**UTL** (200 mg) was added to 12 M hydrochloric acid (32 mL) with stirring. The reaction mixture was hydrolysed for 18 hr at 95 °C. IPC-2P was collected by filtration, washed with water (2 x 50 mL) and dried at 70 °C for 12 hr before calcination at 575 °C.

6.3.2.   IPC-4

Ge-**UTL** (200 mg) was added to 0.1 M hydrochloric acid (32 mL) with stirring. The reaction mixture was hydrolysed for 18 hr at 95 °C. IPC-1P was collected by filtration, washed with water (2 x 50 mL) and dried at 70 °C for 12 hr before calcination at 575 °C.

6.3.3.   IPC-6 (1)

Ge-**UTL** (200 mg) was added to 1.5 M hydrochloric acid (32 mL) with stirring. The reaction mixture was hydrolysed for 18 hr at 95 °C. IPC-6P was collected by filtration, washed with water (2 x 50 mL) and dried at 70 °C for 12 hr before calcination at 575 °C.

6.3.4.   IPC-6 (2)

Ge-**UTL** (200 mg) was added to 12 M hydrochloric acid (32 mL) with stirring. The reaction mixture was hydrolysed for 4 hr at 95 °C. IPC-6P was collected by filtration, washed with water (2 x 50 mL) and dried at 70 °C for 12 hr before calcination at 575 °C.

6.3.5.   IPC-7

Ge-**UTL** (200 mg) was added to 5 M hydrochloric acid (32 mL) with stirring. The reaction mixture was hydrolysed for 18 hr at 95 °C. IPC-7P was collected by filtration, washed with water (2 x 50 mL) and dried at 70 °C for 12 hr before calcination at 575 °C.

6.3.6.   IPC-9

Ge-**UTL** (600 mg) was added to 0.1 M hydrochloric acid (96 mL) with stirring. The reaction mixture was hydrolysed for 18 hr at 95 °C. IPC-1P was collected by filtration, washed with water (2 x 50 mL) and dried at 70 °C for 12 hr.

Choline chloride (60 g) and Ambersep (120 g) were added to water (60 mL) and stirred at room temperature for 12 hr. The suspension was filtered to remove the exchange resin to afford choline-OH.

IPC-1P (415 mg) was charged to choline-OH solution (0.85 M, 20 mL) and stirred at room temperature for 6 hr. IPC-9P was recovered by filtration and washed with water (2 x 20 mL). IPC-9P was dried at 70 °C for 12 hr and calcined at 575 °C.[1]

6.3.7.   IPC-10

Ge-**UTL** (600 mg) was added to 0.1 M hydrochloric acid (96 mL) with stirring. The reaction mixture was hydrolysed for 18 hr at 95 °C. IPC-1P was collected by filtration, washed with water (2 x 50 mL) and dried at 70 °C for 12 hr.

Choline chloride (60 g) and Ambersep (120 g) were added to water (60 mL) and stirred at room temperature for 12 hr. The suspension was filtered to remove the exchange resin to afford choline-OH.

IPC-1P (415 mg) was charged to choline-OH solution (0.85 M, 20 mL) and stirred at room temperature for 6 hr. IPC-9P was recovered by filtration and washed with water (2 x 20 mL). IPC-9P was dried at 70 °C for 12 hr.

A homogenous gel of IPC-9P (125 mg), diethoxydimethyl silane (25 mg) and nitric acid (1 M, 2.5 mL) were charged to a Teflon-lined steel autoclave and heated at 175 °C for 24 hr. The solid IPC-10P was collected by filtration, washed with water (2 x 20 mL) and dried at 70 °C for 12 hr before calcination at 575 °C.[1]

6.3.8. Procedure and Set-up of Hydrolysis in a Brass Environmental Cell [2]

Water, 6 M HCl and 12 M HCl (0.5, 0.6, and 0.6 mL, respectively) were added slowly to calcined **UTL** (120, 80, and 50 mg. respectively) to make a slurry within the cell. Differing amounts of **UTL** were used for each reaction, as the level of viscosity changed dramatically when hydrochloric acid was used. Due to this, more **UTL** was needed to make a slurry within the cell for the reaction run in water. The cell was then placed in a heating mantle with three thermocouples attached. The heating mantle was set to 10 °C above the required temperature to maintain a temperature gradient over the whole cell window (50, 100, and 100 °C).

6.3.9. Procedure and Set-up of Hydrolysis in a Custom-made Flow Cell

Calcined **UTL** was packed in a Kapton (polyimide) capillary and the zeolite capped within the capillary by glass filter paper and glass wool. The capillary was then inserted into the flow cell and the protected thermocouple threaded through the right-hand-side of the capillary. The thermocouple was encapsulated by a thinner Kapton capillary and sealed with epoxy resin to avoid degradation by the hydrochloric acid. The flow cell was tightened into place

and the following flow rates used (see below) to get the hydrolysis media into the desired position within the capillary, so that time was not wasted at the beginning of the reaction but not affecting the zeolite before entry to the X-ray beam.

Flow rates:

5 rpm – 30 sec

2 rpm – 4 min

0.2 rpm – 30 sec

After each completed experiment, the flow cell was flushed through an empty capillary with water, to remove any trace of hydrochloric acid. Air was then flown through to dry the cell.

6.3.10.   PDF Processing and Refinement

Data frames were integrated using the program FIT2D.[3] The resulting *.chi* files were converted to *I(Q)* in PDFGetX2.[4] The initial known sample composition for the structure was entered in order to normalise *I(Q)*. Corrections for multiple scattering, polarization and background were applied to the data in PDFGetX2 to produce *S(Q)* and *F(Q)*. Q_{max} for the Fourier Transform was determined as 20 Å^{-1} by examination of *F(Q)* to determine the maximum distance to which it was possible to see features in the data. For all *ex situ* collected PDFs, a Lorch function was applied to smooth termination ripples.

The PDFGui[5] refinement of IPC-9 and IPC-2P were performed using *C2/m* symmetry constraints applied to atomic positions, occupancies and ADP values. ADP values were refined isotropically by element type. An r_{cut} of 3.38 Å (upper limit of Si-O-Si distance) was used as an estimate for correlated motion, due to the rigidity of the frameworks. All fits had a lower limit of 1.38 Å, peaks below here do not have any physical meaning as heavy atom contacts shorter than this are not possible for germanosilicates. Such peaks can be attributed to experimental and Fourier termination errors. Errors for PDF refinement using the PDFGui program are not outputted as the software does not propagate through the area detector uncertainties. The refinements of IPC-9 and IPC-1P were calculated using DFT models from references 1 and 7 respectively. The refinement of IPC-2P was performed using an idealised structure of –COK-14 from the IZA database (iza-online.org).

6.4. Results and Discussion

The results below show the use of both *ex situ* and *in situ* Pair Distribution Function (PDF) analysis of ADORable zeolites and the mechanism by which the hydrolysis (Disassembly) and rearrangement (Organisation) occur. Modifying the *in situ* experiments to include flow, significantly improve the quality of the results, for reasons that will be explained.

6.4.1. *Ex situ* Analysis

Each daughter zeolite currently able to be produced through the ADOR process from parent Ge-**UTL** (IPC-2, IPC-4, IPC-6, IPC-7, IPC-9 and IPC-10) were analysed by powder X-ray diffraction and Pair Distribution Function analysis in both their hydrolysed and calcined states. Data were collected at Diamond Light Source on Beamline I15 ($\lambda = 0.1722$ Å).

6.4.1.1. Layered Precursor Zeolites

The d_{200} inter-layer spacing peak produced through powder X-ray diffraction was analysed and mapped for each daughter zeolite before calcination: IPC-1P, IPC-1P with choline-OH present, IPC-6P prepared in 12 M HCl, IPC-6P, IPC-10P, IPC-2P, and IPC-7P (Figure 6.1).
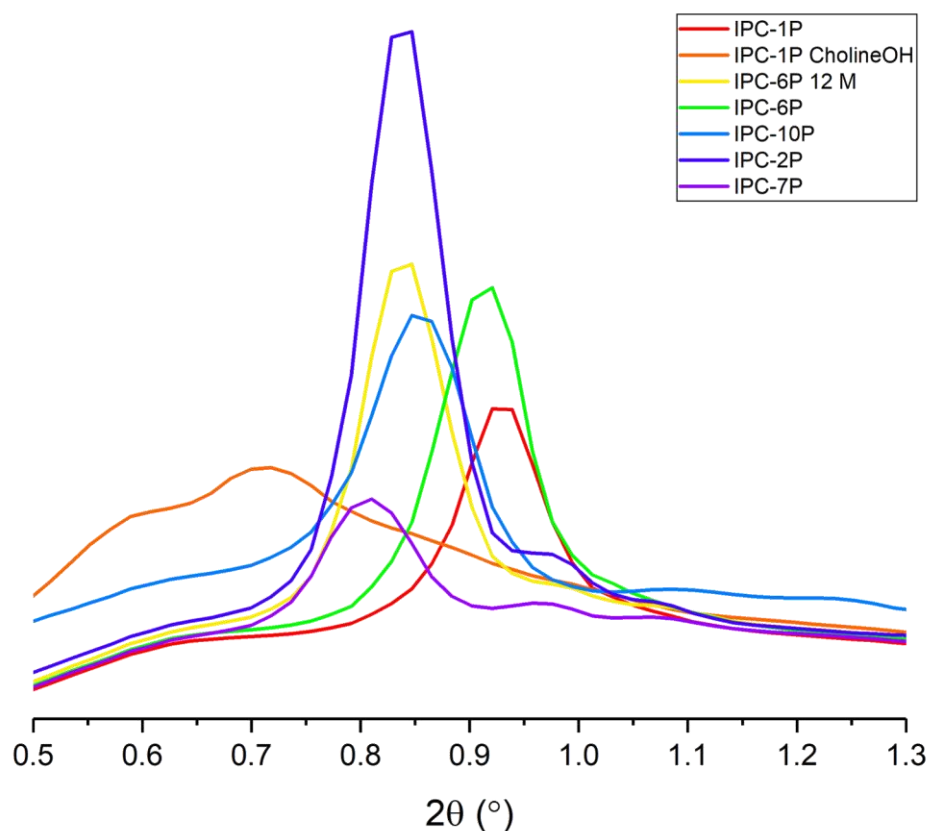
Figure 6.1. The d_{200} inter-layer peak for hydrolysed daughter zeolite precursors collected as XRD data before a Fourier transform to the PDF. Peaks shown in order of inter-layer spacing. IPC-1P – red; IPC-1P with Choline-OH – orange; IPC-6P 12 M – yellow; IPC-6P – green; IPC-10P – light blue; IPC-2P – dark blue; IPC-7P – purple. λ = 0.1722 Å. Data collected on Beamline I15, Diamond Light Source.

In Figure 6.1 the zeolites are recorded in order of increasing inter-layer spacing and the subsequent cubic unit (oxygen bridge, s4r, d4r) that will be produced upon calcination. The *d* spacing for the *200* peak for all layered zeolite precursors are relatively similar with only slight changes between them. This is because the new silicate bonds between the silica-rich layers have yet to be fully formed. However, when IPC-1P is intercalated with large structure-directing agents such as choline-OH, the PXRD shows no real *200* peak, instead shows peaks at higher *d* spacing. This is because the large organic is causing the inter-layer spacing to increase and the channels to become very disordered. As such IPC-1P with choline-OH present shows more of an amorphous nature and diffracts at a much lower intensity that the rest of the layered precursors. As PDF is typically used to probe amorphous materials, the

amorphous nature of the organic species does not affect the peak pattern of inter-atomic distances in the PDF (Figure 6.2).
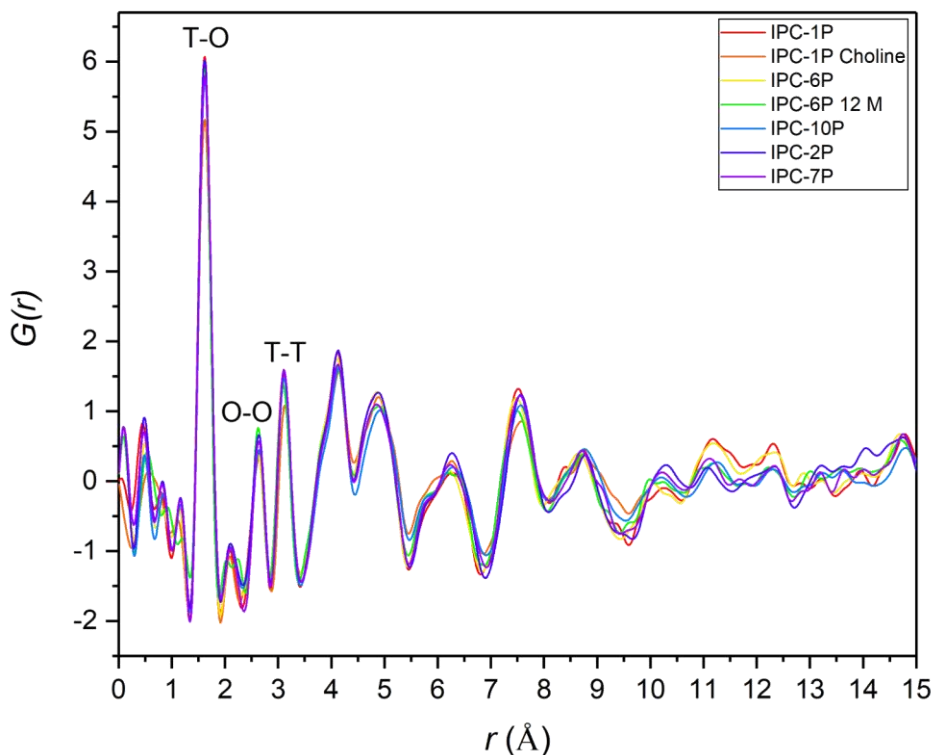

Figure 6.2. Experimental Pair Distribution Function data for *ex situ* hydrolysed daughter zeolite precursors. IPC-1P – red; IPC-1P with Choline-OH – orange; IPC-6P 12 M – yellow; IPC-6P – green; IPC-10P – light blue; IPC-2P – dark blue; IPC-7P – purple.

All layered precursors produce essentially the same PDF *G(r)*, up to 8 Å, this is expected as they all share the same primary and secondary building units. From 8 Å onwards, the PDFs begin to change slightly from one another due to increased amount of overlap between similar sized ring systems and therefore overlap between nearest neighbours. It is, therefore imperative that the precursors are calcined and examined further, to see if the change in inter-layer unit changes the outcome of the PDF.

6.4.1.2. ADORable Daughter Zeolites after Calcination

The hydrolysed zeolite precursors (IPC-1P, IPC-1P with choline-OH, IPC-9P, IPC-6P, IPC-6P in 12 M HCl, IPC-10P, IPC-2P, and IPC-7P) have now been calcined and analysed by PXRD and PDF once again. The powder patterns show a clear change in each d_{200} peak as the inter-layer region has changed upon reassembly. At higher 2θ, the inter-planar spacing between the layers is small, when compared with at low 2θ the inter-spacing is large (Figure 6.3).
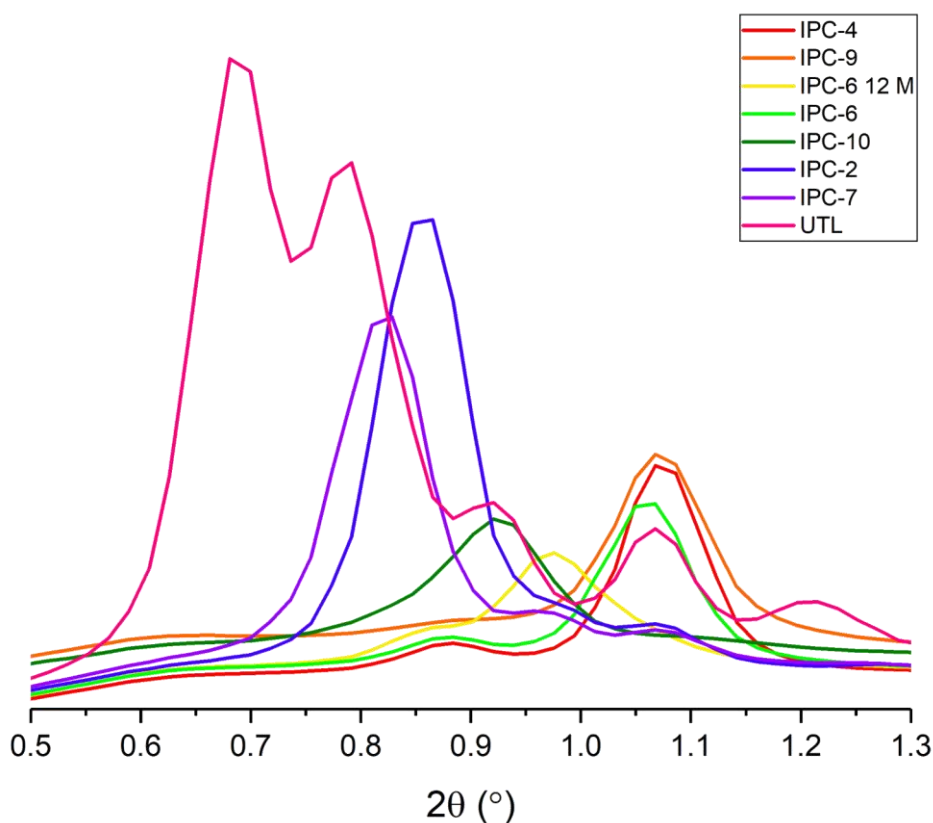

Figure 6.3. The d_{200} inter-layer peak for calcined daughter zeolites collected as XRD data before a Fourier transform to the PDF. Colour coding corresponds to the precursor zeolite in Figure 6.1. IPC-4 – red; IPC-9 with choline-OH – orange; IPC-6 12 M – yellow; IPC-6 – green; IPC-10 – light blue; IPC-2 – dark blue; IPC-7 – purple; **UTL** – pink. λ = 0.1722 Å. Data collected on Beamline I15, Diamond Light Source.

At low angle the d_{200} peak for calcined **UTL**, IPC-7, and IPC-2 (0.68, 0.82, 0.86 2θ respectively) can be seen at high intensity due to containing d4r, d4r and s4r, and s4r respectively, in-between the silica-rich layers. Whereas IPC-9, IPC-4, and IPC-6 dominate at

high angle. IPC-9 and -4 both contain direct oxygen linkages, whilst IPC-6 contains alternating s4r and direct oxygen linkages between the layers. IPC-10, although made with the same SDA as IPC-9 undergoes intercalation with diethoxydimethylsilane to form s4r units between the layers. This data then undergoes processing and a Fourier transform and as can clearly be seen, there is no real change in the PDF. This is expected as each zeolite only contains silicon and oxygen. The only changes are in the relative intensities of each peak, corresponding to the amount of electron density of each nearest neighbour inter-atomic pair distances (Figure 6.4).
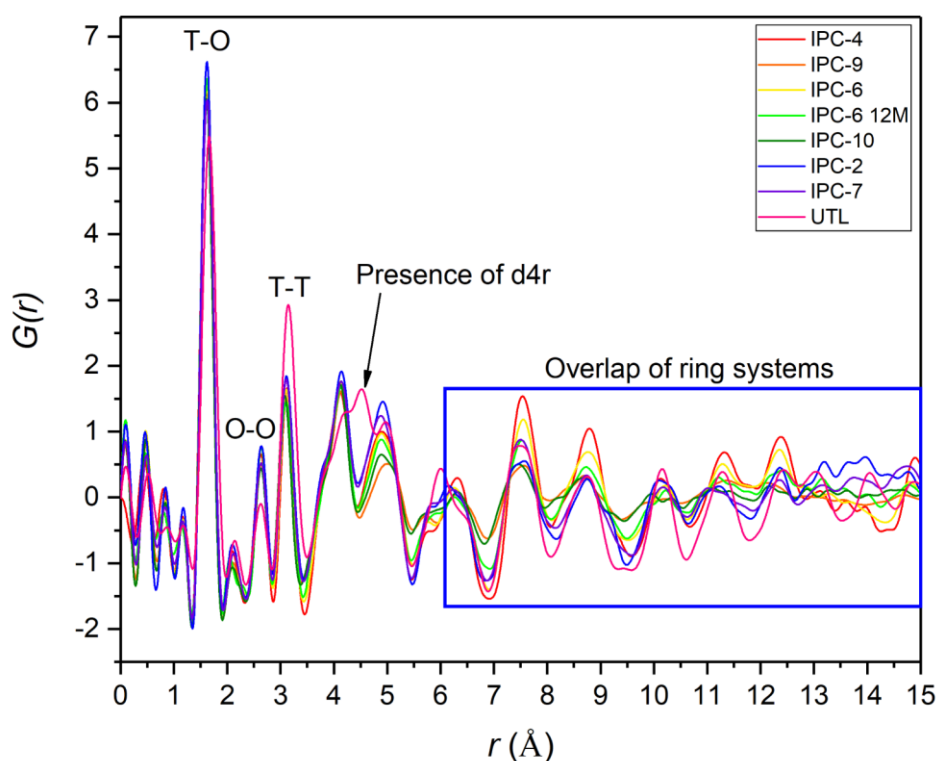

Figure 6.4. Experimental Pair Distribution Function data for *ex situ* calcined daughter zeolites. Colour coding corresponds to the precursor zeolite in Figure 6.2. IPC-4 – red; IPC-9 with choline-OH – orange; IPC-6 12 M – yellow; IPC-6 – green; IPC-10 – light blue; IPC-2 – dark blue; IPC-7 – purple; **UTL** – pink. The presence of the d4r at 4.5 shown. The overlap of ring systems highlighted by a blue box.

The extra peak at 4.5 Å in the *G(r)* for **UTL** is present due to the increased amount of d4r in the framework, when in comparison to the daughter zeolites produced. The level of disorder from ~6 Å is increased when in comparison to the hydrolysed precursors as the ring systems are now well defined and produce overlap with neighbour pair atoms.

6.4.1.2.1. Rietveld-type Refinement of IPC-9

The common question asked "why would you want to use PDF to characterise ADORable zeolites?" becomes apparent when you compare the powder X-ray diffraction patterns for both parent **UTL** and one of its daughter zeolites IPC-9 (Figure 6.5).
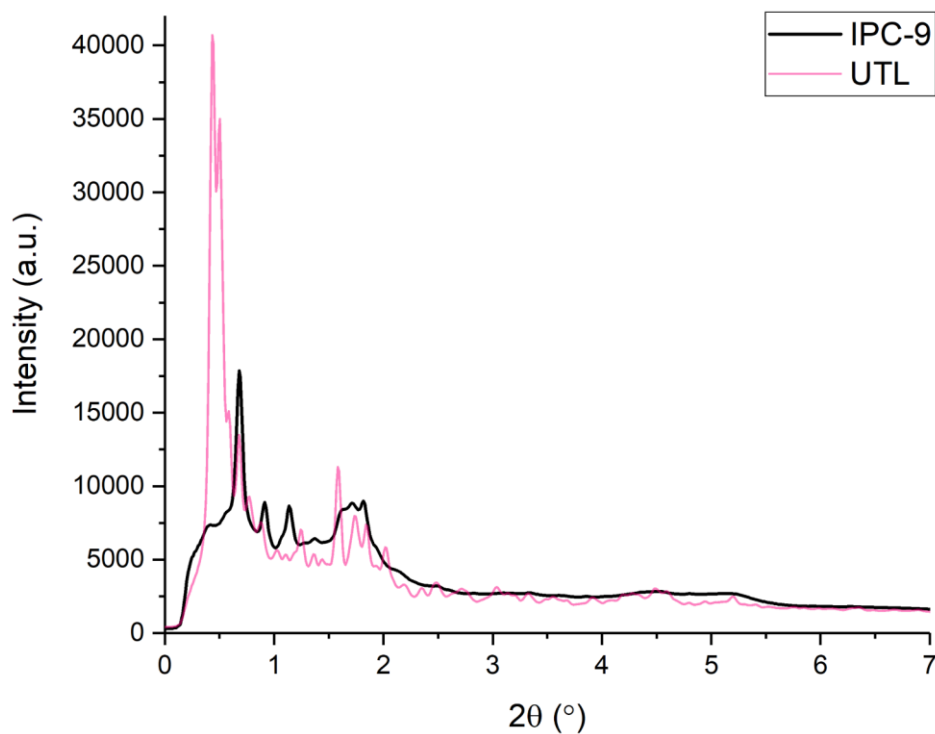

Figure 6.5. PXRD comparison of parent **UTL** (pink) vs. IPC-9 (black). λ = 0.1722 Å.

It is clear to see that the daughter zeolites contain a lot less crystallinity when in comparison to the parent zeolite, and indeed to typical silicates. This is because for the ADOR process to occur, covalent bonds have to be broken and reformed. This is especially important when thinking about IPC-9 and IPC-10. Not only do these zeolites undergo this bond breakage/reformation cycle twice, but they also undergo a layer shift causing more strain and disorder amongst the structure.
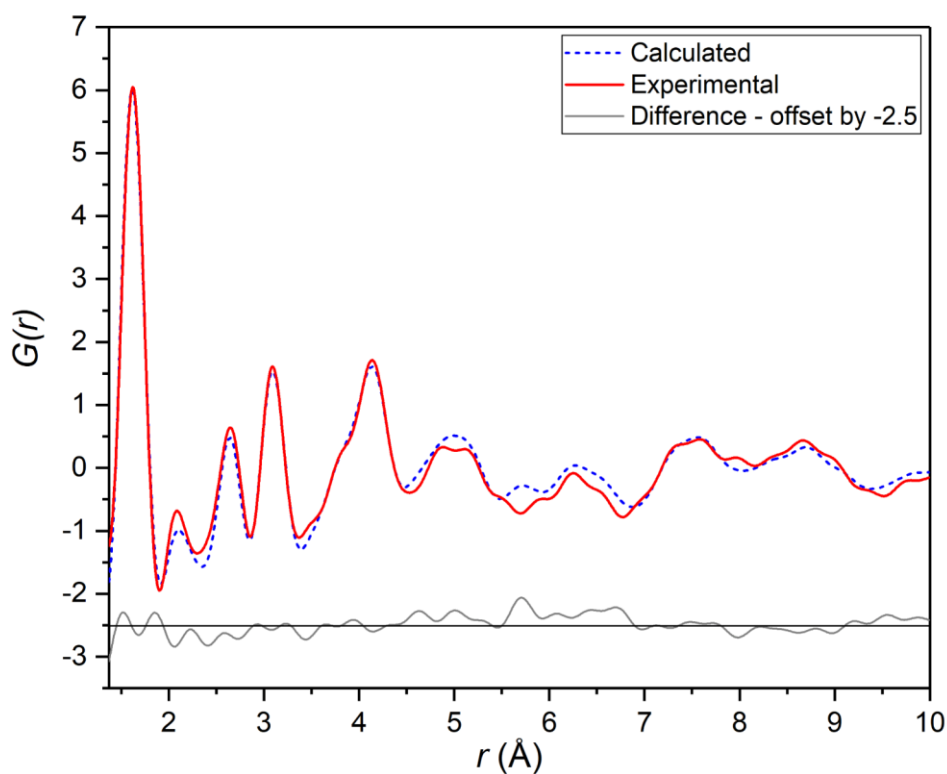
Figure 6.6. Refinement of the IPC-9 model against PDF data. R_w = 14%. The red solid line is the experimental data, the blue dashed line is the calculated PDF from the model and the grey line is the difference between the two offset by -2.5.

Due to the increased amount of diffuse scattering (or background in PXRD) the powder data was converted into a PDF by a Fourier transform. A Rietveld-type refinement of an IPC-9 model against the experimental PDF data was undertaken, and a fit of R_w = 14% achieved (Figure 6.6). The structure of IPC-9 achieved from the fit could be attained (Figure 6.7) and the unit cell compared for both calculated (see ref 1 for model used) and experimental IPC-9 (Table 6.1).[1] There is very good agreement between the calculated and experimental unit cell parameters with a difference in lengths *a*, *b*, and *c* of only ±0.21 Å. α and γ were kept constant at 90.0 ° throughout the refinement and therefore they have not changed. β has changed by 1.21 ° which is a mild discrepancy.
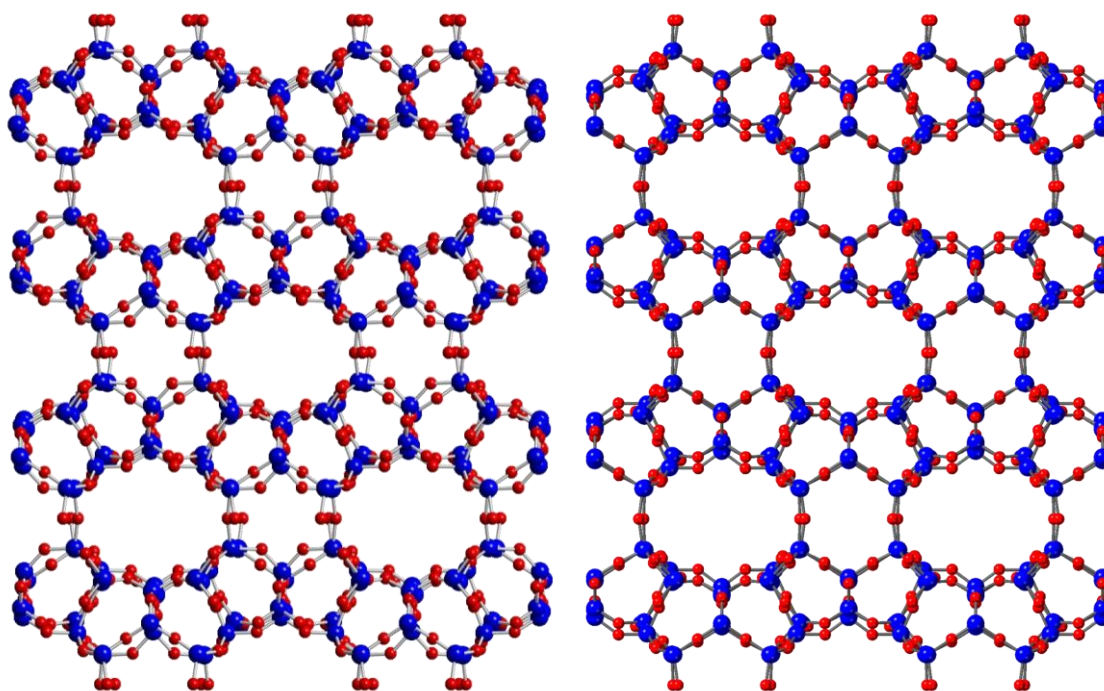
Figure 6.7. The PDF refinement of IPC-9. Calculated – LEFT; Experimental – RIGHT.[1] Si - blue, O - red.

Table 6.1. A structural comparison of calculated and experimental IPC-9, through PDF refinement.[1]

	Calculated IPC-9	**Experimental IPC-9**
Average Si-O bond length / Å	1.62	1.62
***a* / Å**	18.46(3)	18.66(9)
***b* / Å**	13.95(9)	13.89(8)
***c* / Å**	12.19(3)	12.10(2)
α / °	90.0	90.0
β / °	103.19(1)	102.40(9)
γ / °	90.0	90.0

6.4.2. *In situ* Analysis – DLS Beamline I15 [2,6]

A brass environmental cell was used to monitor the low-volume hydrolysis (Disassembly) and rearrangement (Organisation) steps in the ADOR process. The cell walls were made up of a spacer, Kapton windows, Viton and PTFE washers, a piston and a screw, which form an internal void with a diameter of 13 mm with a depth of 3 mm. The cell used could not accommodate agitation or stirring and as such the *in situ* PDF data collected may not be quantitative, but the work does reveal implicit qualitative trends that are useful in determining how the ADOR process proceeds.

6.4.2.1. Water

The Pair Distribution Function, *G(r)* was plotted for **UTL** treated in water over a time period of 8 hr at 100 °C (Figure 6.8). The initial Ge-**UTL** PDF shows broad T-O and T-T peaks due to both Si and Ge contributing to the peaks. The initial Disassembly process occurs quickly, but there is still some evidence of germanium in the materials as there are clear shoulders at longer distance on both the T-O and T-T peaks (the regions showing this best are shown in orange shades in the PDFs).
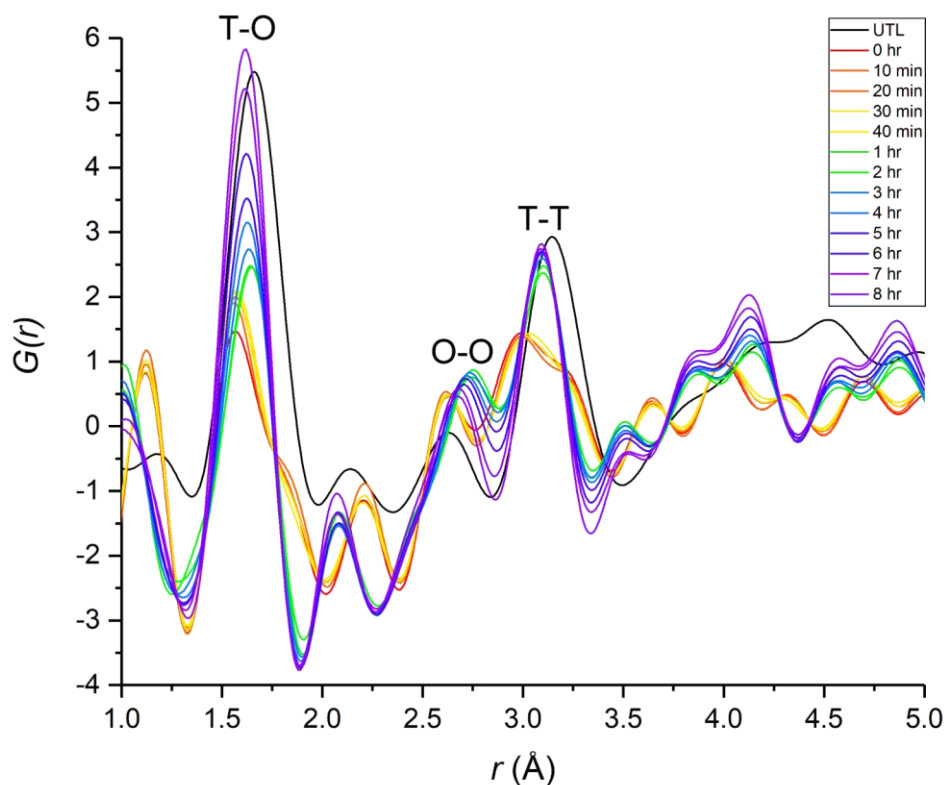
Figure 6.8. Experimental Pair Distribution Function data for the hydrolysis of **UTL** treated in water over a timeframe of 8 hr at 100 °C, with hydrolysis information shown every 10 min for the first hr and every hour thereafter.

Once all the Ge has been removed, there is only Si left contributing to the peaks. These are therefore much sharper than in the parent Ge-**UTL**. At this point the layered IPC-1P is formed and organises itself fairly quickly in to the final PDF, with peak positions that remain broadly unchanged over the remainder of the experiment (this region is shown in purple/green shades in Figure 6.8). At this stage the induction period is still ongoing and never comes to completion before data collection ends.

Over this timeframe changes in the PDF intensities can be seen, with the peak representing T-O (1.62 Å; where T = Si, Ge) distances increasing in intensity over time. This is as expected when hydrolysis occurs, T-O-T linkages are broken down, with an additional oxygen atom added over the linkage, therefore giving rise to two T-O pairs with more atoms (and therefore electrons) contributing to the scattering, and as such leads to an increase in the T-O peak in the PDF histogram. These results were confirmed through the *ex situ* studies shown in Chapter 4 and 5.

The area under the curve for the three most notable peaks, T–oxygen (T–O, 1.62 Å), oxygen–oxygen (O–O, 2.69 Å) and T–T (3.11 Å), in the PDF were plotted as a function of time (Figure 6.9). It is noteworthy to say that the peaks for each shift over time and therefore, the distances given above are an average. A significant increase in the T–O peak can be seen, corroborating with the results from the intensity of the PXRD d spacing (Chapter 4) that the germanium rich d4r have broken down by hydrolysis and the silanol groups that remain in the 2D layers are now coming closer together over time. Again, this change in area follows the same trend as both total scattering *in situ* PDF and the *ex situ* Bragg scattering data.
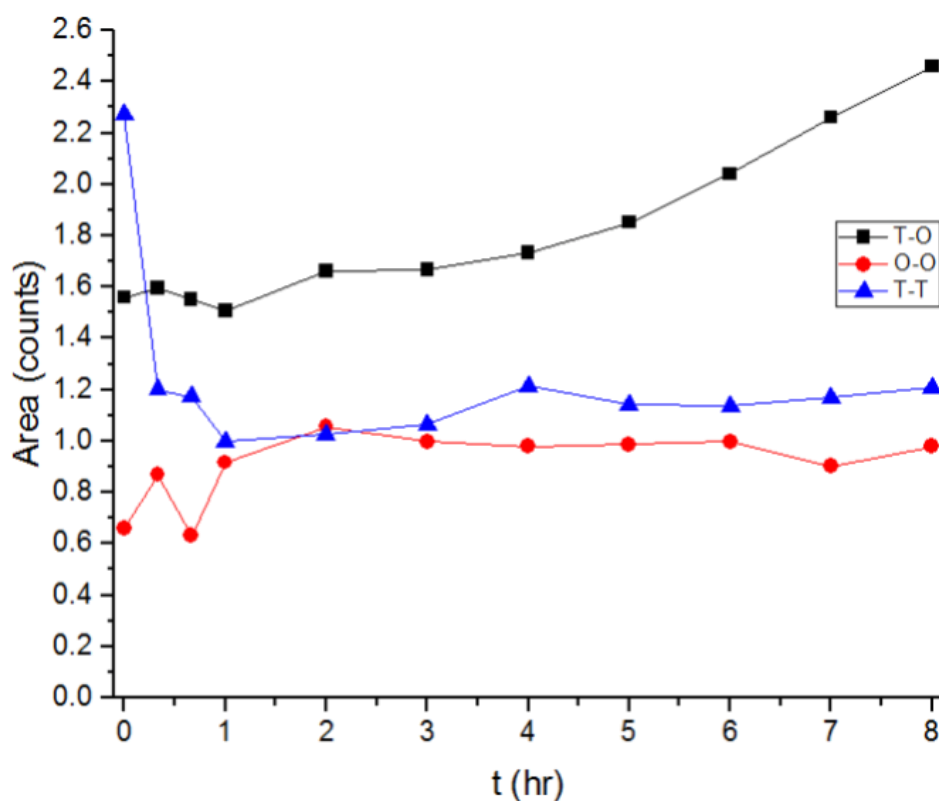

Figure 6.9. Area under the curve for **UTL** treated in water over 8 hr for peaks in the PDF that can be identified as arising from T-O, O-O, and T-T interatomic pairs.

The final *in situ* run was plotted against an existing ADORable daughter zeolite in its hydrolysed state before calcination, specifically IPC-1P (collected *ex situ*; Figure 6.10). IPC-1P is a suitable candidate for comparison as it is formed chemically through the same conditions. From the comparison we can see great similarity between each PDF with only minor discrepancies between the two.
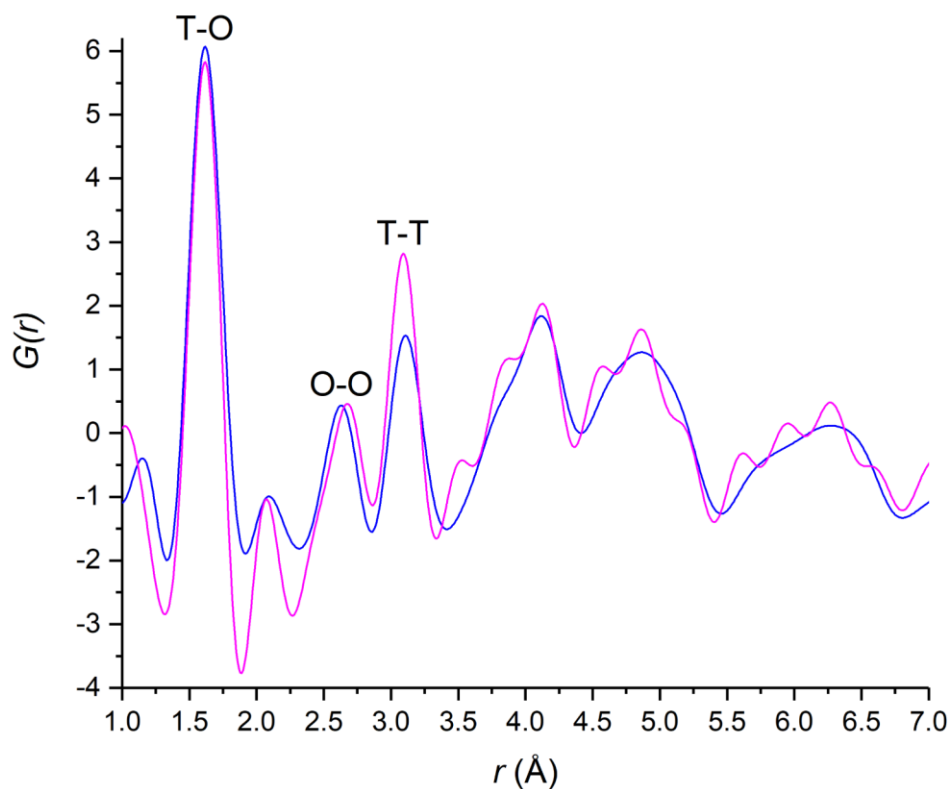
Figure 6.10. Comparison of experimentally derived PDF data for *in situ* **UTL** treated in water at 100 °C (pink) vs. *ex situ* IPC-1P that has been isolated and recovered (blue).

6.4.2.1.1. Rietveld-type Refinement of IPC-1P

To fully confirm these results, a Rietveld-type refinement of a DFT IPC-1P model (see ref 4) against the experimental PDF data was undertaken and its structure obtained (Figure 6.11 and 6.12). It is clear that IPC-1P has been formed, however due to the PDF produced *in situ*, there are free water and germanium oxide/hydroxide species (e.g. the peak at 3.47 Å) present that are not modelled and this leads to a fit with an R_w of only 38%. However, from the PXRD, experimental PDF data and the refinement it is clear that the highly disordered material IPC-1P has been afforded, and the hydrolysis of the d4r within **UTL** has been followed.

There is a level of disorder in the real structure of IPC-1P. In an ideal world (and in the IPC-1P model used)[7] the **UTL**-like layers would stack perfectly in a regular manner with an equal inter-layer spacing throughout. We know this is not the case when producing IPC-1P

through low volume conditions, the layers are not stacked in a regular array and instead some may be on an angle to others.
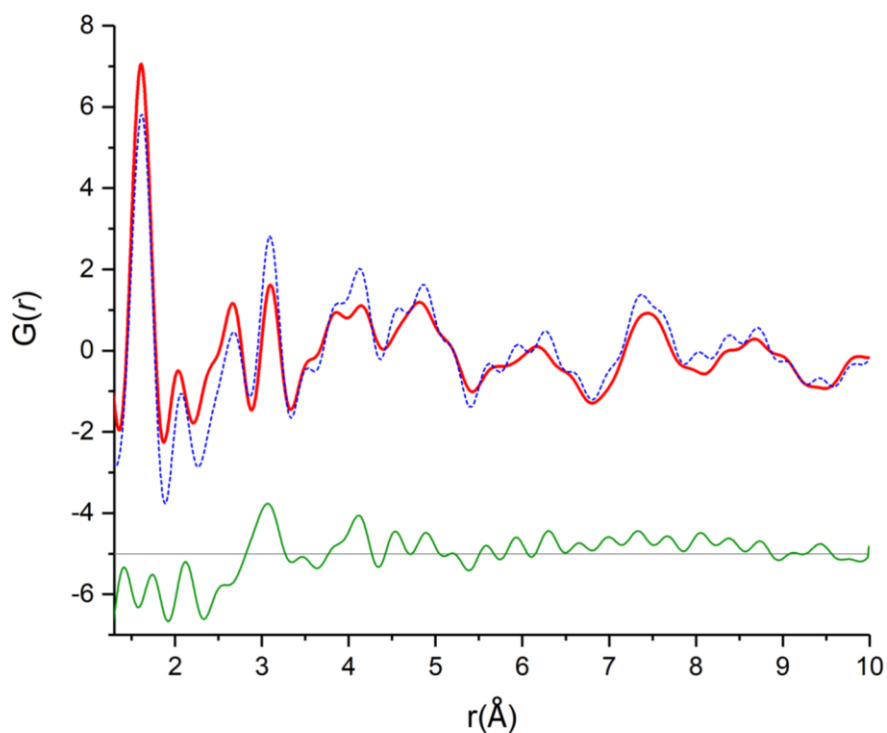

Figure 6.11. TOP: Refinement of the IPC-1P model against *in situ* PDF data. $R_w = 38\%$. The blue dashed line is experimental data, the red solid line is the calculated PDF from the model and the green line is the difference between the two, offset by -5.
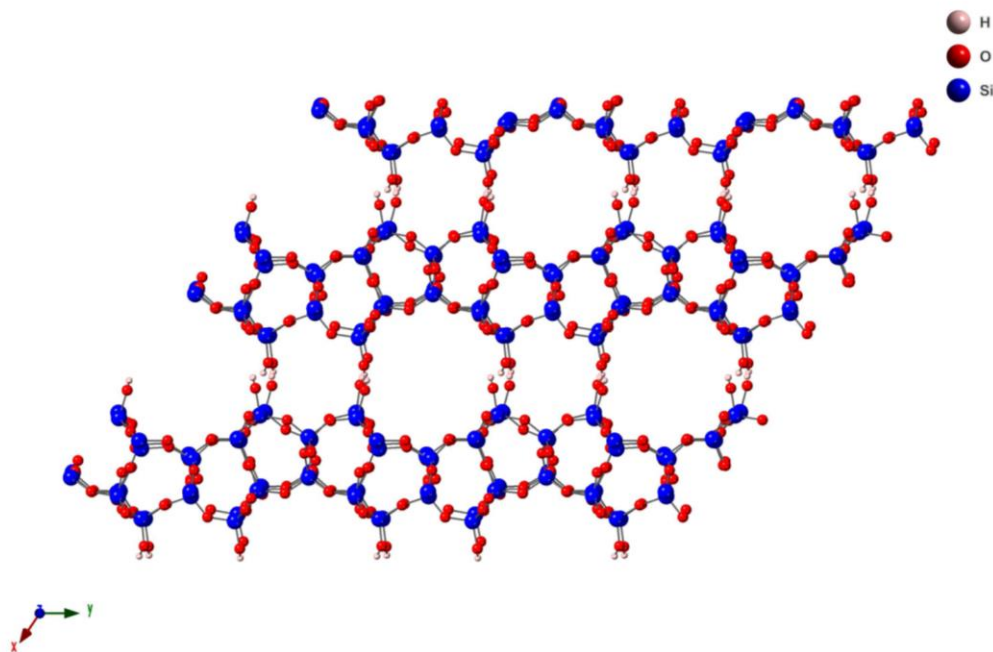
Figure 6.12. The PDF refinement of IPC-1P as viewed across the *c*-axis. Calculated – LEFT; Experimental – RIGHT.[4] Si – blue, O – red, H – pink.

A comparison of the unit cell parameters of both the experimental and calculated IPC-1P from the PDF Rietveld-type refinement show that there is good agreement between them (Table 6.2). The average bond length differs by only 1.2% from the experimental with the unit cell parameters (*a*, *b*, *c*) in agreement ±0.38 Å. Both α and γ are also in very good agreement with the experimental with a difference of ±0.46 °. β however, has refined with a 1.84 ° difference to the experimental suggesting a slight contraction in the inter-layer spacing.

Table 6.2. A structural comparison of calculated and experimental IPC-1P,[7] through PDF refinement.

	Calculated IPC-1P	Experimental IPC-1P
Average Si-O bond lengths / Å	1.61	1.63
a / Å	14.31(7)	14.45(4)
b / Å	13.90(1)	14.12(3)
c / Å	12.11(8)	12.49(6)
α / °	90.49(2)	90.02(9)
β / °	115.21(9)	117.06(0)
γ / °	120.23(4)	119.89(0)

The PDFgui software package was used for PDF refinements throughout this chapter. PDFgui does not allow constraints or restraints to be set within it. As such, bond lengths and angles are allowed to refine haphazardly. As the amount of atoms in the cell used to refine are large, it may be more useful to use a "big box" or Monte-Carlo method and successively refine until a global minima is met. This would also allow for bond restraints to be set and ultimately improve the level of fit for each refinement.

6.4.2.2. 6 M Hydrochloric Acid

The X-ray scattering data for **UTL** treated in 6 M HCl at 100 °C was processed and a Fourier transform performed to formulate the PDF over a time period of 15 hr. Owing to the fairly high HCl concentration, a peak due to a germanium-chloride (Ge-Cl) species can now be seen at 2.08 Å (Figure 6.13), together with an extra peak at ~3.5 Å, which likely corresponds to next neighbour Ge-Ge species. Such features have not been seen before in previous *ex situ* studies. The presence of a Ge-Cl peak that grows with time allows for a better insight into the mechanism of the ADOR process, specifically the hydrolysis (Disassembly) and rearrangement (Organisation) steps. It shows that the germanium is not only hydrolysed by the water content in the aqueous acid but that high [H$^+$] and [Cl$^-$] rapidly speeds up that process and plays a special role in the disassembly mechanism by attacking the d4r.

The initial hydrolysis step, which was observed in water, is now over too quickly to be measured. Little change is seen up to 8 hr, from then on both the T-O and Ge-Cl peaks increase. This fits with the *ex situ* data collected in Chapter 4, that after hydrolysis there is an induction period before the system shows intercalation of silicon species from the solution and rearrangement occurs.
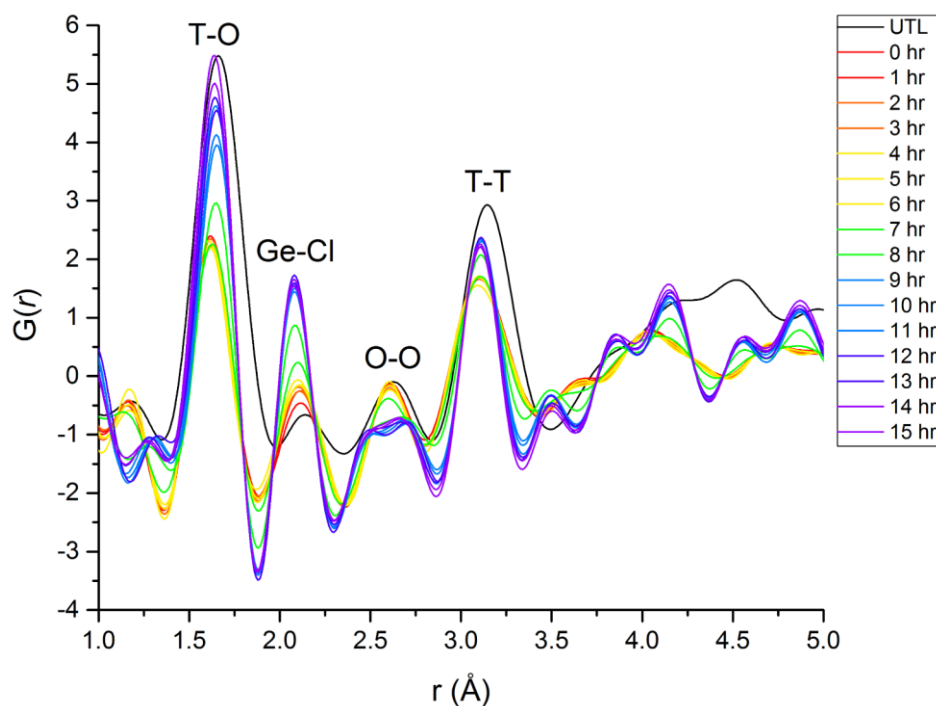
Figure 6.13. Experimental Pair Distribution Function data for the rearrangement of **UTL** treated in 6 M HCl over a timeframe of 15 hr at 100 °C vs. parent **UTL**.

This rearrangement of the layers then begins to occur after approximately 8 hr. The area under each peak were once again recorded and plotted as a function of time, the induction period up to 8 hr can be seen with the rearrangement occurring from 8 up to 15 hr (Figure 6.14).
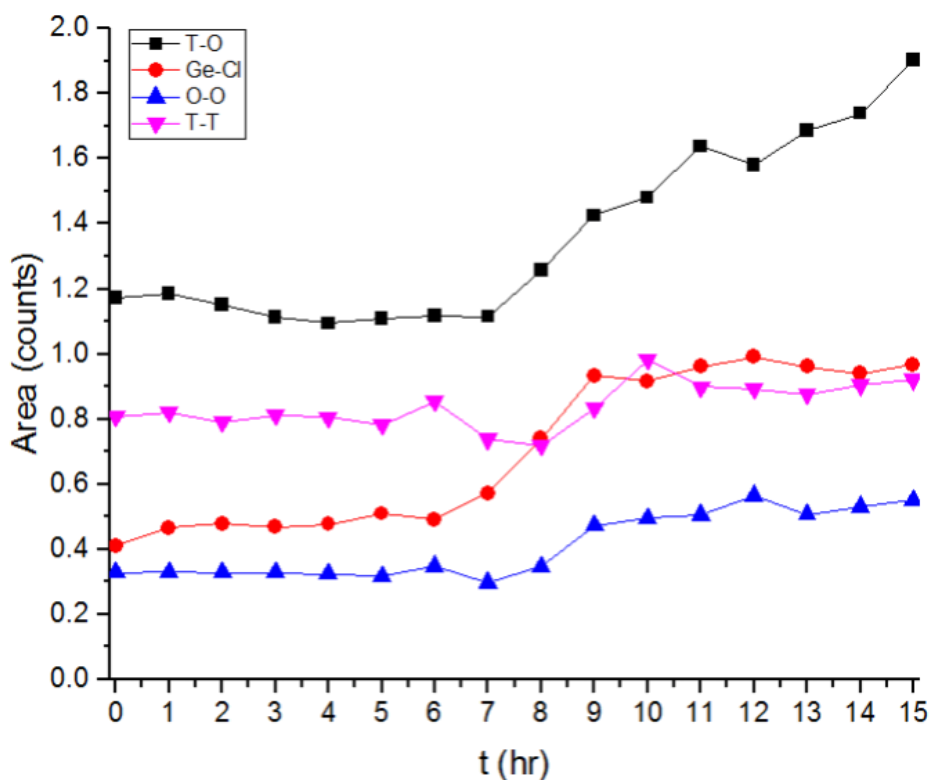
Figure 6.14. Area under the curve for **UTL** treated in 6 M HCl over 15 hr for T-O, Ge-Cl, O-O, and T-T interatomic pairs.

The final *in situ* run at 15 hr of treated **UTL** in 6 M HCl was compared with a synthetic IPC-7P (Figure 6.15). IPC-7P is made from parent zeolite **UTL**, via disassembly into IPC-1P and then rearrangement into IPC-7P. IPC-7P has some rearranged silicon in between the layers, and upon calcination would form IPC-7, containing layers of s4r and d4r. Disregarding the Ge–Cl species at 2.08 Å (ideal Ge–Cl = 2.1 Å) and the peak at about 3.5 Å which would not be present in any *ex situ* measurement of zeolites, it can be said that there are similarities between the PDFs. The T–O and T–T peaks are largely the same, however the significant change in the O–O peak tells us that IPC-7P has not been fully formed. Moreover, the rearrangement process may not have come to an end. The experiment time is limited due to drying of the system, however it can be said that with more reaction time the final product would be IPC-7P.
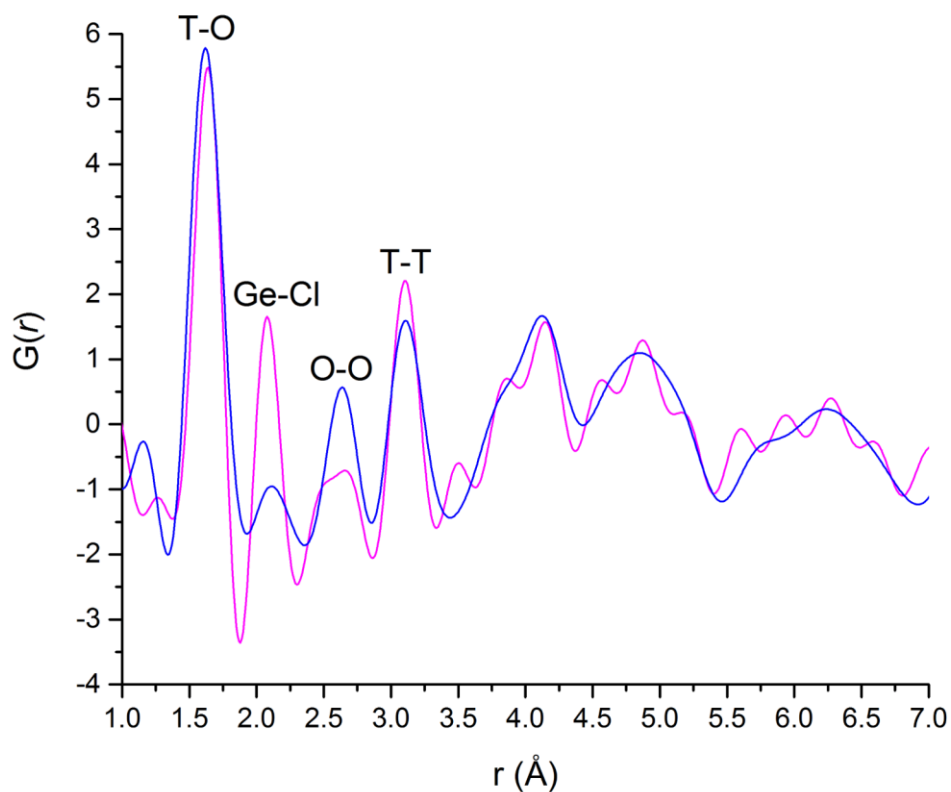
Figure 6.15. PDF comparison of *in situ* **UTL** treated in 6 M HCl at 100 °C (pink) vs. IPC-7P prepared *ex situ* (blue).

6.4.2.3.　12 M Hydrochloric Acid

Finally, a slurry of **UTL** in 12 M HCl was prepared and over 12 hr at 50 °C a clear change can be seen when the PDF is compared to parent **UTL**. Again, the hydrolysis step is missed. However, unlike 6 M HCl, the reaction seems to be almost complete and no induction period can be seen between the hydrolysis and rearrangement processes (Figures 6.16 and 6.17).
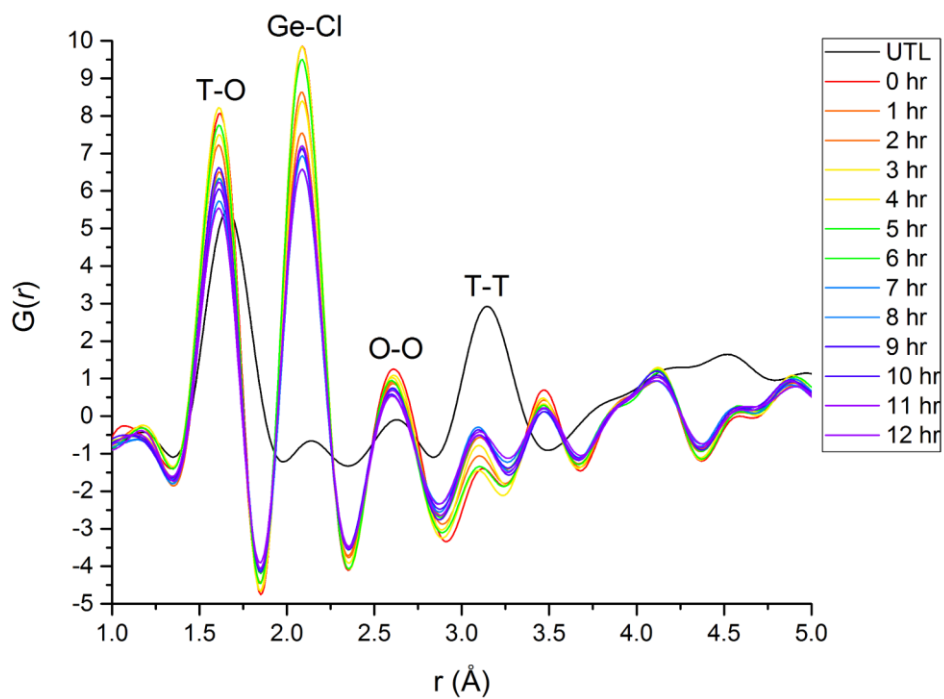
Figure 6.16. Experimental Pair Distribution Function data for the rearrangement of **UTL** treated in 12 M HCl over a timeframe of 12 hr at 50 °C vs. parent **UTL**.

Figure 6.17. Area under the curve for **UTL** treated in 12 M HCl over 12 hr for T-O, Ge-Cl, O-O, and T-T interatomic pairs.

UTL in 12 M HCl was compared against an *ex situ* collected PDF of IPC-2P which is formed through conditions of 95 °C and 12 M HCl (Figure 6.18). Again, extra peaks at 2.1 Å and 3.47 Å can be seen, due to Ge–Cl and next nearest neighbour Ge–Ge inter-nuclear distances produced from the formation of Ge-containing species during hydrolysis of the d4r.
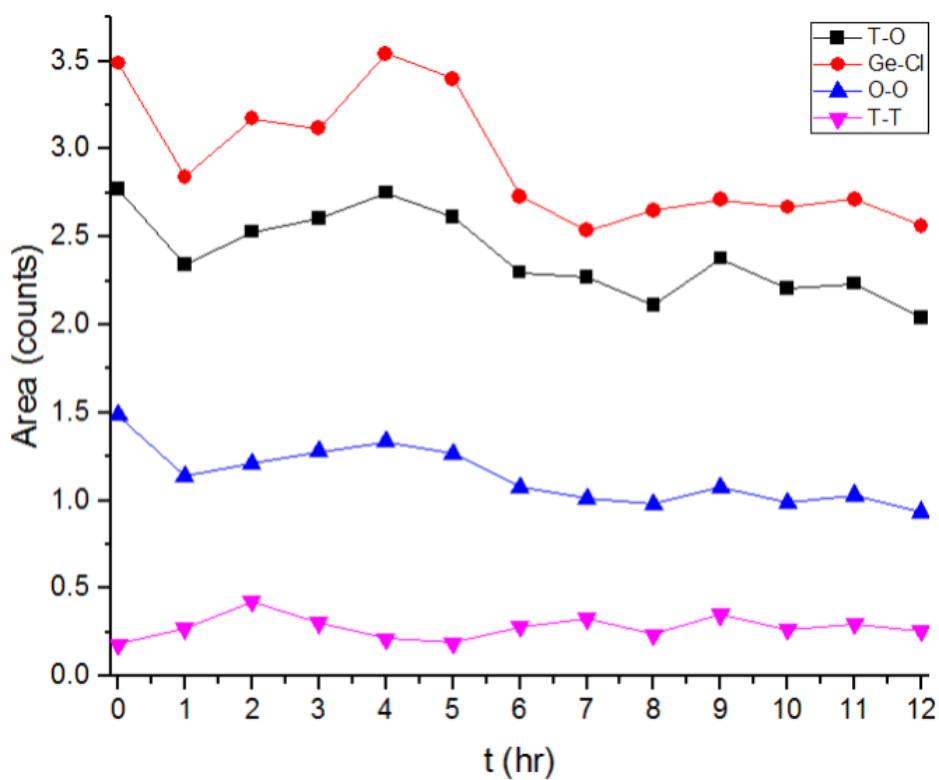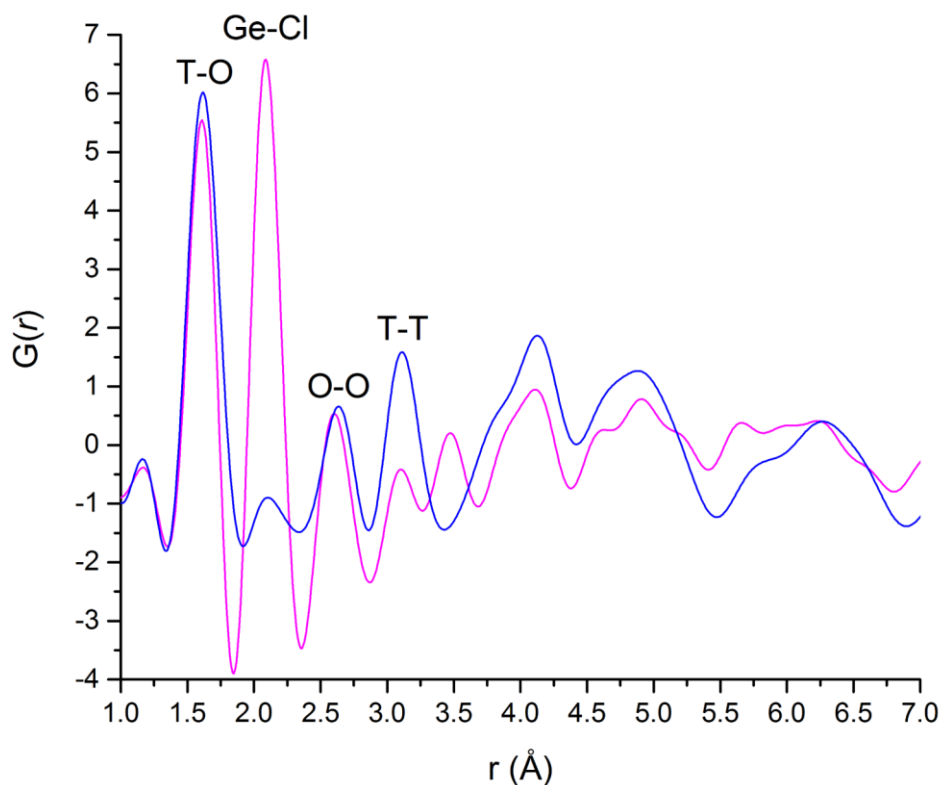

Figure 6.18. PDF comparison of *in situ* **UTL** treated in 12 M HCl at 50 °C (pink) vs. IPC-2P prepared *ex situ* (blue).

6.4.2.4. Mechanistic Conclusions

There is data in all three *in situ* PDF patterns beyond 10 Å (and even out to significantly longer distances). This agrees well with the proposed mechanism of the process discussed in Chapter 4. Because of the selective siting of the germanium atoms in the d4r units that lie between the silica-rich layers, the hydrolysis process has little or no effect on the basic structure of the layers themselves. Therefore, the ADOR process keeps the order in the 2D layers almost intact throughout the process. This is the first time this has been seen in an *in situ* experiment, and answers one of the most often asked questions about the ADOR process: could the final products be explained by a dissolution/crystallisation mechanism.

The *in situ* studies presented in this section show that the mechanism does not occur via such a route. Therefore, the fact that the process of the reaction has been followed *in situ* yields important results that are not available by other means, for example the presence of a Ge-Cl species.

While the order within the layers is retained, the inter-layer order is lost during the Disassembly step of the process, during the Organisation steps in the presence of acid some silicon species reintercalate in between the layers. Simultaneously, this orders the layers somewhat by linking them together, but at the same time also introduces further disorder as the intercalation does not happen in any ordered manner. The region beyond about 5 Å is complex, and it is particularly difficult to assign direct structural features due to the large number of similar sized ring structures causing a large amount of overlap between nearest neighbours. Future work will involve using multi-technique studies to identify the nature of the inter-layer species with more accuracy.

The three different *in situ* X-ray PDF experiments discussed in this section give some important new insights into the ADOR process. Although missing the very initial hydrolysis for two of the reactions we have, for the first time, been able to follow the process *in situ*, through use of different aqueous media (previous work using NMR and XRD only enabled certain parts of the process to be followed). The overall conclusions from this part of the study can be seen in Figure 6.19. Under low acidity conditions hydrolysis to IPC-1P occurs, with loss of Ge and Si from the system. The PDF of IPC-1P *in situ* is similar to that after isolation, which indicates that there is little change of the material on recovery and drying. This material can be calcined to form the zeolite IPC-4. In 6 M HCl, the hydrolysis produces a species that contains Ge–Cl bonds upon hydrolysis, and there is an induction period before the Organisation process occurs. The initial hydrolysis is too fast under these conditions to see. In 12 M HCl the complete process is too fast to observe using the current experimental setup, and no IPC-1P intermediate can be observed.
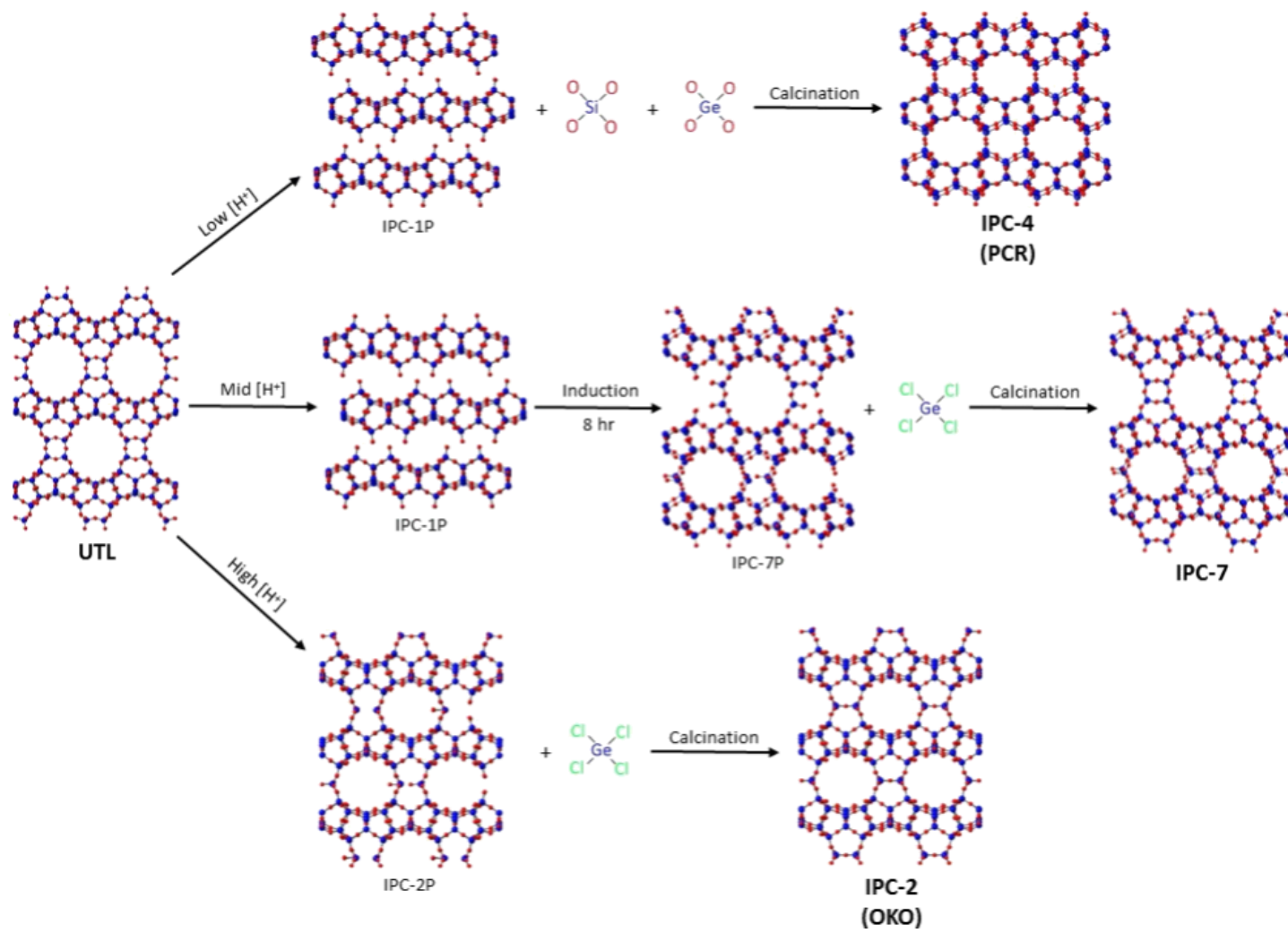
Figure 6.19. The detailed reaction scheme as shown by *in situ* Pair Distribution Function analysis conducted at the Diamond Light Source on Beamline I15.

6.4.3. *In situ* Analysis in Flow – APS Beamline 11-ID-B

Due to the lack of agitation or stirring possible when using the brass environmental cell used at the Diamond Light Source, the experimental conditions were repeated at the Advanced Photon Source, IL. Water, 6 M HCl and 12 M HCl were once again chosen as disassembly media for **UTL** at temperatures of 100, 100 °C and RT, respectively. It was decided that the reaction run in 12 M HCl would be conducted at RT rather than the 50 °C previously, in an attempt to slow down the reaction rate, and allow one to see both the Disassembly and Organisation steps.

The experiments conducted at the APS were done in flow, and as such improved not only the kinetics of reaction, but the deintercalation of germania- and silica-containing species between the layers after the breakdown of the d4r. As seen in Chapter 5, the need for vapour to first break the d4r and also the presence of liquid water to remove the deintercalated species from within the layers can be seen here. Also similarly to the results in Chapter 5, the hydrolysis media was ultimately removed from the system as the reaction proceeded, thus ultimately causing the *d* spacing to drop further than that of IPC-1P before self-rearranging.

This set-up also allowed the experiments to be conducted in high volume, similar to those shown in Chapter 4. This reduced the chances of the d4r not fully collapsing before rearrangement. Similarly to the *ex situ* XRD results in Chapter 4, all experiments afforded IPC-2P as the preferred product. The media, once flown through the capillary, was not recycled back in to the cell. This was to avoid cycling the disassembled germania/silica-species back into the layers, which would affect the Organisation step.

The hydrolysed zeolite layers remained packed in Kapton capillaries after completion of reaction and were analysed by powder X-ray diffraction once returned to the University of St Andrews (Figure 6.20). The powder patterns clearly show the presence of IPC-2P, with d_{200} inter-layer spacing at 7.44 2θ (11.86 Å).

The results presented in this section are produced from preliminary data and as such further work is necessary to fully understand what is occurring.
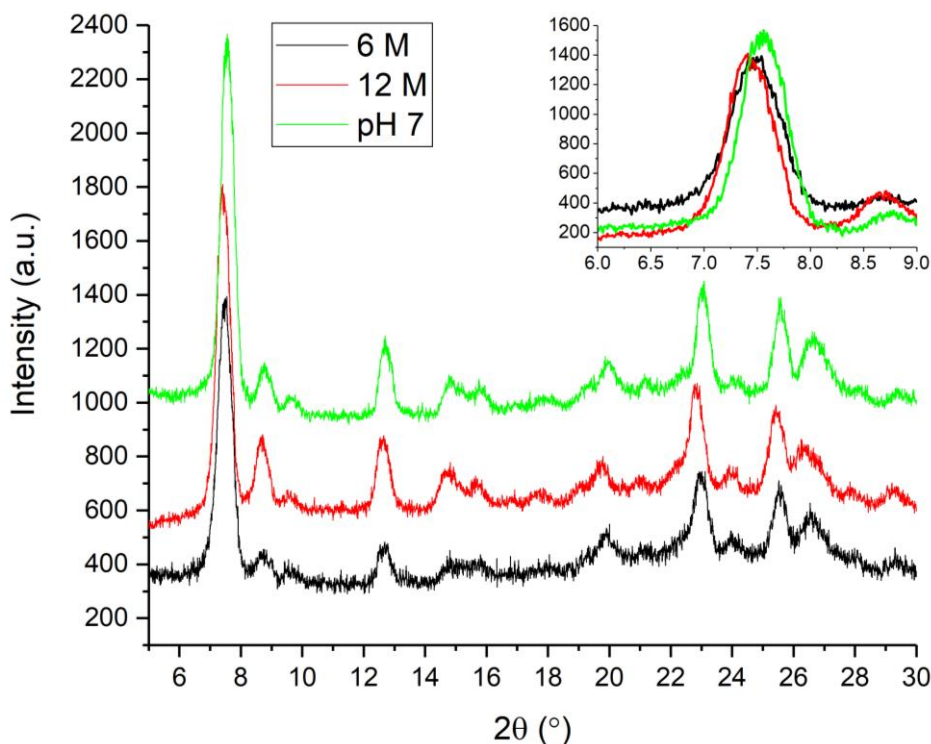
Figure 6.20. Powder X-ray diffraction patterns of **UTL** treated layered materials. Green – water/pH 7; red – 12 M HCl; black – 6 M HCl. All capillaries afforded IPC-2P.

6.4.3.1. Water

Ge-**UTL** was hydrolysed under flow conditions in water at 100 °C for 10 hr (Figure 6.21). Within approximately 1 min, hydrolysis (Disassembly) is complete, and this can be seen by a shift in the T-O (T = Ge, Si) peak from 1.67 to 1.65 Å. Double-four rings in **UTL** are typically made up of 50% Si (Si-O = 1.62 Å) and 50% Ge (Ge-O = 1.74 Å), therefore the T-O peak we see at 1.67 Å is from a mixture of both silica and germania species, and as such the shift to smaller inter-atomic distance accounts for the removal of germania-species in the d4r. This change can also be seen in the T-T (T = Si, Ge) inter-atomic pair distance peak, with a shift from 3.15 to 3.11 Å.
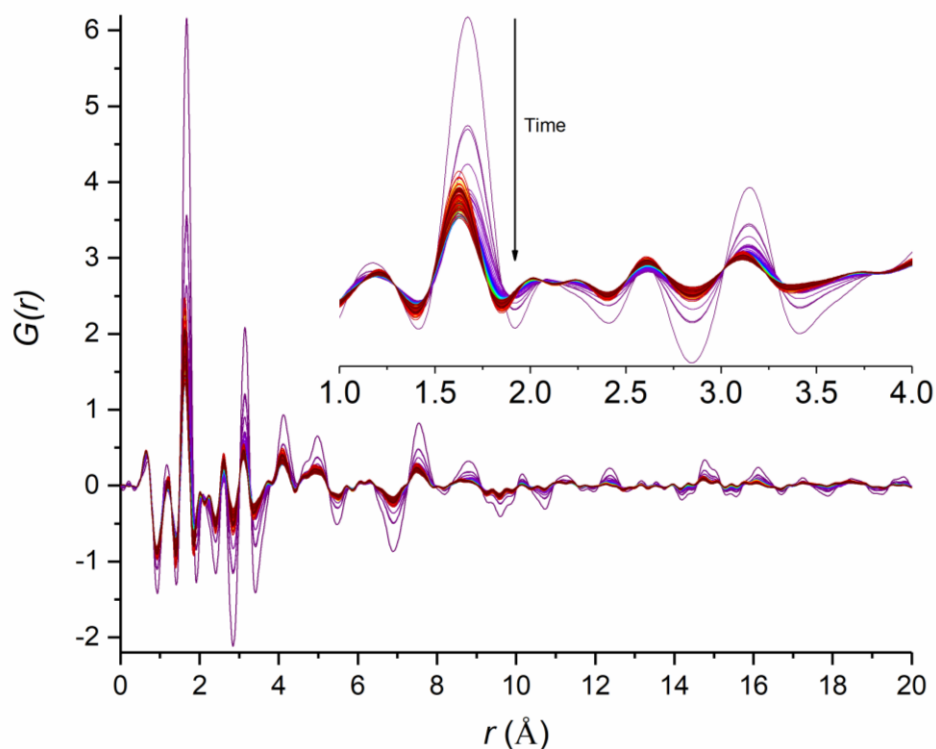
Figure 6.21. Experimental Pair Distribution Function data for the hydrolysis of **UTL** treated in water in flow over a timeframe of 10 hr at 100 °C, with hydrolysis information shown every 10 sec for the first hr and every 45 sec thereafter.

After hydrolysis has completed, an induction time of approximately 1 min can be seen. At this stage the peaks, and therefore the inter-atomic pair distances, remain stable. The T-O peak then shifts again from 1.65 to 1.62 Å, as the remaining germania left in-between the layers is flushed out with fresh water. At this stage only silicate bonds (Si-O-Si) remain. The relative intensity of the T-O and T-T peaks rapidly reduces as hydrolysis occurs, as the d4r is broken down and flushed out of the cell.

6.4.3.1.1. Rietveld-type Refinement of IPC-2P – Water

A Rietveld-type refinement of an IPC-2P model (-COK-14)[8] against *in situ* PDF data collected in water was conducted (Figure 6.22). As the material prepared through hydrolysis (IPC-2P) has not been calcined, the silicate bonds between the layers have not been fully connected, therefore the –COK-14 model (Figure 6.23) was used rather than the fully

connected **OKO**. This fit is currently ongoing and as such the refinement is not perfect and has not found its global minima. Although there are clear discrepancies between calculated and experimental, we can say that IPC-2P has been afforded. This statement is backed up by *ex situ* powder X-ray diffraction collected in-house, and the structural similarities in the unit cell parameters (Table 6.3)
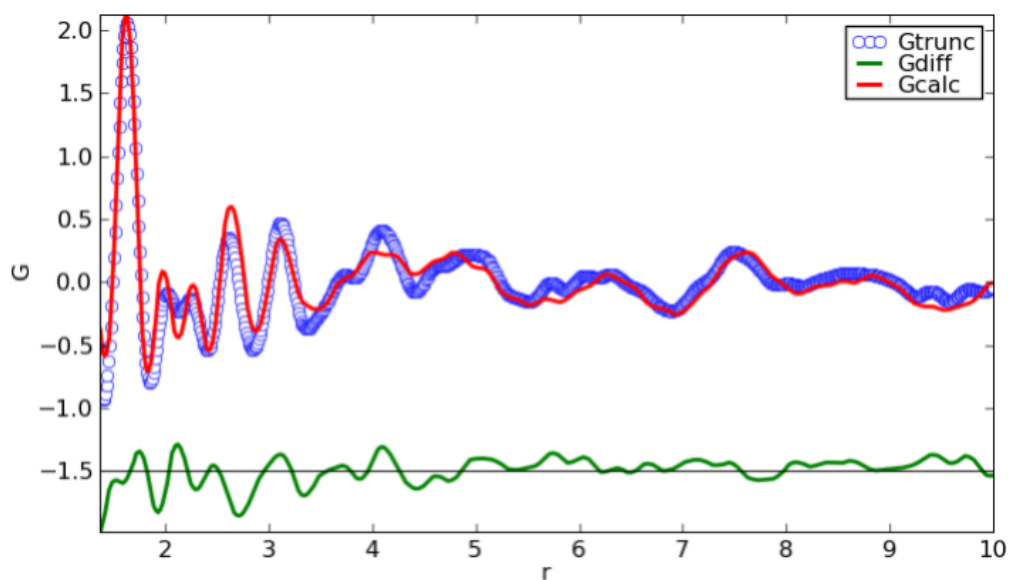
Figure 6.22. Refinement of the IPC-2P model (-COK-14) against PDF data. R_w = 31%. The blue dashed line is the experimental data, the red solid line is the calculated PDF from the model and the green line is the difference between the two offset by -1.5.
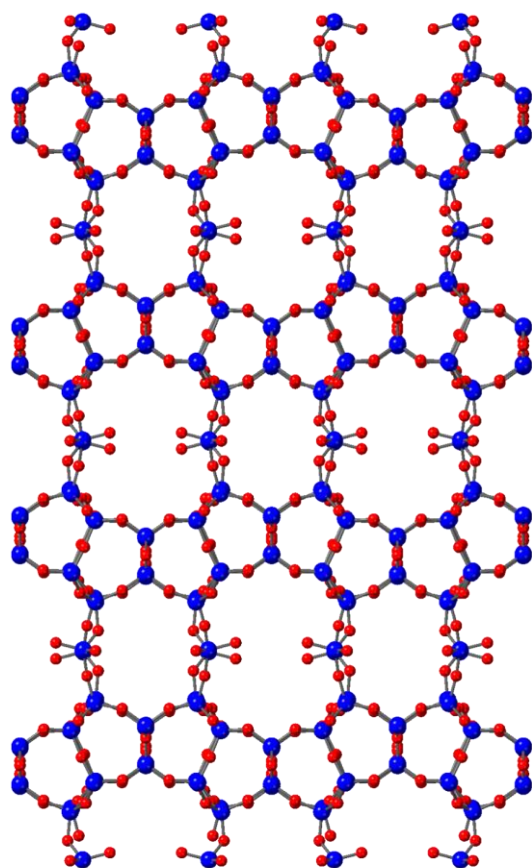
Figure 6.23. –COK-14. Si – blue; O – red.[8]

Table 6.3. A structural comparison of calculated and experimental IPC-2P,[8] through PDF refinement.

	Calculated IPC-2P	**Experimental −COK-14**
Average Si-O bond lengths / Å	1.62	1.61
a / Å	24.51(7)	24.64(0)
b / Å	14.06(6)	13.92(6)
c / Å	12.34(0)	12.25(4)
α / °	90.00	90.00
β / °	108.63(7)	109.19(6)
γ / °	90.00	90.00

6.4.3.2.   6 M Hydrochloric Acid

The hydrolysis of Ge-**UTL** treated in 6 M HCl over 10.5 hr at 100 °C occurs mechanistically similar to that of Ge-**UTL** in water. The collapse of the d4r seen over approximately 1 min before a rearrangement to IPC-2P. In this case, with hydrochloric acid used as the disassembly media, a peak at 2.1 Å can be seen, corresponding to a Ge-Cl species formed through collapse of the d4r. This peak gradually decreases in intensity over the 10.5 hr timeframe and eventually reduces to zero. This is due to fresh hydrochloric acid flushing the Ge-Cl out from between the layers (Figure 6.24). Once again IPC-2P is formed after rearrangement from IPC-1P.

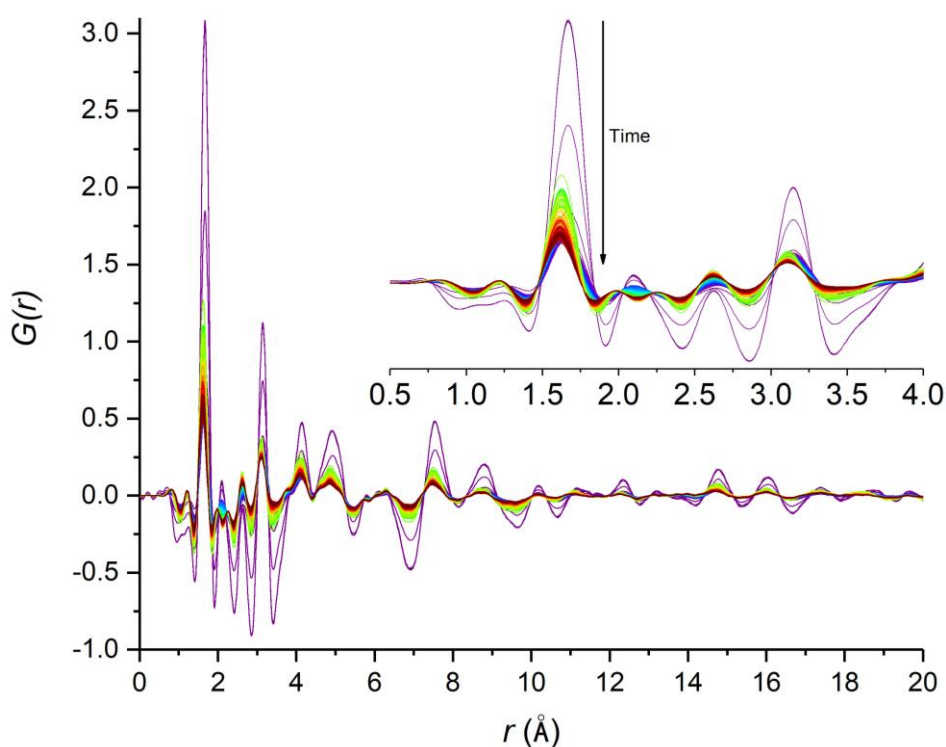**Figure 6.24.** Experimental Pair Distribution Function data for the hydrolysis of **UTL** treated in 6 M HCl in flow over a timeframe of 10.5 hr at 100 °C, with hydrolysis information shown every 10 sec for the first hr and every 45 sec thereafter.

6.4.3.3.   12 M Hydrochloric Acid

Interestingly, when Ge-**UTL** is treated in 12 M HCl, for 4 hr at room temperature (RT), the hydrolysis is much more controlled (Figure 6.25). As the kinetics and rate of reaction are slowed down, the hydrolysis takes approximately 2 hr to complete before a rearrangement to IPC-2P. Due to increased amount of hydrochloric acid in the reaction, the peak at 2.1 Å corresponding to Ge-Cl inter-atomic pair distance never fully reduces back to zero. As such, although the peak does begin to reduce, we can say that the Ge-Cl species produced from disassembly has not been fully flushed through the cell and therefore some still remains within the layers.
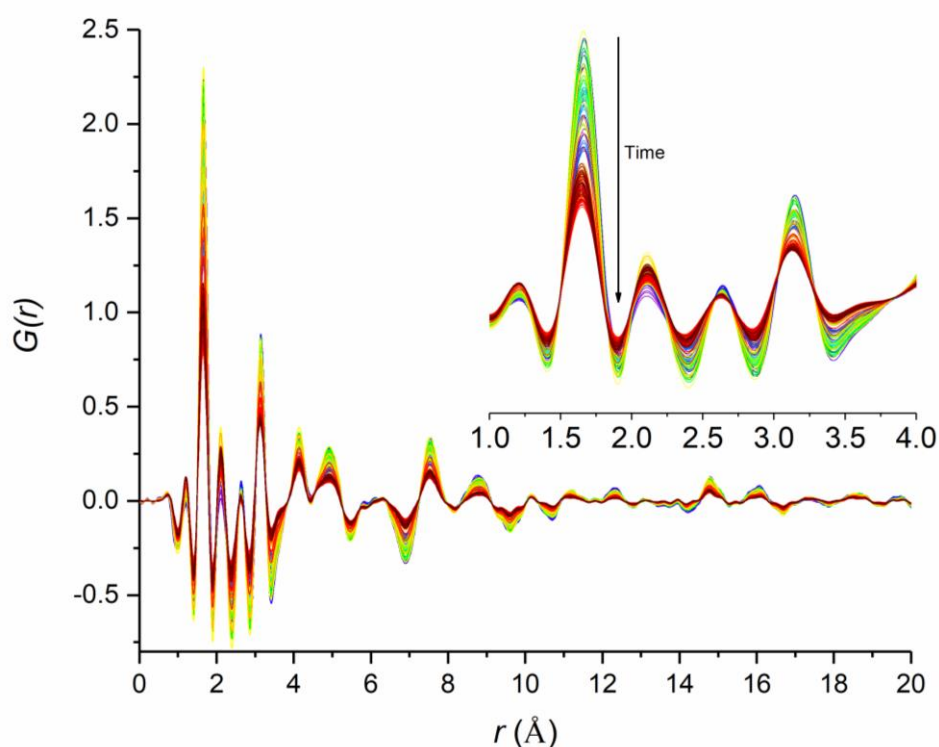
Figure 6.25. Experimental Pair Distribution Function data for the hydrolysis of **UTL** treated in 12 M HCl in flow over a timeframe of 4 hr at 100 °C, with hydrolysis information shown every 10 sec for the first hr and every 45 sec thereafter.

6.4.3.3.1. Rietveld Refinement of IPC-2 – 12 M

Ge-**UTL** treated in 12 M HCl was calcined and the PXRD recorded. Once calcined, the **OKO** (IPC-2) model [9] was refined against the Bragg data and an R_w of 7.1% observed (Figures 6.26 and 6.27). The fit shows very good agreement with the observed model, with only a slight anisotropic disagreement with the d_{200} inter-layer spacing peak.
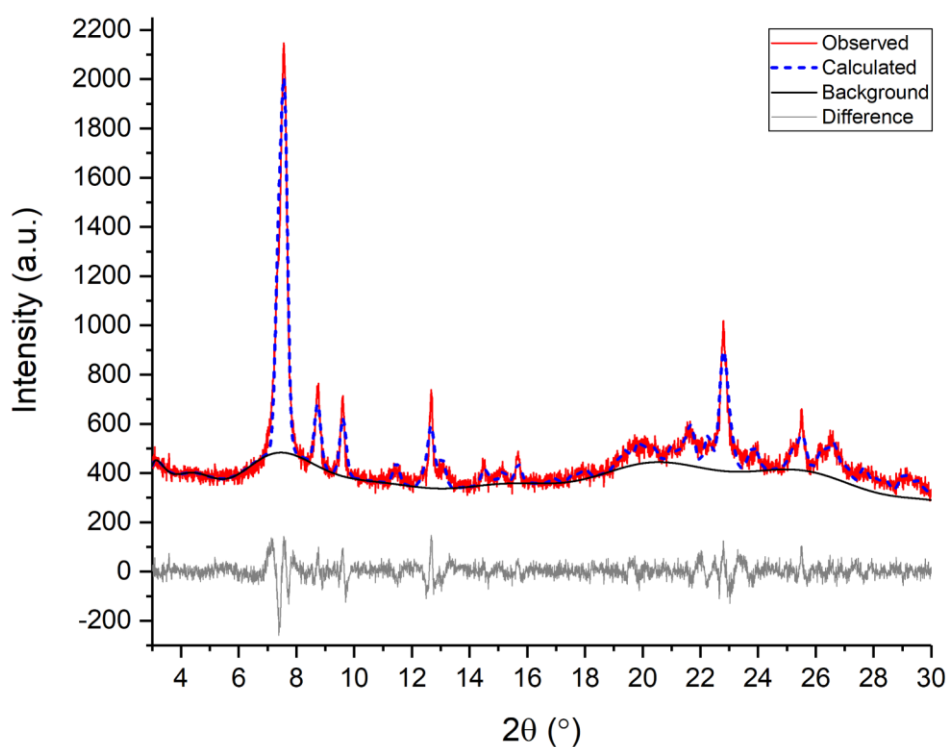
Figure 6.26. Rietveld refinement of the IPC-2 model (**OKO**) against experimental Bragg data. R_w = 7.1%. The red solid line is the experimental data, the blue dashed line is the calculated XRD from the model and the grey line is the difference between the two. λ = 1.5406 Å.

The unit cell parameters for **OKO** [9] and experimental IPC-2 were compared (Table 6.4). The parameters show very good similarity, and as such we can say that IPC-2 has been fully formed.
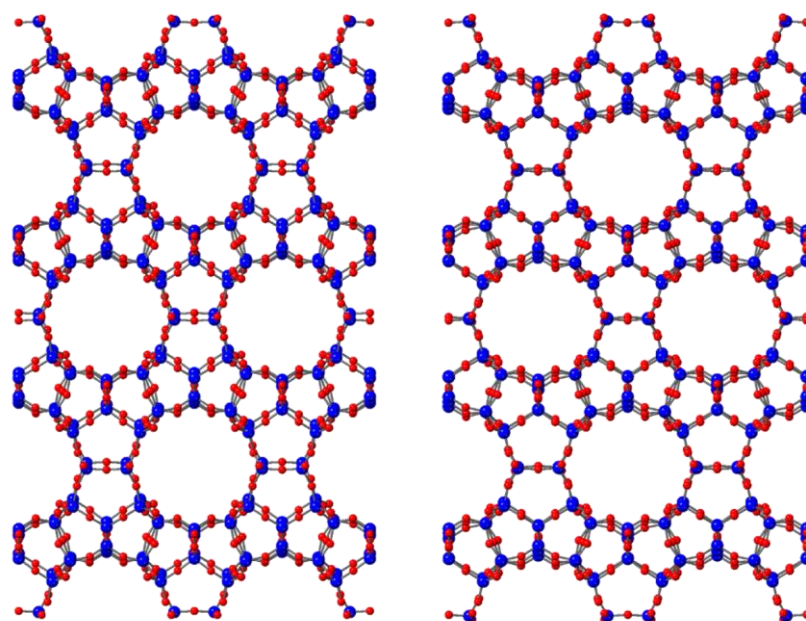
Figure 6.27. Rietveld refinement of IPC-2. Calculated – LEFT; Experimental OKO [6] – RIGHT. Si – blue. O – red.

Table 6.4. A comparison of the structural parameters between calculated and experimental IPC-2,[9] after Rietveld refinement from PXRD.

	Calculated IPC-2	Experimental OKO
Average Si-O bond lengths / Å	1.63	1.62
a / Å	24.77(0)	24.06(3)
b / Å	13.82(3)	13.83(3)
c / Å	12.39(9)	12.35(1)
α / °	90.00	90.00
β / °	108.60(0)	109.12(8)
γ / °	90.00	90.00

6.5.   Conclusion

Using Pair Distribution Function analysis allows the diffuse scattering to be treated and therefore the local order to be probed. Throughout this section, the advantage of using PDF to analyse the daughter zeolites produced through ADOR has become apparent, with the refinement of "unfeasible" IPC-9 conducted.

In situ PDF analysis conducted at the Diamond Light Source on Beamline I15, showed how the ADOR process occurred at low volume, yielding a time course for the reaction in water, 6 M HCl and 12 M HCl (see Mechanistic Conclusions; page 155). Due to lack of stirring the deintercalation process is not complete and as such causes disorder within the layers. The results produced within this section do not correlate with those shown in Chapters 4 and 5, with IPC-7P formed in 6 M HCl. These results however, do agree with the mechanism suggested, by which there is an induction period after hydrolysis and before the layers begin to self-organise. The experiment conducted in water, appeared to still be inducting at the end of the experiment. This induction period then decreased in 6 M HCl and was not present in 12 M. This again corroborates with the results in Chapters 4 and 5, suggesting that the reaction is rapid in high levels of acid. However, it is very clear from both my own work and from previous work done on the ADOR process that the final product is extremely dependent on the conditions used. For example, in Chapter 4 I showed that using liquid water as the hydrolysis medium gives a different product from water vapour – this was explained by the lack of deintercalation in the later experiment. Here, we see a similar issue, in that the conditions in the *in situ* cell (e.g. volume of liquid) give different end points for the reaction. In this case IPC-7P instead of IPC-2P. This is clearly a subtle effect.

Improving the set-up of the reaction conducted *in situ* at the Advanced Photon Source, on beamline 11-ID-B, to include flow, allowed the experimental results to be improved and provide quantitative analysis. Using a flow set-up allowed the results to be compared to large volume procedures and as such each data set (water, 6 M, and 12 M HCl) afforded IPC-2P, corroborating with the *ex situ* data shown in Chapter 4. Once again, IPC-1P is formed as the kinetic product before rearrangement to the thermodynamically stable product IPC-2P. An induction period could be seen for **UTL** treated in water and 6 M HCl. However, due to fresh media being replaced constantly this was small. Treating **UTL** in 12 M at RT allowed the kinetics to be slowed down dramatically and we were able to see the full hydrolysis to IPC-1P before self-rearrangement to IPC-2P. The difference between the static cell used at

Diamond Light Source and the flow cell used at the Advanced Photon Source is that the latter allows for the deintercalation process to occur but then the solution containing the deintercalated species is removed from contact with the zeolite. This is most similar to the situation in Chapter 5 where the liquid is removed half way through the experiment.

Although each PDF refinement shown in this chapter show good agreement with the model and did allow for a qualitative comparison, all PDF refinements showed structural disorder and due to the lack of restraints available in the PDFgui software package, atoms were allowed to refine haphazardly. Therefore, the data will be refined using the Monte-Carlo method, in a hope that the disorder can also be modelled and quantified.

6.6. References

1   M. Mazur, P. S. Wheatley, M. Navarro, W. J. Roth, M. Položij, A. Mayoral, P. Eliášová, P. Nachtigall, J. Čejka and R. E. Morris, *Nat. Chem.*, 2015, **8**, 58–62.

2   G. Sankar and W. Bras, *Catal. Today*, 2009, **145**, 195-203

3   X. Qiu, J. W. Thompson and S. J. L. Billinge, *J. Appl. Crystallogr.*, 2004, **37**, 678.

4   A. P. Hammersley, S. O. Svensson, M. Hanfland, A. N. Fitch and D. Hausermann, *High Press. Res.*, 1996, **14**, 235–248.

5   C. L. Farrow, P. Juhas, J. W. Liu, D. Bryndin, E. S. Božin, J. Bloch, T. Proffen and S. J. L. Billinge, *J. Phys. Condens. Matter*, 2007, **19**, 335219.

6   S. E. Henkelis, S. A. Morris, M. Mazur, P. S. Wheatley, L. N. McHugh and R. E. Morris, *J. Mater. Chem. A*, 2018, **6**, 17011-17018.

7   S. A. Morris, P. S. Wheatley, M. Polozij, P. Nachtigall, P. Eliasova, J. Cejka, T. C. Lucas, J. A. Hriljac, A. B. Pinar, and R. E. Morris, *Dalton Trans.*, 2016, **45**, 14124

8   E. Verheyen, L. Joos, K. Van Havebergh, E. Breynaert, N. Kasian, E. Gobechiya, K. Houthoofd, C. Martineau, M. Hinterstein, F. Taulelle, V. Van Speybroeck, M. Waroquier, S. Bals, G. Van Tendeloo, C. E. A. Kirschhock, J. A. and Martens, *Nature Mater.*, 2012, **11**, 1059-1064.

9   W. J. Roth, P. Nachtigall, R. E. Morris, P. S. Wheatley, V. R. Seymour, S. E. Ashbrook, P. Chlubná, L. Grajciar, M. Položij, A. Zukal, O. Shvets and J. Čejka, *Nat. Chem.*, 2013, **5**, 628–633.

CHAPTER 7: TUNING THE SYNTHESIS OF METAL-ORGANIC FRAMEWORKS

7.1. Aim

The aim of this chapter is to understand the effects of the concentration of base, solvent and temperature on the experimental procedure for CPO-27. Understanding the effects of these conditions allows one to refine and tune the synthesis to afford the MOF with the desired properties, such as size, shape and quantity of crystallite, whilst getting consistent crystallisation of the target material, minimising potential impurity phases.

7.2. Introduction

Coordination polymers and Metal-Organic frameworks (MOFs) are currently of much interest as gas storage and release materials.[1,2] One series that has received particular attention is the CPO-27-M (Coordination Polymer of Oslo; M = Mg,[3] Mn,[4] Fe,[5] Co,[6] Ni,[7] Cu[8] or Zn[9]) family of materials, due to their high stability to solvent loss, comparatively large pore sizes, and ability to maintain structural integrity upon removal of coordinated solvent molecules. The desolvation of this family of compounds generates metal centres with vacant coordination sites, onto which gas adsorbents such as NO,[10] CO,[11] CO_2,[12] H_2S,[13] H_2[7] and C_2H_2 can bind.[14]

The excellent gas adsorption and gas storage properties of CPO-27 MOFs, have led to a rise in interest in the details of their synthesis. For example, it is known that, under solvothermal conditions, increasing the pH of the CPO-27-M (M = Mg or Mn) reaction mixture affords a separate, non-porous coordination framework of composition $M(H_2dhtp)(H_2O)_2$ (M = Mg or Mn) that the authors designate as CPO-26-M.[3,15]

Typical CPO-27 is produced under solvothermal conditions using high pressure and temperature. However, recent developments have been made to the synthesis to reduce the

temperature and scale up the reaction in aqueous conditions. Maspoch and co-workers have created an ideal molar ratio of 1 : 2 : 4 : 304 for the H_4dhtp linker : metal salt : base : solvent and as such as-synthesised materials assume a molecular formula of $[M_2(C_8H_2O_6)(H_2O)_2]\cdot 8H_2O$ (M = Co, Mg, Ni, Zn).[16]

Although polycrystalline materials are desirable for gas adsorption techniques due to their large surface area, single crystal X-ray analysis is of great interest in order to locate cation-anion bonding sites in the structure and monitor how these change with different synthesis conditions. It is most useful to track certain gas soprtion processes in detail. Single crystal analysis has been elusive for many materials from this family of MOFs. Three crystal structures produced through single crystal X-ray analysis are currently recorded in the Cambridge Structure Database (CSD), including CPO-27-Zn,[9] -Mg[3] and -Co[17]. CPO-27-Cu,[2] -Mn,[2] -Fe[18] and –Ni have been structurally characterised by neutron (Cu and Mn) and X-ray (Fe and Ni) powder diffraction. Each of these materials are synthesised with either added liquid water not pertaining to the hydrated salt (CPO-27-Zn, -Co, -Mg, -Mn and –Ni) or base (CPO-27-Mg, and –Cu).

7.3.   Experimental Procedure

All reagents were obtained from commercial sources and were used without further purification.

7.3.1. $Mg(H_2dhtp)(H_2O)_5\cdot H_2O$

A solution of $Mg(NO_3)_2\cdot 6H_2O$ (11.4 g, 44.4 mmol) in water (49 mL) and ethanol (24 mL) was added dropwise to a stirred solution of 2,5-dihydroxyterephthalic acid (3.83 g, 19.3 mmol) in aqueous sodium hydroxide (0.5 M, 77.4 mL, 38.7 mmol) over a period of 4 min. The resulting solution was heated to reflux for 24 hr. The solution was cooled to room temperature and an initial yellow solid collected via filtration, washed with hot ethanol and allowed to dry overnight yielding a yellow powder (CPO-27-Mg, 0.846 g, 2.0 mmol, 10%). The brown mother liquor was allowed to stand at room temperature for a further 3 days, over which time brown crystals (4.145 g, 12.6 mmol, 65%) formed as the solvent slowly evaporated. Elemental analysis calcd. for $C_8H_{16}MgO_{12}$ C: 29.24, H: 4.91, found C: 29.30, H: 4.95%.

7.3.2. Typical CPO-27-M Synthesis at Low Temperature

Zinc acetate dihydrate (1.11 g, 5.00 mmol) was dissolved in methanol (12.3 mL, 304 mmol) with vigorous stirring at 0 °C (referred to as solution A). 2,5-dihydroxyterephthalic acid (0.50 g, 2.50 mmol) was dissolved in sodium hydroxide (1 M, 10.0 mL, 10.0 mmol) and cooled to 0 °C (referred to as solution B). Solution B was then added dropwise over a period of 5 min and the resulting mixture allowed to stir for 6 hr, with a sample taken after 3 hr. The precipitate was collected via filtration, washed with water (3 x 100 mL) and allowed to dry in air overnight to yield a yellow solid (Table 7.1)

Table 7.1. Synthesis conditions for the formation of CPO-27-M (M = Co, Mg, Ni, Zn).

Sample	Composition of solution A		Solution B		
	Metal Salt (g)	Solvent (mL)	Base (mL)	Temperature (°C)	Yield (%)
CPO-27-Co(1)	$Co(OAc)_2 \cdot 4H_2O$, 1.25	MeOH, 17.7	1 M NaOH, 10	78, 25, 0	80, 71, 70
CPO-27-Mg(1)	$Mg(NO_3)_2 \cdot 6H_2O$, 1.28	MeOH, 17.7	1 M NaOH, 10	78, 25, 0, -20	59, 58, 47, 27
CPO-27-Ni(1)	$Ni(OAc)_2 \cdot 4H_2O$, 1.24	MeOH, 17.7	1 M NaOH, 10	78, 25, 0	86, 70, 72
CPO-27-Zn(1)	$Zn(OAc)_2 \cdot 2H_2O$, 1.11	MeOH, 17.7	1 M NaOH, 10	78, 25, 0, -20, -40, -78	60, 58, 42, 39, 39, 15
CPO-27-Zn(2)	$Zn(OAc)_2 \cdot 2H_2O$, 1.11	MeOH, 17.7	TEA + H_2O, 2.15 + 2	78, 25, 0, -20, -40, -78	62, 60, 56, 21, 16, 36
CPO-27-Zn(3)	$Zn(OAc)_2 \cdot 2H_2O$, 1.11	MeOH, 17.7	H_2O, 10	78, 25, 0	75, 72, 72
CPO-27-Zn(4)	$Zn(OAc)_2 \cdot 2H_2O$, 1.11	THF, 12.3	H_2O, 10	78, 25, 0	70, 26, 20
CPO-27-Zn(5)	$Zn(OAc)_2 \cdot 2H_2O$, 1.11	THF, 12.3	1 M NaOH, 10	78, 25, 0, -20, -40, -78	45, 45, 47, 23, 32, 18
CPO-27-Zn(6)	$Zn(OAc)_2 \cdot 2H_2O$, 1.11	THF, 12.3	TEA + H_2O, 2.15 + 2	78, 25, 0, -20, -40	33, 50, 67, 48, 20

7.3.3. Synthesis conditions for Single Crystal

7.3.3.1. UTSA-74

Zinc acetate monohydrate (1.11 g, 5 mmol) and benzoic acid (1.22 g, 10 mmol) were dissolved in *n*-butanol (13.9 mL, 152 mmol) (referred to as Solution A). 2,5-dihydroxyterephthalic acid (0.5 g, 2.5 mmol) was dissolved in DMF (11.7 mL, 152 mmol) with stirring (referred to as Solution B). Solution B was slowly added to Solution A in a Teflon-lined steel autoclave and allowed to react at 150 °C for 48 hr. The crystals were collected by filtration, washed with *n*-butanol (3 x 50 mL) and dried in air to afford UTSA-74 as large gold hexagonal rods.

7.3.3.2. CPO-27-Zn

Zinc acetate monohydrate (1.11 g, 5 mmol) and salicylic acid (1.22 g, 10 mmol) were dissolved in ethanol (8.87 mL, 152 mmol) (referred to as Solution A). 2,5-dihydroxyterephthalic acid (0.5 g, 2.5 mmol) was dissolved in DMF (11.7 mL 152 mmol) with stirring (referred to as Solution B). Solution B was slowly added to Solution A in a Teflon-lined steel autoclave and allowed to react at 150 °C for 48 hr. The crystals were collected by filtration, washed with ethanol (3 x 50 mL) and dried in air to afford CPO-27-Zn as yellow/gold needles.

7.3.3.3. CPO-27-Mg

Magnesium nitrate hexahydrate (0.256 g, 1 mmol) and salicylic acid (0.276 g, 2 mmol) were dissolved in ethanol (1.8 mL, 30.4 mmol) (referred to as Solution A). 2,5-dihydroxyterephthalic acid (0.1 g, 0.5 mmol) was dissolved in DMF (2.40 mL 30.4 mmol) with stirring (referred to as Solution B). Solution B was slowly added to Solution A in a Teflon-lined steel autoclave and allowed to react at 150 °C for 48 hr. The crystals were collected by filtration, washed with ethanol (3 x 20 mL) and dried in air to afford CPO-27-Mg as bright yellow needles.

7.4.   Results and Discussion

7.4.1.   Formation of a Novel Monomeric Mg-dhtp Species[19]

A recent study on the effect of pH on the one-pot reflux synthesis of CPO-27-M describes attempts to prepare CPO-27-Mg using a 2:1 ratio of $NaOH:H_4dhtp$. However they report that no solid product could be obtained from the reaction system. This section describes the synthesis of a novel crystalline material of composition $Mg(H_2dhtp)(H_2O)_5 \cdot H_2O$ (known herein as Mg-dhtp) that may be obtained by lowering the amount of NaOH in reaction mixtures that is normally used to prepare CPO-27-Mg by the reflux method.

All previous literature states that neither CPO-27-Mg (Figure 7.1) or non-porous monomeric Mg-dhtp could be made without the required amount of base present in the synthesis. Not only could a new Mg-dhtp species be produced, but CPO-27-Mg could be synthesised in high purity albeit in low yield. From the synthesis, CPO-27-Mg was produced first as a bright yellow solid in low yield, before the by-product monomeric Mg-dhtp was produced after a further 3 days.
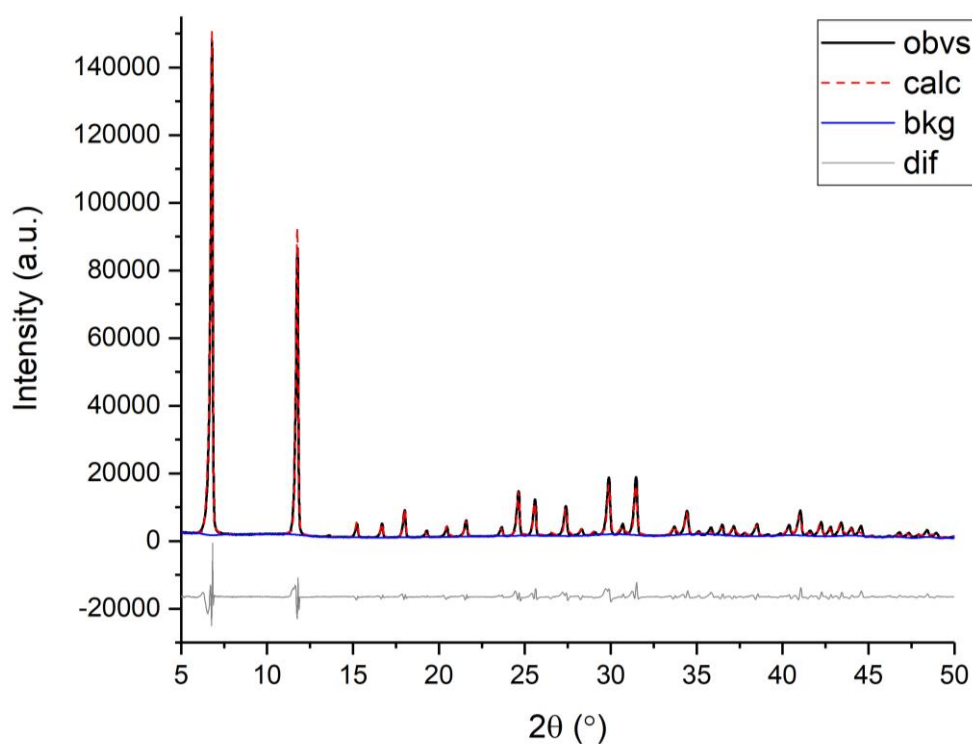

Figure 7.1. Rietveld refinement of dehydrated CPO-27-Mg in GSAS. Observed (black), calculated (red dashed), background (blue) and the difference between observed and calculated (grey). Rp = 9.5 %.

7.4.1.1. Crystal Structure Determination

Crystals of Mg-dhtp were coated in protective oil prior to mounting on a loop. Single crystal data were collected at 173 K on a Rigaku FR-X Ultra-high brilliance Microfocus RA generator/confocal optics and Rigaku XtraLAB P200 diffractometer system ($\lambda = 0.71075$ Å). The structure solution was obtained using SHELXT [20] and refined by full matrix on F^2 using SHELX-2014 [21] within the WINGX suite. All full occupancy non-hydrogen atoms were refined with anisotropic thermal displacement parameters. Aromatic hydrogen atoms were included at their geometrically estimated positions. Hydrogen atoms belonging to free and coordinated water molecules were fixed at a distance of 0.90 Å from the oxygen atom and 1.47 Å from the other hydrogens bound to the same oxygen, and their thermal displacement parameters linked to that of the oxygen to which they are bound.

7.4.1.2. Crystal Structure Analysis

Mg-dhtp was collected in space group $P2_1/n$ as brown single crystals consisting of a mononuclear $Mg(H_2dhtp)(H_2O)_5$ unit in which five water molecules and a monodentate H_2dhtp^{2-} anion are coordinated to an octahedral Mg^{2+} centre (see Table 7.2 for a list of Mg-O bond lengths and O-Mg-O angles). One water molecule of crystallisation is also present with intact phenolic -OH groups participating in intramolecular hydrogen bonds to the carboxylate oxygen atoms.

Table 7.2. Selected bond lengths (Å) and angles (°) for $Mg(H_2dhtp)(H_2O)_5 \cdot H_2O$

Mg(1)-O(1)	2.0231(11)
Mg(1)-O(1W)	2.1134(10)
Mg(1)-O(2W)	2.0402(11)
Mg(1)-O(3W)	2.0903(11)
Mg(1)-O(4W)	2.0416(11)
Mg(1)-O(5W)	2.0490(11)
O(1)-Mg(1)-O(2W)	88.73(4)
O(1)-Mg(1)-O(4W)	89.74(4)
O(2W)-Mg(1)-O(4W)	177.07(5)
O(1)-Mg(1)-O(5W)	178.38(5)
O(2W)-Mg(1)-O(5W)	91.90(4)
O(4W)-Mg(1)-O(5W)	89.57(4)
O(1)-Mg(1)-O(3W)	95.69(4)
O(2W)-Mg(1)-O(3W)	92.15(4)
O(4W)-Mg(1)-O(3W)	90.49(4)
O(5W)-Mg(1)-O(3W)	85.78(4)
O(1)-Mg(1)-O(1W)	90.78(4)
O(2W)-Mg(1)-O(1W)	91.01(4)
O(4W)-Mg(1)-O(1W)	86.50(4)
O(5W)-Mg(1)-O(1W)	87.72(4)
O(3W)-Mg(1)-O(1W)	172.86(4)

The mononuclear Mg-dhtp units are arranged into columns that extend parallel to the *b*-axis (Figure 7.2). Within each column, the $Mg(H_2O)_5$ units like on the two outer edges, whilst the H_2dhtp units are directed towards the centre of the column. As such the H_2dhtp units interdigitate with each other, stacking in an ABAB fashion along the length of the column. Adjacent H_2dhtp anions participate in offset π-π interactions, with close contact C-C separations of 3.35 Å to 4.0 Å and close contact C-O separations of 3.42 Å to 3.43 Å.
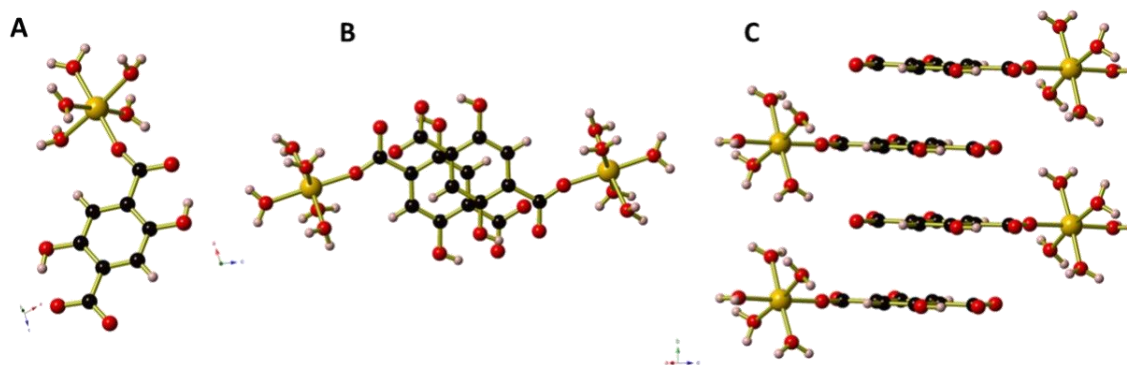
Figure 7.2. a) The monomeric $Mg(H_2dhtp)(H_2O)_5$ unit in $Mg(H_2dhtp)(H_2O)_5 \cdot H_2O$. The columns of $Mg(H_2dhtp)(H_2O)_5$ units as viewed b) parallel to and c) perpendicular to the direction of the column. The water of crystallisation has been omitted for clarity.

Hydrogen bonding interactions between the coordinated water molecules and carboxylate oxygen atoms cross-link the columns to form hydrogen bonded sheets that extend parallel to the 101 plane (Figure 7.3).

Further hydrogen bonds between the coordinated water molecules and phenolic hydroxyl groups connect the mononuclear units into a complex 3-dimensional hydrogen-bonded framework (Figure 7.4). The non-coordinated water molecules occupy the spaces between the sheets, and participate in hydrogen bonds with three mononuclear Mg-dhtp units belonging to two different sheets (see Table 7.3 for hydrogen bond lengths and angles).
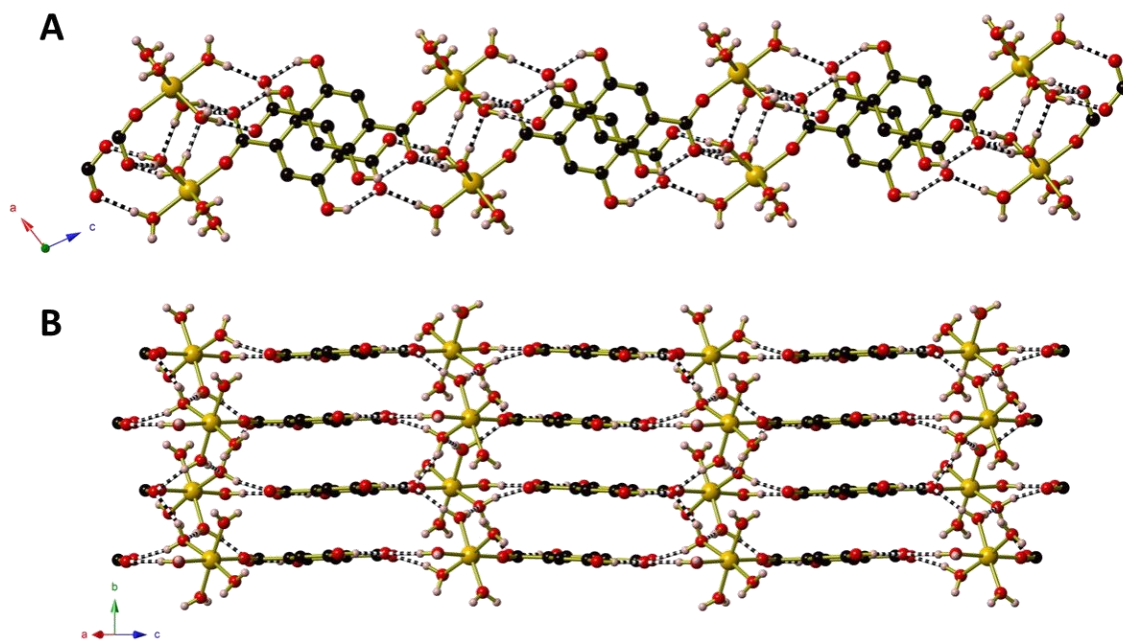
Figure 7.3. The hydrogen bonded sheets of Mg(H$_2$dhtp)(H$_2$O)$_5$ units as viewed a) along the edge of the sheet and b) perpendicular to the plane of the sheet. Hydrogen bonds are depicted as black-and-white striped bonds. Aromatic hydrogen atoms have been omitted for clarity.
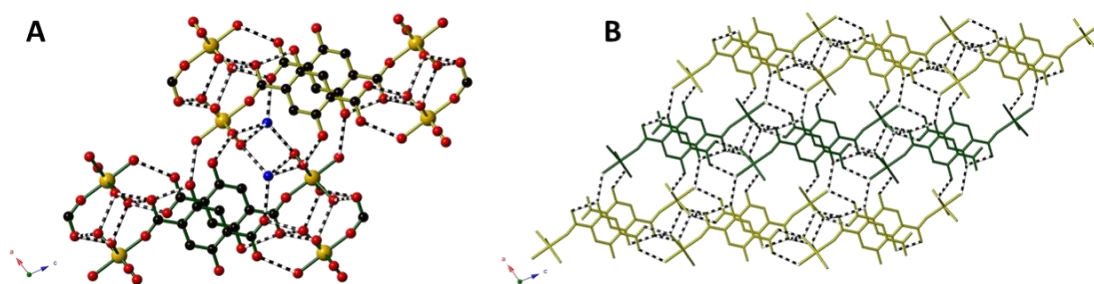

Figure 7.4. The view along the *a*-axis of the hydrogen bonded network of Mg(H$_2$dhtp)(H$_2$O)·5H$_2$O. a) The location of the water molecules (shown in blue) within the hydrogen bonded framework. One hydrogen bonded sheet is highlighted using green bonds. b) The full network. Non-coordinated water molecules and hydrogen atoms have been omitted for clarity.

Table 7.3. Hydrogen bonds for Mg(H$_2$dhtp)(H$_2$O)$_5$·H$_2$O (Å and °).

D-H···A	d(D-H)	d(H···A)	d(D···A)	<(DHA)
O(3)-H(3)···O(2)	0.84	1.79	2.5334(14)	147.2
O(6)-H(6)···O(5)	0.84	1.75	2.4926(14)	147.0
O(2W)-H(2A)···O(6W)	0.892(9)	1.900(10)	2.7825(14)	170.0(15)
O(6W)-H(6A)···O(1W)^I	0.898(9)	2.168(10)	3.0020(14)	154.1(14)
O(5W)-H(5A)···O(5)^{II}	0.897(9)	1.819(9)	2.7154(14)	177.0(16)
O(3W)-H(3W)···O(4)^{II}	0911(9)	1.731(10)	2.6275(13)	167.4(15)
O(2W)-H(2W)···O(6) ^{III}	0881(9)	1.958(10)	2.8236(14)	167.3(15)
O(3W)-H(3A)···O(2) ^{IV}	0.897(9)	1.924(11)	2.7617(14)	154.7(15)
O(4W)-H(4A)···O(3W)^V	0.886(9)	1.849(9)	2.7334(13)	176.4(16)
O(4W)-H(4W)···O(2)^V	0.887(9)	1.885(11)	2.7361(13)	160.2(15)
O(5W)-H(5W)···O(3) ^{VI}	0.891(9)	1.856(10)	2.7416(14)	172.7(16)
O(6W)-H(6W)···O(4) ^{VII}	0.892(9)	1.853(10)	2.7397(15)	172.1(17)

This material is the first non-polymeric Mg-dhtp coordination compound to be reported. A search of the Cambridge Crystallographic Data Centre (CCDC) reveals five different coordination polymers derived from magnesium and the di-anion of 2,5-dihydroxyterephthalate. In addition to the aforementioned CPO-26-Mg and CPO-27-Mg, materials were prepared from DMF,[22] DMF in the presence of NEt$_3$,[23] aqueous DMA,[24] or aqueous N-methyl pyrrolidone.[25] As such, this is the first example of a material prepared from predominately aqueous solution.

7.4.2. The Effect of Base, Solvent and Temperature on the Synthesis of CPO-27[26]

This section focuses on an investigation into the effect of the metal cation, pH and solvent on the formation of CPO-27-Co, -Mg, -Ni, and -Zn at reaction temperatures from 78 °C (reflux) to -78 °C. All solids produced were characterised first by powder X-ray diffraction

(PXRD) and then the materials afforded at the lowest temperatures were investigated further using scanning electron microscopy (SEM).

Each CPO-27-M synthesis was carried out in a modified molar ratio of 2.5 : 5 : 10 : 304 for linker : metal salt : base : solvent. The acetate salt was used for Co, Ni and Zn and the nitrate salt for Mg. Under basic conditions the linker solution is assumed to be fully deprotonated and upon visual inspection of the mixture, the salt appears to be fully dissolved in the organic solvent. For syntheses undertaken at temperatures lower than 0 °C a solvent/dry ice bath was employed. Methanol and water were used as solvent for reactions at −20 °C and −40 °C, with acetone/dry ice used for all reactions considered at −78 °C. All reactions were carried out for 6 hr and a sample was taken halfway through the procedure to check the progress of crystallisation.

7.4.2.1. Characterisation Techniques

Powder X-ray diffraction (PXRD) data were collected on a Panalytical Empyrean diffractometer CuKα₁ radiation monochromated with a curved Ge(111) crystal in reflectance mode. Samples taken halfway through the reaction were loaded into capillaries and analysed on a STOE STADIP diffractometer operating Cu Kα₁ radiation. Powder X-ray patterns have been compared with an X-ray powder pattern of CPO-27-Zn, derived from single crystal data.

SEM imaging was carried out on a FEI Scios Dualbeam, with a resolution of 1 nm and a voltage of 2000 V to 30 kV. For the imaging, the SEM was operated between 1–5 kV at 10-50 pA. The unground sample, as synthesised, was placed on a carbon tab prepared, aluminium stub disc. Furthermore, the samples were brushed with Ag-paste and Au-sputter-coated (15 mA per 30 s).

7.4.2.2. The Effect of the Metal Cation

The study was split into two parts. First, CPO-27-M (M = Co, Mg, Ni, Zn) was formed in methanol as solvent as solvent with 1 M sodium hydroxide (NaOH) as a base to understand the effect the metal cation has on formation of a crystalline, porous MOF (**1**).

CPO-27-Zn(**1**) proved to be the most crystalline material formed, exhibiting high crystallinity and purity down to -78 °C. The two main peaks at 6.8 ° and 11.7 ° 2θ, which are characteristic for the CPO-27-M family, are clearly visible and show high intensity down to −78 °C. The fingerprint region can be seen clearly down to −40 °C. Apart from the latter mentioned, all materials have phase purity, the material obtained at −40 °C shows two additional non-CPO-27 peaks at 9.6 ° and 10.9 ° 2θ of low intensity (Figure 7.5).
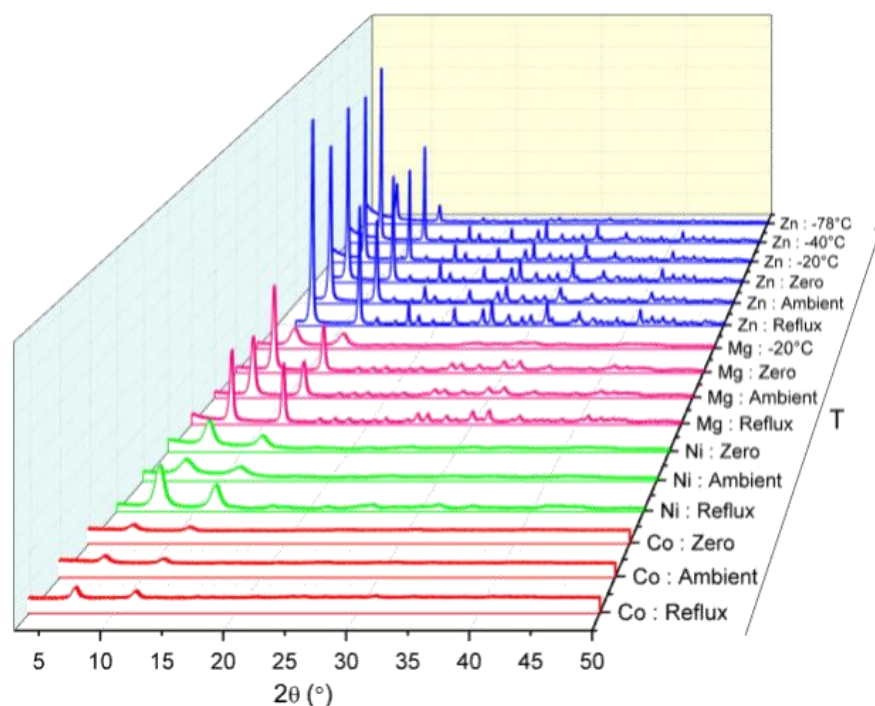

Figure 7.5. Comparison of the powder X-ray diffraction patterns for CPO-27-Co(**1**), -Ni(**1**), -Mg(**1**), and -Zn(**1**) from a MeOH-NaOH solution with increasing temperature. Co - red, Ni - green, Mg - pink, Zn - blue.

The CPO-27-Zn(**1**) sample synthesised at -78 °C shows less intensity in comparison to those synthesised at high temperatures. Therefore, it is assumed that the framework has not fully formed under such conditions, which is consistent with the reduced rate of reaction and reduced crystallinity whilst at lower temperatures.

The magnesium analogue, CPO-27-Mg(**1**), shows an interesting sensitive behaviour regarding the solvent and deprotonation of the acidic proton. Mg^{2+} is a relatively hard, hydrophilic cation, and with methanol as the lone solvent pure CPO-27-Mg(**1**) can be synthesised successfully down to -20 °C. Crystalline samples of the MOF are produced

preferentially at higher temperature (0 – 78 °C), with porous CPO-27-Mg(**1**) afforded. Reducing the temperature to -20 °C, the characteristic CPO-27 peaks can be seen, although visibly broadened, whilst the fingerprint region is no longer distinct.

The XRD patterns for CPO-27-M(**1**) (M = Co, Ni) show a poor signal:noise ratio for all temperatures. However, it can be stated that the framework has still formed, at least in part, as the characteristic CPO-27 peaks are clearly seen. Crystal field theory allows some elucidation into the effects of the d-block metals. We can class H_4dhtp as a weak field ligand as it binds through its oxygen atoms. This causes a small splitting in Δ between the t_{2g} and e_g orbitals, making it more favourable to put the electrons from the ligand into the high energy orbitals, and as such make it high spin. The lability of Co^{2+} is therefore reduced when the spin state is high spin rather than lower spin. For Ni^{2+}, only one paramagnetic spin state is accessible, and these unpaired e_g orbitals are very labile. However, when in comparison with Zn^{2+}, a full outer shell allows the cation to be very labile as it has the ability to rearrange its coordination sphere very readily, and therefore, has no preference to what is bound. From both crystal field theory and the experimental results that the metals behave with an order of lability of $Co^{2+} < Ni^{2+} < Mg^{2+} < Zn^{2+}$.

SEM studies were conducted on each of the materials, obtained from the lowest successful reaction temperature. Each sample was taken as synthesised and prepared for investigation without further grinding. Images were taken at scales of 1 mm – 10 µm to investigate the different morphologies. Figure 7.6 shows selected SEM images to highlight the difference between a transition metal and non-transition metal (Co vs. Zn). All materials show large agglomerates of a few hundred µm size, with sharp edges at 10 µm. At 100 µm the transition metal CPO-27-M(**1**) (M = Ni, Co) remain as large agglomerates and plates with sharp edges, whereas non-transition metal CPO-27-M(**1**) (M = Mg, Zn) show a more powdery, softer morphology. At 1 mm, all materials show small conglomerates with a "cotton-ball" morphology.
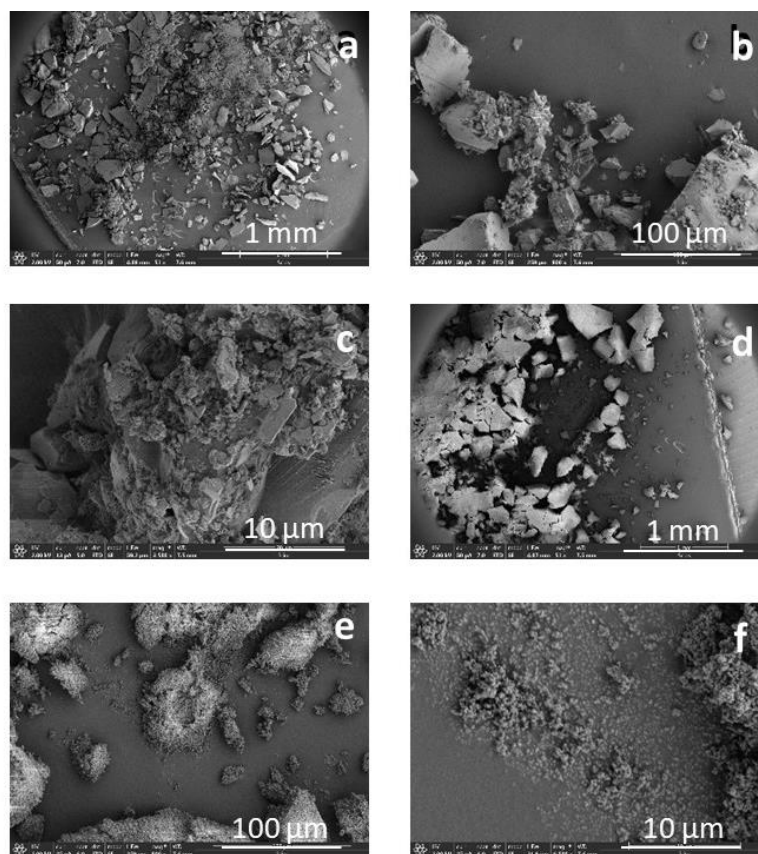
Figure 7.6. SEM images a-c for CPO-27-Co(**1**) afforded from a MeOH-NaOH solution at a reaction temperature of 0 °C; SEM images d-f show CPO-27-Zn(**1**) afforded from a MeOH-NaOH solution at -78 °C.

7.4.2.3. The Effect of Solvent

The second step in the study was to vary solvent and pH whilst keeping the metal cation constant. CPO-27-Zn was the most crystalline material formed down to -78 C in step 1 and was therefore chosen as the most suitable MOF to carry through to step 2. CPO-27-Zn was synthesised in different conditions of solvent and base: MeOH-TEA (**2**), MeOH-no base (**3**), THF-no base (**4**), THF-NaOH (**5**), and THF-TEA (**6**).

7.4.2.3.1. Methanol as Solvent

The synthesis procedure was analogous to the experimental with MeOH-NaOH. Keeping MeOH as a solvent, the base was switched for triethylamine (TEA). This solvent-base system

shows remarkably sustained crystallinity down to temperatures of -78 °C (Figure 7.7). After addition of the basic linker solution to the metal -salt solution, the bulky triethylammonium-ion shields access to the Zn^{2+} cations and therefore leads to a more controlled manner of formation and crystallisation. To monitor the rate of crystallisation, samples were taken half-way through the reaction time at 3 hr. At -78 °C, the characteristic CPO-27 peaks are already visible highlighting just how fast these materials can form even when kinetic motion is slowed down. The materials synthesised at -40 and -78 °C, show a shift of 0.2 2θ of each peak in the XRD. This can be explained by a shrinkage in unit cell dimensions at these lower temperatures. To ensure phase purity, the materials produced at these lower temperatures were compared against phase-pure CPO-27-Zn. No other phase was present in the MeOH-TEA solvent system.
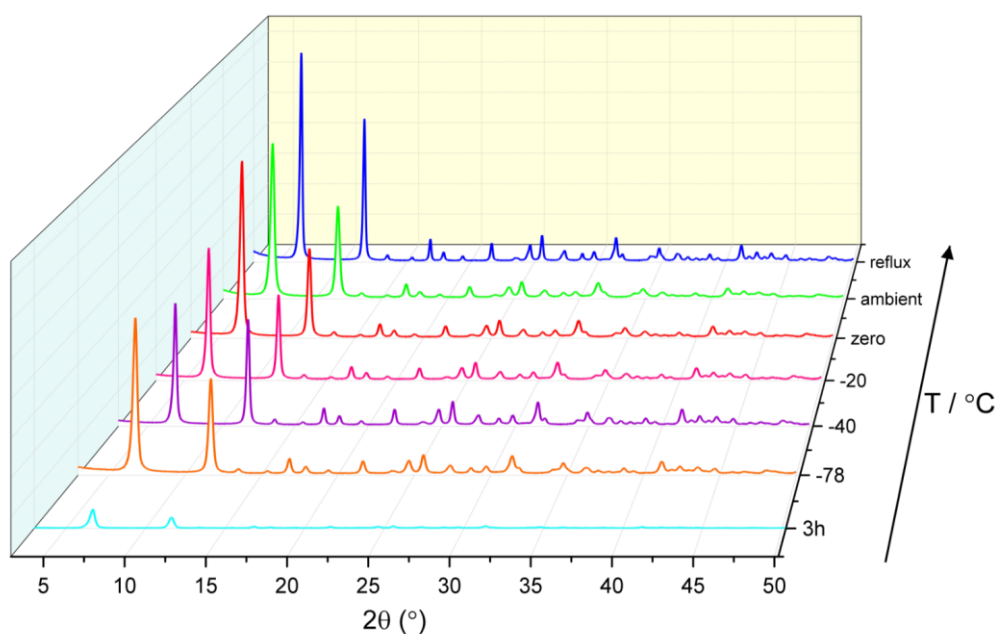

Figure 7.7. Powder X-ray diffraction patterns for CPO-27-Zn(**2**) afforded from a MeOH-TEA solution with temperature ranging from -78 °C to reflux. A sample was taken half way through the synthesis at the 3 hr mark and subsequently analysed, the 3 hr sample for the -78 °C reaction is presented here. Reflux – blue; ambient – green; 0 °C – red; -20 °C – pink; -40 °C – purple; -78 °C – orange; -78 °C 3 hr – cyan.

Similar to the Mg-dhtp monomeric structure previously discussed, a similar non-porous monomeric $Zn(H_2dhtp)(H_2O)_2$ (Zn-dhtp) species can be produced from a MeOH-H_2O solvent mixture at pH 7. This material was first reported in 2007 by Ghermani and co-

workers, and they found that a 3-dimensional non-porous network could be obtained when the linker is not fully deprotonated. In this work, the addition of the H_4dhtp linker to the translucent salt solution produced an off-white solid within minutes of first addition. This material can be produced down to 0 °C, albeit at a slower rate, whilst retaining the crystallinity and without significant structural changes in the unit cell parameters (Figure 7.8).
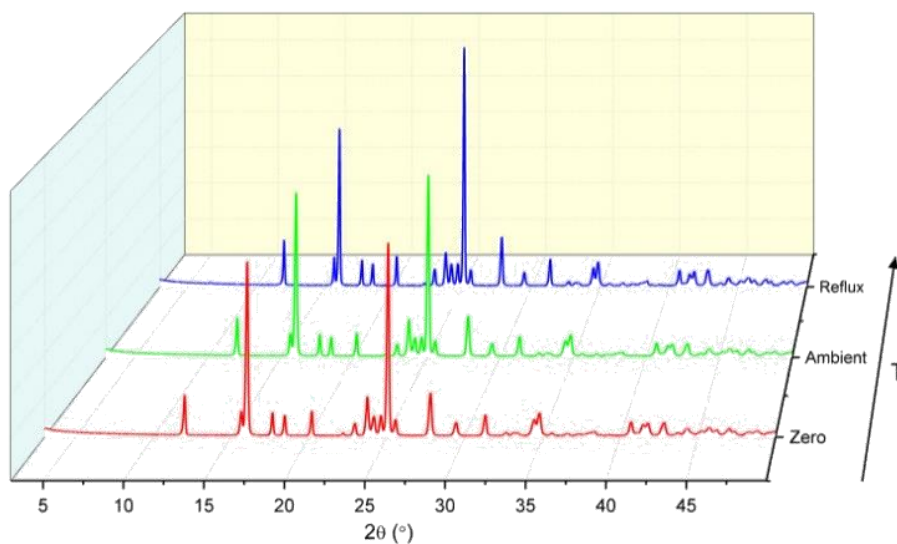

Figure 7.8. Powder X-ray diffraction patterns for a Zn^{2+} complex of 2,5-dihydroxyterephthalic acid afforded from a CPO-27-Zn(**3**) synthesis attempt in a methanolic solution without the presence of base, Reflux - blue; ambient - red; 0 °C - green.

To confirm the Zn-dhtp structure was as predicted, a Pawley refinement using the Topas academic suite was carried out using a model structure produced by Ghermani against in-house X-ray diffraction data (Figure 7.9).
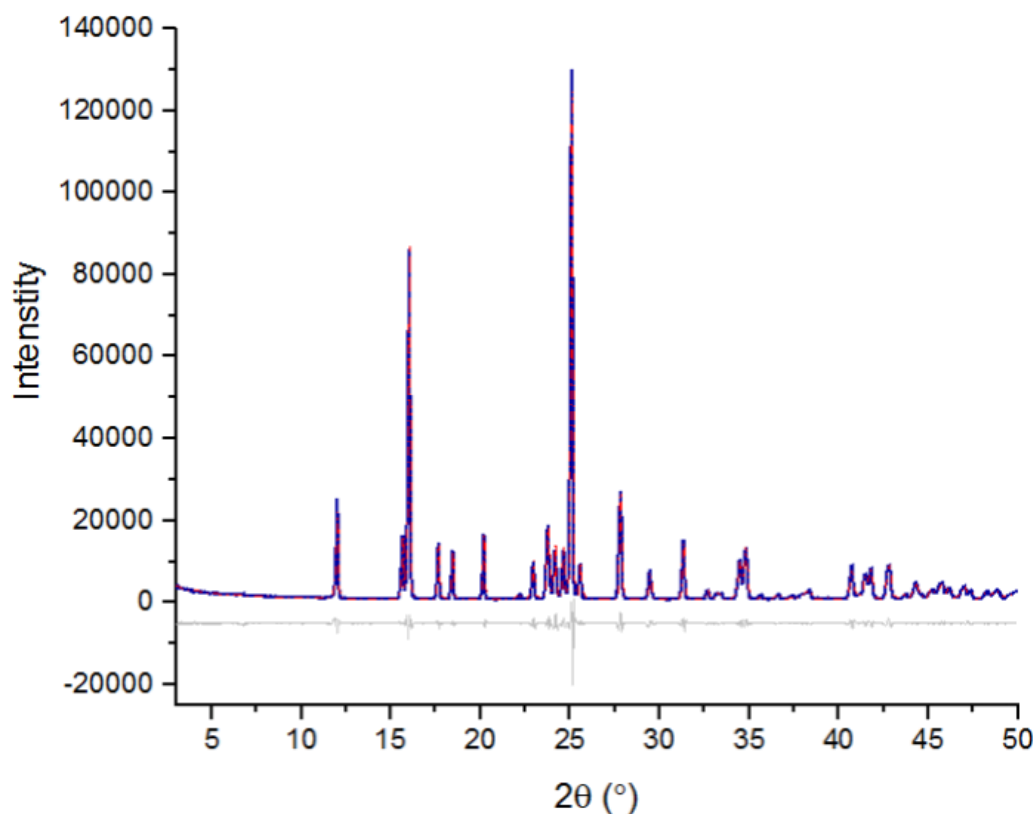
Figure 7.9. Topas Pawley refinement for [Zn(H$_2$dhtp)(H$_2$O)$_2$] afforded from a CPO-27-Zn(**3**) synthesis attempt in in MeOH without the presence of base. Experimental - blue, calculated model - red and the calculated difference plot - grey.

7.4.2.3.2. Tetrahydrofuran as Solvent

To understand the effect of solvent, MeOH was switched for THF and the following experiments conducted: THF-no base (**4**), THF-NaOH (**5**), and THF-TEA (**6**), all with zinc acetate as the metal salt. Interestingly, a different behaviour was observed upon changing the solvent system to aqueous THF.

For THF-no base (**4**), the reaction proceeded similarly to that of MeOH-no base (**3**). Upon addition of the aqueous linker solution to the stirred solution of the metal salt in THF, a milky-yellow suspension is produced after 5 min. This is once again slowed down with decreasing temperature. When the reaction was carried out at reflux and ambient temperature, it was clear to see from a comparison with pure CPO-27-Zn that the product produced is not phase-pure (Figure 7.10). This phase was identified as the monomeric

species discussed earlier. The product synthesized at 0 °C began to show loss of crystallinity when in comparison to higher temperatures, with the XRD pattern showing just the characteristic low angle and fingerprint peaks of CPO-27-Zn. The partial solubility of the H_4dhtp linker in THF can account for this. During the addition of the linker suspension, the linker gradually dissolves in the $THF-H_2O$ solvent mixture, while the dissociated acetate-ion of the zinc salt can slowly, and in a controlled manner, deprotonate the linker. However, the reduction of temperature has a substantial impact on the solubility of each reagent. Therefore, we assume that a further reduction of the reaction temperature may lead to pure CPO-27-Zn but also continue to reduce the solubility and slow down the rate of formation.
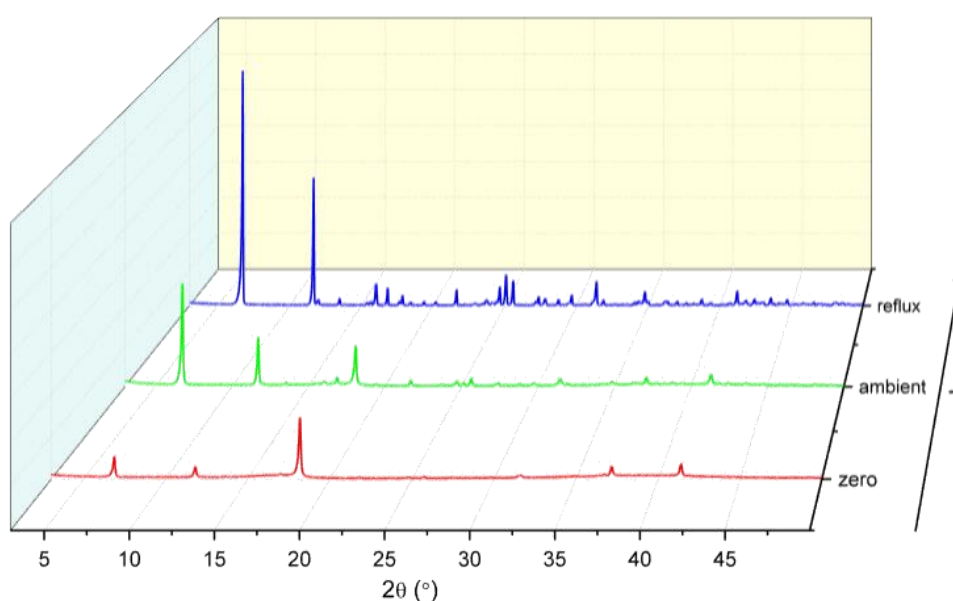

Figure 7.10. Powder X-ray diffraction patterns for CPO-27-Zn(**4**) afforded from a THF solution without base. Products decrease in crystallinity and purity as the temperature is decreased towards 0 °C. Reflux - blue; ambient - green; 0 °C - red.

Comparable to when methanol was used as solvent, both NaOH and TEA were used as base with THF, this produced a more controlled formation of the CPO-27 framework at lower temperatures. With NaOH (Figure 7.11), all patterns show a shoulder at 6° 2θ and another broad peak in the fingerprint area at 33° 2θ. The shoulder on the first main peak gradually loses intensity, as the reaction temperature gets colder.
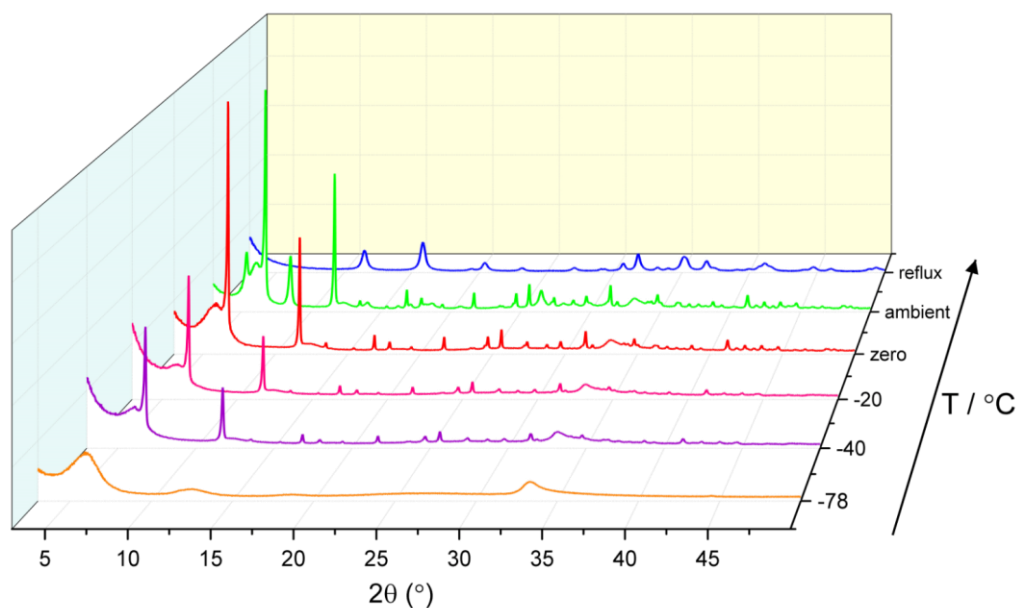
Figure 7.11. Powder X-ray diffraction patterns for CPO-27-Zn(**5**) afforded from a THF-NaOH solution with a temperature range from reflux to -78 °C. Reflux - blue; ambient - green; 0 °C - red; -20 °C = pink; -40 °C - purple; -78 °C – orange.

Interestingly, a sample taken after 3 hr for the reaction at $-40\,°C$ shows neither the shoulder nor the high angle peak, while characteristic parts of the framework are already formed (Figure 7.12), suggesting that a shorter reaction time of 3 hr may be suitable for this solvent system

As the linker is already deprotonated before mixing with the salt solution, it is determined that at warmer temperatures, the deprotonated linker is reactive enough for competing reaction pathways. Cooling the reaction down, slows down the kinetics of the molecules in solution, allowing for a more controlled formation of the MOF.
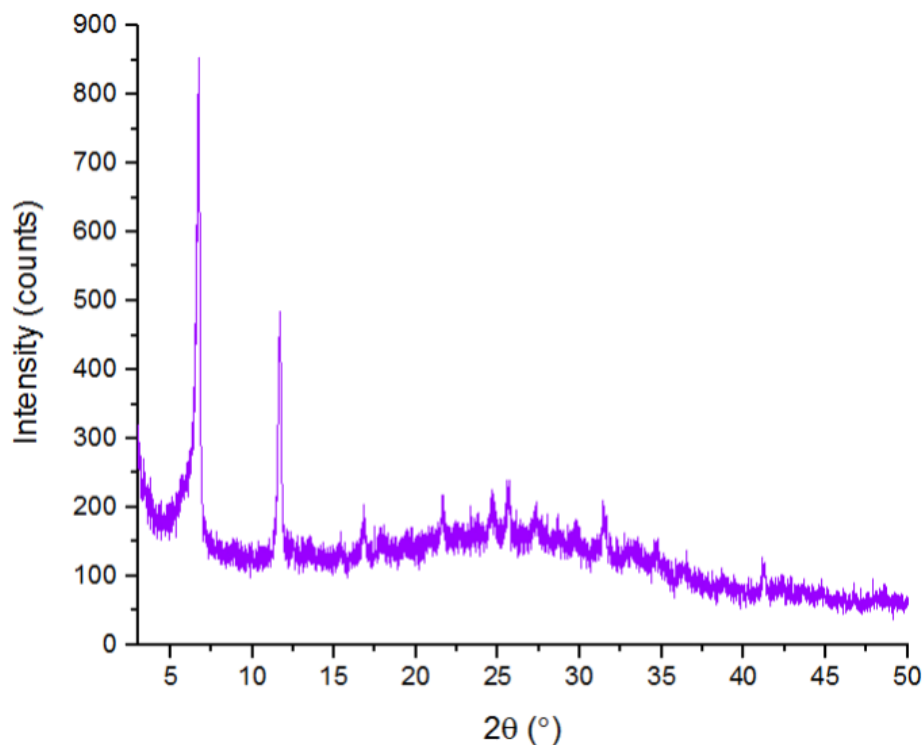
Figure 7.12. Powder X-ray diffraction pattern for CPO-27-Zn (**5**) at -40 °C at 3 hr.

Similar findings can be found for the reaction system THF-TEA, with crystalline samples produced at lower temperatures (Figure 7.13). The desired framework can be afforded by decreasing the temperature to ambient conditions, once again a shoulder at 6° 2θ can be seen indicating a change in the size and shape of the unit cell of the MOF. Further reduction of the temperature to −20 °C yields CPO-27-Zn materials without changes in the unit cell, in a controlled manner. When the synthesis was conducted at −40 °C the material loses crystallinity and the characteristic low angle peaks almost disappear. Again, fully formed crystalline MOF samples can be seen after 3 hr at all temperatures except reflux, as such showing that the reaction time in THF is too long after 6 hr.
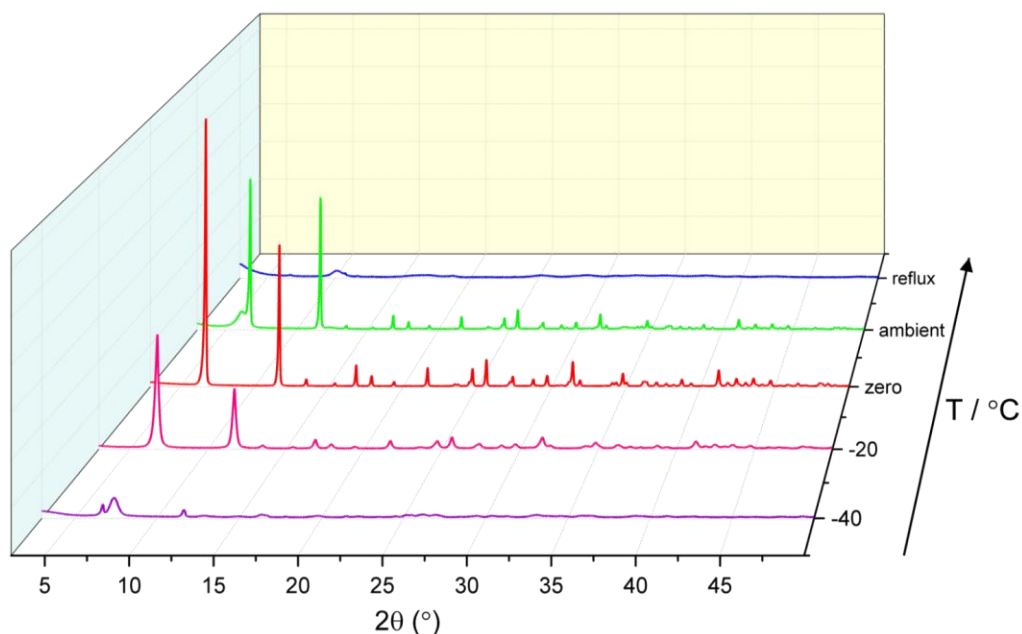
Figure 7.13. Powder X-ray diffraction patterns for CPO-27-Zn(**6**) afforded from a THF-TEA solution with changing temperature. Only products afforded from reactions conducted at 0 and -20 °C yielded phase pure results. Reflux – blue; ambient – green; 0 °C – red; -20 °C – pink, -40 °C – purple.

From the SEM analysis of the remaining zinc samples in different solvent systems, it became clear that the solvent makes a large impact on the morphology of the desired MOF (Figure 7.14). Solids produced from all methanolic solvents afford "cotton-ball" like morphologies with the monomeric species yielding a very fine powder and at higher scale, agglomerates built up from plates. However, when the solvent is changed to THF, the morphology of the MOF changes. For THF with base (NaOH, TEA) low scale images show powdery agglomerates without sharp edges. Flake-like agglomerates, built up from rods are seen at 100 µm. Images at increased scale show these rods more clearly. Interestingly, the cotton-ball like morphology is once again seen for the sample obtained from an aqueous THF solution without base. Therefore, we can conclude that protic solvents, such as methanol, yields ball-like morphologies. Contrary to this, when an aprotic solvent, tetrahydrofuran, is used with a base the morphology changes and elongates into rods.
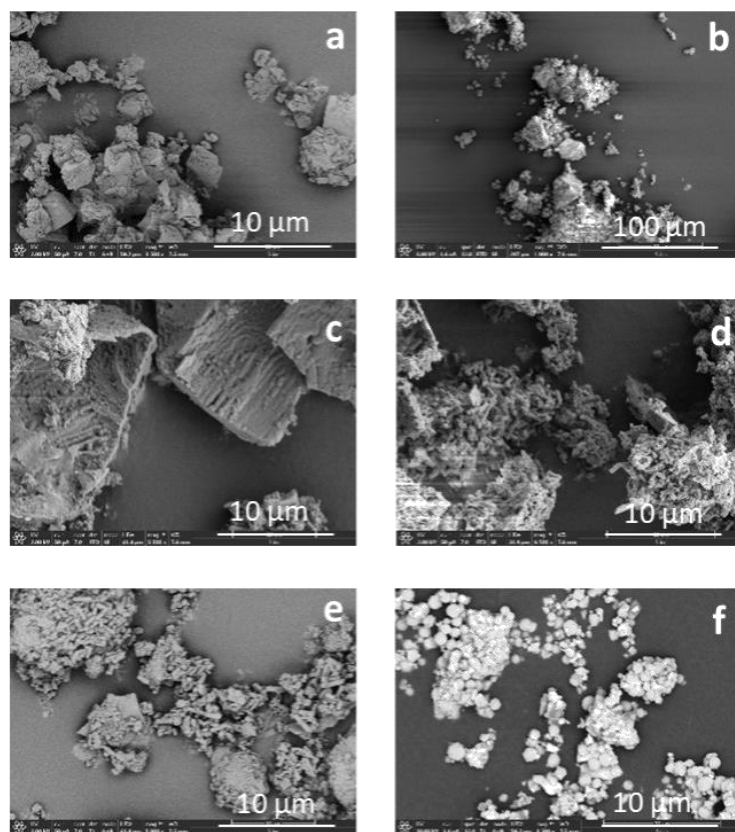
Figure 7.14. SEM images for CPO-27-Zn afforded from: a - MeOH-H_2O solution without base at ambient temperature (**3**); b - MeOH-TEA solution at -78 °C (**2**); c + d – THF-NaOH solution at -40 °C (**5**); e – THF-TEA solution at -78 °C (**6**); f – THF-H_2O solution without base at ambient temperature (**4**).

7.4.3. Acid Modulated Synthesis of CPO-27 and UTSA-74[28]

Single crystals of the CPO-27 family of MOFs have always been elusive and relatively difficult to afford. With previous literature stating that liquid water or base was necessary in the reaction mixture, the aim was to remove the base and replace with a more environmentally friendly acid.

With the use of acid modulators in the reaction system, CPO-27-Mg, -Zn and its recently discovered analogue UTSA-74 have been prepared in high purity, with single crystals large enough to be measured on an in-house diffractometer. Each material was prepared under solvothermal conditions at 150 °C without the need for the necessary base or added liquid water, hence conclusively disputing these components as being essential for synthesis of the target compounds. Base is a problem for the environment so replacing this with an acid

modulator is preferred. The next step would be to remove the harsh organic polar solvent to further decrease the environmental impact.

The MOFs were analysed by powder X-ray diffraction (PXRD), single crystal X-ray diffraction (SCXRD), and scanning electron microscopy (SEM). UTSA-74 is a recently discovered analogue of CPO-27-Zn and is of much interest due to its dual channel system.

7.4.3.1. Characterisation Techniques

CPO-27-Zn, -Mg samples large enough for "in-house" diffraction were collected at 173 K on a Rigaku MM-007HF High Brilliance RA generator/confocal optics taLAB P100 diffractometer [Cu Kα radiation (λ = 1.54187 Å)]. UTSA-74 samples were collected at 93 K on a Rigaku FR-X Ultrahigh Brilliance Microfocus RA generator/confocal optics with XtaLAB P200 diffractometer [Mo Kα radiation (λ = 0.71075 Å)]. The structure solution was obtained using SHELXT and refined by full-matrix least-squares against F^2 using SHELXL-2018-3 within the Olex2 suite. All full occupancy non-hydrogen atoms were refined with anisotropic thermal displacement parameters. Aromatic hydrogen atoms were included at their geometrically estimated positions. CCDC 1863524; 1863523; 1863522 contains the supplementary crystallographic data for this section, where the data can be obtained free of charge from The Cambridge Crystallographic Data Centre. With thanks to Mr Simon Vornholt for SCXRD characterisation.

A Sievers 280i Nitric Oxide Analyser (NOA) was used to determine the amount of NO released in each material. The NO-loaded MOFs were introduced to the NOA and exposed to moisture (relative humidity of 11%), in order to replace the NO bound to the material, with water molecules. The resultant gas expelled can then be recorded in ppm/ppb.

7.4.3.2. The Effect of Acid Modulator

Two acid modulators were employed, benzoic and salicylic acid. Salicylic acid is known for its use in face cream as an acne treatment and therefore we deem it to not have a large environmental impact. When the salicylic acid was employed with ethanol as a solvent, CPO-27-Zn and -Mg were formed as large yellow single crystals with high purity.

Upon changing the modulator from salicylic acid to benzoic acid, yellow-green-coloured crystals of the structural isomer, UTSA-74 were afforded. Each MOF was then analysed through powder XRD to ensure the sample was phase pure and that the bulk matched the single crystal (Figure 7.15). A clear shift in the PXRD to higher 2θ can be seen for UTSA-74, indicating a smaller *d* spacing between the channel systems. The decreased angle around the Zn^{2+} metal site giving a smaller pore volume throughout the material.
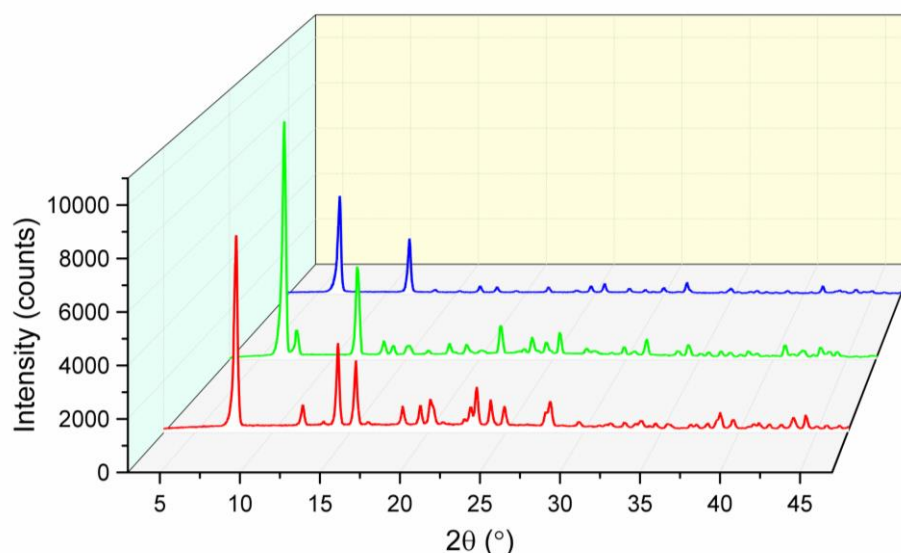

Figure 7.15. Powder X-ray diffraction patterns for CPO-27-Mg – blue, CPO-27-Zn – green, UTSA-74 – red.

7.4.3.3. The Effect of the Metal Salt

After confirming that each material was phase pure through PXRD, single-crystal X-ray diffraction analysis was conducted on each of the three samples. Due to the synthesis conditions, DMF was present in the structure solution and seen to bind to the 2+ metal site with full occupancy for CPO-27-Zn (Figures 7.16 and 7.17). For CPO-27-Mg however, the diffuse electron density was SQUEEZEDed out using the mask command in Olex2. The two hydrated metal salts that were used contained different amounts of water (monohydrate and hexahydrate for Zn and Mg respectively) and as such changed the amount of water present in the reacting mixture.
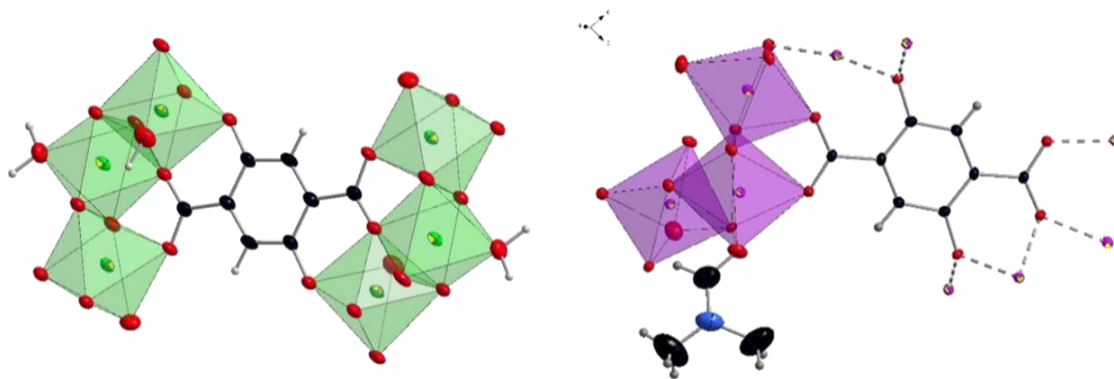
Figure 7.16. The chains of CPO-27-Mg (LEFT) and CPO-27-Zn (RIGHT) highlighting both the 2,5-dihydroxyterephthalic acid linker and attached DMF molecule to the Zn^{2+} metal site and coordinated water to the Mg^{2+} site. Viewed down the *b*-axis.

Figure 7.17. Structures of CPO-27-Zn with DMF molecules bound to the Zn^{2+} site (TOP), and CPO-27-Mg showing water molecules bound to the Mg^{2+} site (BOTTOM). Zn SBU – purple; Mg SBU – green. As viewed down the *a*-axis.

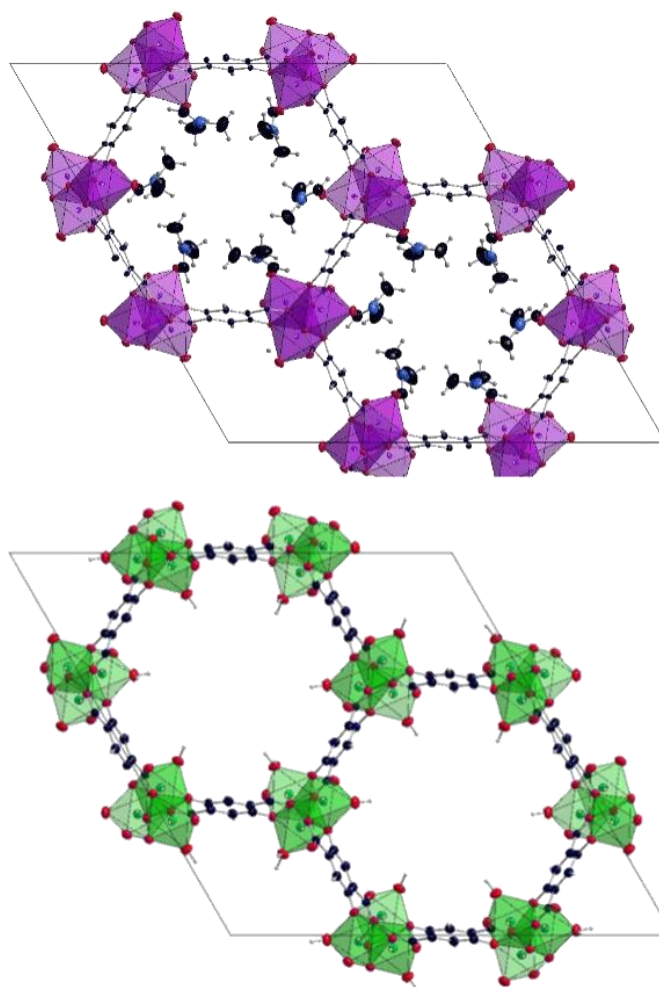Oxo-phyllic Mg^{2+} is a hard metal and as such it prefers to ionically bind through its co-ordinately unsaturated sites, and therefore we see water bind to these CUSs. Zn^{2+} is an intermediate acid (neither soft nor hard), so prefers to bind covalently. In CPO-27-Zn, DMF is seen to preferentially bind through covalent bonds. However, when we change the modulator to form UTSA-74, the pore size is too small to accommodate covalent bonding to DMF, and as such we see water ionically bind.

Both CPO-27 materials are hereby presented in space group $R\overline{3}$ with an R_1 factor of 4.77 and 6.24% for CPO-27-Zn and CPO-27-Mg, respectively. The structural isomer, UTSA-74, exhibited the zinc structural building unit (SBU) in both tetrahedral and octahedral coordination, thus giving rise to a large and small pore channel system (Figure 7.18).

UTSA-74 was prepared in conditions analogous to the CPO-27 materials. However, the proximity of the binding sites (4 Å) are too close to accommodate binding to DMF and as such DMF is not seen in the refinement. Each octahedral Zn^{2+} site has one axial bound water molecule pointing into the pore and one pointing out. Original literature presented the structure in space group $R\overline{3}c$; however, this was only seen when disorder was removed from the structure. We hereby present the space group as $R3c$, with all disorder in the structure accounted for, and an R_1 of 4.29%.
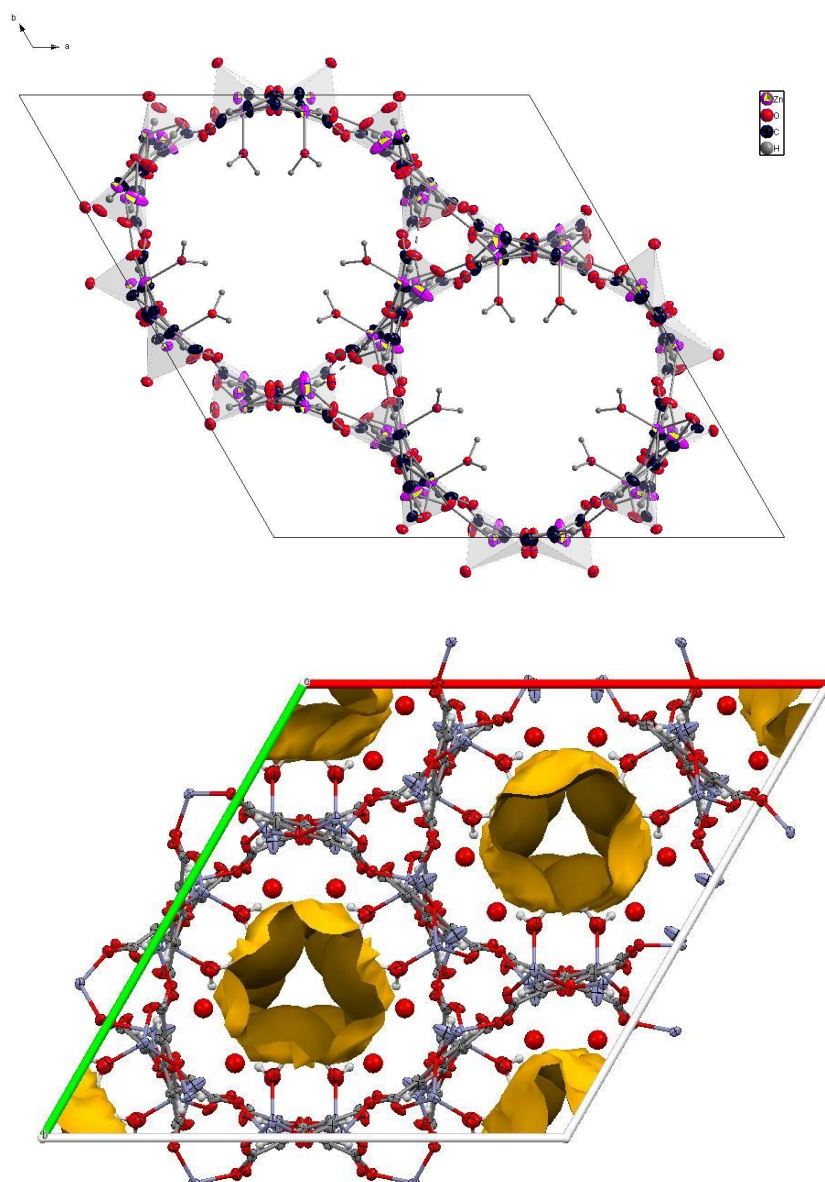
Figure 7.18. Structures of UTSA-74 showing Zn²⁺ in both tetrahedral and octahedral coordination, giving rise to a small and large pore channel system. Each octahedral Zn²⁺ has 1 axial bound water molecule pointing into the pore and 1 pointing out (TOP). Void space with solvent molecules bound, showing the pores are blocked. Solvent access = 14% (BOTTOM). Viewed along the *c*-axis

Each MOF was further analysed by scanning electron microscopy (SEM). Unlike the CPO-27 materials which presented a needle-like morphology, UTSA-74 afforded a morphology of large hexagonal rods (Figure 7.19).

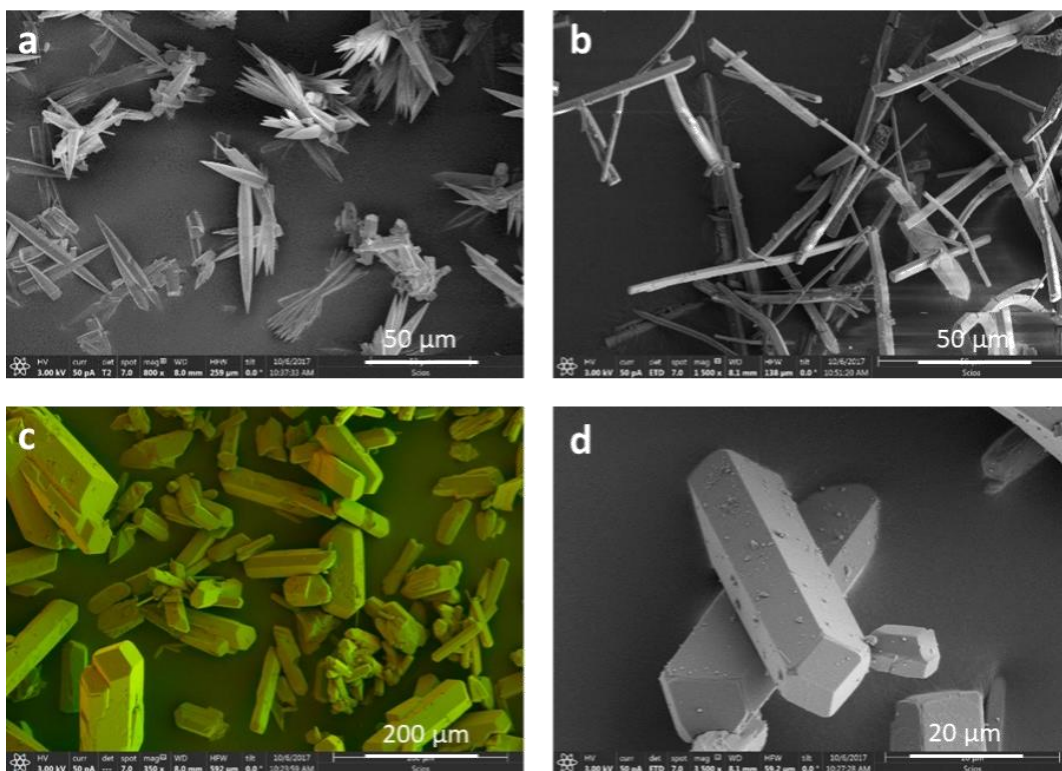**Figure 7.19.** SEM images of: a - CPO-27-Zn, 50 μm; b - CPO-27-Mg, 50 μm; c - UTSA-74, 200 μm; d – UTSA-74, 20 μm. Highlighting a needle morphology for the CPO-27 family and a rod formation for UTSA-74.

7.4.3.4. Activation Procedure

Each MOF underwent a 3-step activation procedure to remove modulator and DMF remaining in the pores.

1. Soxhlet extraction.
2. Solvent exchange.
3. Activation at high temperature and pressure.

First, each material was Soxhlet extracted for 5 days in the corresponding alcohol to remove any remaining modulator used in the synthesis from the pores. Second, each material underwent a solvent exchange procedure to ensure that any DMF remaining in the CPO-27-Mg and UTSA-74 pores and the DMF bound to the 2+ sites in CPO-27-Zn is removed. This was achieved by first activating in chloroform for 24 hr and then in water for 48 hr. To

ensure the structure had remained its integrity and no phase change had occurred, the MOFs were analysed by IR (Figure 7.20). TGA for CPO-27-Zn showed that DMF had been selectively removed and replaced with water (Figure 7.21).
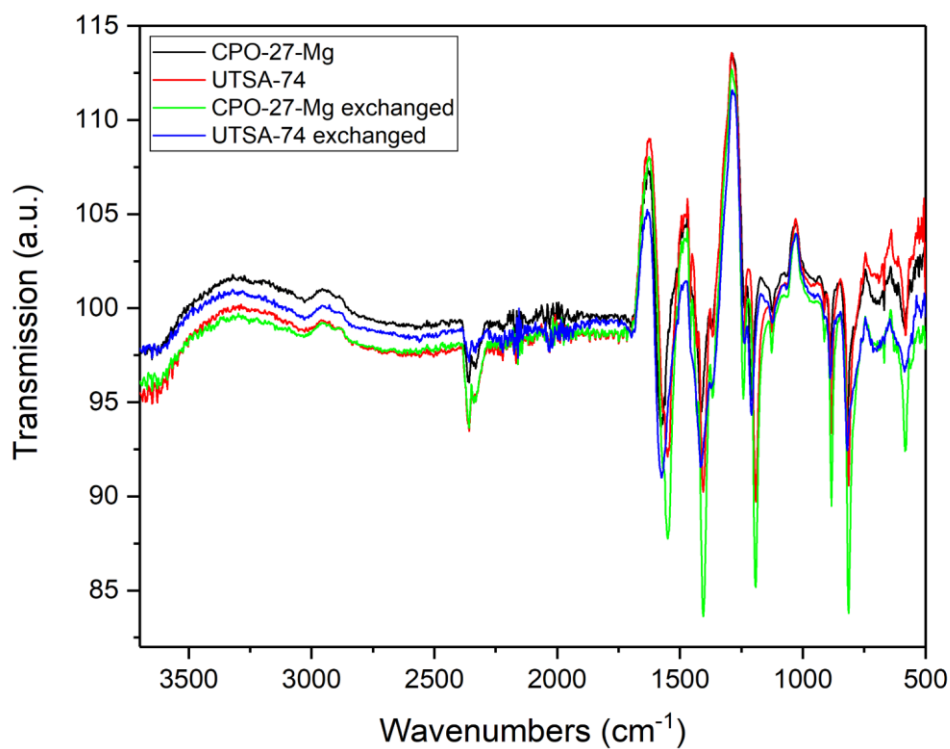

Figure 7.20. Infrared spectra for CPO-27-Mg and UTSA-74 pre- and post-activation with solvent exchange. CPO-27-Mg - black, CPO-27-Mg exchanged - green, UTSA-74 - red, UTSA-74 exchanged - blue.
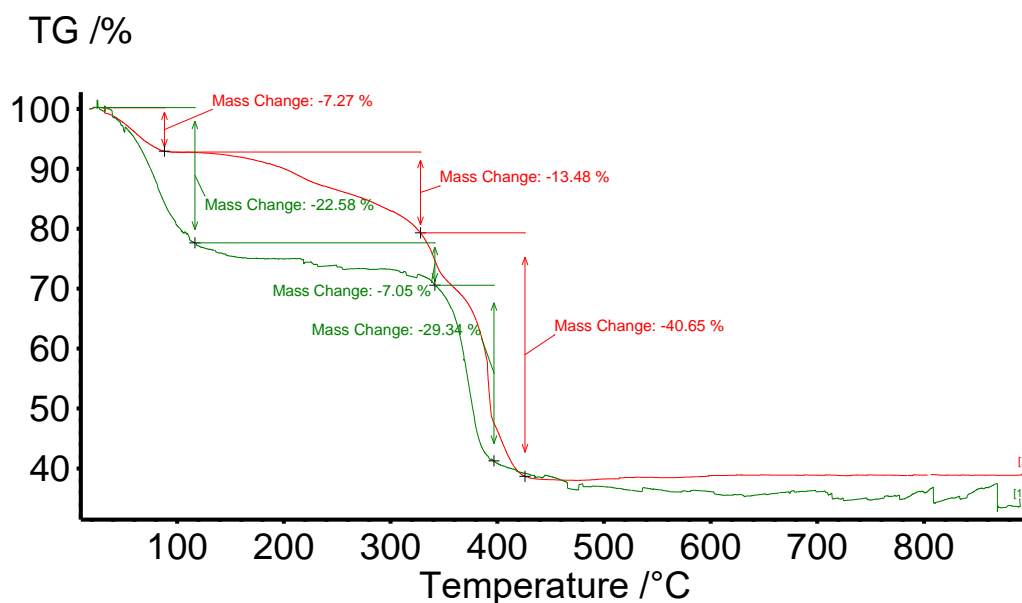
Figure 7.21. Thermogravimetric analysis for CPO-27-Zn. Red - pre-activation; Green - post-activation.

Finally, after exchange, each MOF was activated at 200 °C and 2 x 10^{-4} T. This selectively removes the water molecules bound to the CUSs and thus allows each of these sites to be able to take up and bind to other gas molecules such as nitric oxide.

7.4.3.5. Nitric Oxide Storage and Release

Due to a smaller pore size than the CPO-27 analogue, when coordinated water is present in the structure of UTSA-74, the pores are completely blocked with a solvent access of 14%. Upon activation at 200 °C under dynamic vacuum (2×10^{-4} T), the two axial water molecules can be selectively removed, generating open Zn^{2+} metal sites which are able to bind two gas molecules per metal centre on the pore surfaces of the 1-dimensional channels (Figure 7.22).

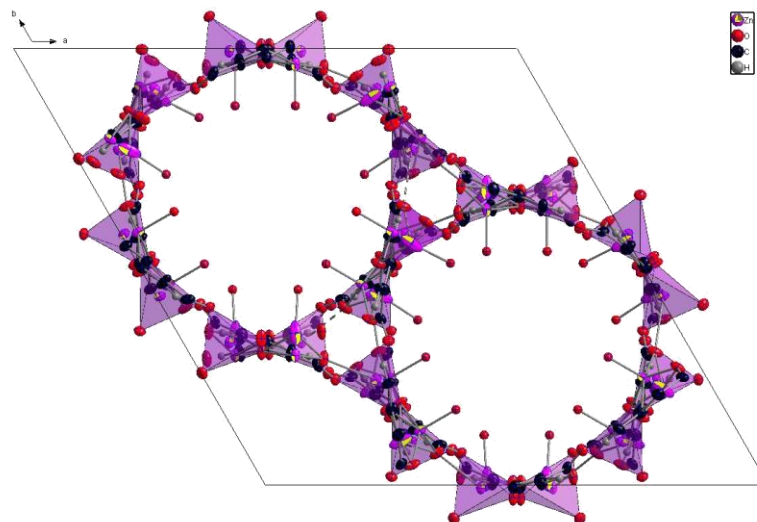**Figure 7.22.** Structures of UTSA-74 showing the coordinated unsaturated Zn^{2+} axial sites after activation. Viewed along the *c*-axis

Nitric oxide has a Jekyll and Hyde personality, in large amounts NO is extremely toxic, however in low doses, NO has a therapeutic vasodilating effect and as such can be incorporated into a MOF and used to coat medical devices such as stents and catheters.

As previously stated, both CPO-27-Zn and UTSA-74 were activated at 200 °C under dynamic vacuum to remove coordinated solvent molecules. The dehydrated materials were then subjected to nitric oxide gas, an immediate colour change, significantly intensifying the green colour, could be seen indicating that the gas had been adsorbed onto the CUSs. Loaded materials were then exposed to three consecutive vacuum/argon cycles to remove excessive physisorbed nitric oxide prior to analysis of nitric oxide release. Both MOFs release a therapeutic amount with CPO-27-Zn releasing slightly more than UTSA-74 with 0.088 and 0.067 mmol, respectively (Figure 7.23). Dependent on the application, either MOF could be used dependent on the length of release necessary.
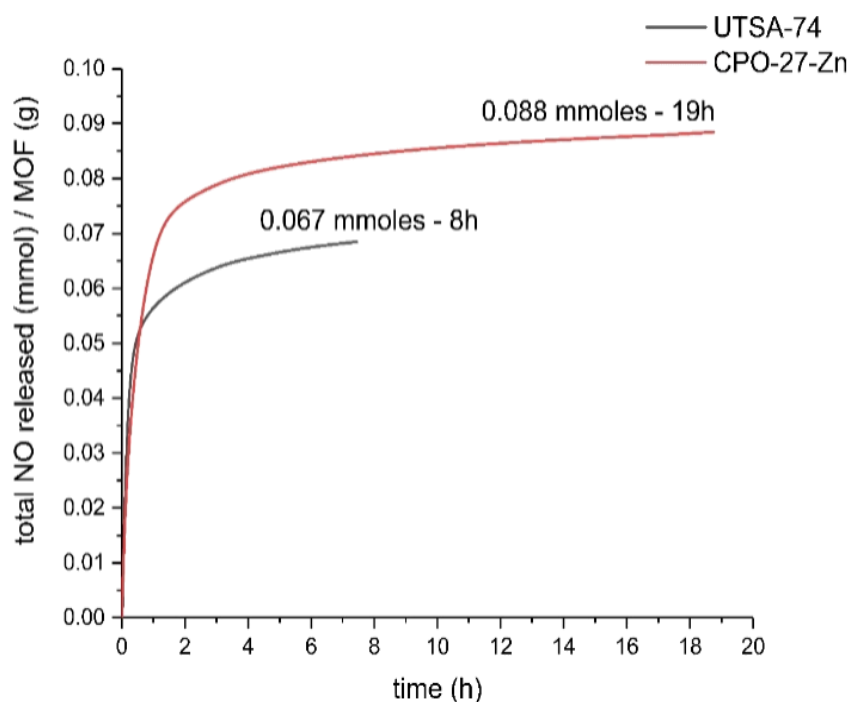
Figure 7.23. Nitric Oxide release profiles for UTSA-74 (black) and CPO-27-Zn (red)

7.4.3.6. The Hydrolysis of UTSA-74

Upon submerging the UTSA-74 crystals in water at room temperature, what at first glance looks to be a rapid single crystal – single crystal transformation is proceeding due to hydrolysis. This phenomenon has been first presented as an *in situ* study by Bueken *et al.*[27] Here we examine this hydrolysis through SEM and SCXRD. As shown in Figure 7.24, the UTSA-74 rods are slowly being "eaten away" and the newly formed CPO-27-Zn needles growing on the surface. From the SEM, it is apparent that a simple single crystal – single crystal transformation is not occurring. The mechanism appears to be in two steps. First a dissolution of the UTSA-74 into the water and then the formation of CPO-27-Zn on the surface of the remaining UTSA-74 crystals. As the newly formed crystals of CPO-27-Zn are not formed in solution, it seems that UTSA-74 is being used as a scaffold. After 3 hr, the UTSA-74 has been fully consumed and CPO-27-Zn is the sole material present. After full hydrolysis, the crystals of CPO-27-Zn are too small to diffract sufficiently for structural determination using an in-house instrument; however, a unit cell check confirmed that the structural transformation to CPO-27-Zn had taken place.
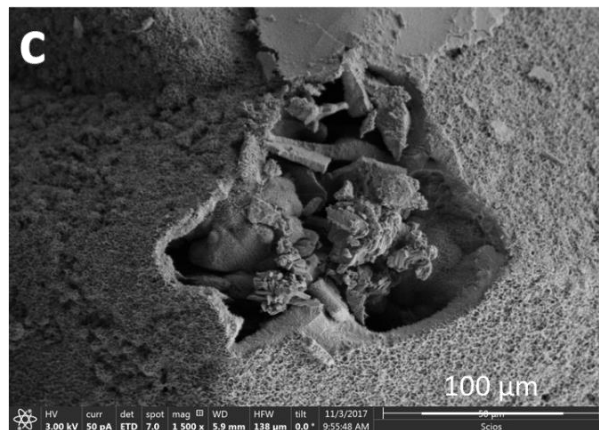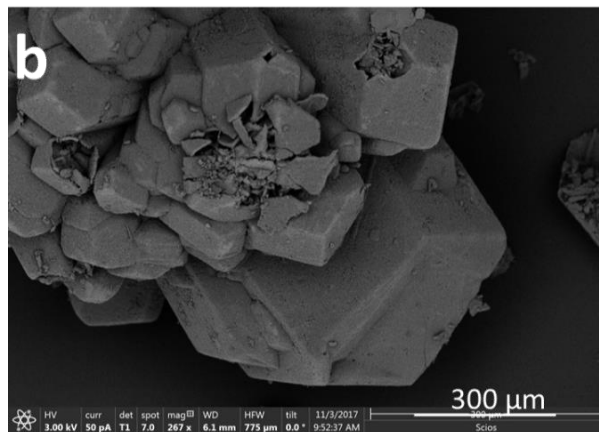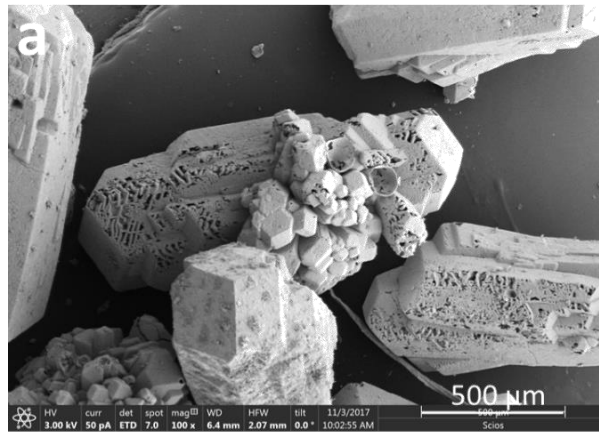
Figure 7.24. The single crystal - single crystal transformation of UTSA-74 to CPO-27-Zn by hydrolysis as shown by SEM images at a scale of: a - 500 µm; b - 300 µm; c - 100 µm.

7.5.   Conclusion

Altering the synthesis conditions drastically changes the outcome of the MOF produced. With a lower amount of base in the synthesis a novel Mg-dhtp non-porous material can be afforded, and removing the base altogether affords non-porous Zn-dhtp. It is now clear that non-transition metals (Mg, Zn) are easier to form than transition metals (Co, Ni), with CPO-27-Zn produced down to -78 °C in MeOH-NaOH and THF-NaOH. Reactions conducted in THF proved more difficult than in MeOH, with only colder temperatures producing a crystalline MOF, due to the relative rate of kinetic motion of molecules drastically slowed down.

Single crystal CPO-27-Mg, -Zn and its structural isomer UTSA-74 have been prepared through use of two acid modulators, salicylic acid and benzoic acid, respectively. Crystals large enough for "in-house" SCXRD were collected, where DMF was seen to bind to the 2+ metal sites in CPO-27-Zn, however although the synthesis conditions were analogous for UTSA-74, DMF is too large to bind due to the proximity of the binding sites (4 Å). The CPO-27 materials were afforded in a needle-like morphology, whilst the UTSA-74 produced larger rods. A clear dissolution-crystallisation transformation of UTSA-74 to CPO-27-Zn via hydrolysis was examined by SEM and a unit cell match confirmed. The uptake and release of nitric oxide was measured for each zinc-containing material and showed that each MOF produced a therapeutic amount of NO.

The work in this chapter clearly shows just how much we can affect the outcome of a synthesis, by changing the synthetic parameters by a little or a lot. This work will hopefully promote the synthesis of new isomers of known MOFs in the future.

7.6.   References

1   A. W. Carpenter and M. H. Schoenfisch, *Chem. Soc. Rev.*, 2012, **41**, 3742–52.

2   M. H. Rosnes, M. Opitz, M. Frontzek, W. Lohstroh, J. P. Embs, P. A. Georgiev and P. D. C. Dietzel, *J. Mater. Chem. A*, 2015, **3**, 4827–4839.

3   P. D. C. Dietzel, R. Blom and H. Fjellvåg, *Eur. J. Inorg. Chem.*, 2008, **2008**, 3624–3632.

4   W. Zhou, H. Wu and T. Yildirim, *J. Am. Chem. Soc.*, 2008, **130**, 15268–15269.

5   E. D. Bloch, L. J. Murray, W. L. Queen, S. Chavan, S. N. Maximoff, J. P. Bigi, R. Krishna, V. K. Peterson, F. Grandjean, G. J. Long, B. Smit, S. Bordiga, C. M. Brown and J. R. Long, *J. Am. Chem. Soc.*, 2011, **133**, 14814–22.

6   P. D. C. Dietzel, Y. Morita, R. Blom and H. Fjellvåg, *Angew. Chemie.*, 2005, **44**, 6354–6358.

7   P. D. C. Dietzel, B. Panella, M. Hirscher, R. Blom and H. Fjellvåg, *Chem. Commun.*, 2006, 959.

8   R. Sanz, F. Martínez, G. Orcajo, L. Wojtas and D. Briones, *Dalt. Trans.*, 2013, **42**, 2392–8.

9   N. L. Rosi, J. Kim, M. Eddaoudi, B. Chen, M. O'Keeffe and O. M. Yaghi, *J. Am. Chem. Soc.*, 2005, **127**, 1504–18.

10   A. C. McKinlay, B. Xiao, D. S. Wragg, P. S. Wheatley, I. L. Megson and R. E. Morris, *J. Am. Chem. Soc.*, 2008, **130**, 10440–10444.

11   S. Chavan, F. Bonino, J. G. Vitillo, E. Groppo, C. Lamberti, P. D. C. Dietzel, A. Zecchina and S. Bordiga, *Phys. Chem. Chem. Phys.*, 2009, **11**, 9811–22.

12   W. L. Queen, M. R. Hudson, E. D. Bloch, J. a. Mason, M. I. Gonzalez, J. S. Lee, D. Gygi, J. D. Howe, K. Lee, T. a. Darwish, M. James, V. K. Peterson, S. J. Teat, B. Smit, J. B. Neaton, J. R. Long and C. M. Brown, *Chem. Sci.*, 2014, **5**, 4569–4581.

13   S. Chavan, F. Bonino, L. Valenzano, B. Civalleri, C. Lamberti, N. Acerbi, J. H. Cavka, M. Leistner and S. Bordiga, *J. Phys. Chem. C*, 2013, **117**, 15615–15622.

14   U. Böhme, B. Barth, C. Paula, A. Kuhnt, W. Schwieger, A. Mundstock, J. Caro and M. Hartmann, *Langmuir*, 2013, **29**, 8592–600.

15   P. C. Dietzel, R. Blom and H. Fjellvåg, *Zeitschrift für Anorg. und Allg. Chemie*, 2009, **635**, 1953–1958.

16   L. Garzón-Tovar, A. Carné-Sánchez, C. Carbonell, I. Imaz and D. Maspoch, *J. Mater. Chem. A*, 2015, **3**, 20819–20826.

17   M. I. Gonzalez, J. A. Mason, E. D. Bloch, S. J. Teat, K. J. Gagnon, G. Y. Morrison, W. L. Queen and J. R. Long, *Chem. Sci.*, 2017, **8**, 4387–4398.

18   M. Märcz, R. E. Johnsen, P. D. C. Dietzel and H. Fjellvåg, *Microporous Mesoporous Mater.*, 2012, **157**, 62–74.

19   S. E. Henkelis, L. J. McCormick, D. B. Cordes, A. M. Z. Slawin and R. E. Morris, *Inorg. Chem. Commun.*, 2016, **65**, 21–23.

20   G. M. Sheldrick, *Acta Crystallogr. Sect. A Found. Crystallogr.*, 2008, **64**, 112–122.

21   G. M. Sheldrick, *Acta Crystallogr. Sect. C Struct. Chem.*, 2015, **71**, 3–8.

22   A. Cheansirisomboon, J. Salinas-Uber, C. Massera, O. Roubeau, S. Youngme and P. Gamez, *Eur. J. Inorg. Chem.*, 2014, **2014**, 4385–4393.

23   K. Jayaramulu, P. Kanoo, S. J. George and T. K. Maji, *Chem. Commun.*, 2010, **46**, 7906–8.

24   A. Douvali, A. C. Tsipis, S. V. Eliseeva, S. Petoud, G. S. Papaefstathiou, C. D. Malliakas, I.

Papadas, G. S. Armatas, I. Margiolaki, M. G. Kanatzidis, T. Lazarides and M. J. Manos, *Angew. Chemie*, 2015, **127**, 1671–1676.

25   A. Douvali, G. S. Papaefstathiou, M. P. Gullo, A. Barbieri, A. C. Tsipis, C. D. Malliakas, M. G. Kanatzidis, I. Papadas, G. S. Armatas, A. G. Hatzidimitriou, T. Lazarides and M. J. Manos, *Inorg. Chem.*, 2015, **54**, 5813–26.

26   S. M. Vornholt, S. E. Henkelis and R. E. Morris, *Dalton Trans.*, 2017, **46**, 8298–8303.

27   B. Bueken, H. Reinsch, N. Heidenreich, A. Vandekerkhove, F. Vermoortele, C. E. A. Kirschhock, N. Stock, D. De Vos and R. Ameloot, *CrystEngComm*, 2017, **19**, 4152–4156.

28   S. E. Henkelis, S. M. Vornholt, D. B. Cordes, A. M. Z. Slawin, P. S. Wheatley and R. E. Morris, CrystEngComm, 2019, Advanced Article.

CHAPTER 8: CONCLUSIONS AND FUTURE WORK

8.1.   Conclusions

All in-depth conclusions are stated within each experimental chapter. As such a brief conclusion for both the zeolite (Chapters 4, 5, and 6) and Metal-Organic framework (Chapter 7) will be stated below.

The ADOR process has 4 steps. The mechanistic analysis of the two most important steps, hydrolysis (Disassembly) and rearrangement (Organisation), has been discussed in Chapters 4, 5, and 6. Through *ex situ* powder X-ray diffraction, *in situ* Pair Distribution Function analysis and the subsequent analysis using solid-state reaction kinetics (Avrami-Erofeev model), an in-depth mechanism has been proposed. From these studies it has become apparent that there are 3 mechanisms occurring – 2 for hydrolysis and 1 for rearrangement. We first thought that there must only be 1 mechanism occurring during hydrolysis, we now know this is incorrect. By investigating the effect of constant humidity on the stability of **UTL**, we found that the bonds in the d4r are broken over a time period of 1 month. The structure then resembled uncalcined **UTL**. Therefore, it was clear that another process must have to be occurring to fully disassemble into IPC-1P. We saw that to fully disassemble into IPC-1P, liquid water is needed to "flush" the deintercalated species out of the layers and allow the layers to come closer together over time. From the PXRD data we know that this is rapid, with 60% of the d4r collapsing within 1 minute. As this is so fast we can conclude that the hydrolysis proceeds without having to overcome an activation barrier.

The rate of reaction for the rearrangement process is linearly related to the temperature of the system. With induction times greatly lengthened with decreasing temperature. This is the first time we have investigated the induction time by PXRD. The kinetics of reaction were quantified and an activation energy of 70.1 kJ mol^{-1} found. We found this to be relatively high for a deintercalation procedure, and it is hypothesised that the layers are too close together for silanol to get between the layers. This hypothesis needs to be researched further to fully understand whether this is indeed correct. At all temperatures above 70 °C, IPC-2P

formed preferentially and therefore we can say that in large volume conditions, all reactions afford IPC-1P first as the kinetic product before rearranging to form the thermodynamic product, IPC-2P.

Using PDF allowed for the mechanism to be studied *in situ*. The reactions conducted at Diamond Light Source used a static environmental cell and therefore could not accommodate stirring. This lack of stirring essentially reduced the removal of deintercalated species to zero and ultimately affected the product formed from reaction. For example, IPC-7P was afforded from a 6 M hydrochloric acid medium rather than the expected IPC-2P. It is clear that the conditions used in the *in situ* experiments must be strictly controlled to allow for direct comparison. Changing the reaction conditions by even a very small amount can have drastic consequences of the results obtained. Repeating these experiments at the Advanced Photon Source using a flow cell allowed for more quantitative results to be produced. As the hydrolysis is "flushed" through the cell, the deintercalated species are removed, and this can be seen by the appearance and disappearance of a Ge-Cl peak in the PDF. Once again, corroborating with the *ex situ* results in Chapter 5, IPC-1P is first produced as the kinetic product before self-rearranging to IPC-2P as the thermodynamic product. This is the first time we have been able to assign kinetic and thermodynamic labels to the mechanism and therefore vastly improves our understanding of the ADOR process. Although undertaking the reactions in flow allowed for more quantitative results to be obtained, the structural work and refinements need to be greatly improved. This can be done by using a Monte-Carlo type refinement that allows for a large amount of atoms whilst restraining the bond angles and lengths so that they refine in a controlled manner.

The synthesis conditions of CPO-27-M (M = Co, Mg, Ni, Zn) were altered and investigated upon. Lowering the amount of base in the synthesis of CPO-27-Mg and –Zn led to the formation of a novel monomeric Mg-dhtp species and the analogous monomeric Zn-dhtp species. Lowering the synthesis temperature, reduced the reaction kinetics, allowing CPO-27-Zn to be formed at -78 °C. Removing base from the system and replacing with acid modulators led to the formation of CPO-27-Mg, -Zn and UTSA-74 as single crystals. A dissolution-crystallisation transformation from UTSA-74 to CPO-27-Zn via hydrolysis was seen. Each MOF underwent nitric oxide storage and release, with a therapeutic release of NO seen for each. As the subtle changes in synthesis conditions greatly affect the outcome of the crystallinity and MOF produced, it is a hope that this will be able to be used in order to produce new isomers of known MOFs in the future.

8.2. Future Work

To complete the work on the ADOR process, the following will be undertaken:

1. The induction period will be analysed by ^{29}Si solid-state NMR to monitor changes in local order that cannot be monitored by powder X-ray diffraction.
2. Use the ADOR protocol devised in Chapter 4, to monitor the mechanism and see which products are able to be produced with other germanosilicates.
3. Calcination of Ge-**UTL** after 1 month at constant humidity, to understand whether after residing in constant humidity, the layered material produced is able to reform.
4. Modelling of each experiment from the *in situ* PDF flow data.

CHAPTER 9: APPENDIX

Table 9.1. Crystal data and structure refinement for CPO-27-Mg.

Identification code	CPO-27-Mg
Empirical formula	$C_8H_6Mg_2O_8$
Formula weight	278.75
Temperature/K	173(2)
Crystal system	trigonal
Space group	R-3
a/Å	25.9434(9)
b/Å	25.9434(9)
c/Å	6.8189(2)
α/°	90
β/°	90
γ/°	120
Volume/Å^3	3974.6(3)
Z	9
ϱ_{calc}g/cm^3	1.048
μ/mm^{-1}	1.444
F(000)	1278.0
Crystal size/mm^3	$0.05 \times 0.01 \times 0.01$
Radiation	CuKα (λ = 1.54184)
2Θ range for data collection/°	6.814 to 136.494
Index ranges	$-31 \leq h \leq 23, -23 \leq k \leq 31, -8 \leq l \leq 8$
Reflections collected	14270
Independent reflections	1617 [R_{int} = 0.0805, R_{sigma} = 0.0378]
Data/restraints/parameters	1617/2/84
Goodness-of-fit on F^2	1.134
Final R indexes [I>=2σ (I)]	R_1 = 0.0624, wR_2 = 0.1823
Final R indexes [all data]	R_1 = 0.0740, wR_2 = 0.1893
Largest diff. peak/hole / e Å^{-3}	0.92/-0.45

Table 9.2. Crystal data and structure refinement for CPO-27-Zn.

Identification code	CPO-27-Zn
Empirical formula	$C_{14}H_{16}N_2O_8Zn_2$
Formula weight	471.03
Temperature/K	173(2)
Crystal system	trigonal
Space group	R-3
a/Å	26.001(3)
b/Å	26.001(3)
c/Å	6.8271(9)
α/°	90
β/°	90
γ/°	120
Volume/Å³	3997.1(11)
Z	9
ϱ_{calc}g/cm³	1.761
μ/mm⁻¹	3.744
F(000)	2142.0
Crystal size/mm³	0.080 × 0.010 × 0.010
Radiation	CuKα (λ = 1.54187)
2Θ range for data collection/°	6.8 to 136.218
Index ranges	-30 ≤ h ≤ 30, -28 ≤ k ≤ 30, -8 ≤ l ≤ 8
Reflections collected	14156
Independent reflections	1615 [R_{int} = 0.0502, R_{sigma} = 0.0240]
Data/restraints/parameters	1615/0/120
Goodness-of-fit on F²	1.071
Final R indexes [I>=2σ (I)]	R_1 = 0.0477, wR_2 = 0.1496
Final R indexes [all data]	R_1 = 0.0567, wR_2 = 0.1578
Largest diff. peak/hole / e Å⁻³	1.97/-0.90

Table 9.3. Crystal data and structure refinement for UTSA-74.

Identification code	UTSA-74
Empirical formula	$C_8H_4O_7Zn_2$
Formula weight	342.85
Temperature/K	93.15
Crystal system	trigonal
Space group	R3c
a/Å	22.931(8)
b/Å	22.931(8)
c/Å	15.931(6)
α/°	90
β/°	90
γ/°	120
Volume/Å^3	7255(6)
Z	18
ϱ_{calc}g/cm^3	1.413
μ/mm^{-1}	2.988
F(000)	3024.0
Crystal size/mm^3	$0.1 \times 0.05 \times 0.05$
Radiation	MoKα (λ = 0.71075)
2Θ range for data collection/°	5.51 to 50.534
Index ranges	$-27 \leq h \leq 27$, $-27 \leq k \leq 26$, $-18 \leq l \leq 19$
Reflections collected	14776
Independent reflections	2934 [R_{int} = 0.0458, R_{sigma} = 0.0331]
Data/restraints/parameters	2934/9/169
Goodness-of-fit on F^2	1.181
Final R indexes [I>=2σ (I)]	R_1 = 0.0426, wR_2 = 0.1360
Final R indexes [all data]	R_1 = 0.0456, wR_2 = 0.1386
Largest diff. peak/hole / e Å^{-3}	0.97/-0.55
Flack parameter	0.278(9)